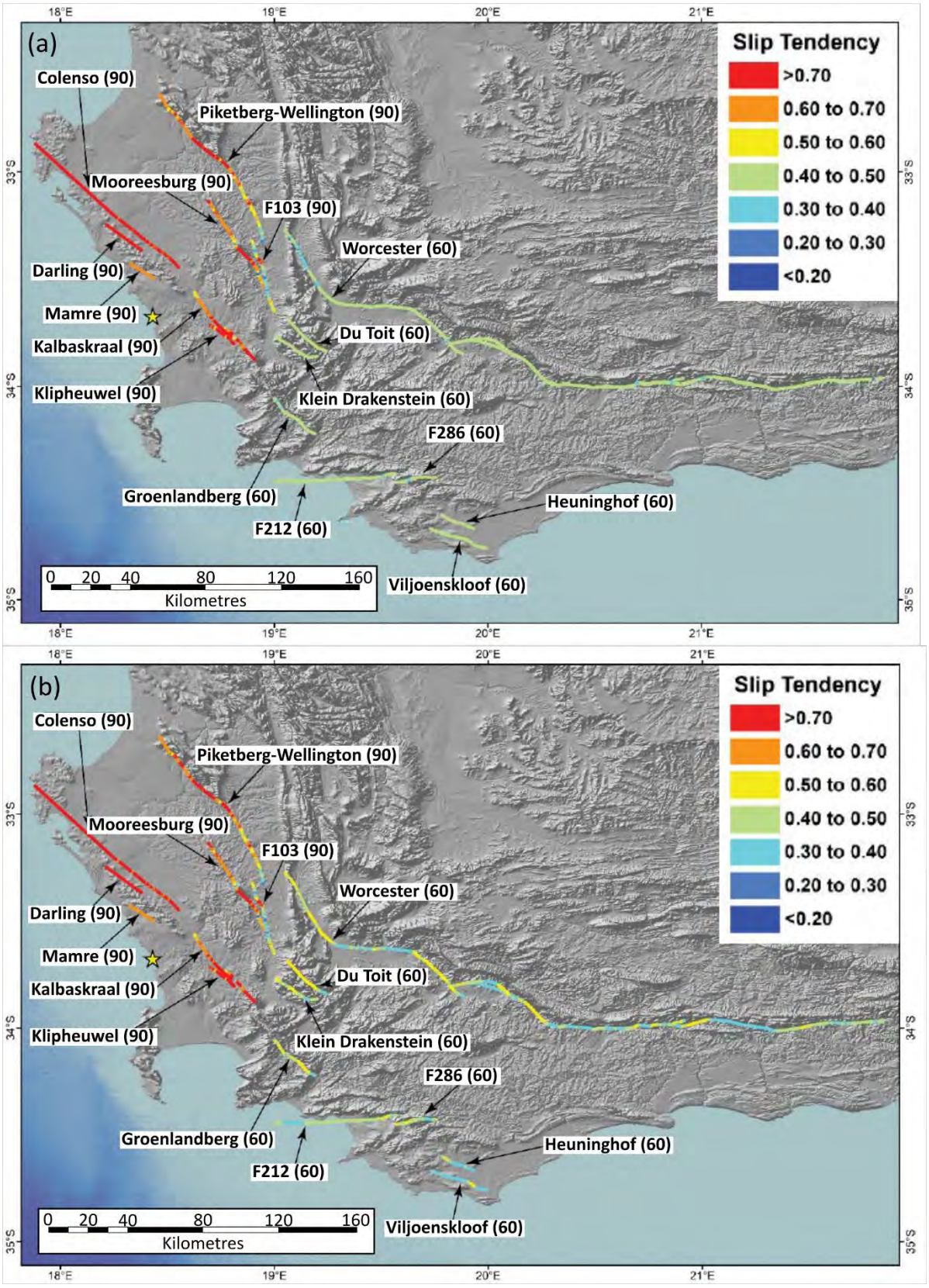

Figure 5-17. Maps depicting slip tendency with the most likely stress-state solution of (a) Φ = 0.54, (b) Φ = 0.29, and (c) Φ = 0.79, applied to a subset of 15-km long faults (90°- and 60°south-dipping) along the southwest coast of South Africa (Smart et al., 2023).

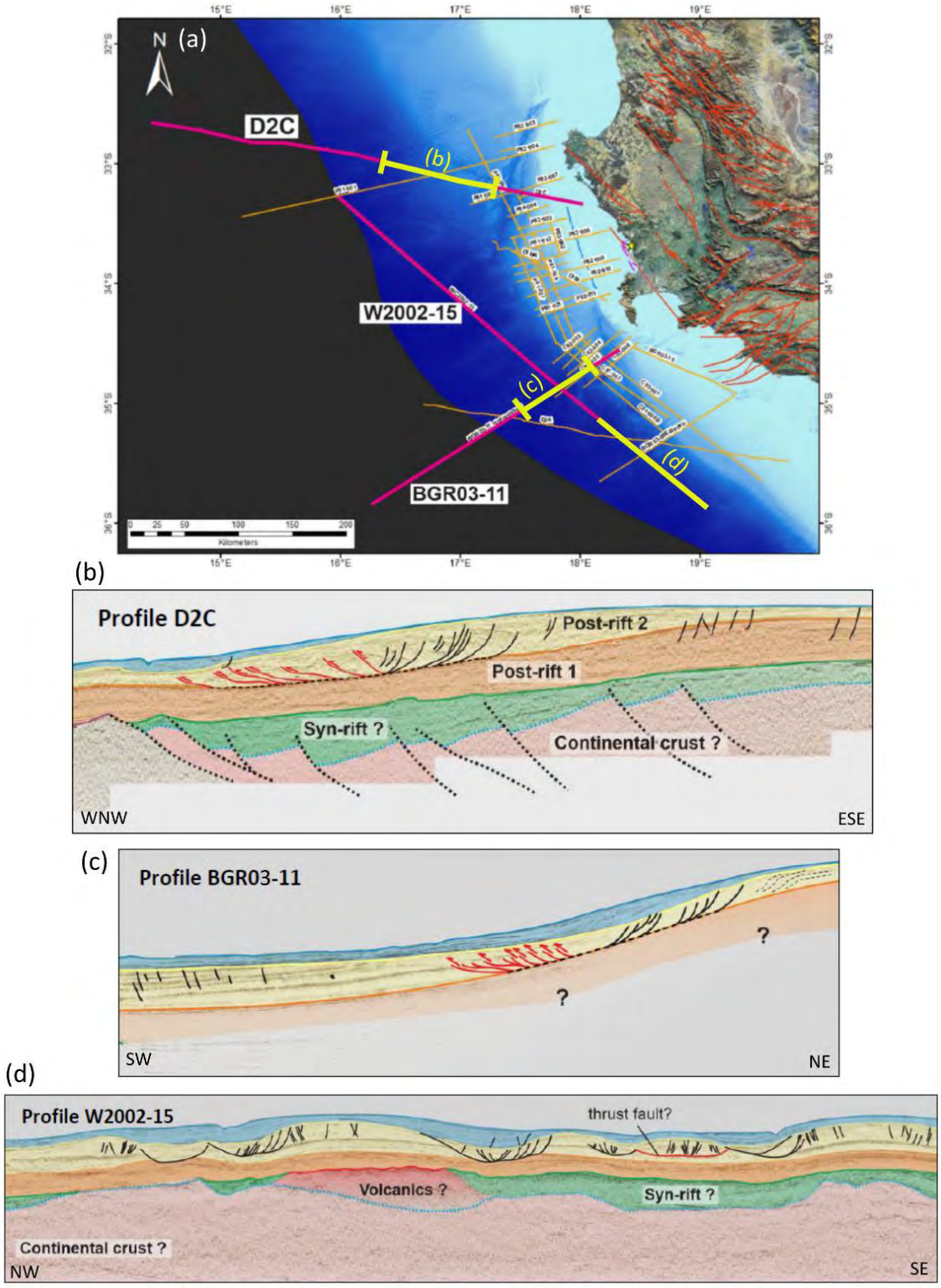

Figure 5-17. (a) Map showing the location of the three offshore seismic PASA profiles (D2C, W2002-15, BGR03-11) examined as part of the overall stress analysis. Sections lighted in yellow along the section lines present the portion of the profile depicted in b–d. (b) A geological interpretation of a portion of profile line D2C, (c) BGR03-11, and (d) W2002-15 (Smart et al., 2023).

5.2.6 Other supporting studies

A variety of supporting studies not affiliated with a specific DDC activity but undertaken in support of the SSM during the period of the Duynefontyn PSHA project are listed in Table 5-1. These studies are included in the SSC database and the findings of each were evaluated by the SSM TI Team. Their findings assisted in reducing epistemic uncertainties associated with the identification and characterisation of seismic sources. A summary of these studies is provided below:

Barker, O., 2023. Koeberg – 1976 To 1978 – Memories, observations and ideas
Oliver Barker mapped and photographed the foundation bedrock excavations during the construction of the Koeberg Nuclear Power Plant between 1976 and 1978 and his report provides photos, records, data and memories of the bedrock geology at the site that were useful in contributing to the Duynefontyn PSHA. Barker (2023) highlights the nature of the marine planated bedrock surface, bedrock lithology, structure (bedding planes, joints and faults) as well as the lack of fault activity derived from undeformed Piddock boring trace fossils that occur throughout the site and across structural discontinuities (Section 4.4, see Figure 4-35). A minimum age of the bioturbated bedrock surface was determined from the overlying sediments, as between 2–5 My.

Cole, J. 2023. 3D Magnetic Modelling of dykes in the area around Duynefontyn
Cole (2023) conducted additional analyses of the offshore marine magnetic data (Cole, 2007; Cole et al., 2007) in the area east of Bloubergstrand, roughly 16 km south of Duynefontyn on a NW-trending negative anomaly that appeared to displace a positive EW-striking anomaly seemingly aligned with the proposed Milnerton Fault. Forward 3D magnetic modelling showed that these anomalies could be modelled in two different ways. In the first model, the negative anomaly was modelled as a reversely magnetised dyke that intruded along a fault that displaced the EW-trending dyke. In the second model, the EW-trending dyke was interpreted as an *en echelon* set that disrupted the reversely magnetised NW-trending dyke. Magnetic properties measured from samples taken in the area (Maré, 2022) constrained the normally magnetised dykes, but the remnant magnetisation direction for the reversely magnetised dykes had to be estimated through synthetic modelling. Since neither of the dykes crop out on the seafloor, it was impossible to confirm their relation by dating. However, Reid et al. (1991) dated normally magnetised dykes as Early Cretaceous in age. Magnetic polarity reversals during this time explain the presence of both normally and reversely magnetised dykes. Whether any of these structures have been reactivated since then cannot be determined from the magnetic data.

The SSM TI Team evaluated and incorporated the data derived from this study into the SSM. Its integration is detailed in Section 8.5.7 (Proposed Milnerton Fault).

5.3 REFERENCES

Albini, P. and Flint, N. (2023). Investigating the Earthquake Records from 1620 to 1969 of Interest for the Duynefontyn Area, South Africa. CGS Report 2022-0127 (Rev. 0). Council for Geoscience, Pretoria, South Africa.

Barker, O. (2023). Koeberg - 1976 to 1978 - Memories, Observations and Ideas. Banzi Geotechnics, CC, Job 214-01-2023. Koeberg Consultations CGS.

De Beer, C.H. (2005). Investigation into Evidence for Neotectonic Deformation within Onland Neogene to Quaternary Deposits between Alexander Bay and Port Elizabeth – South Coast Report. CGS Report 2005-0180, NSIP-SHA-016311#P1-197. Council for Geoscience, Pretoria, South Africa.

Bender, C.M. and Orszag, S.A. (1999). Advanced Mathematical Methods for Scientists and Engineers. Springer. 549-568.

Bierman, P.R. (2012a). Cosmogenic Geochronology, Southern Africa Fault Corridor Investigation, Appendix B.3, In: Hanson, K.; Slack, C. and Coppersmith, R. (2012). Thyspunt Geological Investigations-Kango Fault Study. CGS Report 2012-0035 (Rev. 0). Council for Geoscience, Pretoria, South Africa.

Bierman, P.R. (2012b). Cosmogenic Geochronology, Southern Africa Southern Coast Marine Terraces, Appendix E.2, In: Hanson, K.; Slack, C. and Coppersmith, R. (2012). Thyspunt Geological Investigations-Kango Fault Study. CGS Report 2012-0035 (Rev. 0). Council for Geoscience, Pretoria, South Africa.

Bierman, P.R.; Coppersmith, R.; Hanson, K.; Neveling, J.; Portenga, E.W. and Rood, D.H. (2014). A Cosmogenic View of Erosion, Relief Generation, and the Age of Faulting in Southern Africa. GSA Today 24(9). 4-11.

Bishop, A.W. (1966). The Strength of Soils as Engineering Materials. Géotechnique 16. 91-128.

Brandt, M.B.C. (2014). Focal Depths of South African Earthquakes and Mine Events. Journal of the Southern African Institute of Mining and Metallurgy 114. 855-862.

Cawthra, H.C.; Frenzel, P.; Hahn, A.; Compton, J.S.; Gander, L. and Zabel, M. (2020). Seismic Stratigraphy of the Inner to Mid Agulhas Bank, South Africa. Quaternary Science Reviews 235. 105979.

Cawthra, H.C. and Van Zyl, F.W. (2023). Duynefontyn Data Collection for Offshore Faults. CGS Report 2023-0116 (Rev.0). Council for Geoscience, Pretoria, South Africa.

Chapman, C.H. (1978). A New Method of Computing Synthetic Seismograms. Geophysical Journal of the Royal Astronomical Society 54. 481-518.

Chapman, C.H. and Orcutt, J.A. (1985). The Computation of Body Wave Synthetic Seismograms in Laterally Homogeneous Medium. Reviews of Geophysics 23. 105-163.

Chapman, C.H.; Jen-Yi, C. and Lyness, D.G. (1988). The WKBJ Algorithm. In: Doornbos, D.J. (Ed.). Seismological Algorithms. Academic Press, London, England. 47-74.

Chirenje, E.; Nxantsiya, Z.; Sebothoma, S.; Sekiba, M.; Netsianda, A.; Sethobya, M. and Claassen, D. (2018). Report on the Seismic Refraction and Resistivity Surveys for Marine Terrace and Bedrock Mapping at Duynefontyn, Western Cape, South Africa. CGS Report 2018-0264. Council for Geoscience, Pretoria, South Africa.

Chirenje, E.; Nxantsiya, Z.; Sebothoma, S.; Sekiba, M.; Sethobya, M. and Netsianda, A. (2018b). Report on the Reconnaissance Ground Geophysical Surveys at Duynefontyn, Western Cape, South Africa. CGS Report 2018-0114. Council for Geoscience, Pretoria, South Africa.

Choi, S.J.; Merritts, D.J. and Ota, Y. (2008). Elevations and Ages of Marine Terraces and Late Quaternary Rock Uplift in Southeastern Korea. Journal of Geophysical Research 113. B10403.

Claassen, D.; Mthembi, P. and Black, D.E. (2024). Marine Terrace Studies in Support of the Probabilistic Seismic Hazard Analysis for the Proposed Duynefontyn Site, Western Cape, South Africa. CGS Report 2022-0140. Council for Geoscience, Pretoria, South Africa.

Coppersmith, R.; Slack, C.; Moabi, N.; Dhansay, T.; Cawthra, H.; Claassen, D. and Sethobya, M. (2024). Duynefontyn Onshore Fault Mapping Investigation. CGS Report 2023-0001. Council for Geoscience, Pretoria, South Africa.

Cole, J. (2007). Koeberg Marine Extension: Interpretation of the Marine Magnetic Data. CGS Report 2007-0234. NSIP-NSI-020265#P1-20. Council for Geoscience, Pretoria, South Africa.

Cole, P. (2020). PyGMI-Python Geophysical Modelling and Interpretation (Version 3.1.0). http://patrick-cole.github.io/pygmi/index.html (Accessed 2020). Council for Geoscience, Pretoria, South Africa.

Cole, J. (2023). 3D Magnetic Modelling of Dykes in the Area around Duynefontyn. CGS Report 2023-0002. Council for Geoscience, Pretoria, South Africa.

Cole, J.; Cole, P. and De Beer, C.H. (2007). Geophysical Interpretation of the Marine Magnetic Data Collected in the Offshore Site Area (8 km Radius) of Koeberg. CGS Report 2007-0187. NSIP-NSI-020265#P1-8. Council for Geoscience, Pretoria, South Africa.

Cooper, J.A.G and Green, A.N. (2021). A Standardised Database of Marine Isotope Stage 5e Sea-Level Proxies in Southern Africa (Angola, Namibia and South Africa). Earth System Science Data 13. 953-968.

Council for Geoscience (2004). Safety Report and Final Assessment (2004). CGS Report 2004-0188. Council for Geoscience, Pretoria, South Africa.

Dames and Moore (1976). Geologic Report. Koeberg Power Station, Cape Province, South Africa, for The Electricity Supply Commission, Job 9629-014-45.

Davies, O. (1971). Pleistocene Shorelines in the Southern and South-Eastern Cape Province (Part 1). Annals of the Natal Museum 21(1). 183-223.

Davies, O. (1972). Pleistocene Shorelines in the Southern and South-Eastern Cape Province (Part 2). Annals of the Natal Museum 21(2). 225-279.

Davies, O. (1973). Pleistocene Shorelines in the Western Cape and South-West Africa. Annals of the Natal Museum 21(3). 719-765.

De Beer, C.H. (2007). Potential Onshore and Offshore Geological Hazards for the Koeberg Nuclear Site, Cape Town, South Africa: A Review of the Latest Airborne and Marine Geophysical Data and Their Impact on the Existing Geological Model for the Site Vicinity Area. CGS Report 2007-0276. Council for Geoscience, Pretoria, South Africa.

De Villiers, J. (1944). A Review of the Cape Orogeny: Annal of University of Stellenbosch XXII A. 185-208.

De Wet, W.M. (2013). Bathymetry of the South African Continental Shelf. MSc Thesis (Unpublished), University of Cape Town.

De Wet, W.M. and Compton, J.S. (2021). Bathymetry of the South African Continental Shelf. Geo-Marine Letters 41(3). 1-19.

Erlanger, D.E. (2011). Rock Uplift, Erosion and Tectonic Uplift of South Africa Determined with 26Al and 10Be. MSc Thesis (Unpublished), Purdue University, West Lafayette, Indiana, USA.

Gurrola, L.D.; Keller, E.A.; Chen, J.H.; Owen, L.E. and Spencer, J.Q. (2014). Tectonic Geomorphology of Marine Terraces: Santa Barbara Fold Belt, California. GSA Bulletin 126 (1-2). 219-233.

Gutenberg, B. and Richter, C.F. (1944). Frequency of Earthquakes in California. Bulletin of the Seismological Society of America 34. 185-188.

Guzmán, J.A. (1978). A Package of Computer Programs for the Evaluation of Local Earthquakes and Publication of the Seismological Bulletin. Report Gh 2446. Geological Survey of South Africa.

Hanson, K.L.; Coppersmith R.; Glaser, L.; Roberts, D.L.; Claassen, D. and Black, D.E. (2012). Thyspunt Geological Investigations-Marine Terrace Studies. Volumes. 1-4, Appendixes A-G. CGS Report 2012-0034 (Rev. 0). Council for Geoscience, Pretoria, South Africa.

Hartnady, C.J.H. (2003). Cape Town Earthquakes: Review of the Historical Record. Vers.030522 (Draft). Umvoto Africa, Muizenberg.

Heidbach, O.; Rajabi, M.; Reiter, K.; Ziegler, M.O. and the WSM Team. (2016). World Stress Map Database Release 2016. GFZ Data Services.

Heidbach, O.; Rajabi, M.; Cui, X.; Fuchs, K.; Müller, B.; Reinecker, J.; Reiter, K.; Tingay, M.; Wenzel, F.; Xie, F.; Ziegler, M.O.; Zoback, M.L. and Zoback, M.D. (2018). The World Stress Map Database Release 2016: Crustal Stress Pattern Across Scales. Tectonophysics 744. 484-498.

Henzen, M.R. (1973). Die Herwinning Opberging en Onttrekking van Gesuiwerde Rioolwater in die Kaapse Skiereiland [English: The Recovering and Extraction of Treated Sewage in the Cape Peninsula] 1-2. Report by the National Institute for Water Research, Council for Scientific and Industrial Research.

Horwood, S. (2009). Marine Structural Geology Report, Koeberg Extended Geophysical Site Survey, Table Bay, Cape Town. CGS Report 2009-0005. Council for Geoscience, Pretoria, South Africa.

Horwood, S. and Smith, K. (2007). Marine Geophysical Survey Report, Eskom Site Surveys, South Africa. Koeberg. Volume 1A - Survey Results. Council for Geoscience, Marine Geoscience Unit, Bellville, South Africa.

Karymbalis, E.; Tsanakas, K.; Tsodoulos, I.; Gaki-Papanastassiou, K.; Papanastassiou, D.; Batzakis, D.V. and Stamoulis, K. (2022). Late Quaternary Marine Terraces and Tectonic Uplift Rates of the Broader Neapolis Area (SE Peloponnese, Greece). Journal of Marine Science and Engineering 2022(10)(99).

Li, Y. and Thurber, C. H. (1991). Hypocentre Constraint with Regional Seismic Data: A Theoretical Analysis for the Natural Resources Defence Council Network in Kazakhstan, USSR. Journal of Geophysical Research 96(B6). 10159-10176.

Lienert, B.R.E. and Havskov, J. (1995). A Computer Program for Locating Earthquakes Both Locally and Globally. Seismological Research Letters 66(5). 26-36.

Lisle, R.J.; Orife, R.O.; Arlegui, L.; Liesa, C. and Srivastava, D.C. (2006). Favored States of Palaeostress in the Earth's Crust: Evidence from Fault-Slip Data. Journal of Structural Geology 28. 1051-1066.

MacHutchon, M.R.; De Beer, C.H.; Van Zyl, F.W. and Cawthra, H.C. (2020). What the Marine Geology of Table Bay, South Africa Can Inform about the Western Saldania Belt, Geological Evolution and Sedimentary Dynamics of the Region. Journal of African Earth Sciences 162. 103699.

Mangongolo, A.; Strasser, F.; Saunders, I. and Rathod, G. (2017). Depths of Earthquakes in South Africa. Seismological Research Letters 88(4). 1078-1088.

Maré, L.P. (2022). Magnetic Remanence Study of the False Bay Dolerite Suite in Support of Geophysical Modelling of Existing Duynefontyn High-Resolution Aeromagnetic Data. CGS Report 2022-0152 (Rev. 0). Council for Geoscience, Pretoria, South Africa.

McFarland, J.; Morris, A.P. and Ferrill, D.A. (2012). Stress Inversion Using Slip Tendency. Computers and Geosciences 41. 40-46.

Midzi, V.; Saunders, I.; Brandt, M.B.C. and Molea, T.T. (2010). 1-D Velocity Model for Use by the SANSN in Earthquake Location. Seismological Research Letters 81(3). 460-466.

Midzi, V.; Bommer, J.J.; Strasser, F.O.; Albini, P.; Zulu, B.S.; Prasad, K. and Flint, N.S. (2013). An Intensity Database for Earthquakes in South Africa from 1912 to 2011. Journal of Seismology 17. 1183-1205.

Mine Health and Safety Act (1996). Mine Health and Safety Act No. 29 of 1996. https://www.dmr.gov.za/Portals/0/mhs_act_29_of_19960_1.pdf.

Moabi, N. and Dhansay, T. (2022). Fault Studies. PowerPoint Presentation at PSHA Duynefontyn Workshop 2, June 21, Stellenbosch, South Africa. DNSP-PST-096.

Morris, A.P.; Ferrill, D.A. and Henderson, D.B. (1996). Slip Tendency Analysis and Fault Reactivation. Geology 24. 275-278.

Morris, A.P.; Ferrill, D.A. and McFarland, J.M. (2013). Geological Stress Inversion Using Fault Displacement and Slip Tendency. United States Patent # US 8,589,080 B2, November 19.

Mulabisana, T. (2023). Temporary Network along the Colenso Fault. CGS Report 2023-0082. Council for Geoscience, Pretoria, South Africa.

Musson, R. and Cecić, I. (2002). Macroseismology. In: Lee, W.; Kanamori, H.; Jennings, P. and Kisslinger C. (Eds.). International Handbook of Earthquake and Engineering Seismology. Academic Press 81A, San Diego, California, USA. 807-822.

Musson, R. M. W.; Grünthal, G. and Stucchi, M. (2010). The Comparison of Macroseismic Intensity Scales. Journal of Seismology. 14. 413-428.

Neveling, J. and Chirenje, E. (2023). Project Execution Plan, The Investigation of the Site Geology and Micro-seismic Monitoring in Support of the Probabilistic Seismic Hazard Analyses for the Duynefontyn Site. CGS Document NGG-PLN-001 (Rev. 2). Council for Geoscience, Pretoria, South Africa.

Ottemöller, L. (1995). Explosion Filtering for Scandinavia. Norwegian National Seismic Network, Technical Report: IFJF, University of Bergen, Bergen, Norway.

Ottemöller, L.; Voss, P. and Havskov, J. (2018). The SEISAN Earthquake Analysis Software for Windows, Solaris, Linux, and MacOSX. University of Bergen, Bergen, Norway.

Palan, K.J. (2017). Submarine Canyon Evolution of the Southwest Cape Continental Margin. MSc Thesis (Unpublished), University of KwaZulu-Natal, South Africa.

Reasenberg, P. and Oppenheimer, D.H. (1985). FPFIT, FPPLOT and FPPAGE; Fortran Computer Programs for Calculating and Displaying Earthquake Fault-Plane Solutions. US Geological Survey, Open-File Report 1985. 85-739.

Reid, D.L.; Erlank, A.J. and Rex, D. (1991). Age and Correlation of the False Bay Dolerite Dyke Swarm, South-Western Cape, Cape Province. South African Journal of Geology 94(2). 155-158.

Roberts, D.L. (2006). Dating and Preliminary Correlation of Raised Marine and Estuarine Terraces on the Western and Southern Coasts of South Africa. Final Report. CGS Report 2006-0186. Eskom NSIP-SHA-018230#P1-206.

Saunders I. (2024). Review and Homogenization of an Earthquake Catalogue for the Ceres Area. CGS Report 2023-0162. Council for Geoscience, Pretoria, South Africa.

Saunders, I and Fourie C.J.S. (2015). Reappraisal of Single-Station Locations Reported by the South African National Seismograph Network during the Period 2000-2005, Seismological Research Letters 86(3). 908–916.

Saunders, I.; Brandt, M.B.C.; Steyn, J.; Roblin D.L. and Kijko, A. (2008). The South African National Seismograph Network. Seismological Research Letters 79(2). 203-210.

Saunders, I.; Ottemöller, L.; Brandt, M.B.C. and Fourie, C.J.S. (2012). Calibration of an ML Scale for South Africa Using Tectonic Earthquake Data Recorded by the South African National Seismograph Network: 2006 to 2009. Journal of Seismology 17(2). 437-451.

Saunders, I.; Kijko, A. and Fourie, C.J.S. (2016). Statistical Evaluation of Seismic Event Location Accuracy by the South African National Seismograph Network Over Four Decades. South African Journal of Geology 199.1. 291-304.

Scharf, T. (2012). Denudation Rates and Geomorphic Evolution of the Cape Mountains, Determined by the Analysis of the In Situ-Produced Cosmogenic 10 Be. University of Cape Town.

Smart, K.J.; Cawood, A.J. and Ferrill, D.A. (2023). Geological Stress Analyses to Support a Probabilistic Seismic Hazard Analysis (PSHA) for a Critical Site in South Africa. SwRI® Project 15.27360.

Smit, L.A.; Fagereng, A.; Braeuer, B. and Stankiewicz, J. (2015). Microseismic Activity and Basement Controls on an Active Intraplate Strike-Slip Fault, Ceres-Tulbagh, South Africa. Bulletin of the Seismological Society of America 105 (3). 1540-1547.

Snoke, J.A. (2003). FOCMEC: Focal Mechanism Determinations. In: Lee, W.H.K.; Kanamori, H.; Jennings, P.C. and Kisslinger, C. (Eds.). International Handbook of Earthquake and Engineering Seismology. Academic Press, San Diego, California, USA.

Stamatakos, J. and Watson-Lamprey, J. (2022). Project Execution Plan for the Senior Seismic Hazard Analysis Committee Enhanced Level-2 Probabilistic Seismic Hazard Analysis at the Duynefontyn Nuclear Site. CGS Document NGG-PLN-003 (Rev 0). Council for Geoscience, Pretoria, South Africa.

Strasser, F.O. and Mangongolo, A. (2013). TNSP Earthquake Catalogue. CGS Report 2012-0166 (Rev. 0). Council for Geoscience, Pretoria, South Africa. Appendix A (TNSP Catalogue).

Wessels, W.P.J. and Greeff, G.J. (1980). ‘n Ondersoek na die Optimale Benutting van Eersterivierwater deur Opberging in Sandafzetting of Ander Metodes. [English: Investigation into the Optimal Utilization of Eereste River Water through Storage in Sand Deposits or Other Methods.] Department of Civil Engineering, University of Stellenbosch.

Wiemer, S. and Baer, M. (2000). Mapping and Removing Quarry Blast Events from Seismicity Catalogs. Bulletin of the Seismological Society of America 90. 525-530.

CHAPTER 6: EARTHQUAKE CATALOGUE

6. EARTHQUAKE CATALOGUE

6.1 OVERVIEW

6.1.1 Purpose

The purpose of the project SSM earthquake catalogue is to provide a dataset which the SSM Technical Integration (TI) Team can analyse for the development of future earthquake parameters of seismic sources (e.g. recurrence parameters and spatial density). The SSM earthquake catalogue is used to assess the ratio between small- and larger-magnitude earthquakes (*b*-value), recurrence rates, maximum magnitude, and temporal and spatial density of event occurrence. In addition, the earthquake catalogue is used to develop seismogenic thicknesses and focal depth distributions.

6.1.2 Approach to catalogue development

Earthquake catalogue development generally follows a stepwise process such that the catalogue or catalogues resulting from one step are used in the subsequent step of the process. To develop the SSM earthquake catalogue, the following processing and analysis steps were performed (Figure 6-1):

- Compilation;
- Duplicate removal;
- Identification of non-tectonic events;
- Homogenisation of magnitude;
- Declustering; and
- Assessment of completeness.

Each of the steps is described in further detail in the subsections below. A discussion of clustered and sequenced events is also included, and feeds into the declustering step. For each step of the process, events are flagged accordingly rather than removed, allowing the full earthquake catalogue to be retained in a single file regardless of alternative analysis methods in use.

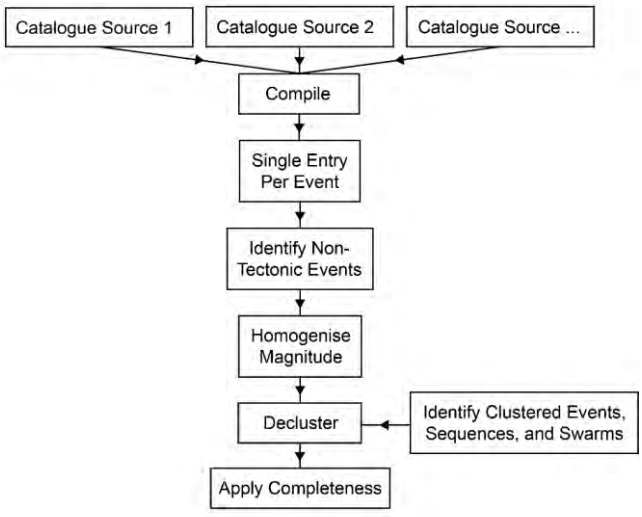

Figure 6-1. Earthquake catalogue development flowchart.

6.1.3 Geographic extent

The project catalogue area was selected to be larger than the coverage of the source zones included in the SSM. The earthquake catalogue includes the area from 15°E to 26°E, and from 28°S to 37°S. The geographic extent for the earthquake catalogue is at least 320 km from the site (Figure 6-2), the recommended regulatory distance cited in USNRC Regulatory Guide 1.208 (USNRC, 2007) for inclusion in the analysis.

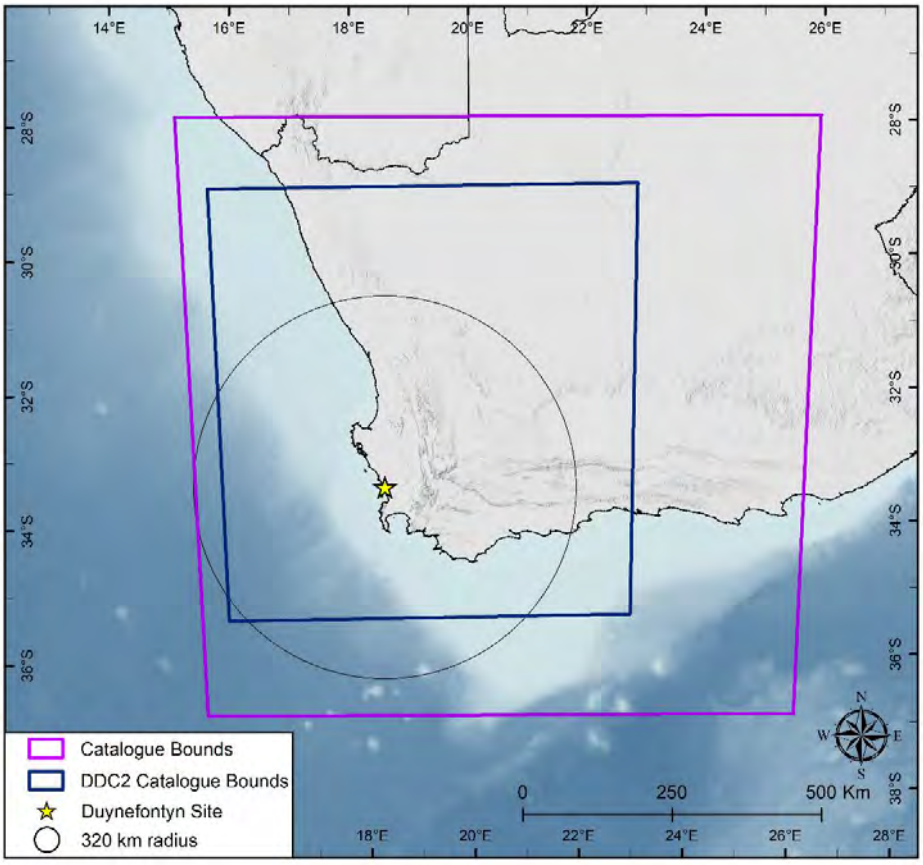

Figure 6-2. Extent of project earthquake catalogue region (purple border), and extent of DDC2 data (blue border).

6.1.4 Collected magnitudes

The Duynefontyn PSHA was developed for a minimum moment magnitude (**M**) of 5.0, following USNRC Regulatory Guide 1.208. However, smaller-magnitude events are included in the catalogue to develop ratios of small- to large-magnitude events for recurrence estimates. The project catalogue therefore includes events with any reported magnitudes of **M** 2.0 and larger. The effect of lower limits on magnitude (e.g. **M** 2.0, **M** 3.0, **M** 4.0) was considered as part of the catalogue evaluation, the results of which are described in the appurtenant sections.

6.1.5 Types of events

The full earthquake catalogue includes tectonic and non-tectonic events. The calculation of seismic hazard focusses on potential shaking levels due to tectonic earthquakes. Therefore,

non-tectonic events are flagged in the catalogue and are not used in the subsequent analyses. The process and results of identification for non-tectonic events are described in Section 6.4.

6.1.6 Time span

Events from all reported dates through 31 August 2022 were included in the earthquake catalogue. Collection efforts for the earthquake catalogue began in September 2022, therefore the terminal date for the earthquake catalogue was selected as the final day in the month prior to the onset of data collection efforts. The early date is necessary as one of the initial tasks required in the PSHA process.

6.2 EARTHQUAKE CATALOGUE COMPILATION

Records for earthquakes in the project catalogue area were collected or downloaded from available regional, local, and global catalogues. Records for events within the project catalogue bounds and with reported magnitude 2.0 and larger were collected. The data sources contributing events to the full project catalogue are outlined in Table 6-1, and include the following:

- CGS: dataset compiled, reviewed, and processed by CGS staff, provided to SSM TI Team via email 21 October 2022.
- Saunders (2024): seismic catalogue developed as part of DDC2 (see Section 5.2.1 for a summary), provided to SSM TI Team via email 17 October 2022.
- Strasser and Mongongolo (2013): earthquake catalogue developed for the Thyspunt SSHAC Level 3 project.
- Albini and Flint (2023): records of historical seismicity developed as part of DDC4 (see Section 5.2.2 for a summary).
- International Seismological Centre (ISC, 2022a): online bulletin of searchable events.
- Advanced National Seismic System (ANSS, 2022): online bulletin of searchable events.

The SSM TI Team attempted to download data from the Global Centroid Moment Tensor (GCMT) Project, but the search did not return any events in the project catalogue area. The ISC-Global Earthquake Model (GEM) catalogue (International Seismological Centre, 2022b) was also reviewed. However, only three events within the ISC-GEM catalogue are within the project catalogue bounds. All three events were found to be duplicative of the events reported by ISC (2022a). Data from the ISC-GEM catalogue does not offer unique entries and is therefore not an authoritative source.

Metadata for the Incorporated Research Institutions for Seismology (IRIS) notes that it sources information from the ISC and is therefore a non-authoritative source. The dataset of events for the Ceres region (a subset of the CGS catalogue) was re-evaluated as part of DDC2 by Mr Ian Saunders (Saunders, 2024). The extent of DDC2 data is included in Figure 6-2 to show that all records are located within the project earthquake bounds. The DDC2 dataset includes events from the following sources:

- South African National Seismological Database.
- Skuifraam Dam seismic recordings.
- Short-term academic networks (Smit et al., 2015).
- Waveform data from the Kaapvaal Craton Seismic Experiment.

In compiling the catalogue data, the SSM TI Team considered each reported magnitude as a different event entry to the catalogue. Each entry in the compiled catalogue was assigned a unique identifier for tracking. Information reported from each data source was preserved.

Table 6-1. Source catalogues of earthquake data used to compile the project catalogue, including the data specifications of each catalogue source.

SOURCE	CGS	DDC2	THYSPUNT	HISTORICAL (DDC4)	ONLINE	
					ISC	ANSS
Entries	2123	130	866	74	1636	33
Magnitude types	M_L, M_W, m_b	M_L, M_W	M_W, M_L	Intensity	M_L, m_b, M_s, M_W, M_D	M_L, M_W, m_b, M_s
Types of non-tectonic event flags	None	Type – P: likely explosion	None	False events Rockfall events	kh – known explosion sh – suspected explosion	None
Magnitude Range	2.0–6.3	2.0–5.6	2.0–6.3	Not defined	2.0–6.6	2.6–6.3
Date Range	1620–2021	1981–2020	1690–2011	1620–1969	1912–2022	1969–2022
Location Errors	Latitude error, longitude error and depth error (in km)	Latitude error, longitude error and depth error (in km)				Horizontal error

CGS – Council for Geoscience, DDC2 – Catalogue for area in and around Ceres as determined by Ian Saunders, ISC – International Seismological Centre, ANSS – Advanced National Seismic System (United States Geological Survey). Magnitude types – M_L – local magnitude, M_W – reported moment magnitude where seismic moment is not available for directly calculation of moment magnitude (**M**), m_b – body wave magnitude, M_s – surface wave magnitude, M_D – duration magnitude

Dr Paola Albini and Ms Nicky Flint carried out a study of historical seismicity in the project region as a PSHA supporting study (DDC4), the findings of which are included in the project earthquake catalogue as an appendix and summarised in Section 5.3. Albini and Flint (2023) did not extend their analysis to determine the location of the epicentres or an estimate of the moment magnitude of the events. To complete the analysis, the SSM TI Team determined the epicentres and magnitudes of those historical earthquakes that had sufficient data to develop a reliable result (Section 5.3).

6.3 SINGLE ENTRY PER EVENT

Earthquake catalogue entries originated from numerous datasets and overlapping geographic extents, timeframes, and reporting station networks, in some cases resulting in multiple entries for a single event. The full, compiled catalogue therefore included duplicate information for many reported events, presented as multiple lines for such events. To condense the entries, the SSM TI Team evaluated the compiled entries and preserved unique information for each event.

First, duplicate entries were identified in the full, compiled catalogue by manual inspection for entries with the same or similar origin date, time, and location. A majority of duplicate sets were found to have reported occurrence times within roughly one minute of each other, in many cases because seconds were not reported by all data sources. Reported latitude and longitude for duplicate sets was within rounding tolerance for the time period of the entries and precision used by the involved data sources. For example, entries early in the catalogue are reported with fewer significant digits compared to entries later in the catalogue and therefore earlier duplicate sets are more likely to have reported locations farther from each other than those that occurred more recently. The duplicate entries were compared to assess differences in reporting precision (e.g. latitude/longitude significant digits), reported error information, and other metadata such as reporting agency for time and location.

For each set of duplicate entries, a single event was selected as the preferred reported entry for the reported location and origin time. If available, error information was also retained from the preferred entry. All reported magnitudes and non-tectonic flags were retained and appended to the preferred entry.

The comparison and selection of preferred entries was performed manually by one SSM TI Team member, then checked by another SSM TI Team member. The selection of preferred entry was made by selecting the event with the best reported error, highest precision location, depth, and/or time, or most reliable reported information (e.g. original evaluation of location, rather than that reported by another agency). A single preferred entry was selected to retain the connections between reported time, location, and depth for those events that were reanalysed. This choice did not affect the analysis of seismogenic thickness (Section 8.2.2) in which all depths reported by DDC2 were considered.

One notable event is the 11 September 1969 event, which has significant location uncertainty as described in Section 5.3.9. Two possible locations are reported for this event: one in the Cape Town region, and the other more than 300 km due east of the site. After assessing the reported event information, the SSM TI Team was unable to select a preferred location. The SSM TI Team therefore included two alternative locations in the earthquake catalogue, with equal weight. Sensitivity to the two locations was performed and is described in Section 6.9.

The full, compiled catalogue includes 4,788 entries. Following duplicate processing and removal, the earthquake catalogue includes 2,648 individual earthquakes.

6.4 IDENTIFICATION OF NON-TECTONIC EVENTS

Input catalogues commonly contain contamination from non-tectonic events. Non-tectonic events include rockfalls, rock bursts, reservoir-induced events caused by inundation and initial filling of reservoirs, and mining or quarry blasts. These types of events were not excluded from the initial data collection efforts. Non-tectonic contamination must be identified and flagged so such events are not used by the SSM TI Team to calculate the recurrence rates of tectonic earthquakes and to avoid artificially inflated rates of seismicity.

In the project catalogue, non-tectonic events were identified using a qualitative flag. Suspected and confirmed non-tectonic events were reported by catalogue data sources or identified by the SSM TI Team using a method similar to that of Wiemer and Baer (2000), Gulia (2010), and Gulia and Gasperini (2021) for possible mining events.

6.4.1 Reported events from data sources

In total, 105 events were flagged by the originators of the data sources as known or likely explosions. The CGS catalogue did not include flags for non-tectonic events. Non-tectonic events were removed from the TNSP final reported catalogue and therefore no such flags were included with those records. DDC4 reported six events as rockfall or rock burst. Such events are sometimes assumed to be earthquakes based on historical accounts of shaking or ground movement. None of these events were in the initial compiled catalogue.

DDC4 identified ten false events that were previously believed to be earthquakes, indicating that these were not true earthquake records and are unsubstantiated as events in the earthquake catalogue. Upon examination of the project earthquake catalogue, 6 of the 10 events were found to be present, and subsequently removed from the earthquake catalogue.

The ISC Bulletin reports nine event types in its downloadable database: meteoritic event, earthquake, chemical explosion, induced event, landslide, mining explosion, nuclear explosion, rock burst, and experimental explosion. Each of the event types is classified as suspected, known, felt, or damaging. For the ISC events downloaded within the project region, only known and suspected chemical explosion flags were included. Although the ANSS portal also reports non-tectonic events, and allows the user to exclude non-tectonic events, there were no reported non-tectonic events from the ANSS data source.

Although there are events flagged by data sources as mining-related events, additional events that were not self-reported by the various data sources are recorded. The SSM TI Team conducted a systematic review of the earthquake catalogue for possible mining events. This is described in the following section.

6.4.2 Possible mining events

South Africa has a long history of mining and quarrying activity, often using blasting techniques. For simplicity, the terms “mine” and “mining event” are used to represent both underground mining and surficial quarry activities. The SSM TI Team worked with Dr Laura Gulia (a specialty contractor) to complete an analysis of possible mining event contamination in the earthquake catalogue. An adaptation of the day-to-night ratio (D/N) assessment method described in Wiemer and Baer (2000), Gulia (2010), and Gulia and Gasperini (2021) was followed. Possible mining events, as identified by the process, were assigned a non-tectonic

flag. The subsections below describe the approach, process, and results of the mining event assessment.

6.4.2.1 Approach

Generally, mining-related events have low magnitudes and can result in overrepresentation of small-magnitude events in the earthquake catalogue, thereby influencing calculations of recurrence and activity. Mining blasts are discharged during daytime working hours. Therefore, in an area with an active mine, the number of events occurring during the day is anticipated to be higher than the number of events occurring at night.

The SSM TI Team used the following approach to assess and identify possible mining events in the project earthquake catalogue:

- Calculated the catalogue-wide D/N ratio using various magnitude bins to assess the potential for overall mining-related contamination.
- Evaluated the maximum magnitude of catalogue-wide contamination.
- Developed a grid of D/N ratios for the project catalogue area.
- Assessed the D/N grid compared to mine and quarry locations.

Elements of the D/N ratio method and background are described in Gulia and Gasperini (2021), Gulia (2010), and Wiemer and Baer (2000). The development implemented for the DNSP project was the inclusion of mapped mine locations and the consultation of available databases as an additional criterion for identifying possible mining events, as described in the following sections.

6.4.2.2 Identification of possible mining events

To determine whether the project earthquake catalogue was contaminated by mining events, histograms of events by hour of occurrence were developed using various magnitude ranges. Events with no reported time were removed from counts. The initial contamination evaluation was performed in two steps. First, the events were binned into 1.0- and 0.5-wide magnitude bins to confirm whether contamination was present (Figure 6-3). After apparent contamination was confirmed, the data was discretised into smaller-magnitude bins to examine the contamination threshold.

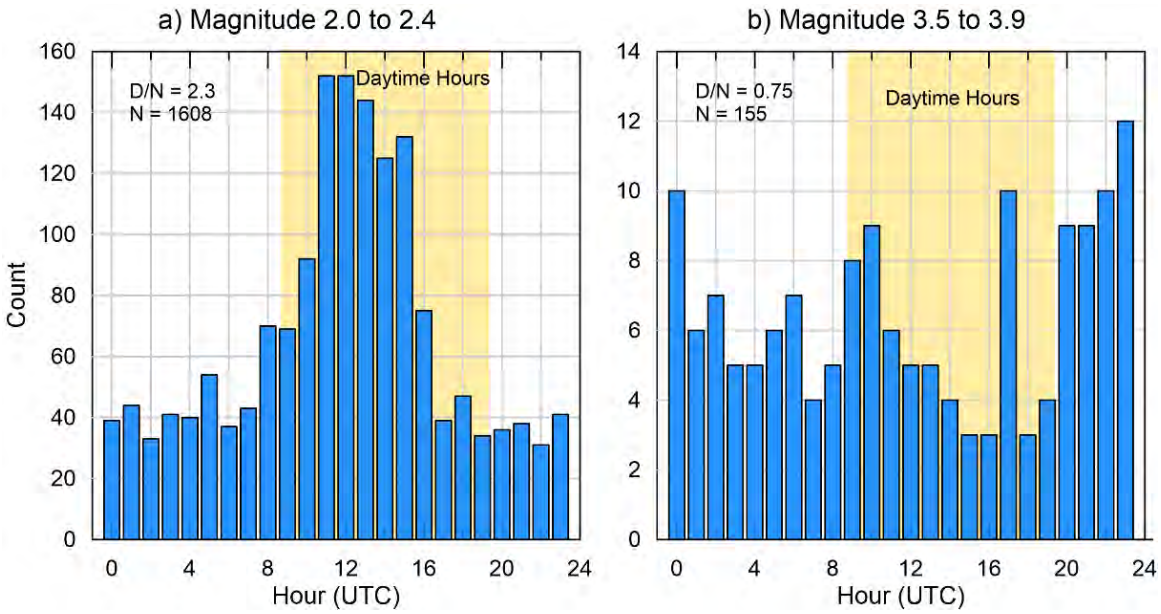

Figure 6-3. Example histograms of events by reported hour of occurrence, showing mining event contamination with (a) large peaks of daytime events and (b) no apparent contamination, with peaks randomly distributed over 24 hours.

Wiemer and Baer (2000) developed the method for contamination testing based on the observation that mine blasting is performed during the daytime. They tested the D/N ratio and concluded that in the case of all-natural events, such values should be roughly 1 or slightly less, due to the lower-magnitude detection threshold at nighttime owing to the lower level of anthropogenic seismic noise. On the contrary, a ratio greater than 1.5 is likely to indicate mining event contamination (Wiemer and Baer, 2000). The D/N ratio accounts for the number of hours divided into daytime and nighttime and therefore the ratio threshold of 1.5 remains consistent regardless of the division of hours into daytime versus nighttime. For reference, the relationship from Wiemer and Baer (2000) is the ratio of the daytime to nighttime event counts multiplied by the ratio of the number of nighttime to daytime hours.

For the SSM project catalogue, daytime hours were selected as being inclusive of 9 to 19 hours UTC (7 to 17 hours local time), based on typical working hours. These hours are consistent through time and space as there is no time zonation or daylight-saving measures across South Africa. A single, non-converted magnitude (referred to as the preferred magnitude) was selected and used in the assessment of each event. The preferred magnitude to use was reported moment magnitude, if available, but most commonly was local magnitude. This was deemed more appropriate than the calculated expected true moment magnitude (E[**M**]), which is developed specifically for recurrence (described in Section 6.6.3).

The initial contamination evaluation used magnitude bins of 0.5 units and confirmed contamination in the catalogue for smaller magnitudes with D/N ratios higher than 1.5. Scattered peaks for larger magnitudes indicated reduced or no contamination at those magnitudes, as shown in Figure 6-3.

The maximum magnitude of potential mine blast events (*MBMmax*) was determined by calculating D/N ratios for 0.1-magnitude bins. Histogram plots for preferred magnitudes from 2.0 to 3.4 are shown in Figure 6-4. The D/N values are consistently 1.5 or larger to at least magnitude 2.7, and fluctuate around a value of 1.5 between magnitude 2.8 and magnitude 3.1. The SSM TI Team selected an *MBMmax* of 3.1 as the upper limit of possible mining

events in the catalogue. The *MBMmax* captures, with certainty, the majority of possible mining events up to preferred magnitude 2.7 and includes the potential for some uncertainty in the upper limit. Although the *MBMmax* was selected as 3.1, larger-magnitude mining events have occurred in South Africa located to the north and east outside of the project earthquake catalogue bounds.

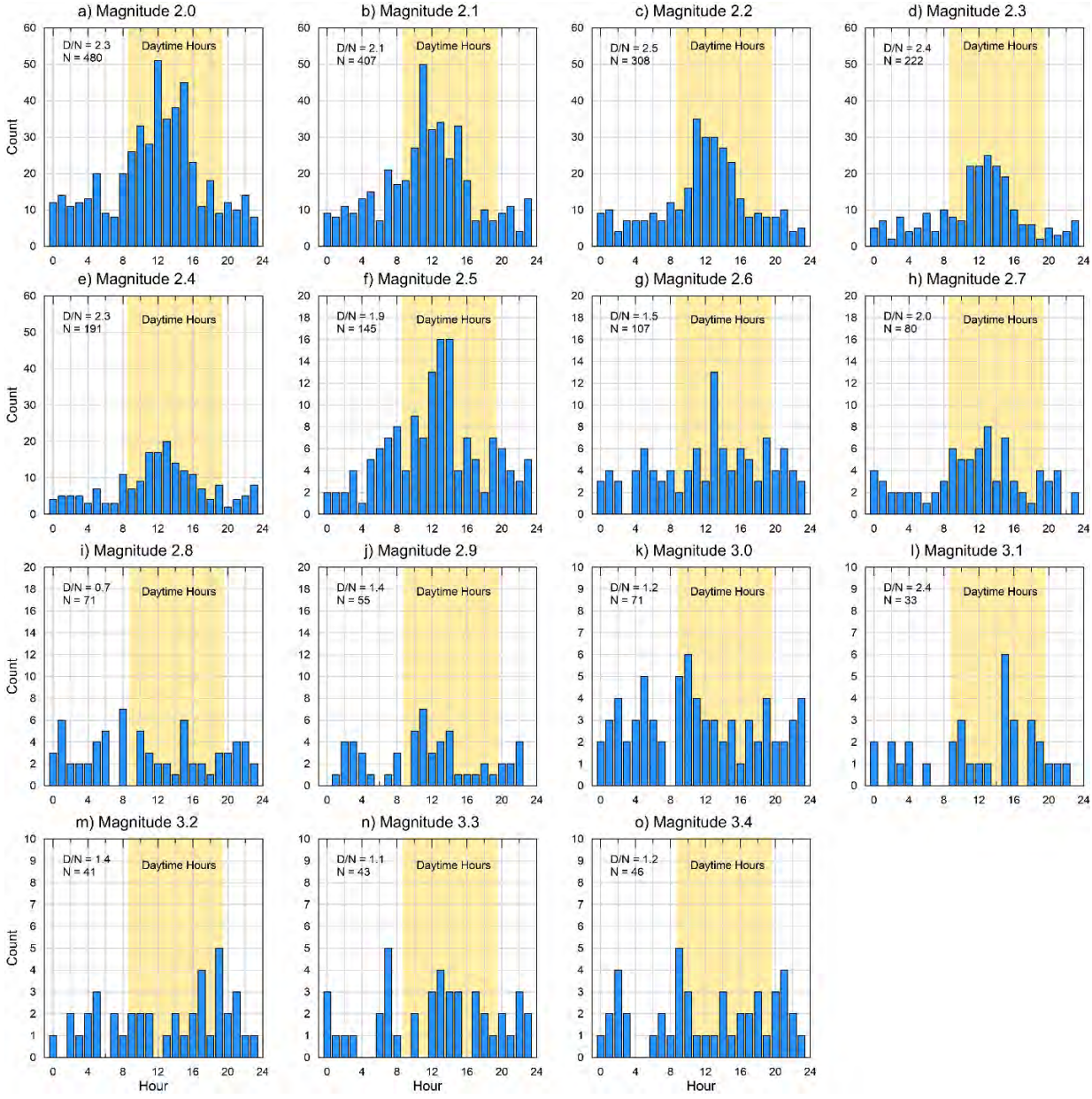

Figure 6-4. Histograms of events by reported hour of occurrence and D/N ratio values for various magnitude thresholds.

Using the *MBMmax* as the upper-magnitude limit, the D/N ratio for the earthquake catalogue was calculated on a regular grid with 10-km spacing. Each of the nodes had a capture radius of 10 km for the events used to calculate the D/N ratio. Preliminary testing of the grid spacing and capture radius was performed, and 10 km for both distances was found to be the most effective at capturing events. The overlap of capture areas between grid points was deemed appropriate, even necessary, to capture sufficient events for the D/N calculations.

The CGS provided the SSM TI Team with a data file containing the locations and attributes of mine locations throughout South Africa. The National Quarry Database was derived from the South African Mineral Deposits database (SAMINDABA), the Department of Mineral Resources and Energy (DMRE), the South African National Roads Agency Limited (SANRAL), the Aggregate and Sand Producers Association of Southern Africa (ASPASA), and Google Earth imagery. The database includes the name of the quarry (where possible), location information with coordinates, commodity, mine status, and other general comments. All quarries or mines in the database, regardless of their status (active, deposit exploited, abandoned, or dormant) were used in this analysis. The mine locations were plotted with the grid of D/N ratio values, as shown in Figure 6-5, below, to highlight areas of elevated D/N ratios in addition to known mines.

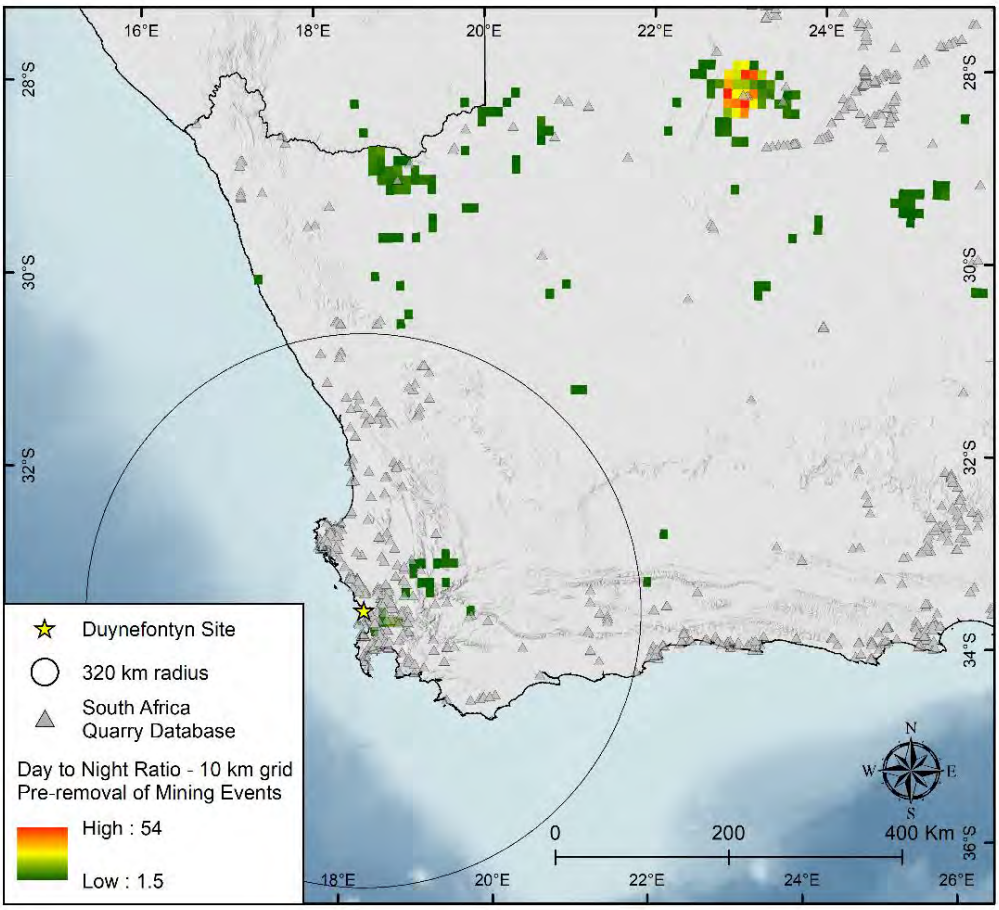

Figure 6-5. D/N ratio and mapped mine locations.

Earthquake catalogue events meeting all the following criteria were flagged as possible mining events:

- Daytime event (UTC hours inclusive of 9 to 19).
- Located within 10 km of grid point with D/N ratio ≥ 1.5.
- Located within 10 km of mapped mine location.
- Magnitude ≤ *MBMmax* 3.1.

The above criteria were followed, and 155 events were identified as possible mining events. The 155 events were removed and when the catalogue was mapped again, it showed that many areas with elevated D/N ratios remained. This indicated that the mapped mine database was incomplete, thereby limiting the effectiveness of that dataset as a screening tool. Clusters of events in the catalogue that meet all but the distance-to-mapped-mine criterion were therefore investigated for nearby quarries or mines that had not been included in the mine dataset. Available aerial photographs (e.g. Google Earth) were assessed and web searches made. Where visual assessment or web searches indicated the presence of nearby mines or quarries, those events matching all the other criteria were flagged as possible mining events. An example of such a search is provided in Figure 6-6.

Following the analysis for possible mining events, the unflagged remainder of the catalogue was used to develop a D/N ratio grid. Comparison to the original D/N grid showed a significant reduction in the number of areas with elevated D/N ratios across the project catalogue.

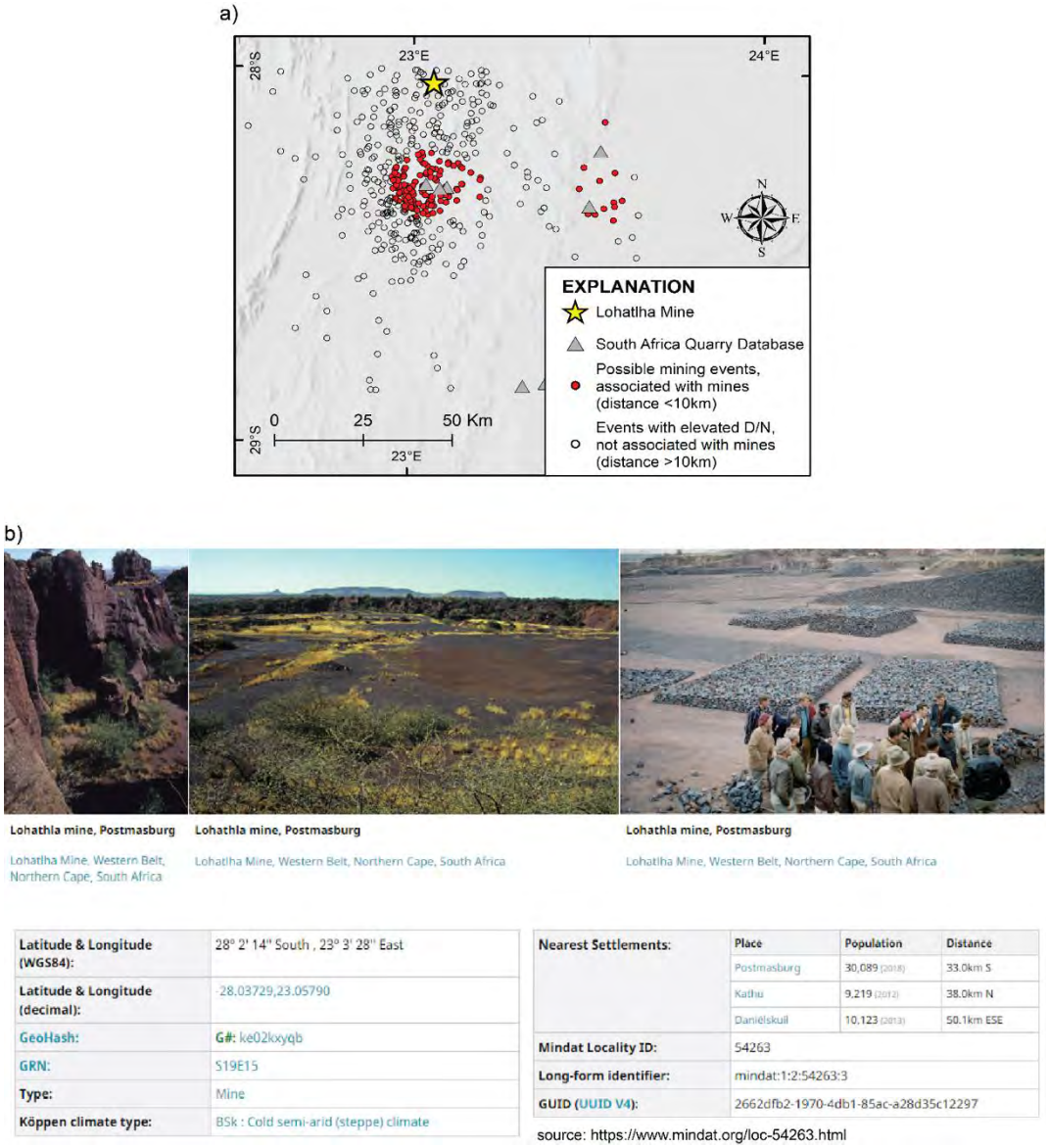

Figure 6-6. Example results of a web search for additional possible mining events showing (a) events with elevated D/N ratios in the region of an identified mine, and (b) of web search and aerial photograph review for an area of clustered, possible mining events.

6.4.3 Results of non-tectonic event evaluation

Identified non-tectonic events, including possible mining events as described above, were assigned an identifier to track the type of non-tectonic event. This includes tracking of events identified by multiple methods (e.g. reported by data source and as a possible mining event). Of the 2,649 events in the SSM project catalogue, the following results were recorded for the non-tectonic event evaluation:

- 663 events in total were assigned non-tectonic flags, all with E[**M**] ≤ 3.2 (preferred magnitude ≤ 3.1).
- 105 events were reported as non-tectonic by data sources.
- 558 possible mining events were identified because of proximity to mines, using the process previously described.
- 1,986 events in the SSM project catalogue remain without non-tectonic flags (i.e. assumed natural tectonic earthquakes).

The full project catalogue and flagged non-tectonic events are depicted in Figure 6-7. The events assigned a non-tectonic flag as described above were not included in the evaluation steps of declustering and assessing completeness. The events assigned a non-tectonic flag are all smaller than the minimum magnitude of E[**M**] 3.3 used in the development of recurrence parameters (see Section 8.2.10). Therefore, the SSM TI Team did not conduct additional research on reported non-tectonic events, or sensitivity assessments on the events assigned non-tectonic flags.

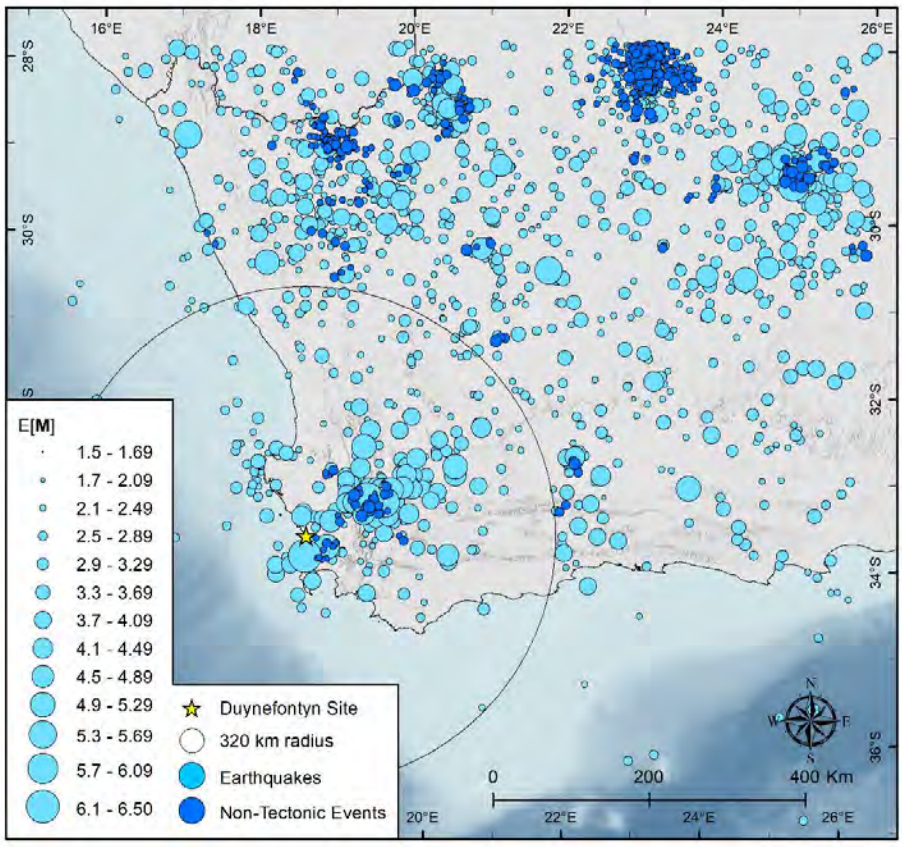

Figure 6-7. Project catalogue showing full catalogue (light blue circles) and flagged non-tectonic events (dark blue circles). Symbols are sized to grade upward with expected true moment magnitude (E[M]).

6.5 CLUSTERED EVENTS AND SEQUENCES

The SSM TI Team identified three spatial and temporal clusters in the Duynefontyn project catalogue on a regional map. Other clusters, which are actually diffuse when zoomed in, are apparent. The SSM TI Team evaluated three clusters: Ceres, Augrabies, and Koffiefontein (Figure 6-8), and assessed the time spans and spatial distributions to test the assumptions of stationarity and recurrence of events in a specific area.

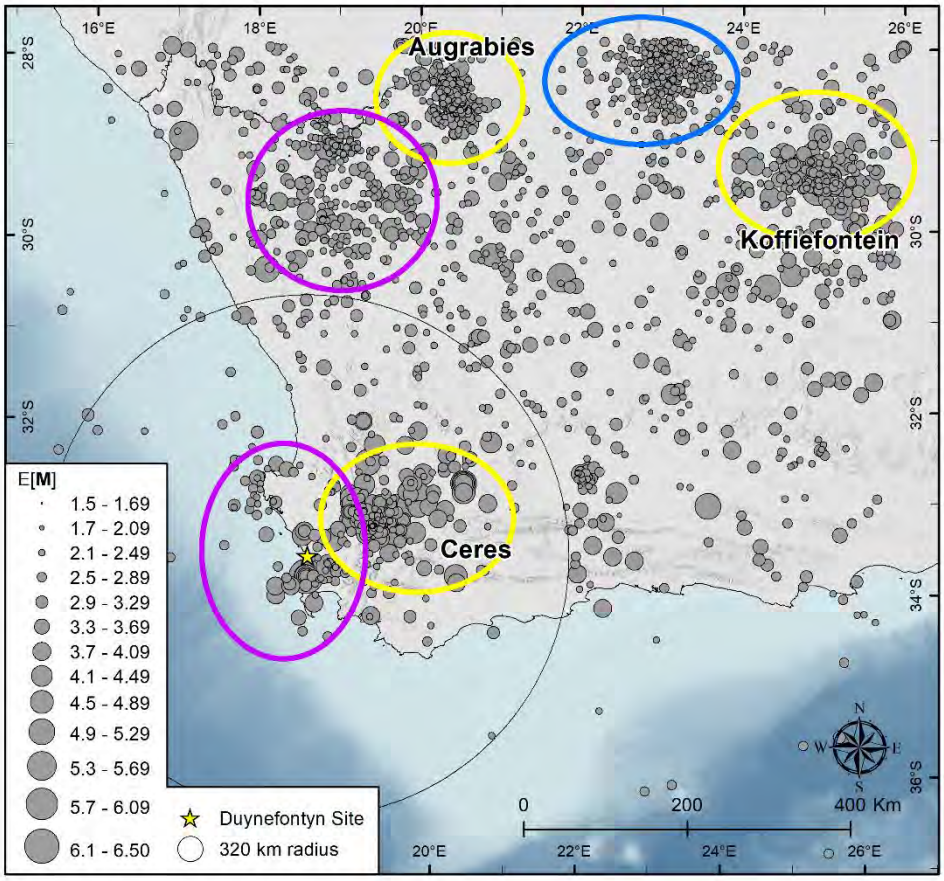

Figure 6-8. Spatial clusters identified from the Duynefontyn project catalogue. Yellow ellipses indicate tectonic clusters, blue ellipse indicates mining event cluster and purple ellipses indicate events which appear to be clustered but are actually sparse when zoomed in.

The SSM TI Team conducted spatial analysis from the seismic map (Figure 6-8), highlighting the location of clustered events, to determine the extent of the clusters. Three classes of clustered events were identified and included tectonic clusters, mining event clusters, and apparent clusters. The extent of each cluster is specific according to the spatial distribution of such class. The temporal distribution of the Ceres cluster shows three clusters: a cluster of events after the 1969 Ceres earthquake, a cluster starting in 1977, and another cluster starting in 2002 (Figure 6-9). The Augrabies cluster occurred in 2010 (Figure 6-10), and the SSM TI Team noted a pronounced cluster in 1977 in Koffiefontein (Figure 6-11).

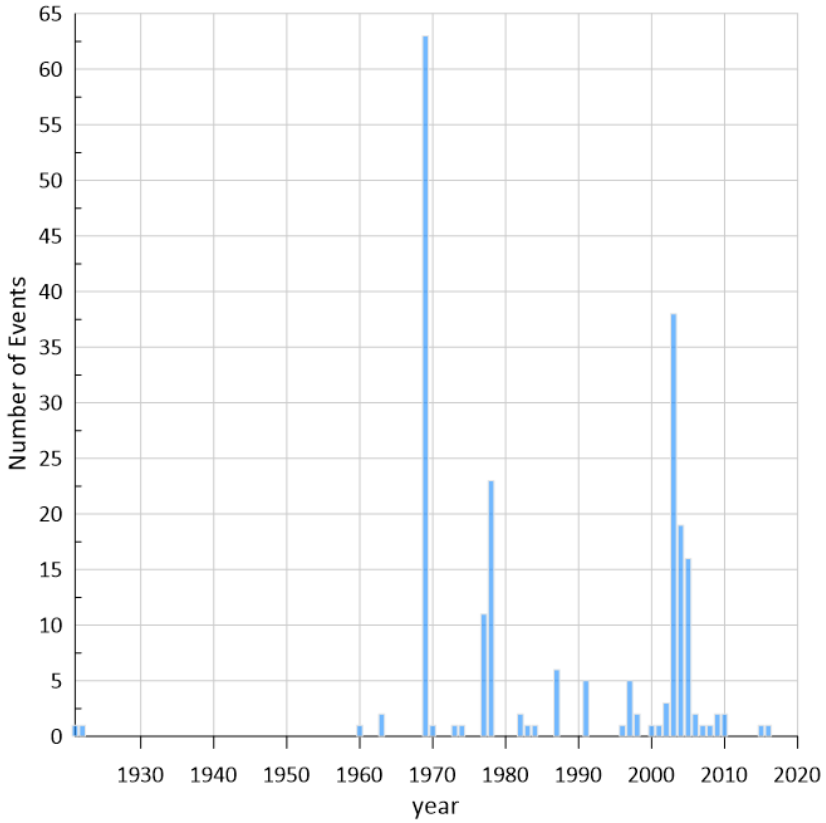

Figure 6-9. Ceres cluster with events E[M]≥2.0 from 1921 to 2015, showing an increase in the number of events in 1969, 1977, and again in 2002.

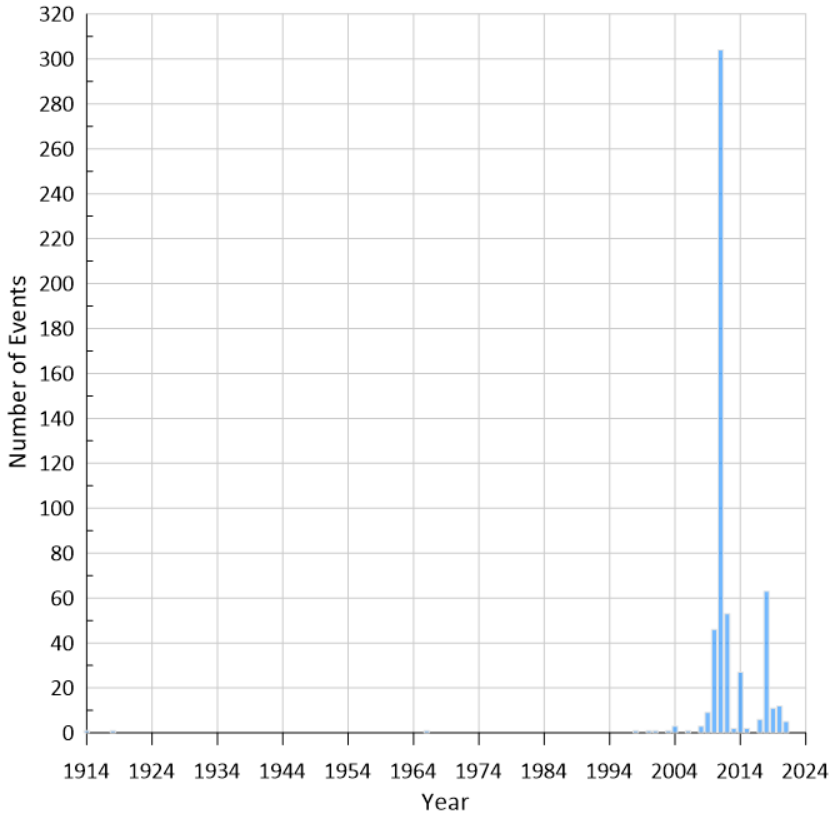

Figure 6-10. Augrabies cluster with events E[M]≥2.0 from 2001 to 2020, showing an increase in events beginning in 2010.

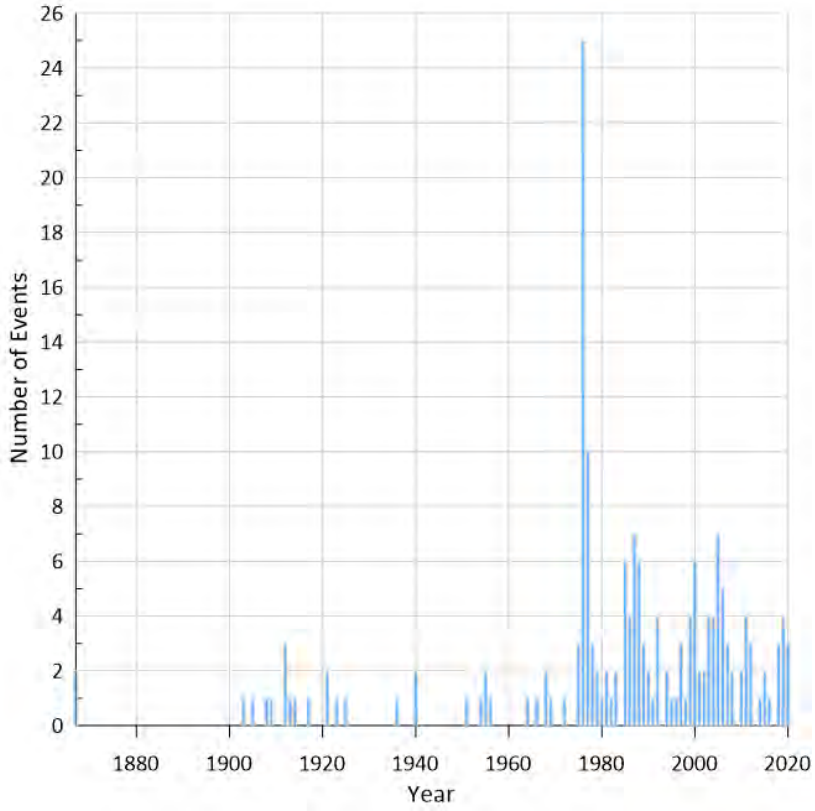

Figure 6-11. Koffiefontein cluster with events E[M]≥2.0 from 1867 to 2020, showing an increase in events in 1977.

The SSM TI Team conducted a statistical analysis using the computer code EQCLUSTER (EPRI-SOG, 1988, volumes 1-3), described in Section 6.7.1.2, to evaluate the duration of the Ceres cluster. The program identifies main and secondary events in the earthquake catalogue using a local cluster algorithm, based on the hypothesis that in a Poisson process, the rate of earthquakes inside a space-time window in the immediate vicinity of an earthquake should not be higher than the rate within a larger space-time window. The program iterates adjusting the size of the local space-time window until the condition is met. Two hypotheses for the duration of the 1969 Ceres cluster were tested by developing alternative sets of input parameters for the magnitude class associated with the Ceres event. In one case, labelled “Short Time Windows”, the time preceding the mainshock is set to 120 days, while the time following the mainshock is set to 365 days. This establishes the initial parameters of the local space-time window. The program is capable of extending the duration of the time window preceding the event to 360 days, and can extend the duration of the time window following the event to four years. Using this set of input parameters, the program can identify clusters with a total duration of up to five years (one prior to the mainshock and four following the mainshock), from 1968 to 1973. In this model, the sequence of events beginning in 1977 is not part of the Ceres cluster.

The alternative set of parameters, labelled “Long Time Windows”, specifies the same duration preceding the mainshock (i.e. 120 to 360 days), but assigns the maximum possible duration allowed by the code to the time following the event, which is 500 days. In addition, the program is capable of extending this duration to 4,000 days. This set of parameters results in a possible

total cluster duration of approximately twelve years (one year prior to the mainshock, and approximately eleven following the mainshock), from 1968 to 1980. In this model, the 1977 sequence could be allowed as part of the Ceres aftershock sequence.

EQCLUSTER returns a cluster duration of approximately three years when applied to this data set using either the “Short Time Windows” or “Long Time Windows” input parameters. In addition, the temporal cluster of events beginning in 1977 is located northeast of the Ceres cluster. Thus, the SSM TI Team interpretation is that statistical cluster analyses performed by EQCLUSTER, as well as the spatial distribution of the events, do not support the hypothesis that the increase in seismicity in 1977 is part of the 1969 Ceres aftershock sequence. The project catalogue includes events of magnitude $2.0 \leq E[\mathbf{M}] \leq 6.2$, thus excluding the cluster of very small magnitudes (reported as magnitude -1.9 to 1.66) from Smit et al. (2015), which shows the spatial and along-depth distribution of the Ceres cluster events.

6.6 MAGNITUDE HOMOGENISATION

The catalogue compilation process, as discussed in Section 6.2, involves combining earthquake records from multiple sources which typically do not report the same type of magnitude. Consequently, all available magnitude types must be converted to a common size measure. In modern PSHA studies, the magnitude measure adopted in the earthquake catalogue is chosen to be consistent with the magnitude scale used in the applicable GMPEs, which is moment magnitude (**M**[1]).

The earthquake catalogue is the primary dataset used to derive earthquake recurrence parameters for spatially distributed zones of seismicity. Studies (e.g. Tinti and Mulargia, 1985; EPRI-SOG, 1988; Musson, 2012) have shown that unless the uncertainty in magnitude estimates is accounted for in the analysis, the resulting recurrence rates will be biased. Section 6.6.1 discusses alternative methodologies for obtaining homogeneous magnitudes and unbiased earthquakes counts and presents justification for choosing the approach in NUREG-2115 (EPRI/DOE/USNRC, 2012).

6.6.1 Methodology for obtaining uniform magnitudes and unbiased earthquake counts

Earthquake magnitudes are calculated as a statistical average of measurements obtained at a number of seismic stations. Although this is not typically reported in network catalogues, there is a degree of uncertainty associated with each magnitude estimate. Additionally, when magnitudes are converted to a target magnitude (e.g. expected moment magnitude, E[**M**], as in the case of the project catalogue), the uncertainty associated with the empirical magnitude conversion relationship is introduced in the resulting converted magnitude. Without consideration of the uncertainty associated with magnitude estimates, it can be shown that the resulting earthquake recurrence rates are biased (Tinti and Mulargia, 1985; EPRI-SOG, 1988, Musson, 2012).

Figure 6-12 is a theoretical example to explain how magnitude uncertainty affects earthquake recurrence estimates. In this figure, three bell-shaped curves represent the uncertainty associated with magnitude 3 (blue), 3.5 (red), and 4 (green). The uncertainty is symmetrically distributed around the magnitude value. In recurrence calculations, earthquake counts are obtained within magnitude bins: in this example, these are centred on magnitudes 3, 3.5, and 4, and extend to ±0.25 magnitude units from the bin centre. The bins are depicted in the figure by vertical dashed lines. Focussing on the magnitude 3.5±0.25 bin, some of the earthquakes in this bin are “true” magnitude 3 earthquakes, but they are counted in the 3.5±0.25 bin due to the uncertainty in the observed magnitude. This is indicated by the portion of the blue bell-shaped curve that is shaded in pink. Similarly, some of the earthquakes in the magnitude 3.5±0.25 bin are “true” magnitude 4 earthquakes, but are counted in this bin by effect of the magnitude uncertainty, as shown by the portion of the green bell-shaped curve shaded in grey.

[1] In this document, when referring to the collected magnitude records, the notation **M** is used to indicate the moment magnitude calculated from seismic moment, while *Mw* is used to indicate moment magnitudes reported in earthquake catalogues for which a seismic moment is not available, or moment magnitudes computed by other means (e.g. from analysis of the Fourier spectrum).

Earthquake counts follow the exponential model (e.g. the Gutenberg-Richter distribution), such that the counts for magnitude 3 are approximately 10x the counts for magnitude 4. Consequently, the number of earthquakes that are shifted from the magnitude 3±0.25 bin to the magnitude 3.5±0.25 bin by effect of the magnitude uncertainty (pink-shaded area) is larger than the number of earthquakes that are shifted from the magnitude 4±0.25 bin to the magnitude 3.5±0.25 bin (grey-shaded area). As a result, the magnitude 3.5±0.25 bin contains more earthquakes than it would if the "true" magnitudes values were known. The same is valid for all other magnitude bins. The effect of shifting more earthquakes from bin m_i to m_{i+1} than from m_i to m_{i-1} is that the recurrence rates obtained without correcting for magnitude uncertainty are higher than the recurrence rates that would be obtained if the "true" earthquake magnitudes were known.

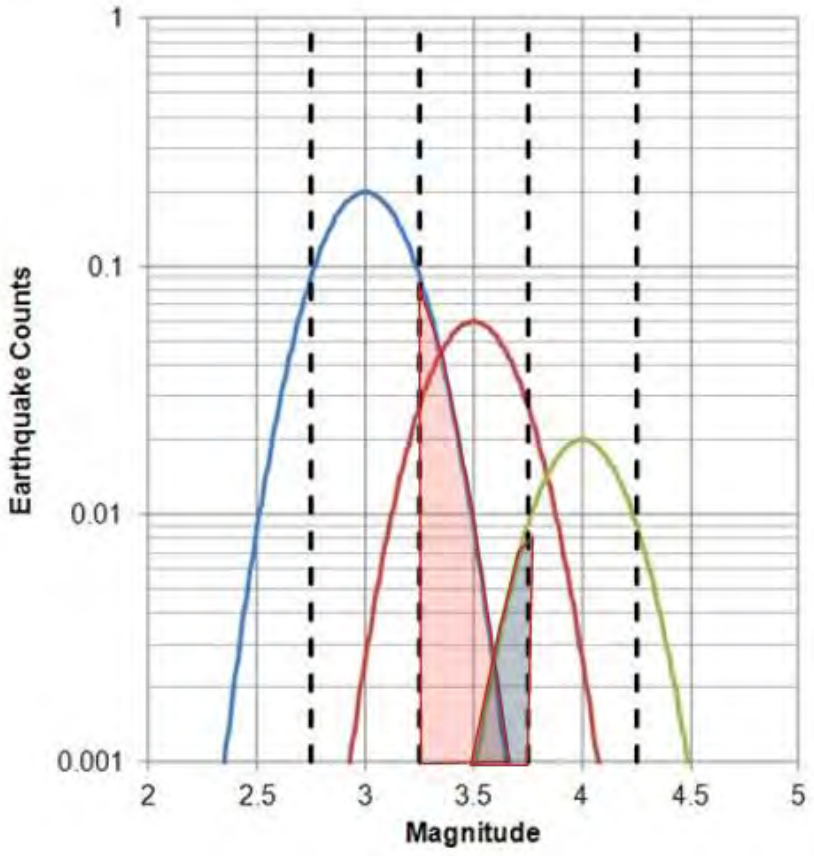

Figure 6-12. Theoretical example illustrating magnitude uncertainty and its effect on the calculation of earthquake recurrence rates. The bell-shaped curves represent the uncertainty associated with magnitude 3 (blue), 3.5 (red), and 4 (green). The bin boundaries are indicated by vertical dashed lines.

To correct the bias, the uncertainty in magnitude estimates needs to be quantified. EPRI-SOG (1988) proposed a variance-weighted methodology to fully incorporate uncertainties in magnitude estimates. The same methodology was later adopted in the Central and Eastern United States (CEUS) model (EPRI/DOE/USNRC, 2012). The process is as follows:

First, all independent magnitude estimates reported for each earthquake record in the compiled catalogue are converted using an appropriate empirical relation. The process produces vectors of the expected moment magnitude given another magnitude estimate ($E[\mathbf{M}|\hat{X}_i]$), and of the corresponding variance ($\sigma^2[\mathbf{M}|\hat{X}_i]$) for each earthquake.

The earthquake catalogue is processed to obtain values of E[**M**] and σ[**M**] for each earthquake using the equation:

6-1

$$\mathrm{E}\left[\mathbf{M} \mid \hat{\mathbf{X}}\right] = \left\{ \sum_i \frac{\sigma^2\left[\mathbf{M} \mid \hat{\mathbf{X}}\right]}{\sigma^2\left[\mathbf{M} \mid \hat{X}_i\right]} \cdot E\left[\mathbf{M} \mid \hat{X}_i\right] \right\} + (R-1)\beta\sigma^2\left[\mathbf{M} \mid \hat{\mathbf{X}}\right]$$

and

6-2

$$\sigma^2\left[\mathbf{M} \mid \hat{\mathbf{X}}\right] = \left\{ \sum_i \frac{1}{\sigma^2\left[\mathbf{M} \mid \hat{X}_i\right]} \right\}^{-1}$$

where $\hat{X}_i$ is a single member of the vector $\hat{\mathbf{X}}$, R is the number of observed size measures, and β is the *b*-value in natural log units ($\beta = b\ln(10)$).

For records with moment magnitudes computed directly from seismic moments, the process is slightly different. The expected value of the true moment magnitude (E[**M**]) can be obtained from the observed moment magnitude ($\hat{\mathbf{M}}$) given its uncertainty $\sigma[\mathbf{M}|\hat{\mathbf{M}}]$, using the following equation:

6-3

$$E\left[\boldsymbol{M}\middle|\hat{\boldsymbol{M}}\right] = \hat{\boldsymbol{M}} - \beta\sigma^2\left[\boldsymbol{M}\middle|\hat{\boldsymbol{M}}\right]$$

Two alternative approaches were proposed to correct the bias. EPRI-SOG (1988) suggested adjusting the magnitudes to correct the bias, and proposed the following correction for observed moment magnitudes ($\hat{\mathbf{M}}$):

6-4

$$\mathbf{M}^* = \hat{\boldsymbol{M}} - \beta\sigma^2\left[\boldsymbol{M}\middle|\hat{\boldsymbol{M}}\right]/2$$

This approach is commonly referred to as "**M*** approach".

Using simulations, EPRI/DOE/USNRC (2012) shows that recurrence rates computed with **M*** slightly overestimate the recurrence rates computed with the "true **M**", while rates computed using E[**M**] underestimate the "true" recurrence.

Tinti and Mulargia (1985) proposed adjusting the earthquake counts and applying a correction factor to the entire catalogue to correct the bias in the recurrence rates.

EPRI/DOE/USNRC (2012) adopts the Tinti and Mulargia (1985) approach to correct the counts, but applies the correction to individual E[**M**] counts rather than to the entire catalogue. This allows for individual earthquakes to be corrected differently depending on the error associated with E[**M**]. This approach is commonly referred to as "N* approach", where N* represents the corrected count and is computed using the following equation:

$$N^* = \exp\left\{\frac{\beta^2\sigma^2\left[\boldsymbol{M}\middle|\widehat{\boldsymbol{M}}\right]}{2}\right\}$$

or

$$N^* = \exp\left\{\frac{\beta^2\sigma^2[\boldsymbol{M}|\boldsymbol{X}]}{2}\right\}$$

where $\hat{\mathbf{M}}$ is the observed moment magnitude obtained from the seismic moment, while M|X represents a vector of moment magnitudes converted from other magnitude types.

While the effect of magnitude errors on earthquake counts is well understood, its effect on *b*-value estimates is more controversial. For example, Rhoades and Dowrick (2000) concluded that the error causes an underestimation of *b*-values, whereas Marzocchi and Sandri (2009) and Marzocchi et al. (2019) argued that errors in magnitude do not significantly affect the estimation of *b*-value for a catalogue with homogeneous magnitude, and Taroni (2022) showed that non-uniform error distribution in magnitude can lead to overestimation of the *b*-value.

Simulations described in EPRI/DOE/USNRC (2012) test the effectiveness of the N* approach compared to the **M*** approach in obtaining unbiased rates and *b*-values when the catalogue is homogeneous (i.e. instrumental magnitudes only, or macroseismic intensities only) or non-homogeneous (i.e. a combination of macroseismic intensities and instrumental magnitudes), and completeness intervals vary by magnitude and over time. The results of the simulations shown in EPRI/DOE/USNRC (2012) show that the average percent errors between the "true" N(**M**≥4) and *b*-values and the corresponding values of N(**M**≥4) and *b* obtained with N* and **M*** are consistently smaller for N*. Specifically, percent errors for N(**M**≥4) are less than 2% for N*, but up to 50% for **M***, while percent errors for *b*-value are less than 1% for N* and up to 12% for **M***.

The N* approach is followed in this study because it has been demonstrated to produce unbiased earthquake counts and *b*-values. In computing earthquake counts for recurrence calculations, each earthquake is represented by its E[**M**] and by its N* value, which is generally slightly larger than 1.

6.6.2 Target magnitude and available magnitude

As discussed in Section 6.6.1, the earthquake magnitudes need to be converted to moment magnitude (**M**) to be consistent with the ground motion models adopted in the PSHA. The project earthquake catalogue contains 2,648 events with at least one size measure. 784 events report at least one additional magnitude estimate and many of these report more than one. Most of the earthquake events report one or more estimates of local magnitude (M_L) (3,284 values in total). The remaining data is divided between M_W, body-wave magnitude (m_b and m_{bLg}), and other magnitude measures including surface-wave magnitude (M_S), and duration magnitude (M_D).

Table 6-2. Magnitude types in the project earthquake catalogue.

Magnitude Type	Number of Occurrences[1]
M_L (including M_{BUL})	3,284
m_b (including m_b[2] and m_{btmp}[3])	71
m_{bLg}[4]	5
M_W	67
M_S	13
M_D	33
L	122
W[5]	34
M[6]	88
Total	3,717

[1] May be more than one occurrence for each earthquake event
[2] m_{b1} is a short-period body-wave magnitude reported by ISC
[3] m_{btmp} is a short-period body-wave magnitude reported by ISC, with depth fixed at the surface.
[4] m_{bLg} is Lg-wave magnitude
[5] W is *Mw,* from Ian Saunders, reported in DDC2 (Saunders, 2023).
[6] **M** is moment magnitude computed by the TI Team from seismic moment, using the formula by Hanks and Kanamori (1979).

6.6.2.1 Available moment magnitude

Table 6-2 shows that there are only 101 estimated moment magnitudes. These were supplemented by two datasets developed for the GMM TI Team by Dr Peter Stafford and Dr Ben Edwards, respectively. Dr Stafford and Dr Edwards were provided with a catalogue of earthquakes in southern Africa (extending beyond the boundaries of the project earthquake catalogue) for which recordings were available and tasked with inverting the data to assess parameters for use by the GMM TI Team. Because the inversion techniques used by each expert are different, even if they started from the same catalogue, their data selection differs. The relevance of these datasets to the SSM TI Team is that each expert computed moment magnitudes from analysis of the Fourier spectra for the earthquakes they selected.

Dr Peter Stafford provided the SSM TI Team (P. Stafford email communication to V. Montaldo Falero, 22 June 2023, subject: Moment Magnitude Estimates) with two files (one by Dr Stafford, one by Dr Edwards) containing earthquake records with M_L, calculated moment magnitude (M_W), and an estimate of the error (σ_{Mw}) in the calculated magnitude. Dr Stafford's dataset includes 368 earthquakes with M_W and σ_{Mw}, 101 of which are included in the project earthquake catalogue based on location and minimum magnitude threshold. Dr Edwards' dataset includes 134 earthquakes with M_W and σ_{Mw}, of which 32 are included in the project earthquake catalogue based on location and minimum magnitude threshold. None of the catalogue records for which Dr Stafford and Dr Edwards provided M_W has a value of M_W from another agency or author.

6.6.3 Estimation of E[M] from M_L and other magnitudes

The following subsections provide details about the empirical magnitude conversion relations used to estimate E[**M**] from the magnitudes available in the project earthquake catalogue.

6.6.3.1 E[M] from M_L

Seismic networks in Africa routinely assign local magnitude (M_L) to recorded earthquakes, but there are differences between agencies, as well as over time, in the way these M_L were calculated. The differences are largely due to changes in the instrumentation, which require the use of different relations to compute M_L from recorded amplitudes. Manzunzu et al. (2021) developed alternative linear relationships between M_L and M_W, depending on the time period, to address the changes in instrumentation of the South African National Seismic Network (SANSN). These relationships cannot be directly used to implement the N* approach for two reasons: (1) the variance-weighted calculation of E[**M**] implicitly assumes a least-squares regression (Arabasz et al., 2016), while Manzunzu et al. (2021) adopted generalised orthogonal regression; and (2) as discussed in EPRI/DOE/USNRC (2012), if the variance of the observed magnitudes used in conversion is included in the adjustments, the corrected magnitudes provide a better approximation of the "true" rates (i.e. the rates that would be obtained if we knew the true **M** of the earthquakes).

As shown in Table 6-2, there are 122 magnitudes in the catalogue identified as "L" and 88 identified as "M". The "L" magnitudes were obtained by Ian Saunders as part of DDC2 (Saunders, 2024) and are nominally M_L; the "M" magnitudes are reported by the Goetz Observatory in Bulawayo, Zimbabwe (agency code "BUL") and should also be M_L. To avoid confusion between these "M" magnitudes and **M**, the magnitude type will be referred to as M_{BUL} hereinafter. Both size measures (L and M_{BUL}) are interpreted to be equal to M_L, therefore, their relationship to M_L obtained by other agencies was explored. Figure 6-13 shows 86 pairs of M_L and L (blue), and 70 pairs of M_L and M_{BUL} (orange). The figure shows a clear linear trend between M_L and M_{BUL}, consistent with M_{BUL} being the same as M_L. On the contrary, L shows a large scatter and no obvious trend with M_L. Consequently, the SSM TI Team decided to consider $M_{BUL} = M_L$ and to disregard L unless no other size measure is available. In that case, the SSM TI Team decided that L should be assumed to be equal to M_L.

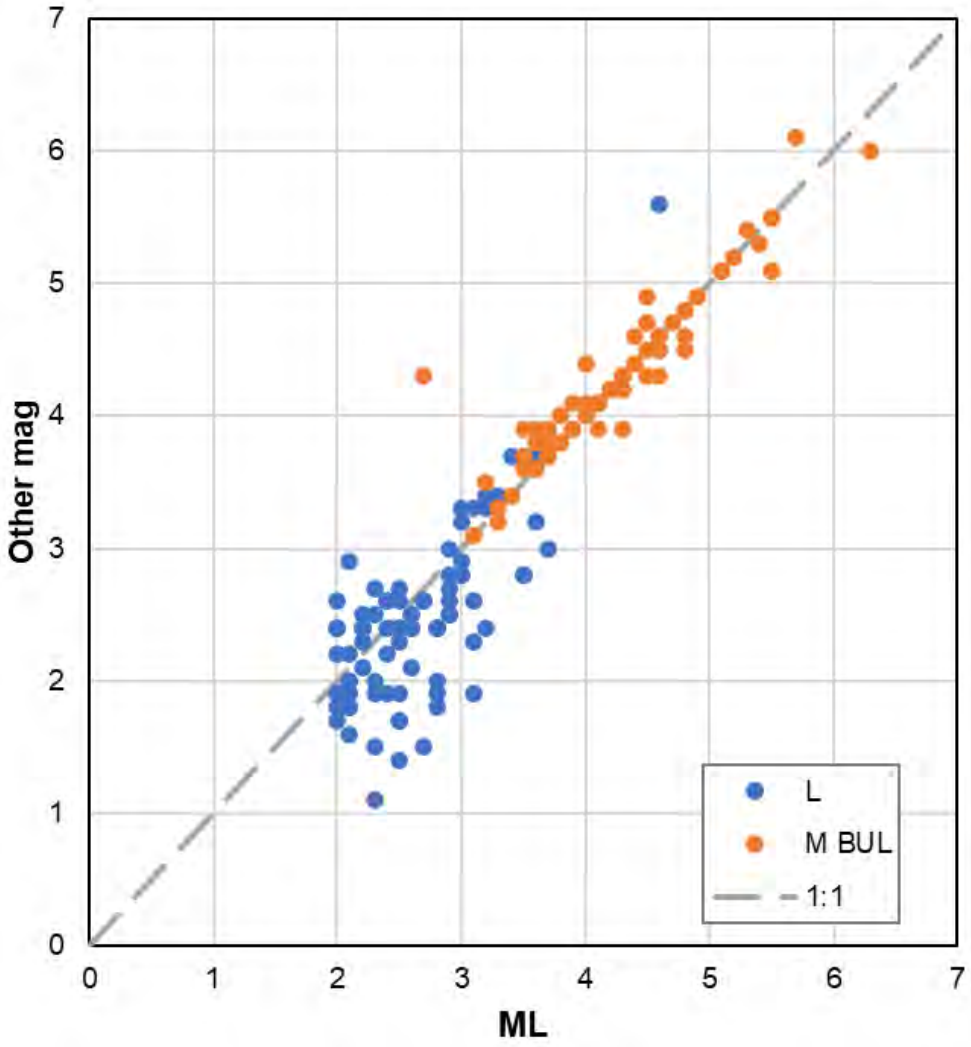

Figure 6-13. M_L data vs L and M_{BUL}.

Disregarding L and considering M_L and M_{BUL}, the earthquake catalogue contains 107 pairs of M_L and M_W, which are shown in Figure 6-14 by the black dots. This data is augmented by the datasets provided by Dr Stafford and Dr Edwards, bringing the total to 609 M_L and M_W pairs (shown in Figure 6-14 by open circles and crosses, respectively), which are used in developing a project-specific magnitude conversion relationship.

The dataset is shown in Figure 6-14 by different symbols. The data is fitted by a quadratic model given by the relationship:

6-6

$$E[\boldsymbol{M}|M_L] = 1.422 + 0.271 \cdot M_L + 0.075 \cdot M_L^2$$

$$\sigma_{E[\boldsymbol{M}|M_L]} = 0.228$$

where $\sigma_{E[\boldsymbol{M}|M_L]}$ is calculated from the regression variance (var_{regr}=0.24882) less the average variance of the **M** data used ($var_{\mathbf{M}}$= 0.0992).

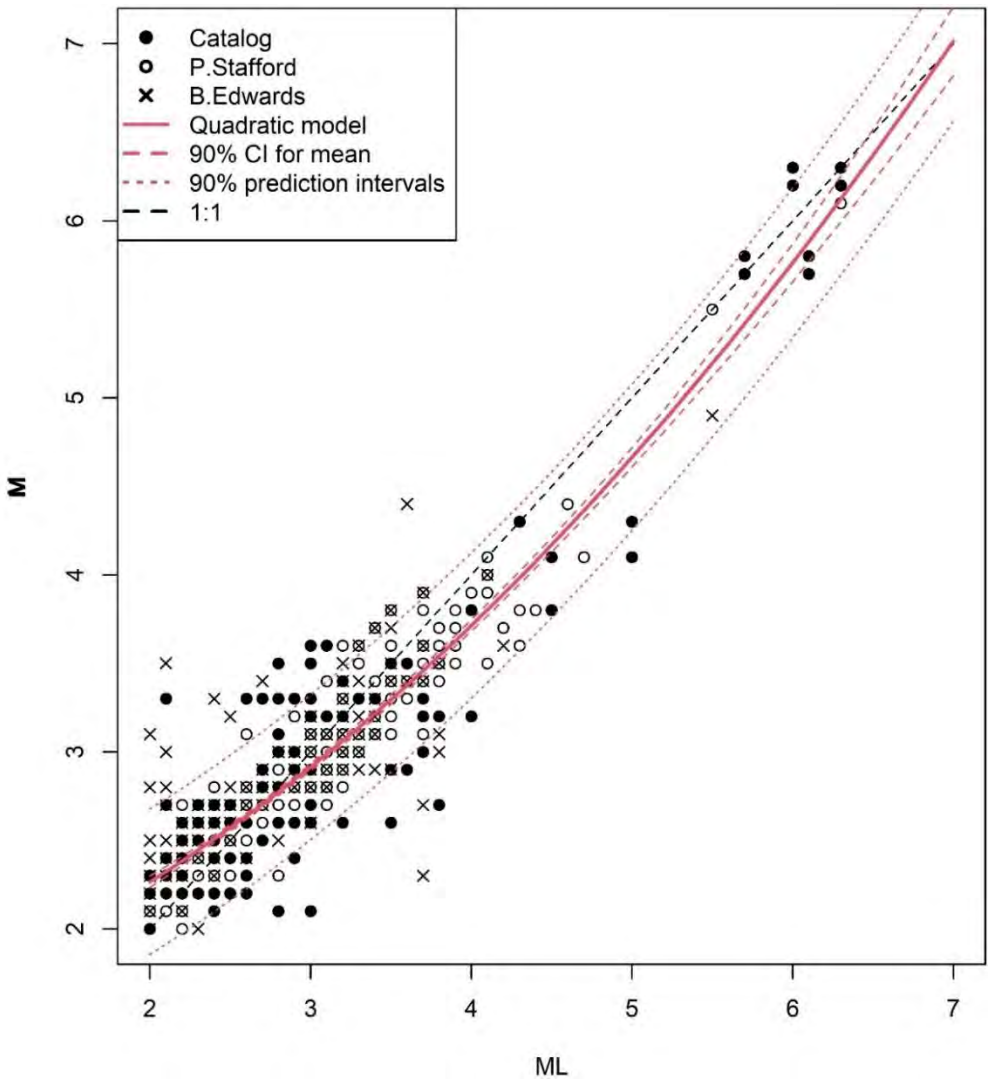

Figure 6-14. M_L to M conversion.

6.6.3.2 E[M] from M_W

Section 6.6.2.1 discusses the availability of M_W data in the earthquake catalogue and the additional M_W datasets obtained by Dr Stafford and Dr Edwards.

The SSM TI Team agreed to consider M_W = **M**. The associated σ_{Mw} was chosen to be either the direct estimate obtained by Dr Stafford or Dr Edwards for M_W in their dataset, or the average σ_{Mw}=0.14 obtained from Dr Stafford's data for all other M_W records.

In cases where multiple M_W values are available, they were combined in a weighted average using the formulation presented in EPRI/DOE/USNRC (2012), assuming all estimates have equal weight.

6.6.3.3 E[M] from body-wave magnitudes

The available data is insufficient to derive a project-specific magnitude conversion for body-wave magnitudes, or to test the applicability of existing relationships. For this reason, the SSM TI Team decided to adopt the conversion relation by Johnston et al. (1994), applicable to CEUS, with its standard deviation:

6-7

$$M_W = 0.9773 \cdot m_b + 0.153$$

$$\sigma_{mb}=0.263$$

This relation was adopted in the Thyspunt PSHA study (Strasser and Mongongolo, 2013). The SSM TI Team chose to use m_b data only if no other size measure is available for an earthquake record, and to treat M_W computed from Equation 6-7 as E[**M**|m_b]. This is the case for only two records in the catalogue.

*6.6.3.4 E[**M**] from M_S*

The available data is insufficient to derive a project-specific magnitude conversion relation for surface-wave magnitudes, or to test the applicability of existing relationships. For this reason, the SSM TI Team chose to only use M_S values greater than 5.0 under the assumption that in this magnitude range M_S=**M**. This choice is applied to four earthquakes, for a total of six M_S values between 5.4 and 6.6. IASPEI (2009) summarizes multiple relations with slope approximately 1 for M_S as low as 6.1, albeit most of these relations are derived for plate boundary regions. The magnitude conversion relationship derived by EPRI/DOE/NRC (2012) from Central Eastern United States M_S data is approximately linear between M_S 5.5 and 6. The SSM TI Team decided to apply the average σ_{Mw}=0.14 obtained from Dr Stafford's data to M_S.

*6.6.3.5 E[**M**] from other magnitude types*

The SSM TI Team decided to treat any additional magnitude types listed in Table 6-2 that are not specifically addressed in Sections 6.6.3.1 through 6.6.3.4 as equal to M_L, adopting Equation 6-6 to obtain E[**M**|M_L]. This applied to 33 reported duration magnitudes (M_D) in the compiled earthquake catalogue.

6.7 DECLUSTERING

For the PSHA, earthquake recurrence is assumed to be a Poisson process, and all future earthquakes are assumed to be independent events occurring at a consistent rate over long timeframes. To resemble the Poisson assumption, the declustering process aims to identify and remove (or flag) events such as foreshocks and aftershocks that are linked to a main shock event. The assumption is that dependent events are at least partly controlled by the occurrence of previous earthquakes and therefore would introduce bias to the frequency of ground motion exceedance if considered as individual, recurring contributors to ground motion occurrence.

6.7.1 Available declustering methods

Various declustering methods are described below, with a focus on the inputs or requirements most pertinent to the SSM project catalogue.

6.7.1.1 Window method

Time and distance window methods are generally the simplest declustering method to implement. Using this method, dependent events are identified by their proximity and occurrence related to another event of larger magnitude. Only the most basic information is required for successful application to an earthquake catalogue, therefore, many time and distance window relationships have been developed for various regions. Gardner and Knopoff (1974), Grünthal (1985), Uhrhammer (1986), Peláez et al. (2007) and Instituto Geográfico Nacional (2013) are all examples of time and distance window-based methods. Gardner and Knopoff (1974) and Uhrhammer (1986) windows were developed from earthquakes in California. Grünthal (1985) windows were developed based on earthquakes in Germany and surrounding areas. Peláez et al. (2007) windows are modified Gardner Knopoff windows based on earthquakes in Morocco. The Instituto Geográfico Nacional (2013) method was developed based on earthquakes in Spain.

Figure 6-15 shows plots comparing the distance (a) and time (b) windows by magnitude for each of the publications listed above. It also shows the counts of events in the full project catalogue, using bin widths of 0.1-magnitude units. The maximum magnitude in the SSM project catalogue is E[**M**] 6.2. Figure 6-15 a shows little difference in the distance windows for the full range of magnitudes in the project catalogue, but greater variation in time windows for E[**M**] 5 and larger events (Figure 6-15 b). However, because very few events in the project catalogue fall within this range, only minor differences in the number of events were realised by applying the different window relationships. Additionally, the differences between identified dependent events for the various window relationships primarily affected small-magnitude events. Evaluations of the various methods indicated no significant effect on *b*-value. Of the window relationships tested, the Gardner and Knopoff (1974) relationship was derived from the most comprehensive dataset and has been more widely tested than the others. The SSM TI Team selected the Gardner and Knopoff (1974) declustering method to represent the window declustering method.

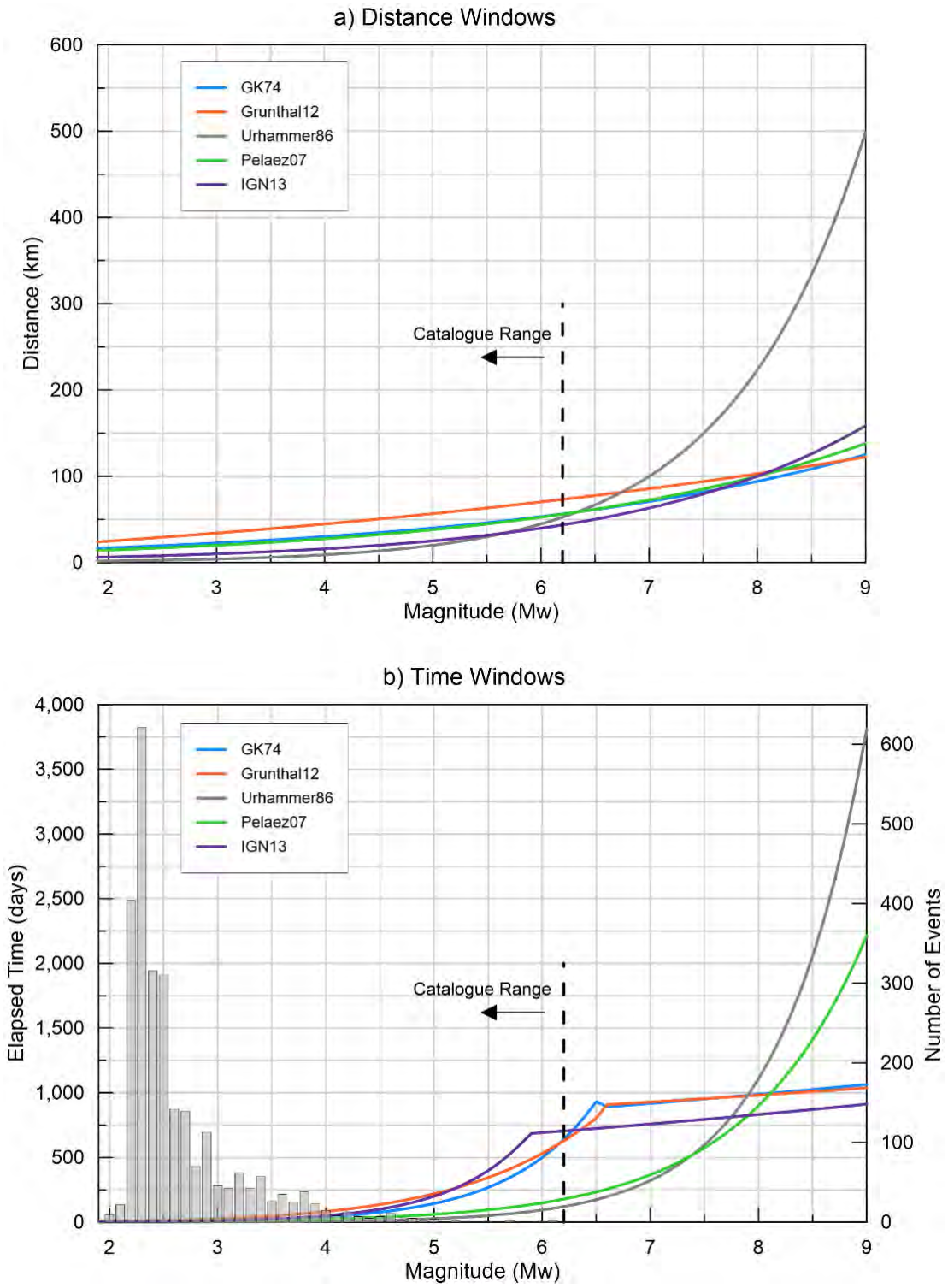

Figure 6-15. Comparison of (a) distance and (b) time window relationships by magnitude. Histogram in (b) shows the number of events in the catalogue using bins of 0.1 magnitude units.

6.7.1.2 Statistical method

Statistical and cluster methods use statistical analysis to identify a cluster of events and retain one event as the mainshock. The remaining events in the identified cluster are flagged as dependent events (foreshocks or aftershocks). The program EQCLUSTER (EPRI-SOG, 1988, volumes 1-3) is an example of the statistical method that has been used in previous SSHAC

projects. The algorithm first orders the earthquake catalogue from the largest to the smallest magnitude earthquake, then it constructs a local space-time window in the immediate vicinity of the selected earthquake, and a much larger extended window. The null hypothesis used by the algorithm is that, assuming a Poisson process, the seismicity should not be elevated in the local window. If the null hypothesis is rejected, the algorithm continues to test adjacent space and time windows until it finds the local space-time window within which the seismicity is not elevated compared to the extended window. The final step in the process is to reduce the earthquake counts in the cluster region to match the background rate in the extended window. The process is repeated a second time, after removing all events identified as secondary during the first step. The methodology was used in the EPRI/DOE/USNRC (2012) study as the single methodology for declustering the catalogue. EPRI/DOE/USNRC (2012) lists the advantages of the EQCLUSTER approach as (1) being insensitive to incompleteness because a homogeneous Poisson process is only assumed in proximity to the earthquake sequence being tested, and (2) not assuming an *a priori* shape for the clusters. The SSM TI Team selected the EQCLUSTER declustering method to represent the statistical declustering method.

6.7.1.3 Epidemic-type aftershock sequence (ETAS) method

The ETAS method describes the implementation of a stochastic model of earthquake occurrences. It was originally applied to seismicity by Hawkes and Adamopoulos (1973), and further developed by Ogata (1988, 1998) and Ogata and Zhuang (2006). The ETAS model has been applied to regions outside of active plate boundary regions by Chu et al. (2011). Additionally, Kattamanchi et al. (2017) proposed a non-stationary ETAS approach that allows the background rate to vary.

The ETAS method is the most difficult declustering method to implement. Many input parameters are required for implementation. The method can therefore be computationally intensive because iterative testing is often needed to determine the optimal set of parameters.

6.7.2 Analysis and selected approach

The SSM TI Team chose not to use the ETAS declustering method because of the high degree of uncertainty in the array of input parameters combined with the sparsity of events in the catalogue.

Preliminary assessment of the window and statistical methods was performed. The window method was represented by Gardner and Knopoff (1974), while the program EQCLUSTER was used for the statistical method.

The reported time and distance windows from EQCLUSTER were nearly the same as the Gardner and Knopoff (1974) windows for the same magnitude intervals. Comparison of the results showed a statistically insignificant difference in the number of independent event outputs by the two methods, and showed that differences were limited to magnitudes less than **M** 4.5.

Based on these comparisons, the SSM TI Team established that while EQCLUSTER is an alternative methodology to Gardner and Knopoff (1974), the remarkable similarity for **M**>4.5 for this data set between results of the two methods does not warrant inclusion in the logic tree. The SSM TI Team decided to use Gardner and Knopoff (1974) as a single declustering

algorithm, largely because it removes fewer events for small magnitudes (Figure 6-16), thus providing more data for the application of methods to obtain the *b*-value such as the *b*-positive approach (van der Elst, 2021).

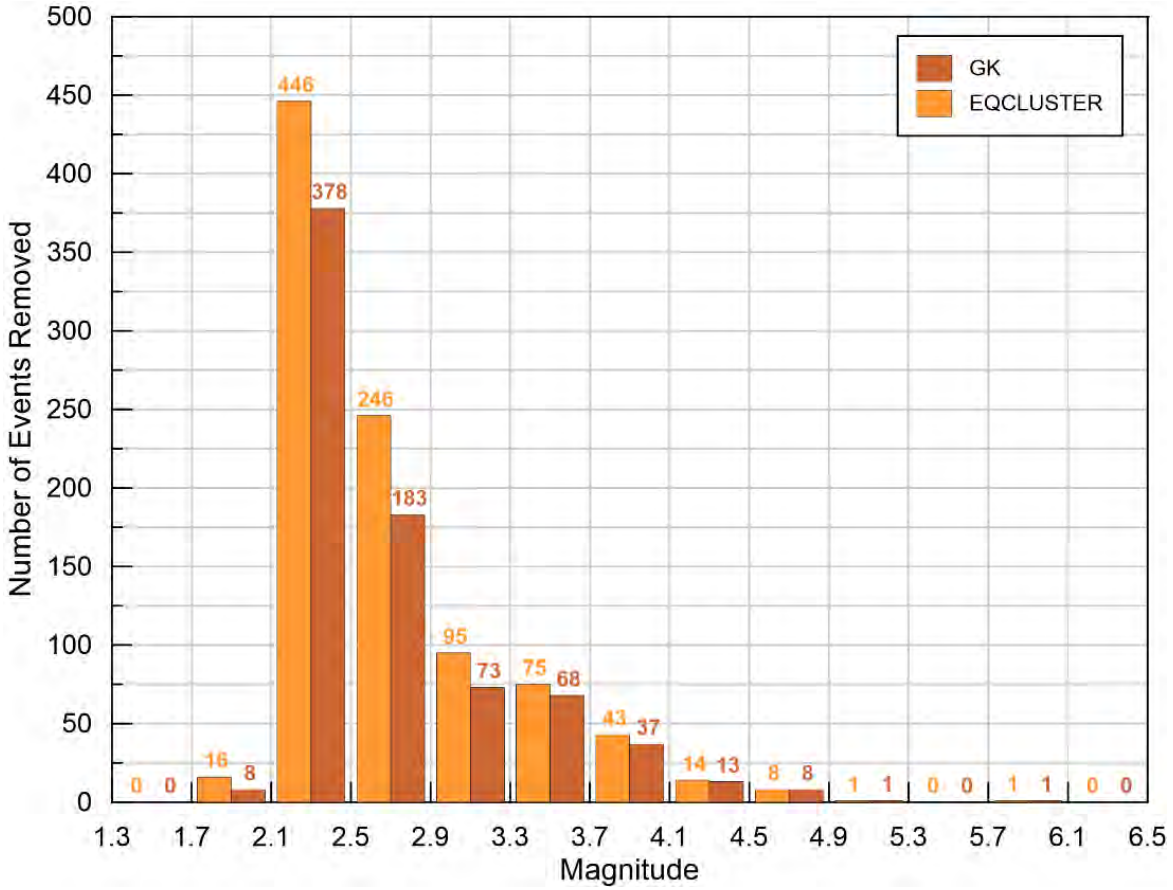

Figure 6-16. Comparison of the dependent event counts by magnitude, using bin width (dM) of 0.4. Counts of events marked for removal are shown for the EQCLUSTER method (left bars, light orange) and Gardner and Knopoff (1974) method (right bars, dark orange).

6.7.3 Declustering results

The SSM TI Team implemented the Gardner and Knopoff (1974) declustering method to identify independent and dependent events. Events with non-tectonic flags were not included in the declustering analysis. After declustering, the independent catalogue includes 1,373 events. Independent and dependent events are shown in Figure 6-17. Note the strong clustered behaviour of the dependent events in Figure 6-17. Histograms of events by magnitude before and after declustering are shown in Figure 6-18.

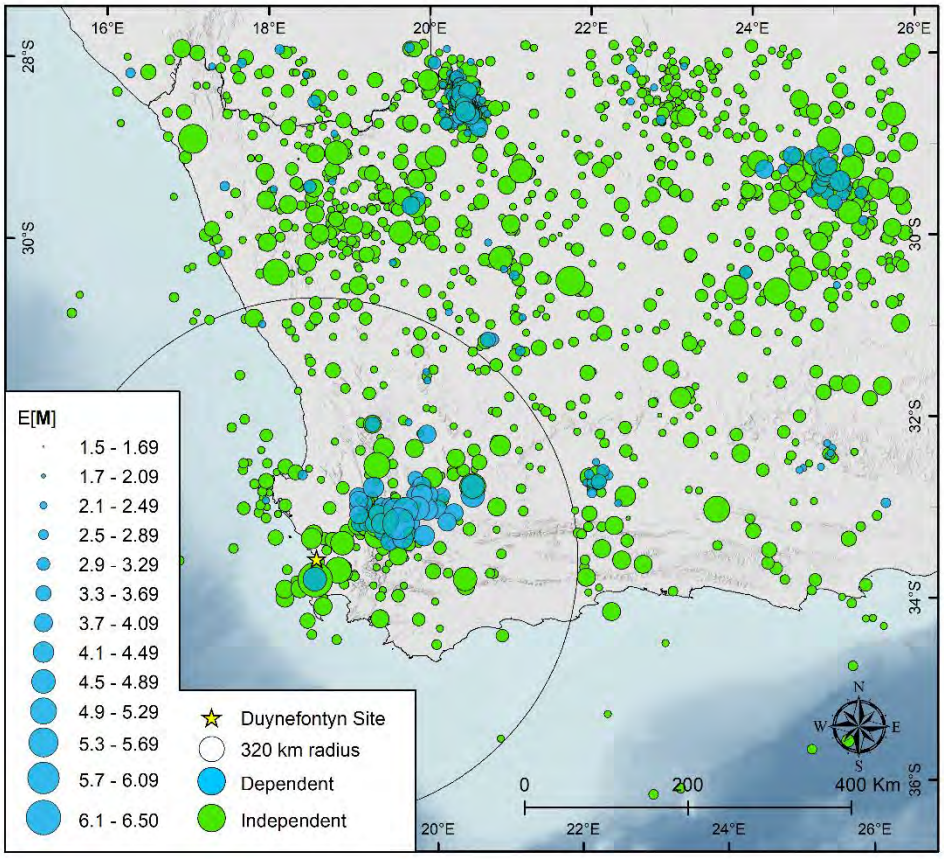

Figure 6-17. Independent and dependent events. See Section 6.5 and Figure 6-8 for identification and discussion of specific regional clusters.

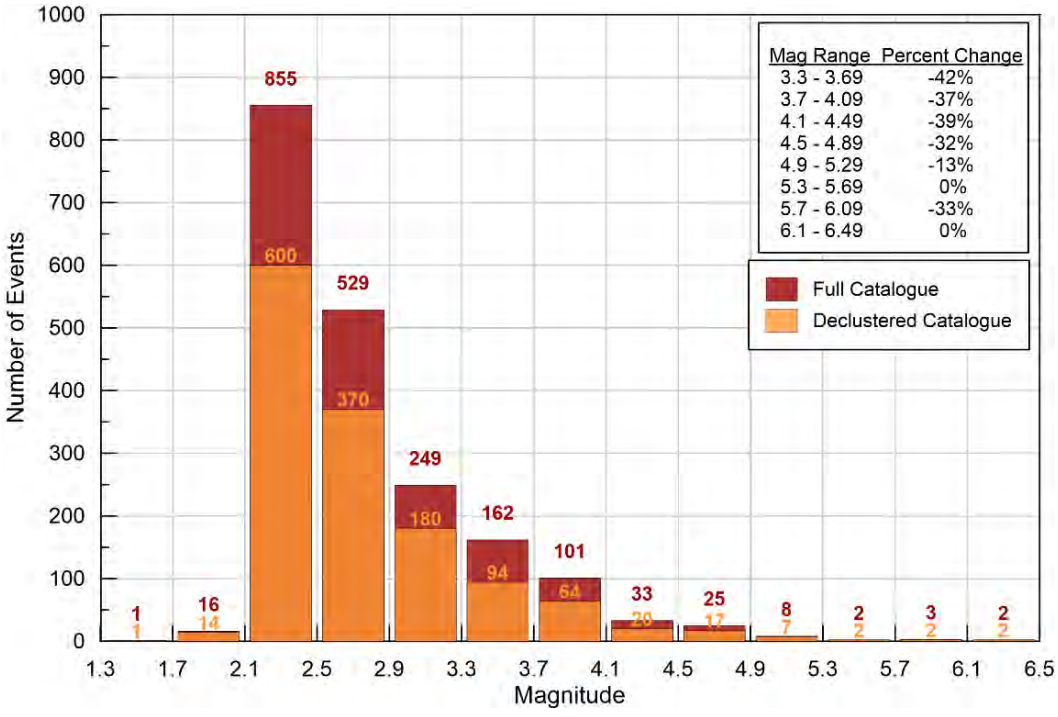

Figure 6-18. Histograms of events by magnitude before and after declustering. Darker-coloured bars are counts prior to declustering, lighter-coloured bars show counts after declustering.

Testing of the location of the 11 September 1969 event (described in Section 5.3.9) indicated that there was no impact on the declustering results.

To confirm that the declustered earthquake catalogue follows a Poisson process in time, a Kolmogorov-Smirnov (K-S) statistical test was conducted for various magnitude thresholds. In this test, which is illustrated in Figure 6-19 and described in Luen and Stark (2012), the cumulative density function (CDF) of the observed annual number of earthquakes above a threshold magnitude (blue curve) is compared to the CDF of the predicted annual number of earthquakes that would be observed in a perfectly Poissonian catalogue with a rate equal to the mean annual rate of observed earthquakes in the same time period (65 years in the figure). The mean Poisson CDF is shown by the solid orange curve, while the dashed yellow curves represent 5% confidence intervals on the prediction.

Various magnitude thresholds were tested, starting at E[**M**] 2.2. The results of the K-S test indicated that for magnitudes less than 3.7, the null hypothesis that the declustered catalogue follows a Poisson process in time is rejected at the 5% confidence interval. For E[**M**]≥3.7, as shown in Figure 6-19a, the null hypothesis is not rejected, indicating that the declustered catalogue is not inconsistent with a Poisson process at the 5% confidence interval. Figure 6-19b, the null hypothesis is rejected, indicating for E[**M**]≥2.5 the declustered catalogue is inconsistent with a Poisson process at the 5% confidence interval.

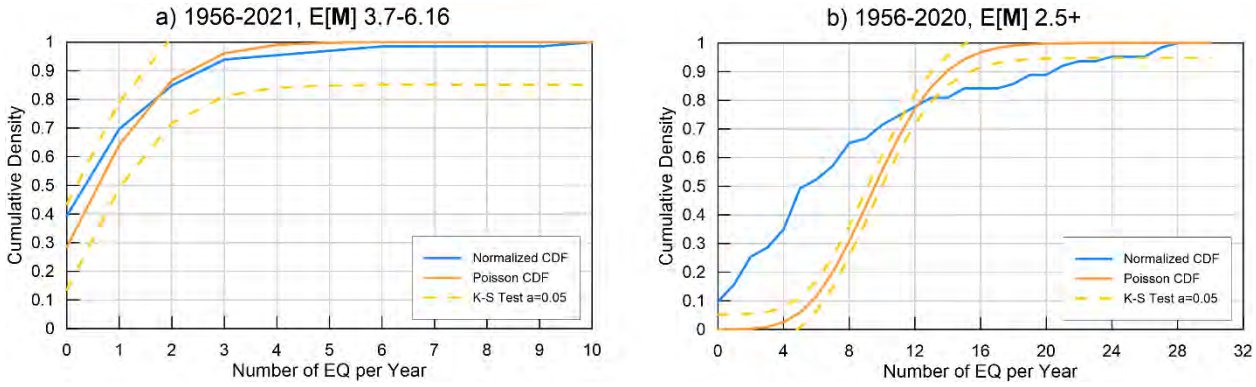

Figure 6-19. Poisson check of earthquake catalogue declustered following the Gardner and Knopoff (1974) method, for events between 1956 and 2021. Blue lines are calculated using the earthquake catalogue and orange lines are the K-S test bounds for comparison. Plot (a) shows the successful test for E[M] 3.7 to 6.16 events whereas (b) shows that using E[M] 2.5 and larger events did not pass the Poisson check.

6.8 COMPLETENESS

The applicability of recurrence rates developed using the earthquake catalogue is, in part, dependent on the completeness of the earthquake catalogue. A catalogue is considered complete if it includes all earthquakes that occurred over the catalogue time period, typically assessed for different magnitude ranges. Incompleteness for each magnitude can vary over time and space and can be attributed to changes in earthquake detection capabilities. This is due to population density and recording practices for the historical portion of the catalogue, and coverage and sensitivity of seismic instrumentation for the instrumental portion of the catalogue. Catalogue incompleteness can introduce bias to estimations of seismicity rates and *b*-values, and must therefore be accounted for in the catalogue.

6.8.1 Available approaches

6.8.1.1 Magnitude cutoffs

Following the method of Stepp (1972), completeness is defined for a specific magnitude range by counting those events within the range, starting from the latest event in the catalogue and moving back in time. The cumulative rate is calculated for each additional event in the catalogue, as the time period increases going back in time. For a magnitude range following a Poisson process, the rate of events during the complete time interval is consistent (e.g. roughly horizontal when plotted). The rate of events decreases rapidly during the incomplete time, plotting as a downward slope. The point in time where the slope breaks away from roughly horizontal is the earliest point of the complete period. The same assessment is applied to the full series of magnitude ranges in an earthquake catalogue to determine the period of completeness for each magnitude range.

Applying the Stepp (1972) method to determine completeness period cutoffs for each magnitude range, earthquakes in the catalogue are either within the completeness period or outside it. Only the events that occurred within the effective time of completeness (*TE*) for each magnitude range are used in calculations of earthquake recurrence.

6.8.1.2 Probability of detection

The probability of detection (P^D) method was originally introduced by Veneziano and Van Dyck (1985) and evolved into the methodology used in the EPRI-SOG (1988) project. This method is based on the assessment of the P^D as a function of earthquake magnitude, time, and completeness region, defined as a spatial zone that shares the same completeness. Under the assumption that seismicity follows a stationary Poisson process in time, the rate of observed earthquakes v_i for magnitude interval m_{i-1} to m_i is illustrated by the equation:

6-8

$$\nu_i = \lambda_i P_i^D(t)$$

where λ_i is the true rate of earthquakes (which is unknown) in the specified magnitude interval, and $P_i^D(t)$ is the P^D of earthquakes in that magnitude bin as a function of time.

If the entire length of the catalogue is subdivided into *J* time periods such that within each *j* period the P^D can be assumed to be relatively constant, the probability of observing the recorded number of earthquakes (n_{ij}) is given by the Poisson distribution:

6-9

$$P(N = n_{ij}) = \frac{(\nu_i t_j)^{n_{ij}} e^{-\nu_i t_j}}{n_{ij}!}$$

Combining Equations 6-8 and 6-9, the likelihood of observing the recorded earthquakes in the magnitude interval m_{i-1} to m_i is given by:

6-10

$$L(\lambda_i, P_{ij}) = \prod_{j=1}^{J} \frac{(\lambda_i t_j P_{ij}^D)^{n_{ij}} e^{-\lambda_i t_j P_{ij}^D}}{n_{ij}!}$$

where P_{ij}^D is the P^D of earthquakes in the i-th magnitude interval in the time-period j.

If it is imposed that larger magnitudes are complete at present and that P^D decreases monotonically from the present time, Equation 6-9 can be maximised to obtain the parameters most likely to represent the Poisson process that produces the observed earthquake catalogue. From this, an equivalent time of completeness (TE_{ij}) is obtained by:

6-11

$$TE_{ij} = \sum_{j=1}^{J} P_{ij}^D \quad t_j$$

When the Stepp plot method (Stepp, 1972) is used to identify completeness time intervals, the rate of observed earthquakes ν_i for magnitude interval m_{i-1} to m_i is given by the observed number of earthquakes (n_{ij}) in the complete time-period j, divided by the duration of the completeness time period (T_{ij}):

6-12

$$\nu_i = \frac{n_{ij}}{T_{ij}}$$

When the P^D method is adopted, the equivalent time of completeness TE_{ij} replaces T_{ij} in Equation 6-12, and is used to obtain earthquake recurrence rates.

6.8.1.3 Completeness zones

The use of completeness zones indicates that assessments of the availability and quality of data can be completed as a historical study (e.g. Stucchi et al., 2009). This method focusses on identifying spatial and temporal differences in data reporting or data collection, and allows incorporation of instrumental and historical information that may affect the collection and reporting of earthquakes for different areas at different times. The result is typically a division of the project catalogue area into completeness zones to delimit areas with similar reporting histories. The completeness zones are then paired with magnitude cutoffs or P^D methods to define the appropriate temporal bounds of completeness for each completeness zone. The SSM TI Team considered the history of seismic station reporting (Section 6.8.2.2) and stationarity (Section 8.2.3) to determine whether completeness zones are appropriate for the application of completeness.

6.8.2 Completeness assessments

To set up and divide the catalogue appropriately for completeness method application, the declustered catalogue was used in assessments of magnitude binning and seismic station distribution. The distribution of magnitude values was reviewed to select appropriate magnitude binning such that intensity peaks are properly divided. The location and timing of earthquake occurrence was compared to operational periods and locations of seismic stations across the region to help determine whether completeness zones are appropriate for the application of completeness. Following these two items the two identified methods of completeness, Stepp plot and probability of detection, were applied to the declustered catalogue.

6.8.2.1 Magnitude binning

The project earthquake catalogue contains a mixture of instrumentally recorded magnitudes, and magnitudes obtained from macroseismic intensities. Because intensities are discrete variables, when converted to magnitudes, they concentrate counts at specific values. This is illustrated on the left-hand side histogram in Figure 6-20, which shows the number of events per 0.1-magnitude intervals starting at E[**M**] 3.3. Figures in this section show a lowest magnitude of E[**M**] 3.3 consistent with the smallest magnitude used in recurrence calculations, described in Section 8.2.10. In selecting the appropriate magnitude bin size to use in recurrence calculations, it is important that the converted-intensity peaks are not grouped into the same bin, or they will anomalously increase the earthquake counts. Figure 6-20 illustrates grouping of magnitude counts using bins of 0.4 magnitude units, while also separating major peaks in the magnitude counts which we interpret to be due to intensity-converted magnitudes.

Upon review of the catalogue event counts by magnitude, the SSM TI Team selected a magnitude bin size (d**M**) of 0.4 with the first bin anchored at a lower bound of E[**M**] 3.3, so that the first magnitude bin includes earthquakes with E[**M**] 3.5±0.2, the second includes earthquakes with E[**M**] 3.9±0.2, etc. As shown by the dashed vertical bars on the left-hand side histogram on Figure 6-20, choosing this d**M** ensures that converted intensities are not combined in the same bin. The right-hand side histogram shows the resulting counts for use in recurrence analyses. Assessments of completeness are done using the same magnitude bins (from the lower inclusive bound of E[**M**] 3.3, with d**M**=0.4).

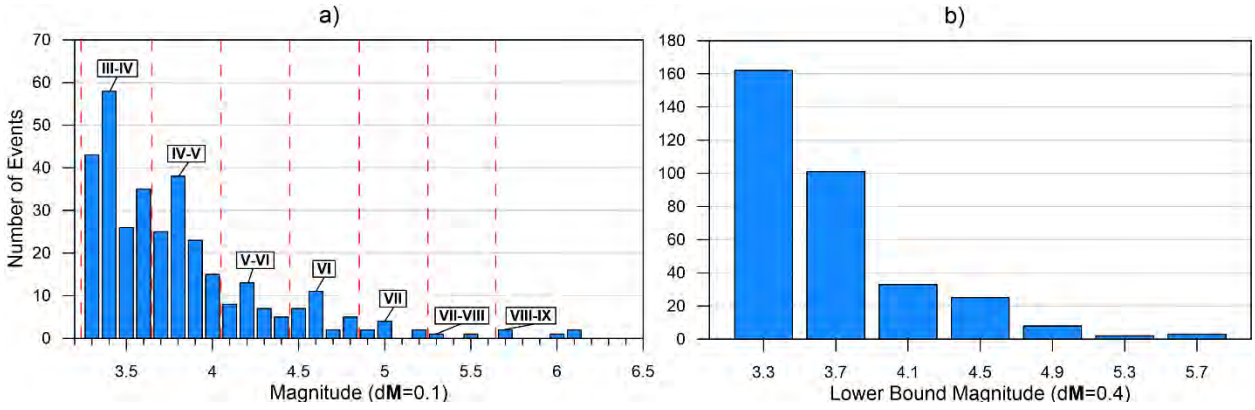

Figure 6-20. Event count by magnitude. (a) Events binned by 0.1 magnitude units, with intensity values in Roman numerals. Red dashed lines illustrate breaks between bins from M 3.3 to M 5.7. (b) Events binned by 0.4 magnitude units, with label indicating lower bound of bin.

6.8.2.2 Temporal and spatial seismic station distribution

To determine whether completeness zones are applicable, the SSM TI Team examined the evolution of the South African seismograph network. The first seismograph in South Africa was installed in Cape Town in 1899 at the Royal Observatory. Between 1920 and 1970, monitoring was limited to two stations, recording sporadically, and operated by disparate institutions. Following the 1969 Ceres earthquake, seven seismic stations were installed and the South African National Seismograph Network (SANSN) was formed. By 1997, the network had been expanded to include 27 operational stations. The network currently operates 57 stations, however, the stations are widely spaced in the southern and central portions of the country and densely concentrated in the mining regions of northeastern South Africa. The SSM TI Team analysed the evolution of the seismic station spatial coverage against the smaller events in the project catalogue through time. The analysis showed a general lack of coverage over time rather than areas with strong and consistent station coverage. The SSM TI Team concluded that no strong correlations could be found, and that spatial completeness zones were therefore not justified.

6.8.2.3 Stepp method

The declustered earthquake catalogue was assessed for completeness periods following the method described by Stepp (1972). Plots of annual event rate for events within each magnitude bin were plotted against the catalogue time period (Figure 6-21). The *TE* for each magnitude bin was selected at the point where there is a marked change in slope. Generally, this is where the rate decreases sharply going back in time, with the inflection point representing the maximum time of complete reporting for that magnitude bin. The sparsity of events in the project catalogue does not yield a strong consistent rate (e.g. horizontal trend) during the complete period (Figure 6-21). Plots of cumulative event counts within each bin, such as in Figure 6-21b, provide a secondary way to assess potential trends and were reviewed to aide selection of completeness intervals. For magnitude bins with very few events or plotted rates and counts lacking marked changes in slope, the completeness interval was adopted directly from the immediately adjacent smaller magnitude bin. In this way, the completeness intervals progress toward longer periods as magnitude increases because it is expected that the completeness interval does not become shorter as magnitude increases. The completeness interval periods are applied as a progressive step function by magnitude bin for continuity with recurrence assessments where cumulative counts are calculated and plotted by magnitude bin.

After close examination of the rate plots as described immediately above, the SSM TI Team selected the completeness cutoff years as listed in Table 6-3. Events in the earthquake catalogue within the completeness period for their magnitude bin were assigned a weight of 1.0 for completeness.

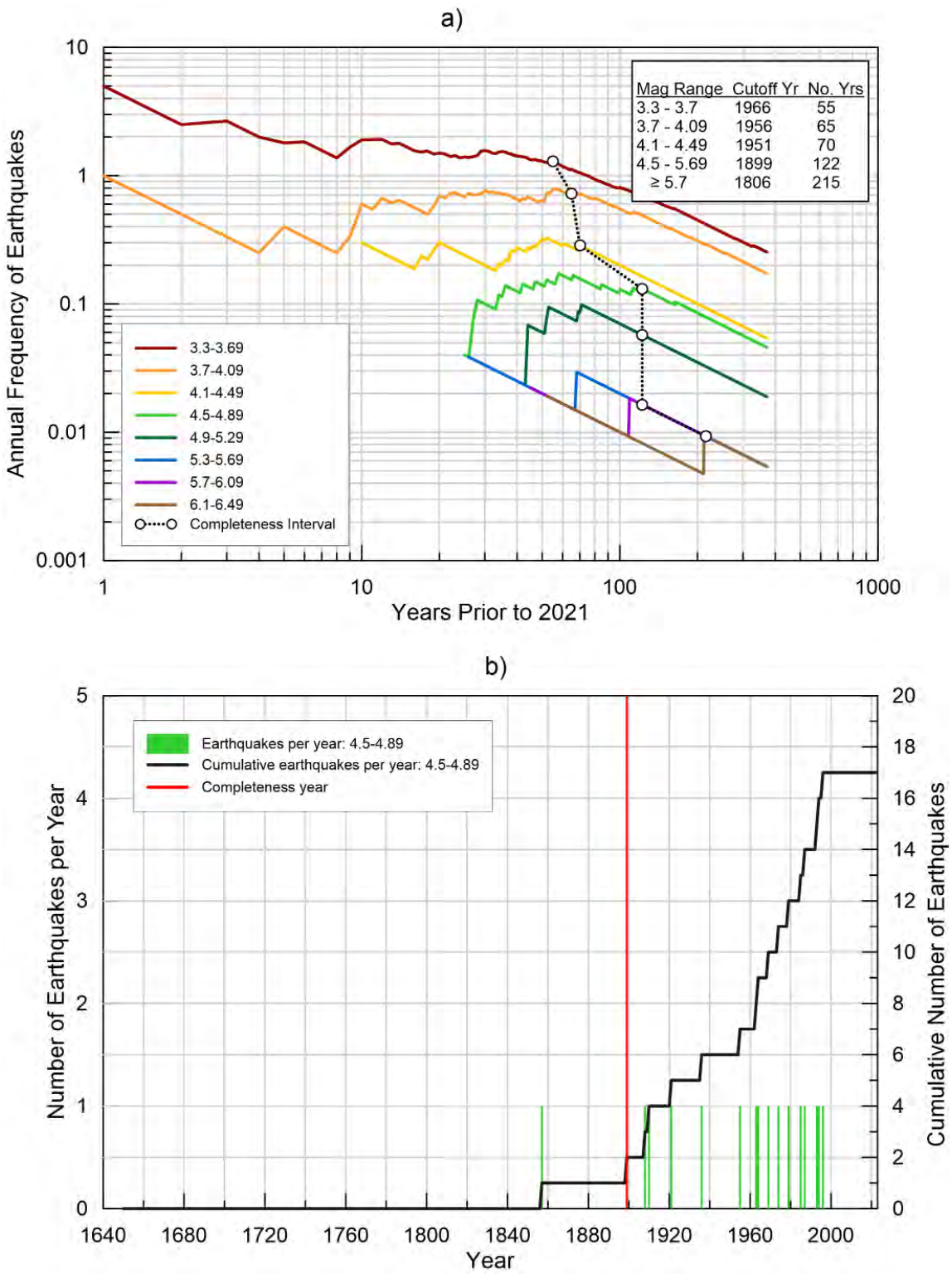

Figure 6-21. (a) Annual frequency plots after Stepp (1972), each line representing a magnitude bin with width dM = 0.4. Annual rate is calculated over the catalogue period. (b) Linear-linear plot of earthquake counts for E[M] 4.5 to 4.89, over the catalogue period. Earthquake occurrence is marked by the green vertical lines. The vertical red line marks the beginning of the completeness interval in 1899 where the cumulative count of events (black line) steadily captures events of this magnitude.

Table 6-3. Completeness cutoffs for the SSM earthquake catalogue, using the Stepp (1972) plot method.

Lower Bound Magnitude (E[M])	Cutoff Year	Complete Number of Years
3.3	1966	55
3.7	1956	65
4.1	1951	70
4.5	1899	122
4.9	1899	122
5.3	1899	122
5.7	1806	215
6.1	1806	215

6.8.2.4 Probability of detection method

In applying the P^D method, the time intervals (t_j in Equations 6-8 through 6-11) within which the P^D can be assumed to be relatively constant were determined to be (inclusive full years): 1690 to 1800, 1801 to 1900, 1901 to 1950, 1951 to 1968, 1969 to 2000, and 2001 to 31/12/2021.

Table 6-4 lists the resulting probabilities of detection for the catalogue region by magnitude bin and time interval, which can be interpreted as the probability of observing an earthquake of a given magnitude in a specified time period. The corresponding equivalent time of completeness, computed with Equation 6-11, for use in earthquake recurrence analyses is shown in the last column (labelled *TE*).

Table 6-4. Probability of detection values for SSM project catalogue.

Lower Bound Magnitude (E[M])	Probability of Detection Values						*TE*
	1690–1800	1801–1900	1901–1950	1951–1968	1969–2000	2001–2021	
3.3	0	0	0	0.26	0.54	0.54	33.30
3.7	0	0	0.06	0.47	0.84	0.84	55.98
4.1	0	0	0.07	0.86	1	1	71.98
4.5	0	0.06	0.07	0.87	1	1	78.16
4.9	0	0.11	0.17	0.87	1	1	88.16
5.3	0	0.2	0.21	0.87	1	1	99.16
5.7	0	0.22	0.22	0.87	1	1	101.66
6.1	0	0.87	0.87	0.87	1	1	199.16

6.8.3 Completeness results

Assessments of catalogue completeness indicated no strong basis for division of the project region into completeness zones based on the history of seismic station operation and available historical accounts. The completeness cutoff (CC) (e.g. Stepp, 1972) plot method and P^D method were considered as alternatives for the final earthquake catalogue, as these are two conceptually different approaches and both are considered valid for the project catalogue. Sensitivity assessment of the two methods indicated no significant difference in the calculated regional *b*-values. However, differences between the methods are apparent in the spatial smoothing evaluation (Section 8.2.4). The SSM TI Team chose to include both CC and P^D completeness methods with equal weight to represent equal validity of the two methods. The result was two final earthquake catalogues used in developing recurrence parameters. The complete project catalogue using CC completeness, with a total of 167 earthquakes E[**M**]≥3.3, is shown in Figure 6-22. The complete project catalogue using P^D completeness, including 184 earthquakes, is shown in Figure 6-23.

The complete, independent catalogues were used in calculations of recurrence parameters (Section 8.2.10). The full project catalogue is provided in Appendix C and includes all flags for non-tectonic events, dependent events, and the two completeness methods.

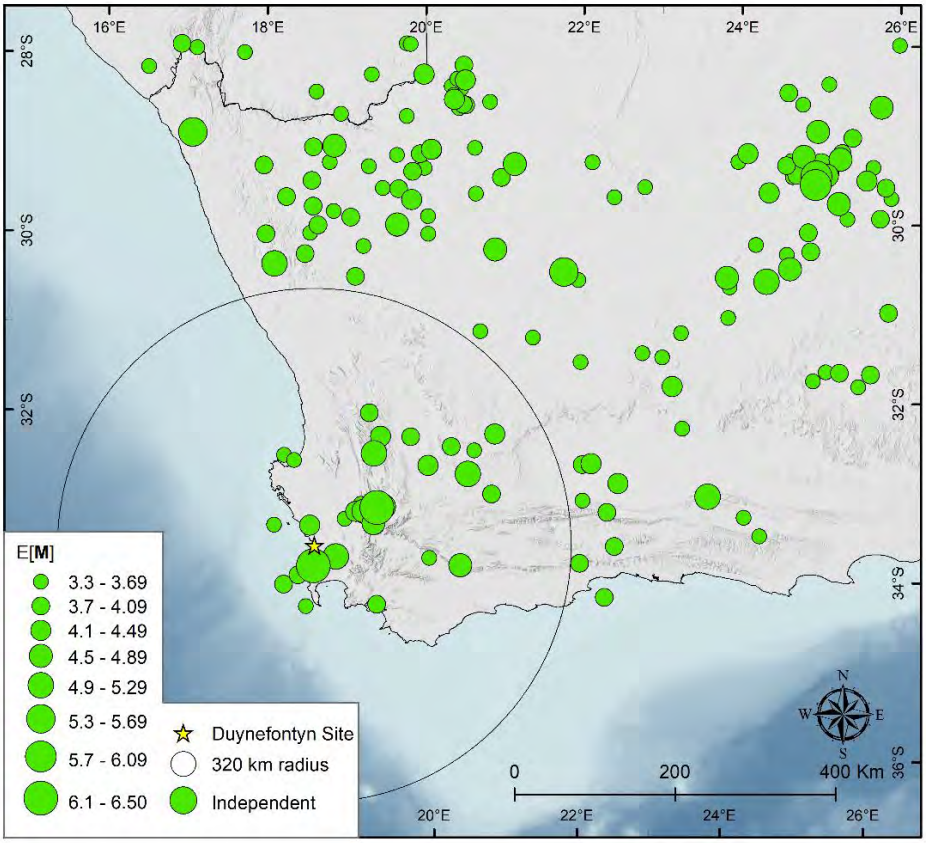

Figure 6-22. Independent, complete catalogue using the catalogue cutoff method after Stepp (1972).

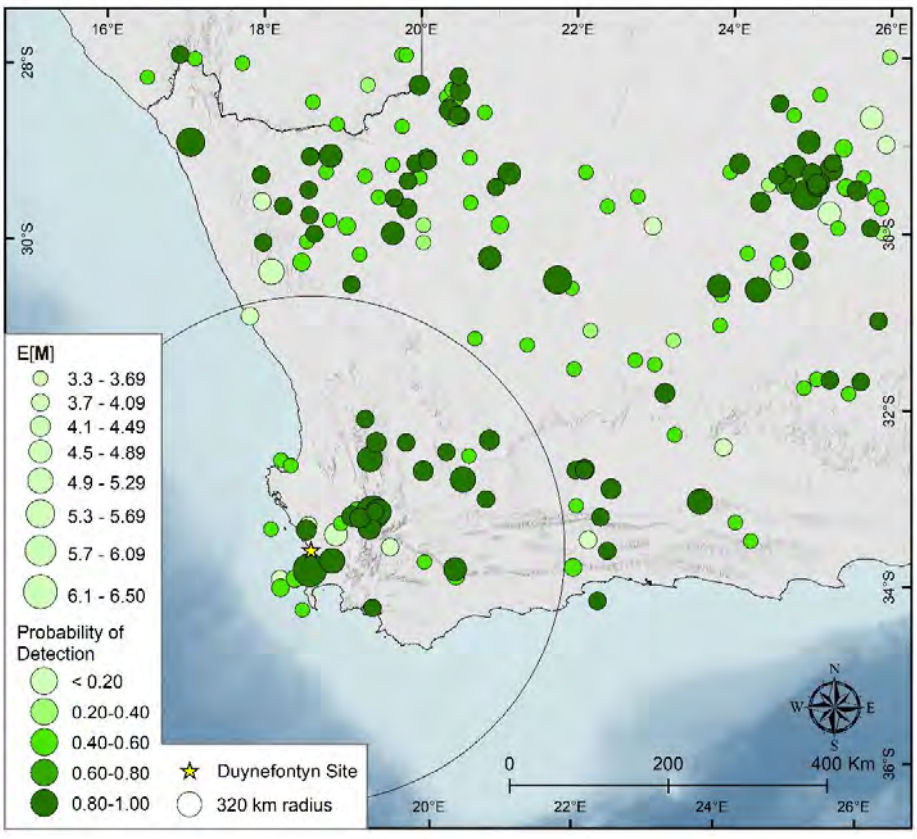

Figure 6-23. Independent, complete catalogue using the probability of detection (P^D) method. The shading indicates the probability of detection value.

6.9 INCORPORATING HISTORICAL EVENTS IN ESTIMATING SOURCE ZONE PARAMETERS

All the historical earthquakes characterised in Section 4.3 were added to the project catalogue and used by the SSM TI Team in the analyses described in Sections 6.4 through 6.8. In addition, the SSM TI Team evaluated and assessed three important historical earthquakes (4 December 1809, 11 September 1969, and 29 September 1969) to determine how to treat them in the source zone analyses. These additional assessments were needed due to significant uncertainties in the locations of the epicentres and their possible association with fault sources.

6.9.1 4 December 1809

Available records and reports for the 4 December 1809 Cape Town earthquake were studied and described in DDC4 and the epicentre location evaluated in Section 4.3.1. The traditional conclusion was that the epicentre was close to Cape Town (e.g. Brandt et al., 2005), based on observations of surface damage at Jan Biesjes Kraal, a farm near Milnerton, as mentioned by Von Buchenroder (1830, p.20-21). However, this epicentre location interpretation may be biased because the population at the time of the earthquake was concentrated in the Cape Colony in Cape Town, thereby focussing the post-earthquake observation near this location. This epicentre location near Cape Town was also cited in support of the proposed Milnerton Fault (e.g. Hartnady, 2003), as described in Section 8.4.2.7. Based on the MEEP2 analyses provided in Section 4.3.1, the SSM TI Team determined an alternative location for the epicentre at the northwestern point of Cape Town (Figure 6-24), but with acknowledged relatively large uncertainty. Because of the SSM TI Team's reassessed epicentre and location uncertainty for the event, the SSM TI Team cannot conclusively assign the 11 September 1809 earthquake to any specific fault source (see also Section 8.4.2.7).

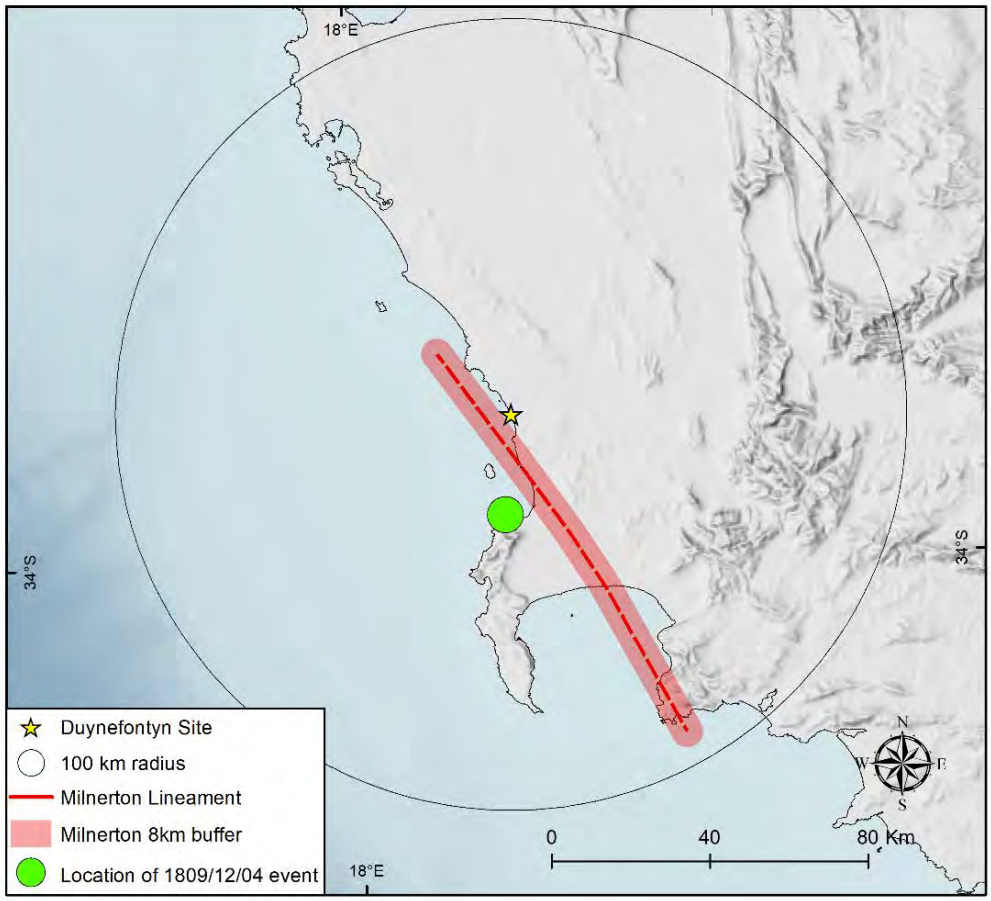

Figure 6-24. Location of the 4 December 1809 event.

6.9.2 11 September 1969

The 11 September 1969 event location uncertainty is discussed in Section 4.3.9. As stated, the SSM TI Team assessed two locations to determine the epicentre (Figure 6-25). The two alternative locations place the event in the host zone (Saldania) or in the neighbouring Agulhas zone to the east. The 11 September 1969 event has a magnitude of E[**M**] 4.93. Because of the sparsity of earthquakes with **M**>4.0 in the project catalogue, placing this epicentre within two different seismic source zones has a small impact on the results of spatial smoothing described in Section 8.2.4. However, based on a sensitivity study conducted by the Hazard Analysis Team, the differences in the spatial density from these alterative epicentre locations results in a less than 3% change in hazard results, the maximum difference occurring only at very long return periods, as shown in Figure 6-26. Close review of the results shown in Figure 6-26 and additional tests indicate that the difference in results is influenced by the virtual fault rupture sampling within the SDZ (Section 8.2.5) and can result in higher hazard even if the earthquake is placed in the AGZ (as in Figure 6-26). A test modelling point sources in both zones confirmed that placement of the earthquake in the SDZ resulted in higher hazard compared to placement within the AGZ, for that specific condition. Thus, the SSM TI Team placed the epicentre in the host zone for the subsequent analyses.

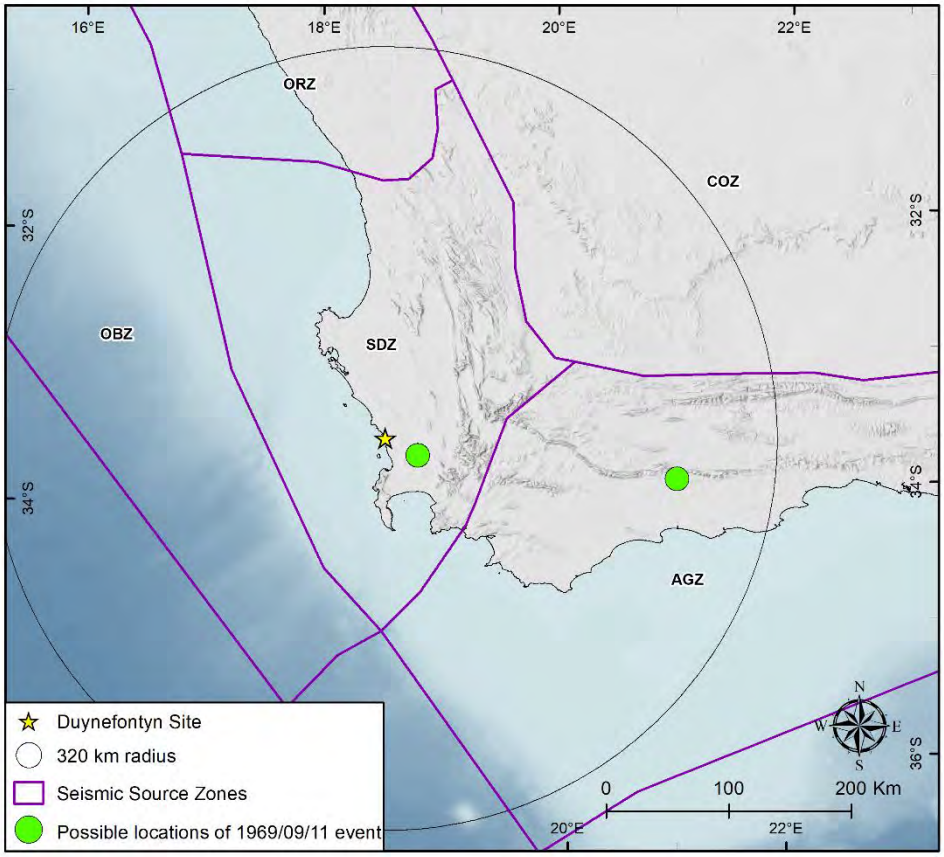

Figure 6-25. Alternative locations for the 11 September 1969 event. The SSM TI Team selected the location within the host zone for the SSM.

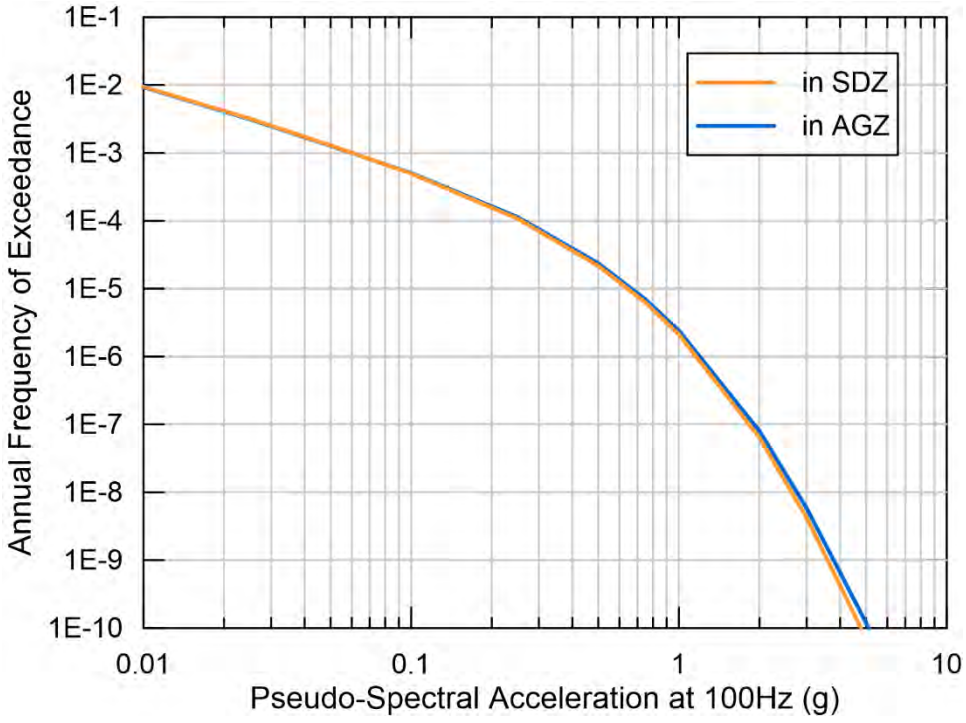

Figure 6-26. Normalised hazard sensitivity results at 100 Hz for the location of the 11 September 1969 event, where SDZ is the host zone, AGZ is the neighbouring zone to the east, and the *x*-axis is the normalised pseudo spectral acceleration (g).

6.9.3 29 September 1969

The Ceres earthquake occurred on 29 September 1969 to the northeast of the site (Figure 6-27), with E[**M**] 6.16. This earthquake has been the subject of numerous studies (e.g. Green and Bloch, 1971; Smit et al., 2015; Kruger and Scherbaum, 2014). Of importance to the SSM, the Ceres event is considered a characteristic earthquake on the Groenhof fault source (GFS). The GFS is discussed further in Section 8.4.2.6, including representation of the Ceres event in the recurrence model for the fault source.

Because the Ceres event is included in recurrence activity on the GFS, the SSM TI Team removed it from the cumulative occurrence of earthquake activity for the local seismic source zone (host zone SDZ) and from spatial smoothing counts. The technical basis for this decision was to avoid double counting the event in earthquake recurrence. The SSM TI Team decided to include the Ceres event in the regional project catalogue calculation of the *b*-value, which allows the event to be represented as a possible occurrence in the region. The technical basis for this latter decision was that the recurrence model is expected to remain true even with the inclusion of characteristic earthquakes on individual faults within the region.

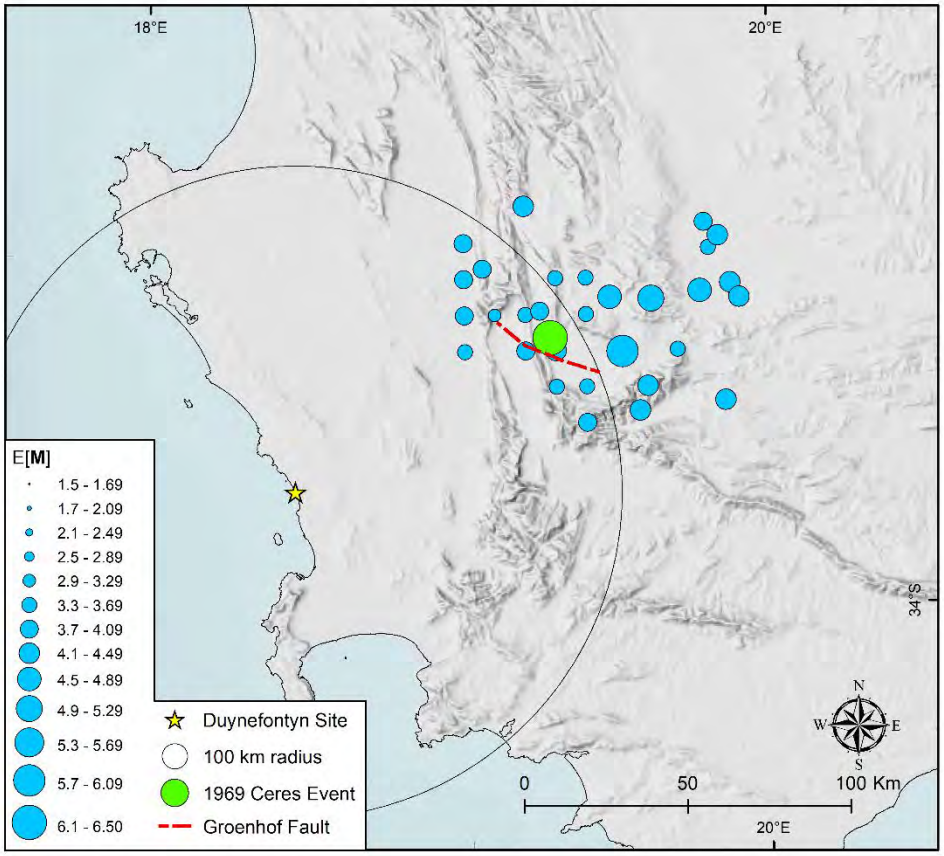

Figure 6-27. Location of the 29 September 1969 Ceres event and aftershocks, with Groenhof fault source. Showing only events from the project earthquake catalogue.

6.9.4 Other Historic Data

The results of event location reanalysis for the earthquakes described in Section 4.3 have been included in the project earthquake catalogue as described above. Historic information available for events in the region in 1969 and earlier, as presented by Albini and Flint (2023),

has also been incorporated into the project earthquake catalogue. No palaeoseismic data are available for past earthquakes in the region to augment the magnitudes, dates, or locations of events within the historic or instrumental catalogue. The lack of palaeoseismic data for the project catalogue region is recognized in DDC4 (Albini and Flint, 2023), described in Section 5.2.2, and is also reflected in the results of the consideration of fault sources in the SSM provided in Section 8.5.

6.10 REFERENCES

Advanced National Seismic System (ANSS). (2022). Search ANSS Comprehensive Earthquake Catalog. https://earthquake.usgs.gov/earthquakes/search/ (Accessed 21 September 2022).

Albini, P. and Flint, N. (2023). Investigating the Earthquake Records from 1620 to 1969 of Interest for the Duynefontyn Area, South Africa. CGS Report 2022-0127 (Rev. 0). Council for Geoscience, Pretoria, South Africa.

Arabasz, W.J.; Pechmann, J.C. and Burlacu, R. (2016). A Uniform Moment Magnitude Earthquake Catalog and Background Seismicity Rates for the Wasatch Front and Surrounding Utah Region. Appendix E of Earthquake Probabilities for the Wasatch Front Region in Utah, Idaho, and Wyoming. Utah Geological Survey Miscellaneous Publication 16(3).

Brandt, D.; Andreoli, M.A.G. and McCarthy, T.S. (2005). The Late Mesozoic Palaeosoils and Cenozoic Fluvial Deposits at Vaalputs, Namaqualand, South Africa: Possible Depositional Mechanisms and Their Bearing on the Evolution of the Continental Margin. South African Journal of Geology 108(2). 271-284.

Chu, A.; Schoenberg, F.P.; Bird, P.; Jackson, D.D. and Kagan, Y.Y. (2011). Comparison of ETAS Parameter Estimates Across Different Global Tectonic Zones. Bulletin of the Seismological Society of America 101(5). 2323-2339.

Electric Power Research Institute/ Department of Energy/United States Nuclear Regulatory Commission (EPRI/DOE/USNRC) (2012). Central and Eastern United States Seismic Source Characterization for Nuclear Facilities. NUREG-2115. US Nuclear Regulatory Commission, Washington DC, USA.

Electric Power Research Institute – Seismicity Owners Group (EPRI-SOG) (1988). Seismic Hazard Methodology for the Central and Eastern United States. EPRI Technical Report NP-4726-A. 11 Volume Proprietary Report.

Gardner, J.K. and Knopoff, L. (1974). Is the Sequence of Earthquakes in Southern California, With Aftershocks Removed, Poissonian? Bulletin of the Seismological Society of America 64(5). 1363-1367.

Green, R.W.E. and Bloch, S. (1971). The Ceres, South Africa, Earthquake of September 29, 1969: I. Report on Some Aftershocks. Bulletin of the Seismological Society of America 61(4). 851-859.

Grünthal, G. (1985). The Updated Earthquake Catalogue for the German Democratic Republic and Adjacent Areas – Statistical Data Characteristics and Conclusions for Hazard Assessment. Proceedings of the 3rd International Symposium of the Analysis of Seismic Risk, Liblice Castle, Czechoslovakia.

Gulia, L. (2010). Detection of Quarry and Mine Blast Contamination in European Regional Catalogues. Natural Hazards 53(2). 229-249.

Gulia, L. and Gasperini, P. (2021). Contamination of Frequency-Magnitude Slope (b-Value) by Quarry Blasts: An Example for Italy. Seismological Research Letters 92(6). 3538-3551.

Hartnady, C.J.H. (2003). Cape Town Earthquakes: Review of the Historical Record. Draft Vers030522. Umvoto Africa, Muizenberg, South Africa. 16.

Hawkes, A.G. and Adamopoulos, L. (1973). Cluster Models for Earthquakes-Regional Comparisons. Bulletin of the International Statistical Institute 45(3). 454-461.

Instituto Geográfico Nacional (IGN) (2013). Actualización de Mapas de Peligrosidad Sísmica de España 2012 [English: Update of Seismic Hazard Maps of Spain 2012]. Instituto Geográfico Nacional [English: National Geographical Institute], Madrid, Spain.

International Seismological Centre (ISC) (2022a). Online Bulletin Event Catalogue Search. http://www.isc.ac.uk/iscbulletin/search/catalogue/ (Accessed 26 September 2022).

International Seismological Centre (ISC) (2022b), ISC-GEM Global Instrumental Earthquake Catalogue, Version 9.0.

Johnston, A.C.; Coppersmith, K.J.; Kanter, L.R. and Cornell, C.A. (1994). The Earthquakes of Stable Continental Regions: Final Report Submitted to Electric Power Research Institute (EPRI): TR-102261, 5-Volume Proprietary Report Prepared for Electric Power Research Institute, Palo Alto, California, USA.

Kattamanchi, S.; Tiwari, R.K. and Ramesh, D.S. (2017). Non-Stationary ETAS to Model Earthquake Occurrences Affected by Episodic Aseismic Transients. Earth, Planets and Space 69(1). 1-14.

Kruger, F. and Scherbaum, F. (2014). The 29 September 1969, Ceres, South Africa, Earthquake: Full Waveform Moment Tensor Inversion for Point Source and Kinematic Source Parameters. Bulletin of the Seismological Society of America 104(1). 576-581.

Luen, B. and Stark, P.B. (2012). Poisson Tests of Declustered Catalogs. Geophysical Journal International 189(1). 691-700.

Manzunzu, B.; Brandt, M.B.C.; Midzi, V.; Durrheim, R.J.; Saunders, I. and Mulabisana, T.F. (2021). Towards a Homogeneous Moment Magnitude Determination for Earthquakes in South Africa: Reduction of Associated Uncertainties. Journal of African Earth Sciences 173. 104051.

Marzocchi, W. and Sandri, L. (2009). A Review and New Insights on the Estimation of the b-Value and Its Uncertainty. Annals of Geophysics 46(6). 1271-1282.

Marzocchi, W.; Spassiani, I.; Stallone, A. and Taroni, M. (2019). How to Be Fooled Searching for Significant Variations of the b-Value. Geophysical Journal International 220(3). 1845-1856.

Ogata, Y. (1988). Statistical Models for Earthquake Occurrences and Residual Analysis for Point Processes. Journal of the American Statistical Association 83(401). 9-27.

Ogata, Y. (1998). Space-Time Point-Process Models for Earthquake Occurrences. Annals of the Institute of Statistical Mathematics 50(2). 379-402.

Ogata, Y. and Zhuang, J. (2006). Space-Time ETAS Models and an Improved Extension. Tectonophysics 413(1-2). 13-23.

Peláez, J.A.; Chourak, M.; Tadili, B.A.; Aït Brahim, L.; Hamdache, M.; López Casado, C. and Martínez Solares, J.M. (2007). A Catalog of Main Moroccan Earthquakes from 1045 to 2005. Seismological Research Letters 78(6). 614-621.

Rhoades, D.A. and Dowrick, D.J. (2000). Effects of Magnitude Uncertainties on Seismic Hazard Estimates. 12WCEE Paper 1179.

Saunders, I. (2024). Review and Homogenization of an Earthquake Catalogue for the Ceres Area. CGS Report 2023-0162 (Draft). Council for Geoscience, Pretoria, South Africa.

Smit, L.; Fagereng, A.; Braeuer, B. and Stankiewicz, J. (2015). Microseismic Activity and Basement Controls on an Active Intraplate Strike-Slip Fault, Ceres–Tulbagh, South Africa. Bulletin of the Seismological Society of America 105(3). 1540-1547.

Stepp, J. (1972). Analysis of Completeness of the Earthquake Sample in the Puget Sound Area and Its Effect on Statistical Estimates of Earthquake Hazard. In Proceedings of the 1st International Conference on Microzonation, Seattle, USA. 897-910.

Strasser, F.O. and Mangongolo, A. (2013). TNSP Earthquake Catalogue. CGS Report 2012-0166 (Rev. 0). Council for Geoscience, Pretoria, South Africa.

Stucchi, M.; Meletti, C.; Rovida, A.; D'Amico, V. and Gómez Capera, A.A. (2009). Historical Earthquakes and Seismic Hazard of the L'Aquila Area. Progettazione Sismica 1 [English: Seismic Design 1]. 23-34.

Taroni, M. (2022). The Effect of Magnitude Uncertainty on the Gutenberg-Richter Estimation and the Magnitude-Frequency Distribution: "What Hump?". Geophysical Journal International 231(2). 907-911.

Tinti, S. and Mulargia, F. (1985). Effects of Magnitude Uncertainties on Estimating the Parameters in the Gutenberg-Richter Frequency-Magnitude Law. Bulletin of the Seismological Society of America 75(6). 1681-1697.

United States Nuclear Regulatory Commission (USNRC) (2007). A Performance-Based Approach to Define the Site-Specific Earthquake Ground Motion. Regulatory Guide 1.208. US Nuclear Regulatory Commission, Washington DC, USA.

Uhrhammer, R. (1986). Characteristics of Northern and Central California Seismicity. Earthquake Notes 57(1).

Van der Elst, N.J. (2021). B-Positive: A Robust Estimator of Aftershock Magnitude Distribution in Transiently Incomplete Catalogs. Journal of Geophysical Research, Solid Earth 126(2).

Veneziano, D. and Van Dyck, J. (1985). Statistical Discrimination of Aftershocks and Their Contribution to Seismic Hazard. In Seismic Hazard Methodology for Nuclear Facilities in the Eastern US 2(A-4). EPRI/SOG Draft 85-1.

Von Buchenröder, W.L. (1830). The Cape Town Earthquake of 1809. South African Quarterly Journal 1 (Oct 1829 - Sept 1830), Cape Town. 18-25.

Wiemer, S. and Baer, M. (2000). Mapping and Removing Quarry Blast Events from Seismicity Catalogs. Bulletin of the Seismological Society of America 90(2). 525-530.

CHAPTER 7: GROUND MOTION DATABASE

7. GROUND MOTION DATABASE

7.1 OVERVIEW OF GROUND MOTION DATABASE

The procedure used to develop a site-specific ground-motion model for this project involved adapting published ground-motion prediction equations (GMPEs) to estimate ground-motions at the Duynefontyn site that are consistent with the seismogenic nature of the Western Cape and the dynamic properties of the near-surface profile at the Duyenfontyn site. This adaptation includes the following adjustments.

1. Adjustments for the earthquake source characteristics such as median stress drop for earthquakes in the Western Cape.
2. Adjustments for the path from the earthquake to the site such as anelastic attenuation of the earthquake energy through the crust in the Western Cape.
3. Adjustments for the site to account for impedance contrasts and damping in the strata directly beneath the Duynefontyn site.

To estimate these adjustments and develop a GMM that is consistent with the Western Cape and Duyenfontyn site, the GMM TI Team used several types of local and regional seismological and geotechnical data. The GMM TI Team, in collaboration with the CGS staff and specialty contractors, compiled several databases for use in these adjustments. These databases include:

1. Ground-motion recordings from the site, surrounding region, and across South Africa (Section 7.4).
2. Site data in the form of dispersion curves and velocity profiles derived from multichannel analysis of surface waves (MASW), and velocity profiles from P-S logging and downhole bore logs (Section 4.5).
3. Dispersion curves and velocity profiles derived from MASW performed for South African National Seismograph Network (SANSN) stations (Section 7.3).

The evaluation of this data informed the decisions made by the GMM TI Team in constructing the logic-trees for median ground-motions and their aleatory variability, as well as the logic-trees for the site profile and site amplification model. The final GMM is described in Chapter 9 along with a discussion of this data's evaluation. Chapter 7 focuses on the data collection and processing.

7.2 DUYNEFONTYN STATION INSTALLATION

Ground-motion recordings are essential for estimating various components of a GMM. They provide regional and site-specific data that the GMM TI Team can use to estimate the relevant physical parameters in the Western Cape and at the Duynefontyn site and evaluate the interaction of seismic waves with these parameters. Ground-motion recordings provide information that can be used to assess the items in the following list.

1. Site decay parameter (κ_0), used to infer site damping
2. Stress drop and anelastic attenuation
3. Site amplification
4. Topographic effects
5. Basin effects

At the beginning of the SSHAC EL-2 PSHA project, the closest permanent ground-motion recording station was approximately 70 km from the Duynefontyn site. The GMM TI Team discussed the value of installing a seismometer at the Duynefontyn site with the CGS during the Baseline Study and at Workshop 1. The benefit to the current project of a seismometer at the Duynefontyn site would be to reduce epistemic uncertainty in the site characterisation and site amplification model, most significantly for the κ_0 parameter that affects high spectral frequencies near the site. The GMM TI Team recommended installing two vertical downhole arrays at the Duynefontyn site as part of the planned site investigation. The locations of the two arrays, SA100 and DA100, are shown in Figure 7-1.

Figure 7-1. Locations of SA100 and SD100 with respect to Duynefontyn

The GMM TI Team recommended installing the arrays at various depths to better constrain the near-surface site response. The first depth is at the “surface” to measure the site amplification and κ_0 at the top of the sand. The second depth is at 30 m to measure site amplification and κ_0 at a level that would be below the sand. The thickness of this layer varies over the site and represents an equivalent to “top-of-rock”. The deepest array is at 90 m, the anticipated maximum limit of the boreholes, to provide deep, within-rock ground-motions for comparison to ground-motions at shallower depths when estimating site amplification and κ_0. The CGS placed instruments at the recommended depths whether or not the boreholes extended deeper, so that the depths were consistent between the two locations.

It is worth noting that these vertical arrays will also have significant benefits for future projects. The short timeframe for data collection during the SSHAC EL-2 PSHA meant that only small-magnitude earthquakes were recorded. Given a longer time frame, larger-magnitude earthquakes will be recorded at the site, yielding information directly regarding site amplification at the Duynefontyn site and informing estimates of local stress drops and anelastic attenuation.

The CGS installed the two vertical microseismicity borehole arrays using five integrated Nanometrics seismometers and one Kinemetrics accelerometer. The new stations were incorporated into the SANSN, and the recorded data contributes to the main seismic database of the SANSN (Jele et al., 2024). Figure 7-2 shows the series configuration of the seismograph station utilised in each array installation. Seismic housings for each instrument are at the surface and mounted on composite slabs constructed of various states of cement, sand, mesh, and concrete, the dimensions of which are shown in Figure 7-2. Additional information about the installation can be found in Jele et al. (2024).

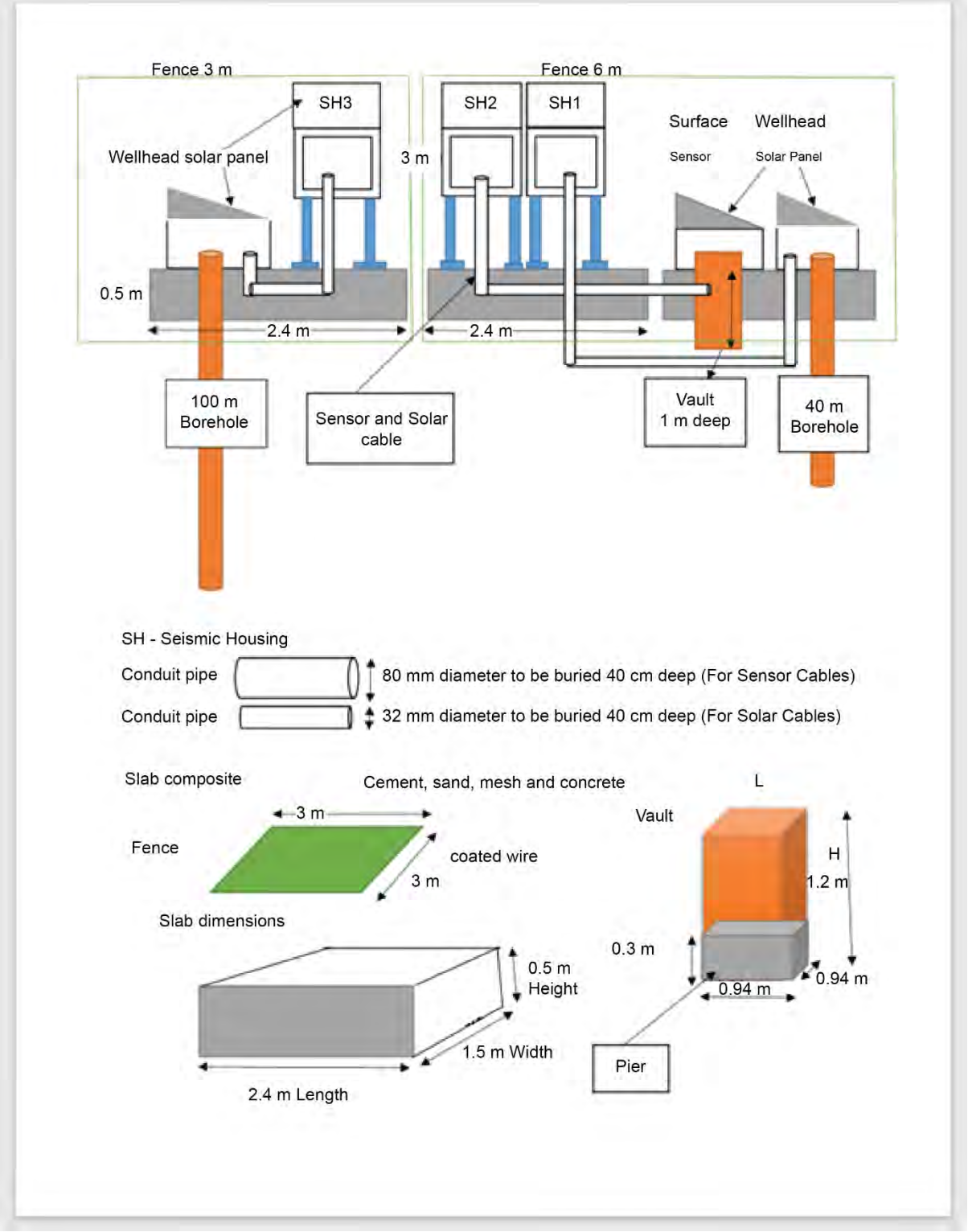

Figure 7-2. Schematic design of the Duynefontyn borehole seismicity array (from Jele et al., 2024).

Stations DUYN4, DUYN5, and DUYN6 are installed at SA100, and DUYN1, DUYN2, and DUYN3 are installed at DA100. Table 7-1 presents the basic station information for the Duynefontyn array stations. Detailed information for each station is given in Jele et al. (2024). Jele et al. (2024) additionally lists the seasonal temperatures for each station, the station orientation in the borehole, the ground surface type, the distance to potential noise sources,

and the details about how each station is powered. Specifications for the Nanometrics and Kinemetrics sensors are listed below.

Instrument specifications

- Nanometrics Centaur 6 channels s/n: 004102
  Nanometrics Trillium Cascadia TTC120-PH1 s/n: 001421, IP 2.24.5.141
  Accelerometer Module ASM 18336 rev X2

- Kinemetrics Obsidian 4 X s/n: 1120
  Hyposensor (FBA ES-DH) s/n: 557

Table 7-1. Duynefontyn station information.

ARRAY	SENSOR	DEPTH (m)	SENSOR TYPE	DURATION	LAT	LON	INSTALL DATE
DA100	DUYN 1	Vault at Surface	Cascadia Nanometrics	Permanent	-33.6647	18.4305	30/03/2023
	DUYN 2	30	Cascadia Nanometrics	Permanent	-33.6647	18.4305	04/01/2023
	DUYN 3	90	Cascadia Nanometrics	Permanent	-33.6648	18.4307	14/02/2023
SA100	DUYN 4	Vault at Surface	Cascadia Nanometrics	Permanent	-33.6572	18.4266	24/04/2023
	DUYN 5	30	Cascadia Nanometrics	Permanent	-33.6572	18.42659	31/03/2023
	DUYN 6	90	Kinemetric HYPOSENSOR	Permanent	-33.6572	18.4266	04/03/2023

Information about the data recorded by the Duynefontyn stations is presented in Section 7.4.5.

7.3 MASW FOR SOUTH AFRICAN NATIONAL SEISMOGRAPH NETWORK STATIONS

A significant component of the evaluation was the GMM TI Team's assessment of ground-motion data inversions performed by the GMM TI Team and a specialty contractor to estimate stress drop and anelastic attenuation for the Western Cape (see Chapter 9). At the start of the SSHAC EL-2 PSHA, there was no available shear-wave velocity (V_S) profile information for the SANSN stations where the ground-motion data for the inversions was recorded. Without V_S profiles, the inversions can only provide relative differences in site amplification between stations. To tie these differences to a physical property that can be modelled, information is needed about the V_S at the recording sites.

The GMM TI Team discussed this lack of site information with the CGS during the Baseline Study and the CGS offered to perform MASW analyses at stations close to the Duynefontyn site to provide the necessary data. MASW uses the measured dispersion of surface waves to model the V_S profile in 1D (depth) or 2D (depth and surface location) format. It works by creating a seismic energy source in the low-frequency range (e.g. 1–30 Hz) that is recorded by a multichannel (24 or more channels) recording system and a receiver array deployed over a couple metres to a couple hundred metres along a profile on the ground (e.g. 2–200 m). A forward model, which is a computation of a theoretical response based on remotely measured physical properties, was used to develop the V_S profile. The site strata was first developed with appropriate geotechnical properties, including V_S, and these properties were then adjusted until the dispersion in the model matched the measured dispersion from the MASW data. MASW was performed by the CGS staff at the Ceres (CER), Elim (ELIM), and Matjiesfontein (MATJ) stations, as shown in Figure 7-3. Additional information about the MASW performed can be found in Manzunzu and Sebothoma (2022). Information about the site conditions and data collection at the selected MASW sites is presented in the sections that follow.

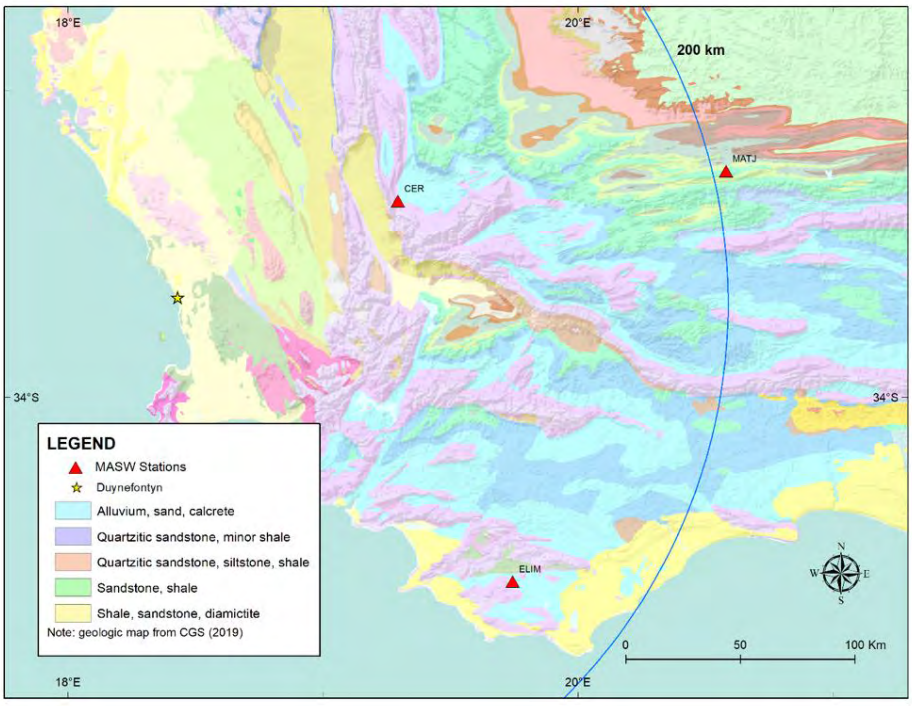

Figure 7-3. SANSN stations where MASW was performed.

7.3.1 Ceres

The CER station location is near an electric substation, and the MASW traverse was located on wet ground. These conditions resulted in noisy data acquired at this station. According to the CGS, it is likely that the ground was highly charged, and since water is a good conductor, it allowed a flow of current from one geophone to the other. The data was acquired at geophone spacings of 2 m and 1 m and at source-receiver offset distances of 40 m, 20 m and 4 m, as described above. The centre of the spread, which is also the location of the velocity profile, was located approximately 10 m from the station. The field setup is shown in Figure 7-4. Additional information can be found in Manzunzu and Sebothoma (2022).

The CGS analysed the collected data and provided the GMM TI Team with a V_S profile, shown in Figure 7-5. Dispersion curve data was not provided to the GMM TI Team. The GMM TI Team's opinion is that the uncertainty in the profile is likely larger than what is indicated in the figure. The GMM TI Team used the V_S profiles to estimate V_{S30} at the site but did not use the V_S profiles directly. Additional information can be found in Manzunzu and Sebothoma (2022).

Figure 7-4. Field setup at Ceres (modified from Manzunzu and Sebothoma, 2022 to add "dx").

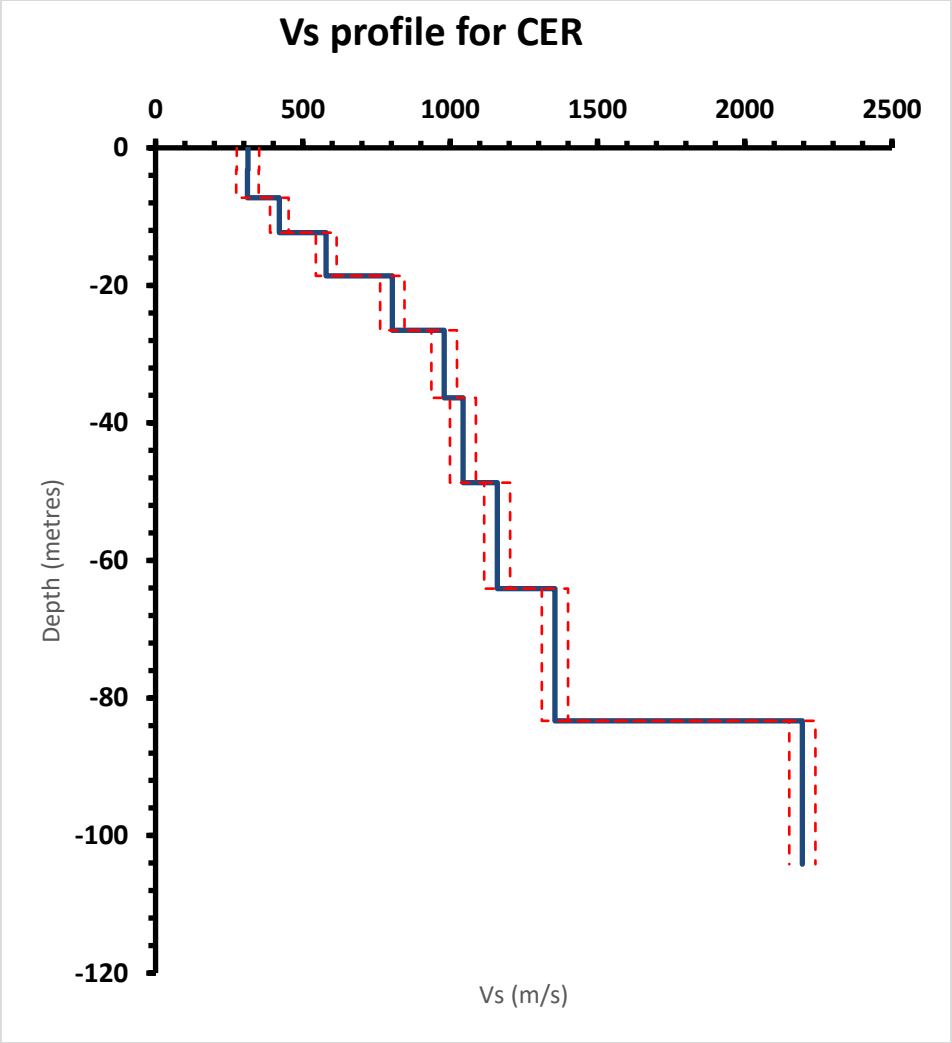

Figure 7-5. Final V_S profile (solid blue line) for the CER seismic station and estimates of the standard deviation (dashed red lines) (from Manzunzu and Sebathoma, 2022).

7.3.2 Elim

The Elim (ELIM) station is on top of a small hill with a few rock outcrops visible nearby. The CGS conducted the survey along a gravel road just after it rained, but the CGS determined that the rain did not have a similar negative effect on the data as with the CER station. The data was acquired at geophone spacings of 2 m and 1 m, and at source-receiver offset distances of 40 m, 20 m and 4 m. The centre of the spread was also located approximately 10 m from the station. The field setup is shown in Figure 7-6. Additional information can be found in Manzunzu and Sebothoma (2022).

The CGS analysed the collected data and provided the GMM TI Team with a V_S profile, shown in Figure 7-7. Dispersion curve data was not provided to the GMM TI Team. The GMM TI Team used the V_S profiles to estimate V_{S30} at the site but did not use the V_S profiles directly. Additional information can be found in Manzunzu and Sebothoma (2022).

Figure 7-6. Field setup at Elim (from Manzunzu and Sebothoma, 2022).

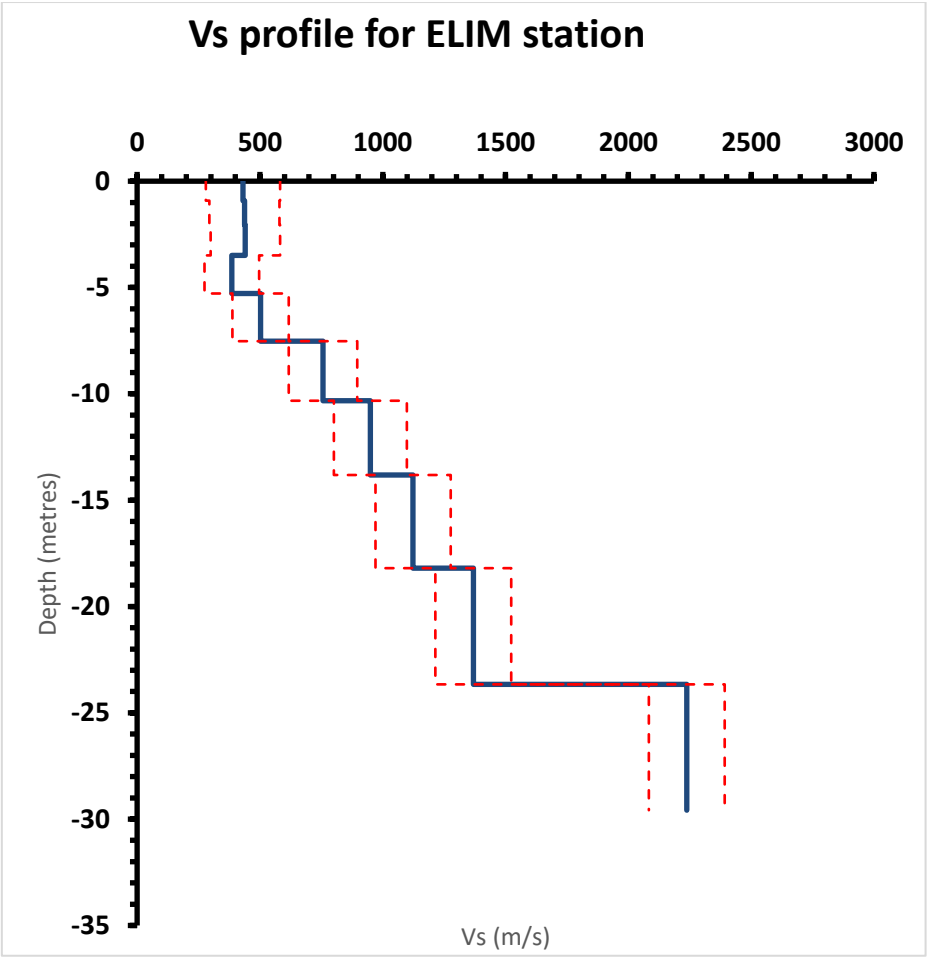

Figure 7-7. Final V_S profile (solid blue line) for the ELIM seismic station and estimates of the standard deviation (dashed red lines) (from Manzunzu and Sebathoma, 2022).

7.3.3 Matjiesfontein

The MATJ station is surrounded by rock debris, requiring careful selection of the survey traverse to achieve good coupling of the geophones with the ground and to maintain the desired location of the velocity profile. The data was acquired at geophone spacings of 2 m and 1 m, and at source-receiver offset distances of 40 m, 20 m, and 4 m. The centre of the spread was located adjacent to the station location. The field setup is shown in Figure 7-8. Additional information can be found in Manzunzu and Sebothoma (2022).

The CGS analysed the collected data and provided the GMM TI Team with a V_S profile, shown in Figure 7-9. Dispersion curve data was not provided to the GMM TI Team. The GMM TI Team used the V_S profiles to estimate V_{S30} at the site but did not use the V_S profiles directly. Additional information can be found in Manzunzu and Sebothoma (2022).

Figure 7-8. Field setup at Matjiesfontein (from Manzunzu and Sebothoma, 2022).

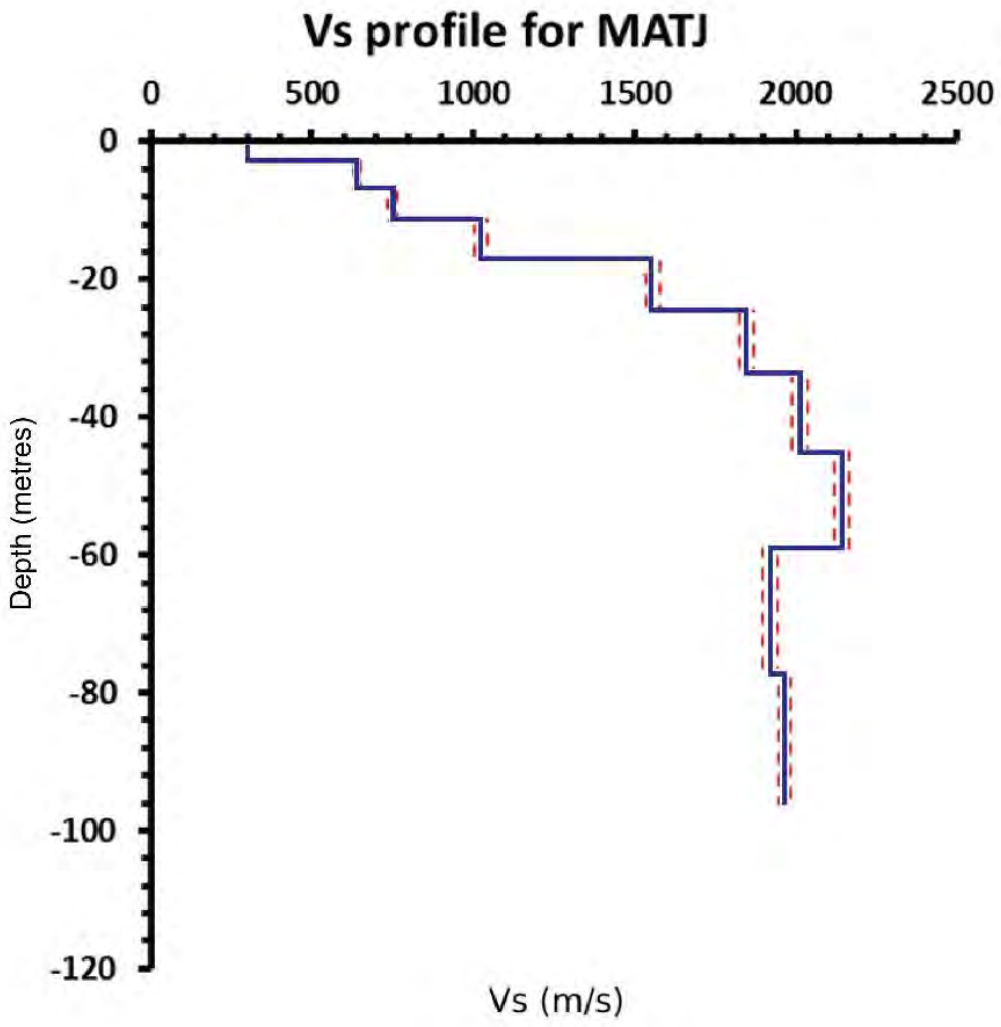

Figure 7-9. Final V_S profile (solid blue line) for the MATJ seismic station and estimates of the standard deviation (dashed red lines) (from Manzunzu and Sebathoma, 2022).

7.4 GROUND-MOTION DATABASES

As discussed in Section 0, ground-motion recordings are essential for estimating various components of a GMM. The GMM TI Team developed three ground-motion databases (GMDBs) from available earthquake data, each targeted at improving a specific aspect of the GMM. These were the Inversion GMDB, the κ_0 GMDB, and the Duynefontyn GMDB. The CGS also made two additional databases available to the GMM TI Team during the project, the Colenso GMDB (See Section 0) and the Temporary Array GMDB (see Section 7.4.6). An overview of the properties and uses for the ground-motion databases is provided in Table 7-2.

Table 7-2. Properties and uses for the GMDBs

Ground-motion database	Uses	Properties
Inversion	GMPE Inversion	Earthquakes from South Africa-wide catalogue compiled by the SSM TI Team and waveforms from the SANSN provided by the CGS. This catalogue is declustered and includes no dependent events.
κ_0	Determination of κ_0	Earthquakes with reported magnitudes ≥ 1, within 700 km of KNPS from the following databases: * Advanced National Seismic System (ANSS), * the CGS South Africa Seismic Hazard Analysis (SASHA) events, and * the CGS Ceres aftershock records. This catalogue is not declustered to preserve the small magnitude earthquakes in the dataset.
Duynefontyn	Determination of κ_0	A set of 12 earthquakes collected on arrays installed by the CGS between February and April of 2023 that started collecting significant data in April 2023.
Colenso	Determination of κ_0	An array along the Colenso fault that recorded 15 earthquakes during its deployment.
Temporary Array	Determination of κ_0	One earthquake recorded on a temporary array was by University of Cape Town researchers near the Dueynfontyn site from 24 July 2021 to 27 October 2021

The GMM TI Team developed the Inversion GMDB for use by the GMM TI Team and a specialty contractor to invert for seismic properties in the region such as stress drop and anelastic attenuation. In general terms, within the inversion, the point-source stochastic model is used to predict ground-motion given a set of seismic parameters (see Chapter 9). The predicted ground-motion is compared to the observed ground-motion and a misfit is calculated. The seismic parameters are then adjusted through a set of iterations to reduce the

misfit. The result is a set of seismic parameters that yield the best fit between the predicted ground-motion from the point-source stochastic model and the observed ground-motion that the GMM TI Team used to adjust existing GMPEs to account for South African stress drop and anelastic attenuation. Additional information about this process is found in Section 9.2. The Inversion GMDB is based on the South Africa-wide catalogue and focuses on larger-magnitude earthquakes (see Section 0).

The GMDBs were particularly important for evaluating κ_0 at the Duynefontyn site, because this parameter has a significant impact on the high-frequency ground-motion and there was no site-specific data at the beginning of the SSHAC EL-2 PSHA to constrain it. The GMM TI Team worked with the CGS to have a seismic station installed at the Duynefontyn site, but it was not known if this station would be installed early enough to provide data for the SSHAC EL-2 PSHA project. The GMM TI Team developed additional GMDBs to serve as backup to protect against the station either not getting installed in time for use on this project or failing to record enough earthquakes

The κ_0 GMDB uses the GMM earthquake catalogue as its basis because it contains close-in, small-magnitude earthquakes that are often eliminated in the declustering process and are important for the evaluation of κ_0. Based on the evaluation performed by the GMM TI Team (see Section 9.4.3), this data was given a weight of zero in the κ_0 estimates (see Section 7.4.3).

The Colenso GMDB consists of data from the Colenso Array installed by the CGS to monitor microseismicity in the region (see Section 5.2.4.3). The GMM TI Team requested the waveform data for potential use in the evaluation of κ_0. Through the GMM TI Team's evaluation (see Section 9.4.3), this data was given a weight of zero in the κ_0 estimates (see Section 7.4.4).

Concurrent with the development of the κ_0 GMDB, the GMM TI Team worked with the CGS to have two vertical arrays installed at the Duynefontyn site (see Section 7.2). The Duynefontyn GMDB is composed of a single earthquake recorded at the Duynefontyn stations and was used to obtain site-specific estimates of κ_0. Through the GMM TI Team's evaluation (see Section 9.4.3), this data was given a significant weight in the κ_0 estimates (see Section 7.4.5).

Finally, a temporary array was deployed by Drs Quiros and Sloane of Cape Town University before the SSHAC EL-2 PSHA project started. The GMM TI Team became aware of this array during Workshop 2 and the CGS subsequently engaged them as specialty contractors to estimate κ using their data. Drs Quiros and Sloane developed the Temporary Array GMDB as a result. Through the TI Team's evaluation (see Section 9.4.3), this data was given a low weight in the κ_0 estimates (see Section 7.4.6).

7.4.1 Data processing

All these GMDBs began with raw, unprocessed time histories and followed the same processing procedures. This section describes the data processing performed for the ground-motion data in the Inversion GMDB, κ_0 GMDB, Duynefontyn GMDB, and Colenso GMDB; the Temporary Array GMDB data was processed by the specialty contractors. The GMM TI Team processed the raw records using two independent software codes: the industry standard IRIS Seismic Analysis Code (SAC) by Goldstein et al. (2003) and Goldstein and Snoke (2005), and

the Obspy software developed in Python by Beyreuther et al. (2010). The GMM TI Team applied the same general processing steps for all databases.

All waveforms for this project were cut from continuous waveforms. P-wave and S-wave arrival times were calculated for each station based on the earthquake distance, depth, and origin time. The GMM TI Team estimated arrival times using TauP, a seismic travel time calculator developed by Crotwell et al. (1999), with the *iasp91* velocity model developed by Kennett and Engdahl (1991). Travel-time estimates provided the GMM TI Team with the ability to cut records to an appropriate length for data processing. Record cutting is often magnitude dependent, and records are typically cut to preserve at least a minute of pre-event noise and capture the earthquake signal through the coda. The P-wave and S-wave arrival times were also used as the reference point for selecting appropriate noise and signal+noise windows for the calculation of the signal-to-noise ratio for each record. Sixty-second windows of both pre-event noise and earthquake signal were cut from the records following the procedure presented later in this section.

For each of the cut records, the GMM TI Team performed three basic processing steps to prepare the raw data for further processing as shown in Figure 7-10. First, for each record, they removed the mean of the record trace to centre the y-axis at zero, as demonstrated in Figure 7-10. For this record, removing the mean resulted in the left side of the seismogram being higher than the right side. Second, after the mean was removed, the GMM TI Team removed a straight-line trend fit using least squares and subtracted it from the data, as shown in Figure 7-10. This step results in a waveform that oscillates about the y=0 line. Finally, the ends of the waveform trace were tapered to force the record to start and end at zero, as shown in Figure 7-10. This step applies a symmetric Hamming taper with a width of 0.05. A Hamming taper is a raised cosine taper that is used to smooth discontinuities at the beginning and end of a sampled signal, and the width of the taper controls the extent of tapering on the signal ends with larger numbers increasing the amount of taper. Tapers are used to reduce the ringing that sharp discontinuities produce in the Fourier transform process.

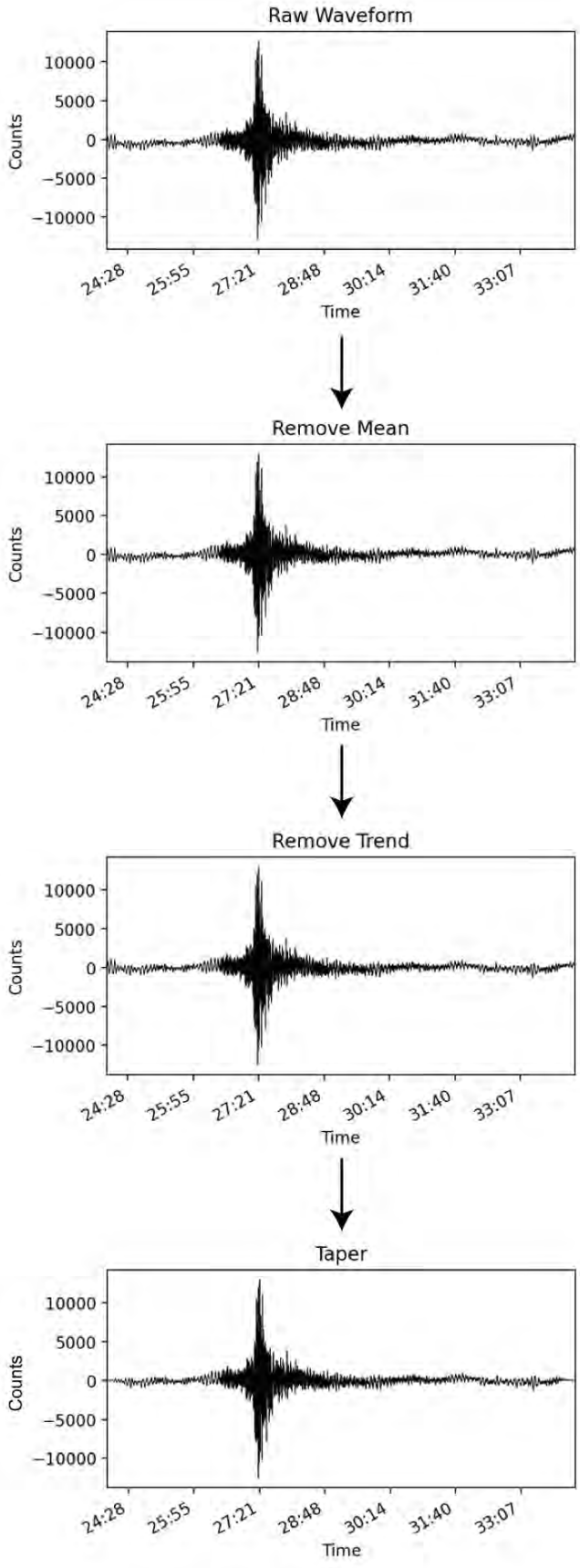

This is an example of a raw waveform with no processing applied.

Removing the mean results in a waveform with a mean of y=0, but there is still a linear trend as the left side of the trace is aove y=0 and the right side of the trace is below.

Removing the linear trend results in a waveform with no linear drift. It is completely centered about the y=0 line.

Tapering the ends of the waveform results in a waveform that equals zero at the ends

Figure 7-10. Example of waveform processing steps: removal of mean, removal of linear trend and tapering of ends.

After the basic processing, the GMM TI Team filtered the data to reduce signal amplitudes outside of the pass band that introduce noise in the removal of the instrument response and the computation of the Fourier amplitude spectra (FAS) using the Discrete Fourier Transform (DFT) methodology to convert a signal in the time domain to a representation in the frequency domain. The GMM TI Team computed FAS in both SAC and Python where each datafile was padded with zeros to the next power of two before the transform was performed, allowing for the most efficient computation of the FAS by using symmetries in the calculated terms that are highest when the signal has a length that is a power of two. The GMM TI Team compared the results obtained in SAC and from the Python *scipy.fft* package and confirmed that they produced the same result. The displacement and acceleration amplitude spectra from the Python outputs were saved and used for further analysis.

The prefiltering tapers the signal at the high and low ends using four frequency corners defined at 0.01 Hz, 0.02 Hz, f_N*0.5 Hz and f_N, where the Nyquist frequency (f_N) is equal to one-half of the sampling rate. The shape of the prefilter is shown with a red line in the top panel of Figure 7-11, and the displacement FAS is in blue. The GMM TI Team explored the impact of shifting the third corner of the filter to slightly higher frequencies (f_N*0.7 Hz and f_N*0.8 Hz) for the κ_0 GMDB, the Duynefontyn GMDB, and the Colenso GMDB. The higher third corner did not have a significant impact on the estimation of κ_0 for these databases so the algorithm maintained f_N*0.5 Hz for the third corner.

The GMM TI Team also removed the instrument response from the prefiltered signal, a standard processing step to remove the portion of the signal imparted by the recording instrument. The shape of the instrument response is shown with a red line in the bottom panel of Figure 7-11, and the prefiltered displacement FAS is in blue. The GMM TI Team conducted tests on the data to confirm that the same result was obtained regardless of the order in which the prefilter and instrument response removal steps were applied. There was an insignificant difference in the FAS from the two orders of operation. Instrument response files are transfer functions that define the instrument response characteristics in pole-zero format where the numerator and denominator are factored into polynomials. Solutions to the numerator are defined as the system zeros, and solutions to the denominator are defined as the system poles. Pole-zero files were obtained from IRIS or the CGS, depending on the dataset.

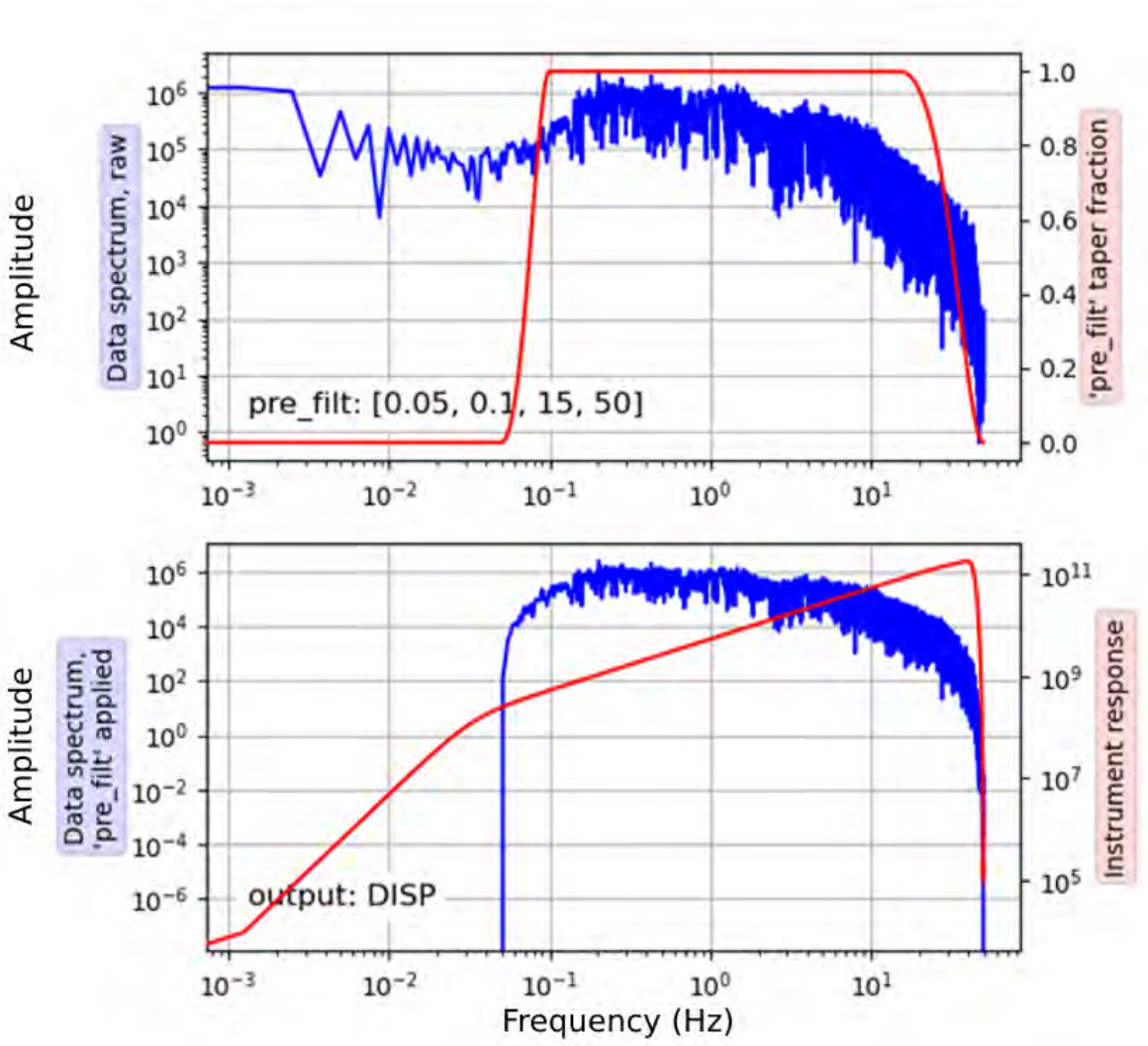

Figure 7-11. Prefiltering the data (top panel) dampens the data where the signal-to-noise ratio (SNR) is low. The red line shows the shape of the prefilter applied to the data, and the blue line is the displacement FAS. Removing the instrument response (bottom panel) deconvolves the instrument response from the seismic signal. The red line shows the shape of the instrument response, and the blue line is the prefiltered displacement FAS.

After removing the instrument response, the GMM TI Team baseline corrected the records by repeating the basic processing steps of removing the mean, removing the trend, and tapering the data. The GMM TI Team computed FAS from the baseline corrected records for the acceleration and displacement time series to use in magnitude-dependent κ_0 calculations, where κ was picked from the displacement FAS for small-magnitude earthquakes (**M** < ~3) and κ was picked from the acceleration spectra for larger-magnitude earthquakes (**M** > ~4). Since it is difficult to pick κ for earthquakes between approximately **M** 3 and **M** 4 due to an insufficient amount of data in the useable frequency range on both the displacement and acceleration FAS, earthquakes in this range were not considered for κ.

The GMM TI Team developed a screening criterion for the GMDBs to quickly screen out records with a low signal-to-noise ratio. The screening criterion is an average signal-to-noise ratio (SNR) over the frequencies from 5 Hz to 20 Hz. The GMM TI Team decided that records falling below the SNR of 3 are of insufficient quality to include in the evaluations.

To calculate the SNR, the pre-event noise was sampled from 65 seconds before the predicted P-wave arrival to 5 seconds before the predicted P-wave arrival. The signal+noise was sampled from 5 seconds before the predicted S-wave arrival to 55 seconds after the predicted S-wave arrival. The selected time windows are shown in the top panel of Figure 7-12. The cut noise and signal+noise windows were used to calculate acceleration FAS following the steps described above. SNRs were calculated at data points from 5 Hz to 20 Hz, as shown in the bottom panel of Figure 7-12. Figure 7-13 provides an example of how the signal+noise and noise were picked for a M 1.7 earthquake record with a SNR of 7, and it shows the resulting FAS in acceleration, velocity, and duration. The GMM TI Team reported the mean of the window from 5 Hz to 20 Hz as the SNR for each record.

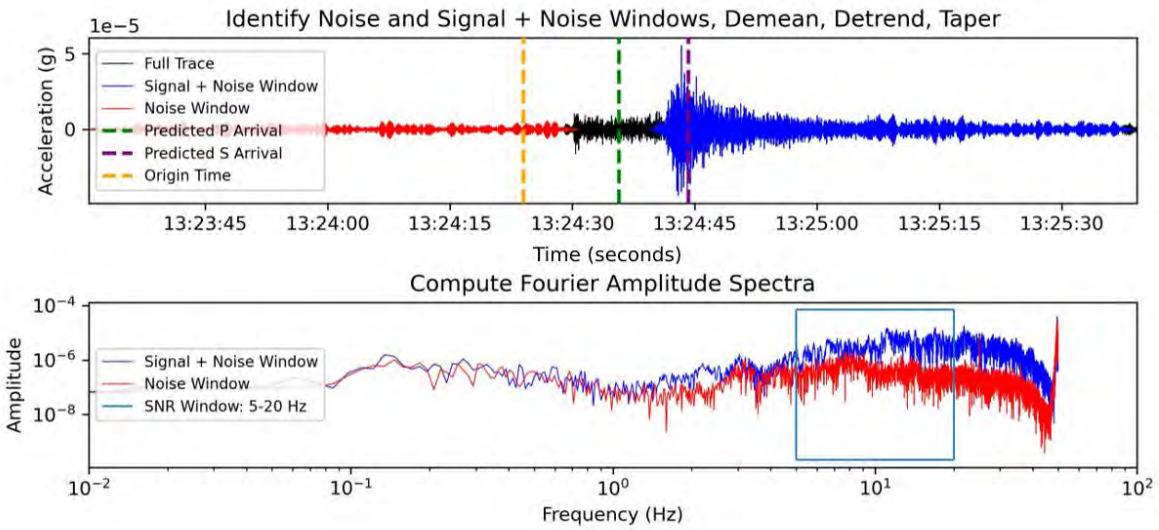

Figure 7-12. Picking the noise and the sample+noise windows for computing the SNR (top panel) and selecting the SNR window (bottom panel).

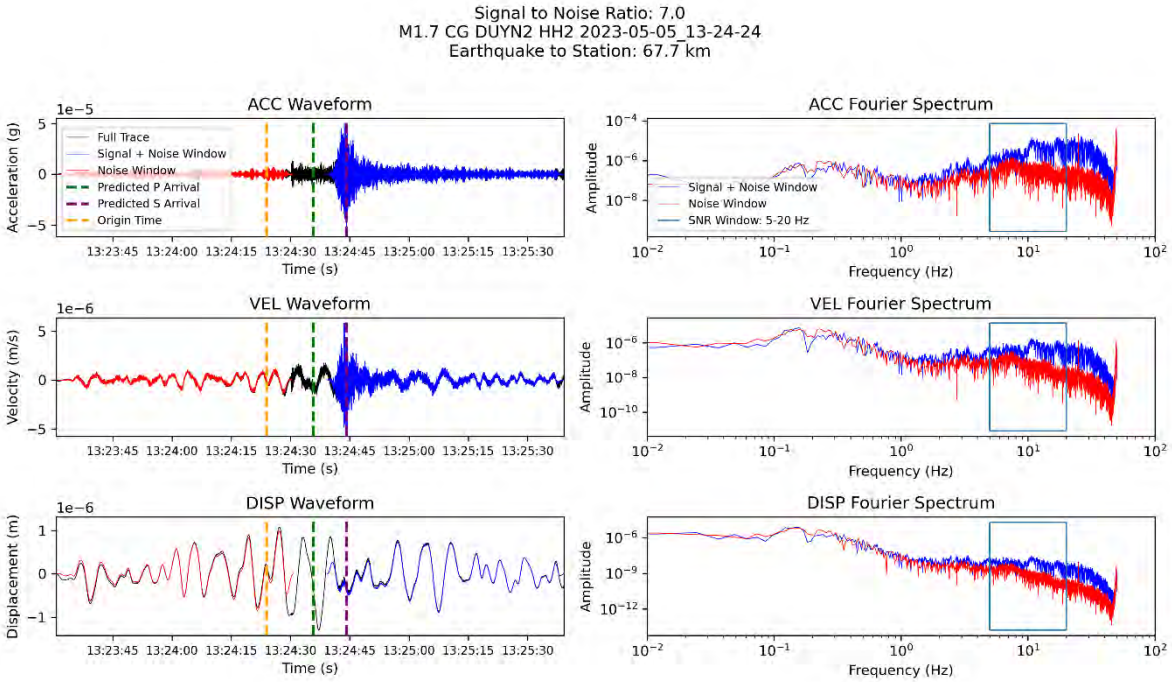

Figure 7-13. Picking the noise and the sample+noise windows for computing the SNR (left) for acceleration (top), velocity (middle) and displacement (bottom) and selecting the corresponding SNR windows (right) for a M 1.7 earthquake recording with an SNR of 7.

7.4.2 Inversion ground-motion database

The GMM TI Team compiled the Inversion GMDB using the earthquake locations and event times from the South Africa-wide Catalogue compiled by the SSM TI Team (Chapter 6) and waveforms from the SANSN provided to the GMM TI Team by the CGS. From the 2,100 earthquakes within the declustered SSM earthquake catalogue, 1,313 events produced at least one waveform recording captured by the network of available stations shown in Figure 7-14.

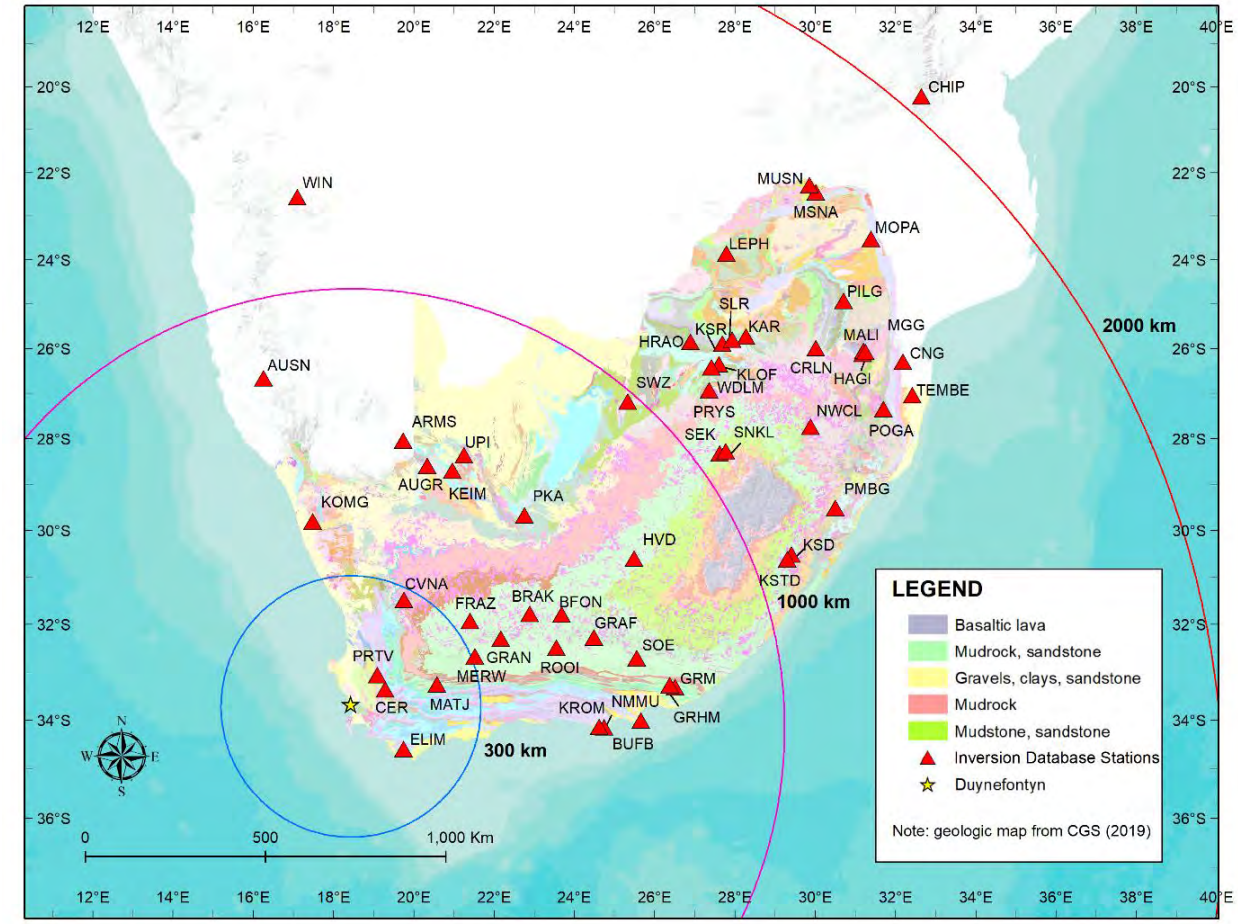

Figure 7-14. Surface geology with the SANSN stations included in the Inversion GMDB.

The GMM TI Team applied the below criteria to records from the GMDB to select catalogue events for the ground-motion inversion analysis. The GMM TI Team reserved evaluating record exclusion criteria for a later project phase.

1. Recordings from 2007 or later, the year in which multiple SANSN stations were installed near the Duynefontyn site.
2. Sampling rates higher than or equal to 100 samples per second to provide sufficient high frequency content for inversion.
3. Station records with available instrument response files.

The GMM TI Team filtering criteria resulted in 30,945 records from 1313 earthquakes for consideration in the Inversion GMDB. Figure 7-15 shows a comparison between the earthquakes in the SSM catalogue (red circles) and the earthquakes that produced records that passed through the above criteria (blue circles). The magnitude and distance coverage of the 15,138 paired records with both N–S and E–W record components available in the Inversion GMDB is shown in Figure 7-16.

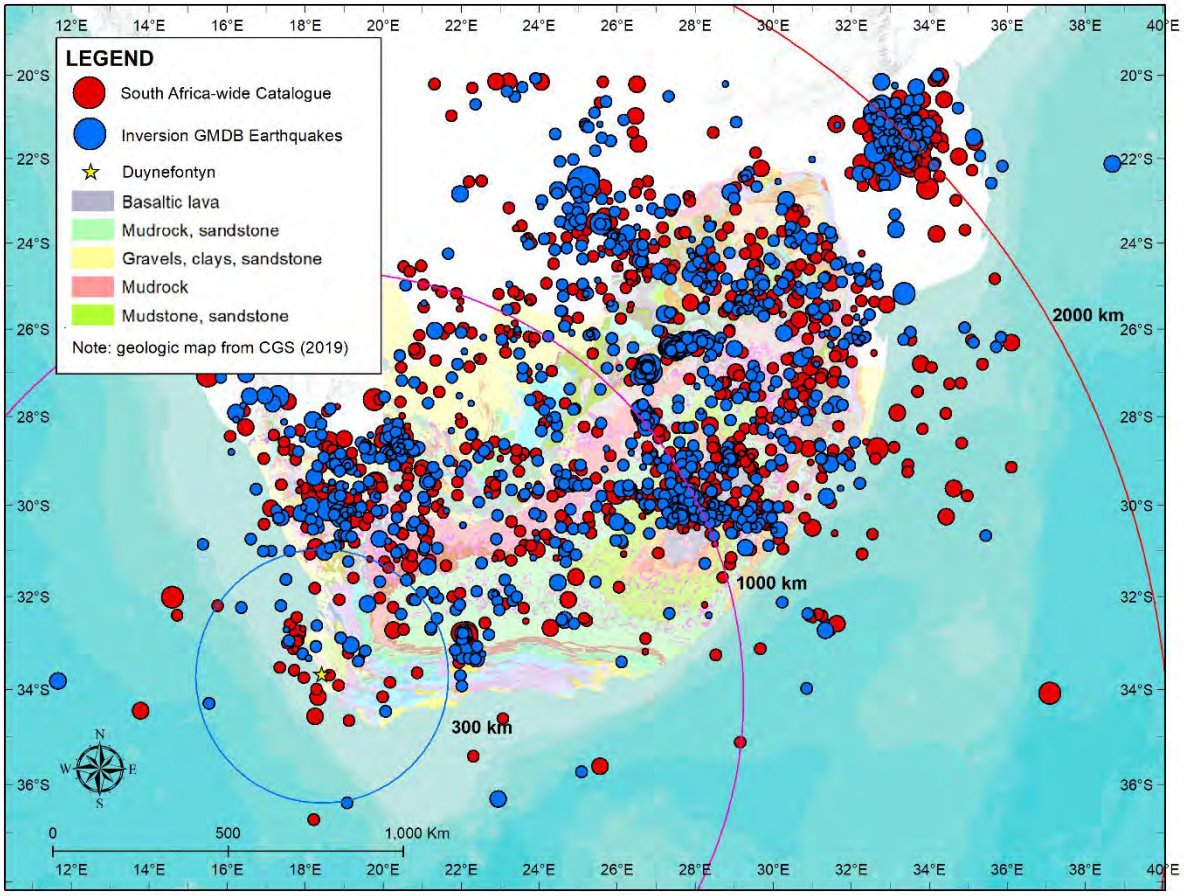

Figure 7-15. Comparisons of earthquakes in the South Africa-wide Catalogue (red circles) and the Inversion GMDB (blue circles).

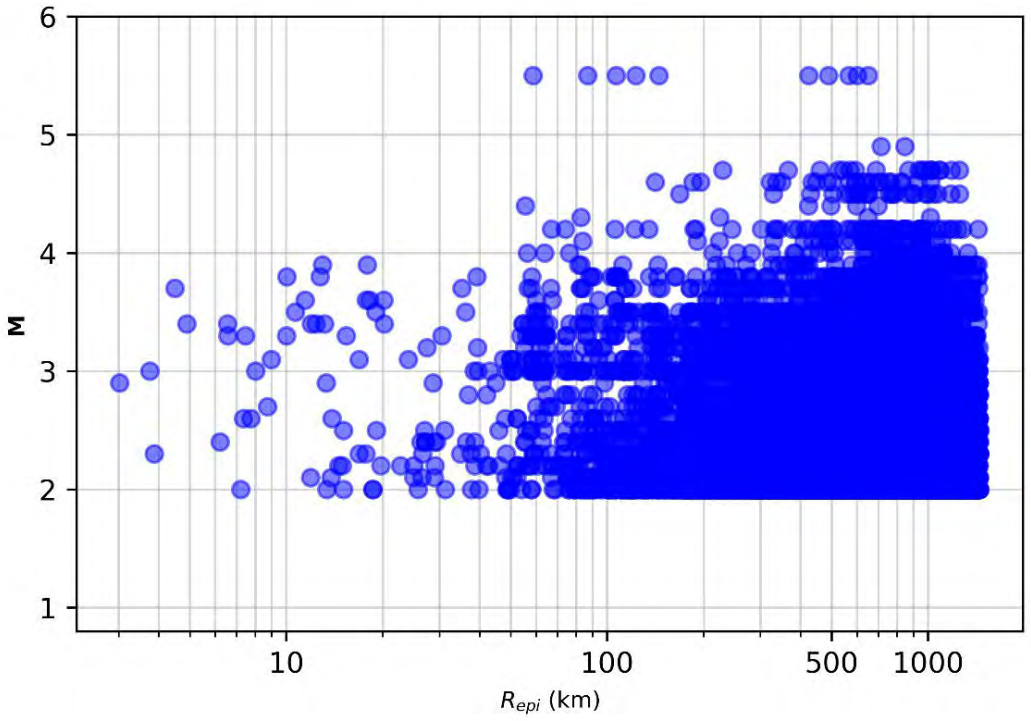

Figure 7-16. Magnitude vs. epicentral distance (R_{epi}) for the records in the Inversion GMDB.

The GMM TI Team then applied the SNR filter criteria described in Section 7.4.1. This criterion reduced the 15,138 paired records to 5,070 pairs, recorded at 48 stations, shown in Figure 7-17, where the colour of the station reflects the number of pairs of horizontal components recorded at each station. The magnitude–distance coverage of the record pairs with an SNR ≥ 3 is shown in Figure 7-18.

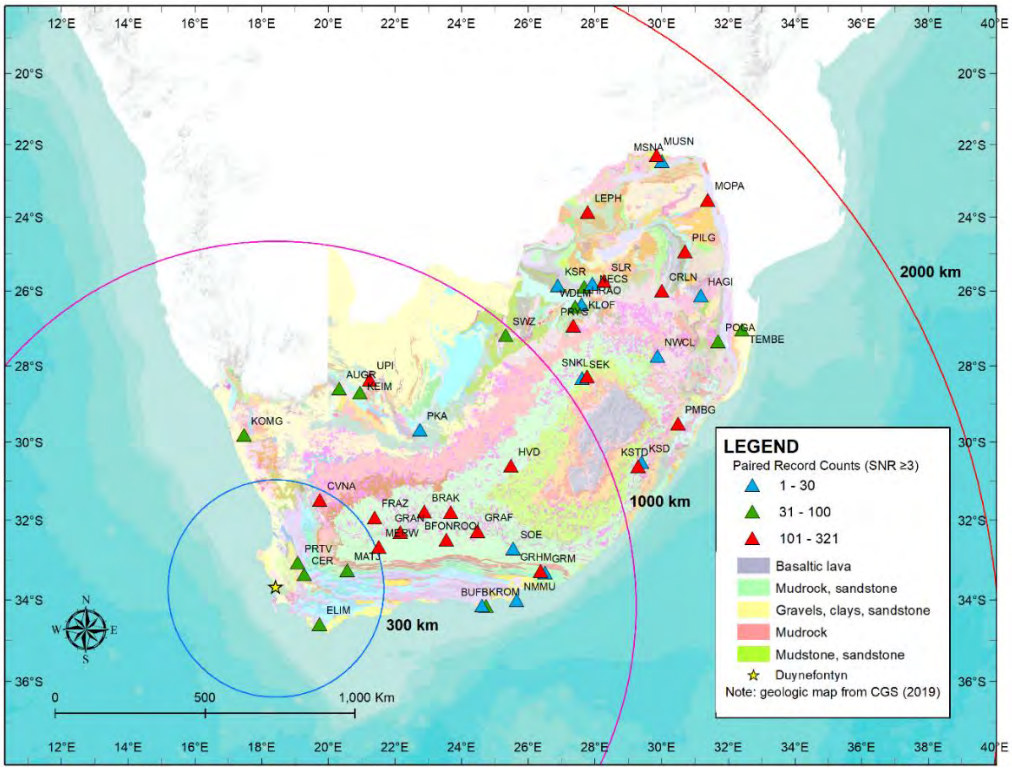

Figure 7-17. Station map for the Inversion GMDB with stations coloured according to the number of recorded paired earthquake records where SNR is ≥ 3.

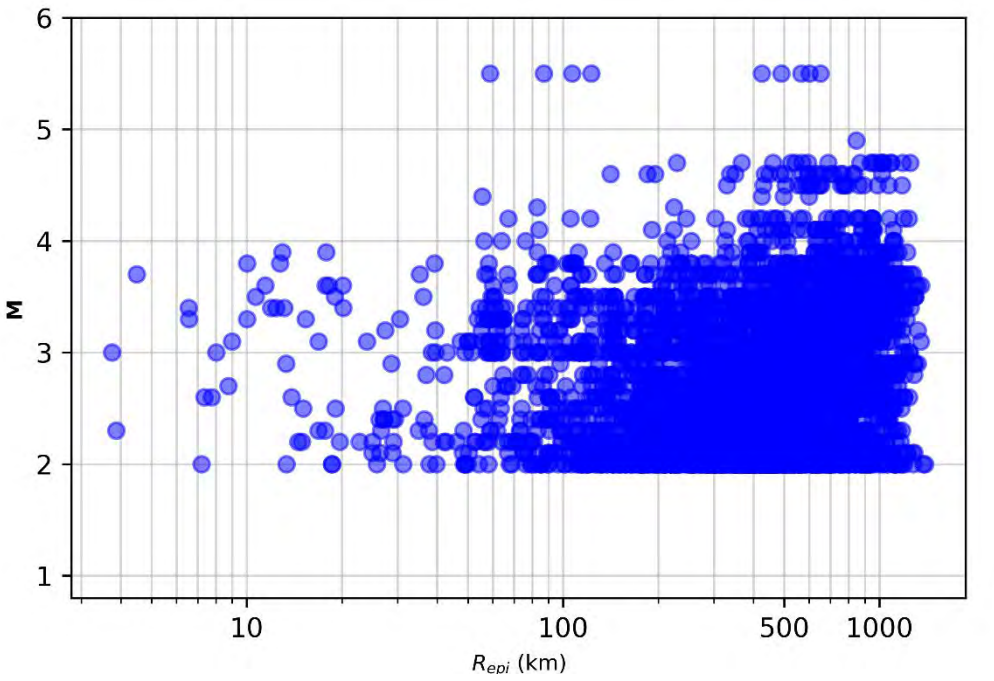

Figure 7-18. Magnitude vs epicentral distance (R_{epi}) for the records with SNR ≥ 3 in the Inversion GMDB.

To visually inspect the path coverage of the recorded ground-motions, source-to-station rays for the paired horizontal earthquake records with SNR ≥ 3 are traced in Figure 7-19 with grey lines. There are 5,070 raypaths shown in Figure 7-19.

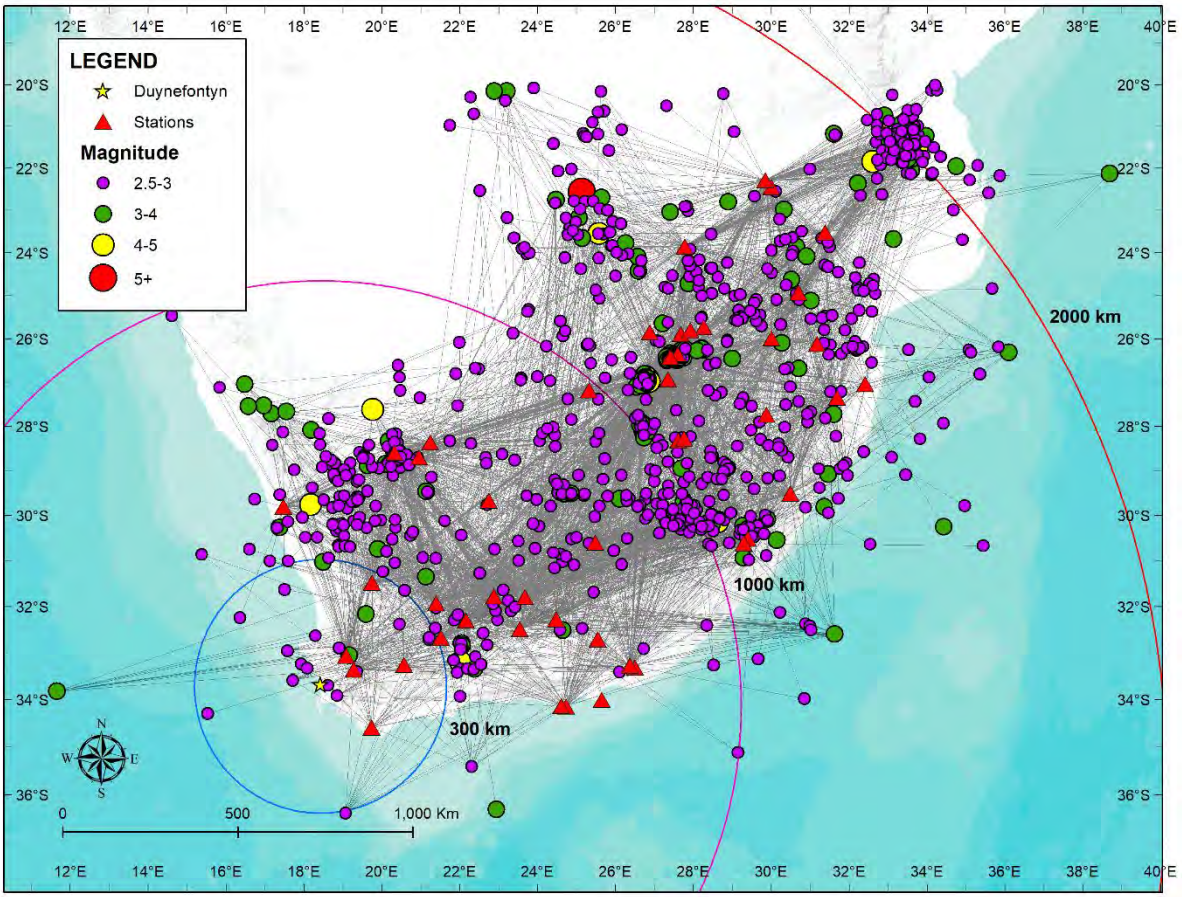

Figure 7-19. Raypaths for paired horizontal earthquake records with SNR ≥ 3 in the Inversion GMDB.

7.4.3 κ_0 Ground-motion database

The GMM TI Team compiled the κ_0 GMDB for the evaluation of site-specific high-frequency spectral decay parameters, typically referred to as κ_0. κ is a distance dependent parameter. When evaluating κ_0, local earthquakes are of great importance to evaluate the spectral decay parameter at the site, though recordings over various distances can also provide constraint. Because the SSM catalogue only focussed on larger earthquakes as these are the most significant for hazard, a new catalogue needed to be compiled for evaluating κ_0.

To develop the κ_0 GMDB, the GMM TI Team compiled a catalogue separate from the SSM catalogue, called the GMM catalogue. The GMM catalogue includes earthquakes with reported magnitudes ≥ 1, within 700 km of KNPS from the following databases: Advanced National Seismic System (ANSS) events from the USGS ranging in years from 2001 to 2020, the CGS South Africa Seismic Hazard Analysis (SASHA) events ranging in years from 1996 to 2019, and the CGS Ceres aftershock records ranging in years from (1996 to 2017). In total, this consists of 2,210 earthquakes, of which 253 earthquakes produce at least one waveform

recording over the network of stations that were selected based on the selection criteria described below.

The GMM TI Team applied the following selection criteria to records from the GMM catalogue to select an appropriate earthquake dataset that ensures high-quality records for the evaluation of κ_0:

1. Only stations within 1,000 km of the Duynefontyn site were used.
2. Sampling rates were required to be higher than or equal to 100 samples per second to provide sufficient high-frequency content for inversion.
3. Only stations with available instrument response files were used.

The stations used in the κ_0 GMDB are shown in Figure 7-20. The GMM TI Team filtering criteria resulted in a total of 1,429 records from 245 earthquakes for consideration in the κ_0 GMDB. The GMM catalogue is compared to the SSM catalogue in Figure 7-21, showing the earthquakes in the SSM database (red circles) and the earthquakes that produced records processed according to the filtering criteria above (blue circles). The magnitude and distance coverage of the earthquake in the κ_0 GMDB is summarised in Figure 7-22.

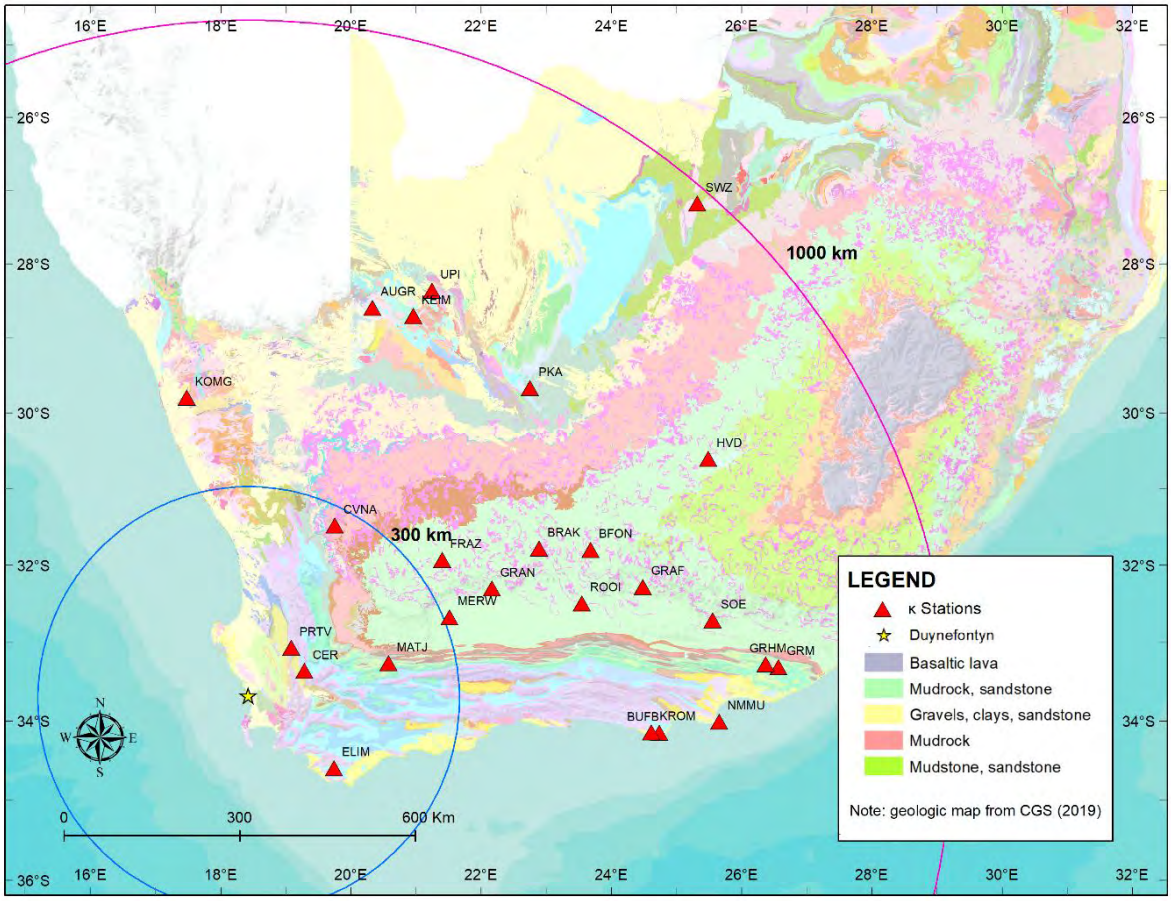

Figure 7-20. SANSN stations included in the κ_0 GMDB.

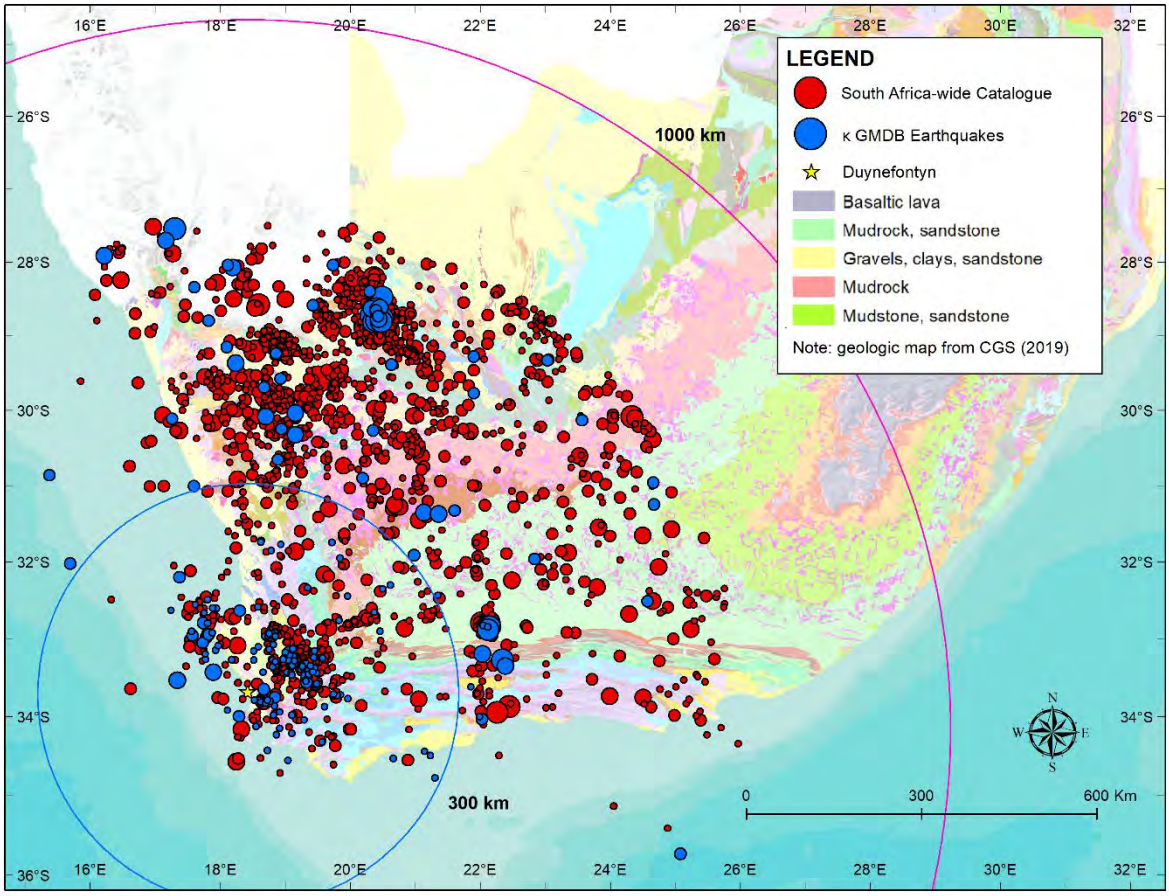

Figure 7-21. Comparison of earthquakes in the SSM catalogue (red circles) and the processed records in the κ_0 GMDB (blue circles).

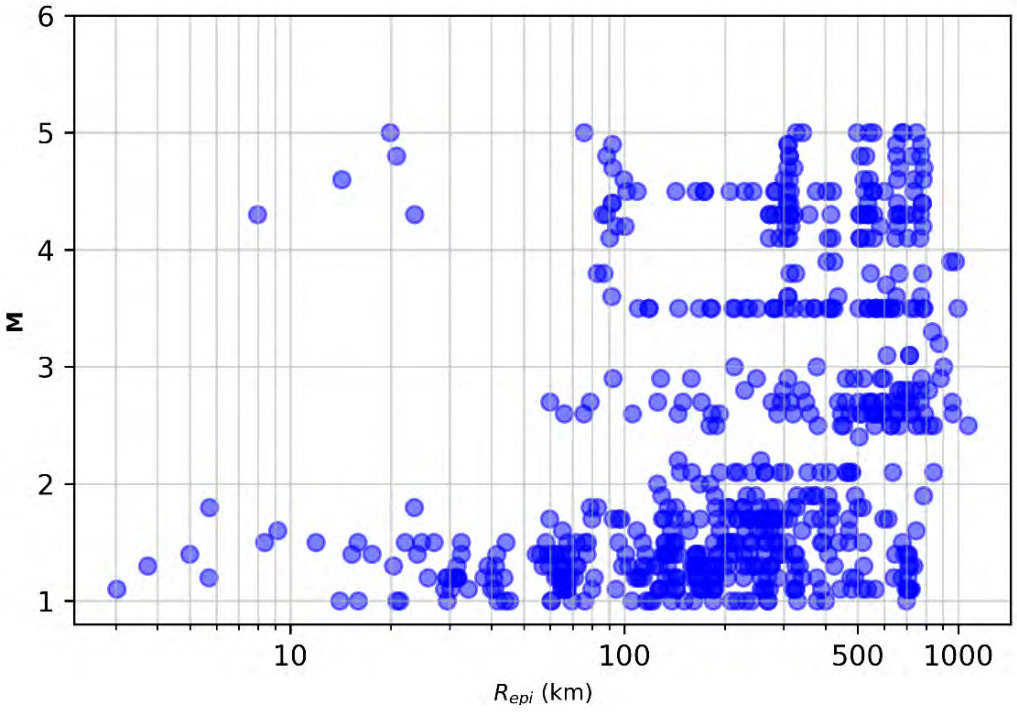

Figure 7-22. Magnitude vs epicentral distance (R_{epi}) for the earthquake records in the κ_0 GMDB.

The GMM TI Team then applied the SNR filter criteria described in Section 7.4.1. This criterion reduced the 627 paired records to 287 pairs recorded on 25 stations, as shown in Figure 7-23. The magnitude–distance coverage of the 627 record pairs with an SNR ≥ 3 is shown in Figure 7-24.

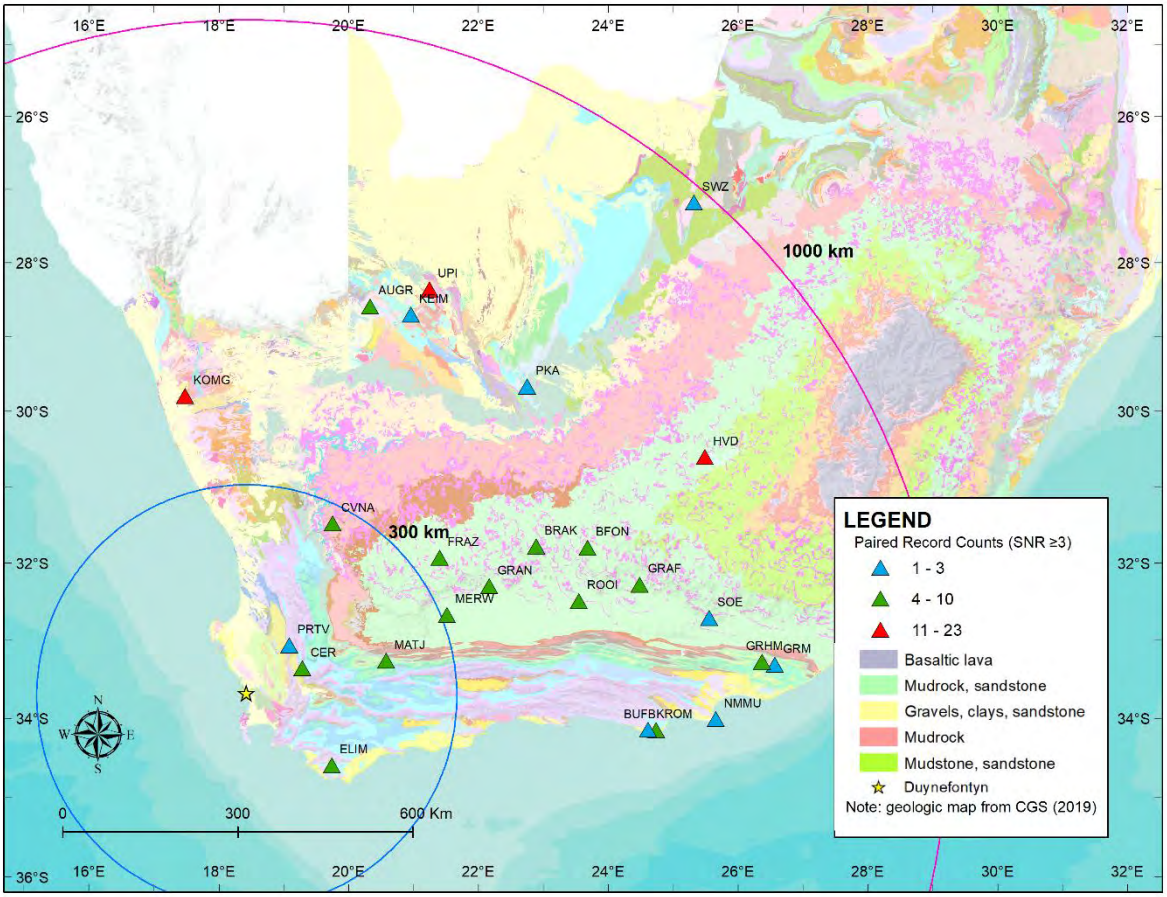

Figure 7-23. Station map for the κ_0 GMDB with stations coloured according to the number of recorded paired earthquake records where SNR is ≥ 3.

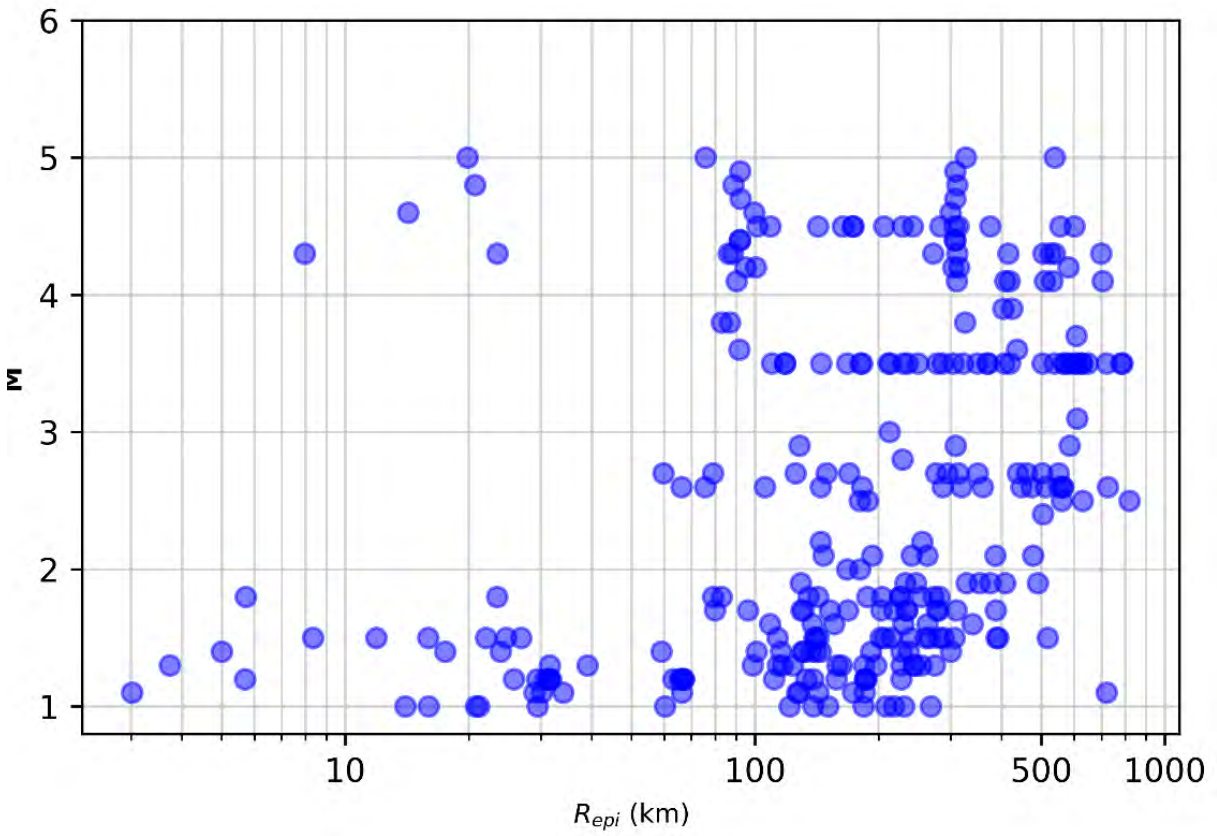

Figure 7-24. Magnitude vs epicentral distance (R_{epi}) for the records with SNR ≥ 3 in the κ_0 GMDB.

To visually inspect the path coverage of the recorded ground-motions, raypaths for the paired horizontal earthquake records with SNR ≥ 3 are traced in Figure 7-25 with grey lines. In total, there are 287 raypaths in Figure 7-25.

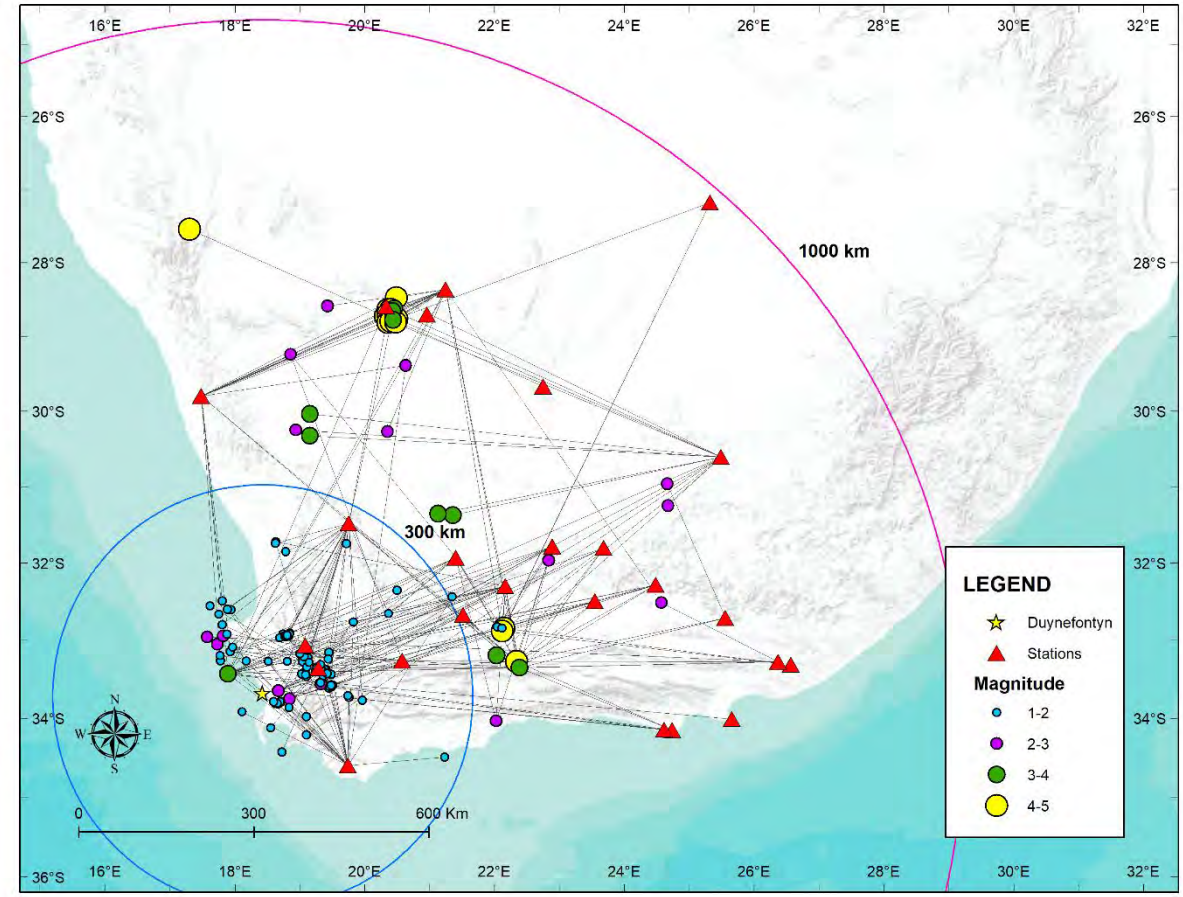

Figure 7-25. Raypaths for paired horizontal earthquake records with SNR ≥ 3 in the κ_0 GMDB.

7.4.4 Colenso ground-motion database

The Colenso Array was deployed by the CGS at the request of the SSM TI Team to investigate microseismicity along the Colenso Fault. Concurrent with the installation of the Duynefontyn stations and after the development of the κ_0 GMDB, the GMM TI Team requested the data from the Colenso Array to evaluate its use as a data source for κ_0 evaluations at the Duyenfontyn site. The Colenso Array stations are shown in Figure 7-26. The Colenso Array recorded 15 earthquakes during its deployment, also shown in Figure 7-26. The Colenso GMDB consists of all earthquakes and recordings from the Colenso Array.

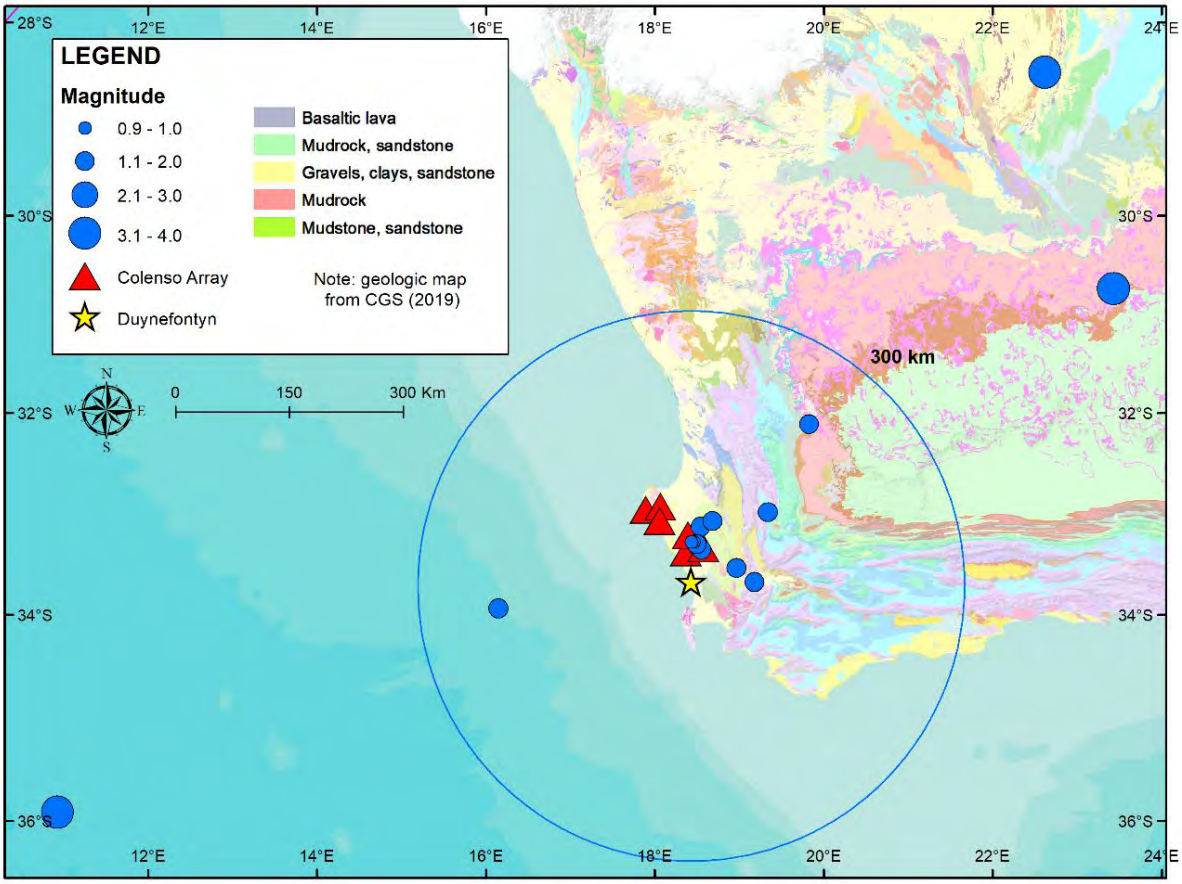

Figure 7-26. Colenso GMDB stations and earthquake locations.

The Colenso GMDB consists of 36 record pairs from 6 stations and 15 earthquakes. If the SNR is restricted to a value ≥ 3, there are 11 record pairs from 6 stations and 5 earthquakes. Figure 7-27 shows the magnitude–distance plots for records with SNR ≥ 3.

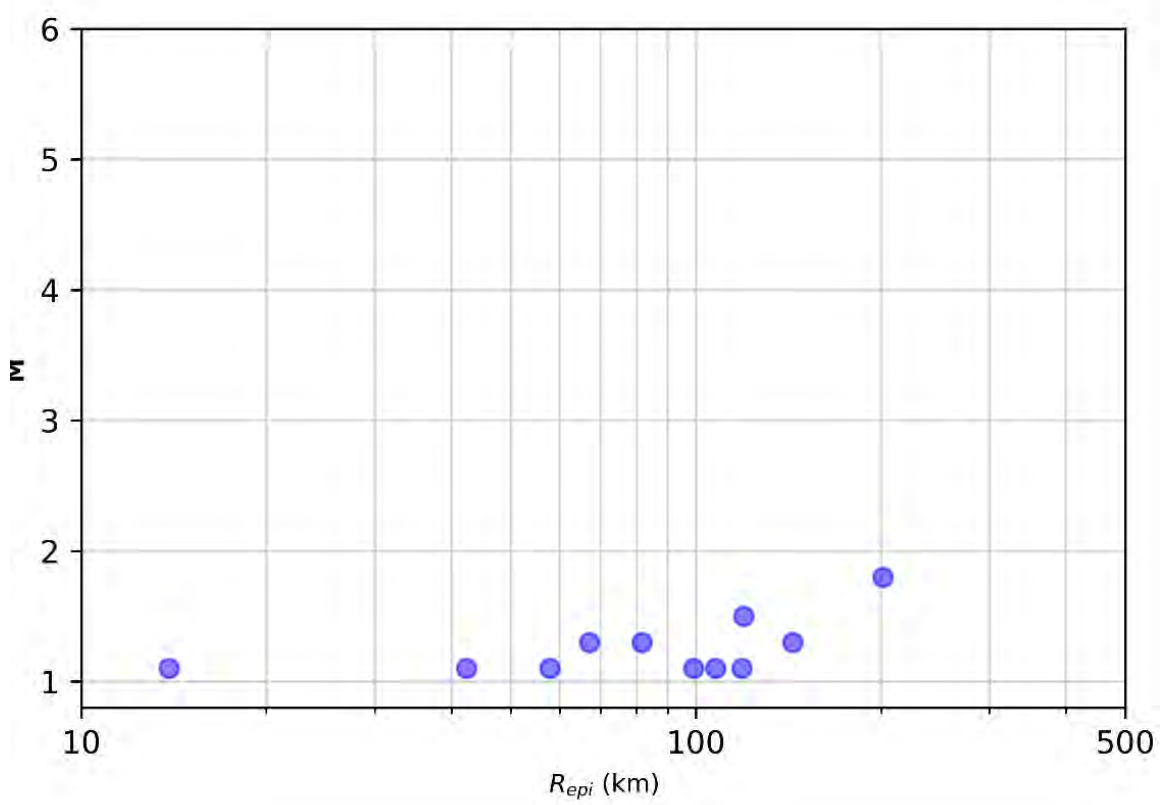

Figure 7-27. Magnitude vs epicentral distance (R_{epi}) for the records with SNR ≥ 3 in the Colenso GMDB.

To visually inspect the path coverage of the recorded ground-motions, raypaths for the paired horizontal earthquake records with SNR ≥ 3 are traced in Figure 7-28 with grey lines. Earthquake magnitude is indicated by colour and marker size. There are 11 records in Figure 7-28.

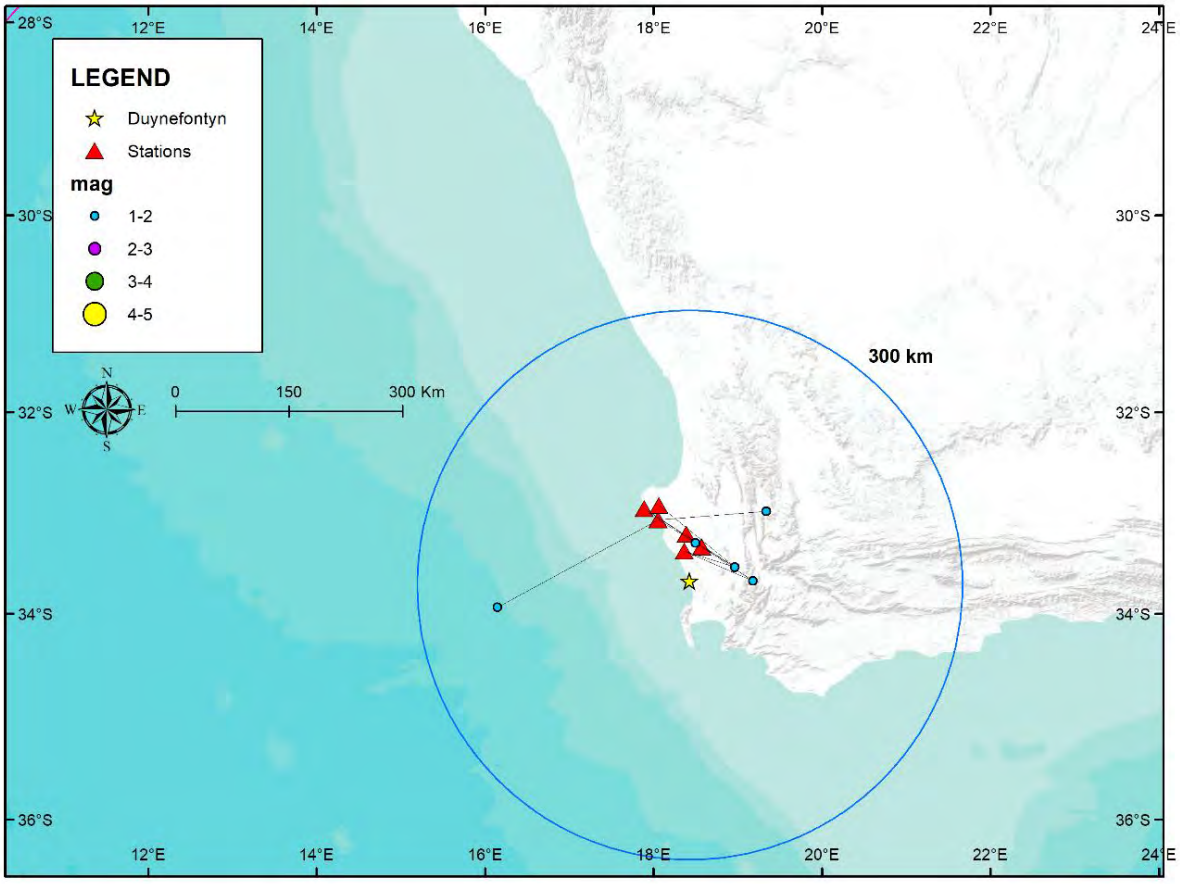

Figure 7-28. Raypaths for paired horizontal earthquake records with SNR ≥ 3 in the Colenso GMDB.

7.4.5 Duynefontyn ground-motion database

The Duynefontyn station arrays were installed by the CGS between February and April of 2023 and started collecting significant data in April 2023. The CGS provided the data from these stations to the GMM TI Team on 26 June 2023. During the period of data collection, the stations recorded 12 earthquakes. The station locations and epicentres of the earthquakes recorded are shown in Figure 7-29. The periods during which each of the DUYN seismometers were in operation with event origin times from the CGS catalogue are shown in Figure 7-30. There were 12 earthquakes recorded at DUYN2 and DUYN5, with fewer earthquakes recorded at the other four stations, as shown in the histogram in Figure 7-31.

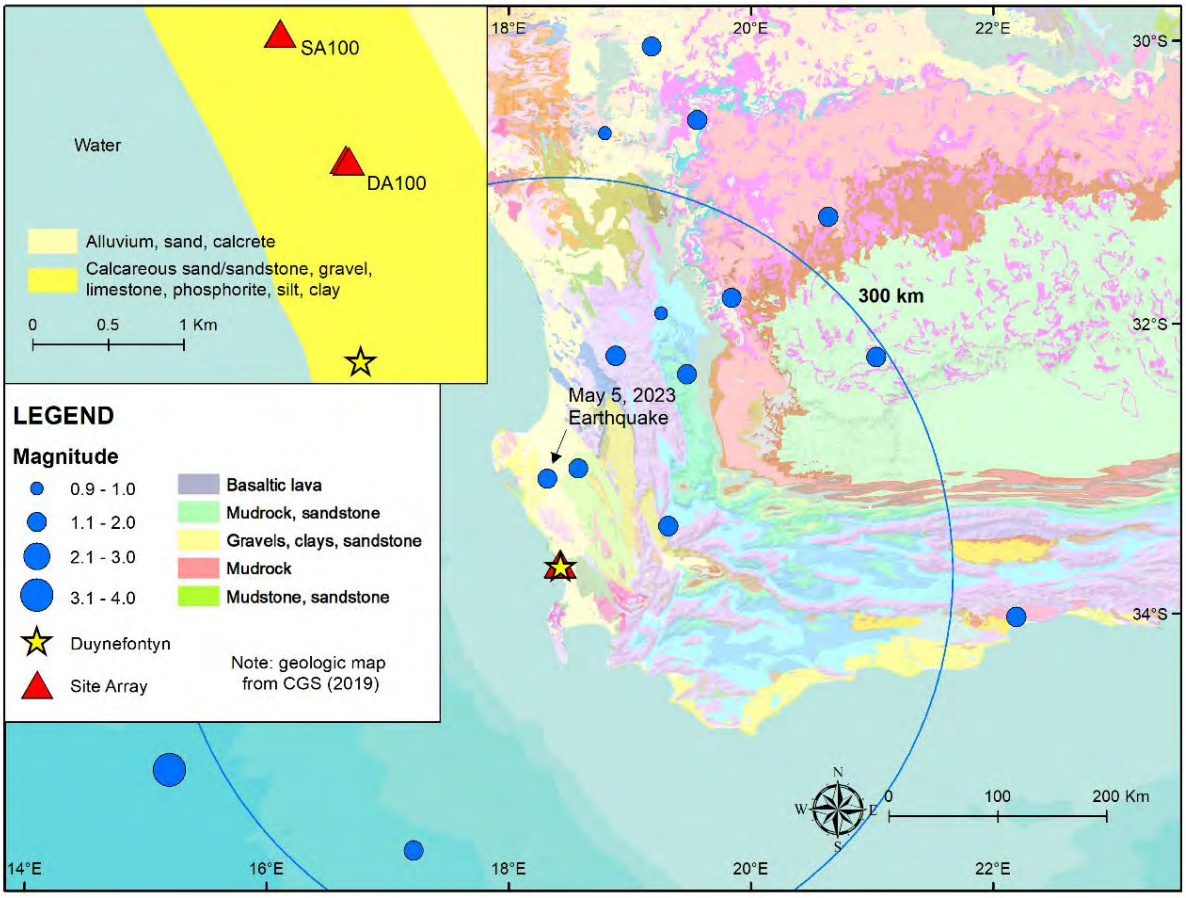

Figure 7-29. Duynefontyn GMDB stations and earthquakes recorded by the station from 8 April 2023 through 27 June 2023.

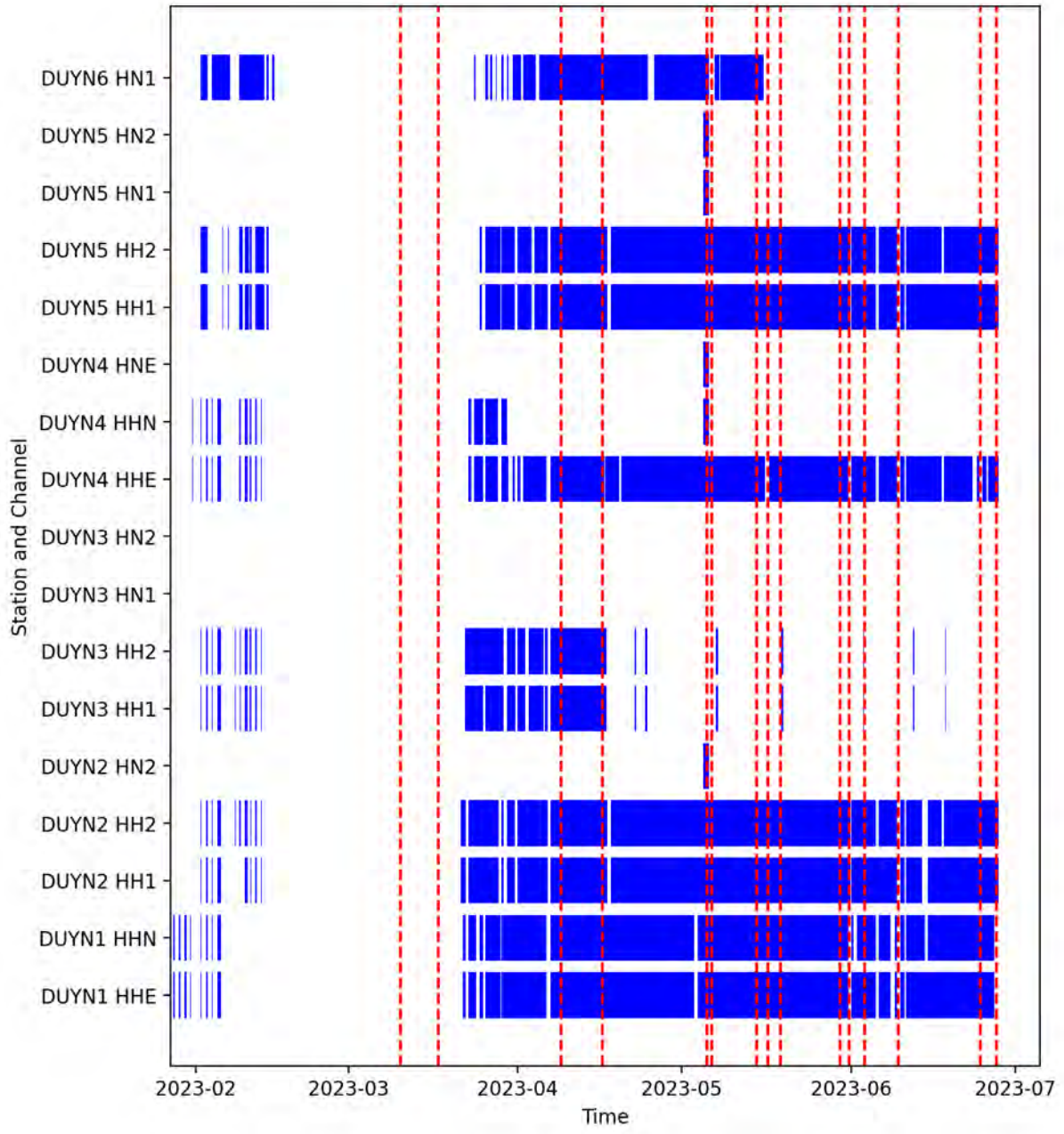

Figure 7-30. Visualisation of DUYN array waveform availability and coincident earthquakes. Horizontal blue bars represent available horizontal waveform records. Vertical dashed red lines represent earthquake origin times in the catalogue received from the CGS. The three letter codes on the Y-axis following the DUYN station numbers are network codes. The first letter (H) indicates a broadband sensor type, the second letter (H) indicates a weak-motion sensor that measures velocity and (N) indicates a strong-motion sensor that measures acceleration, and the third character (N/E) indicates one component of a directional orthogonal pair and (1/2) indicates one component of a nondirectional orthogonal pair.

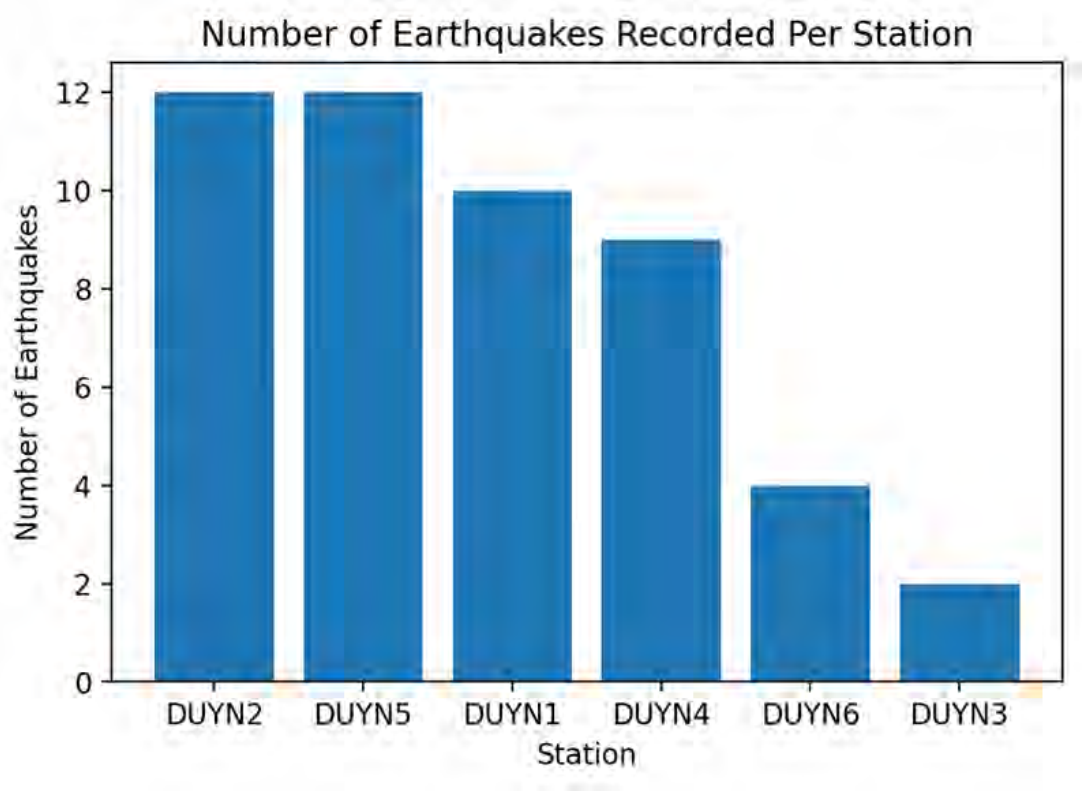

Figure 7-31. Histogram of number of earthquake records processed at each station.

The magnitude and distance coverage of the earthquake in the Duynefontyn GMDB is summarised in Figure 7-32.

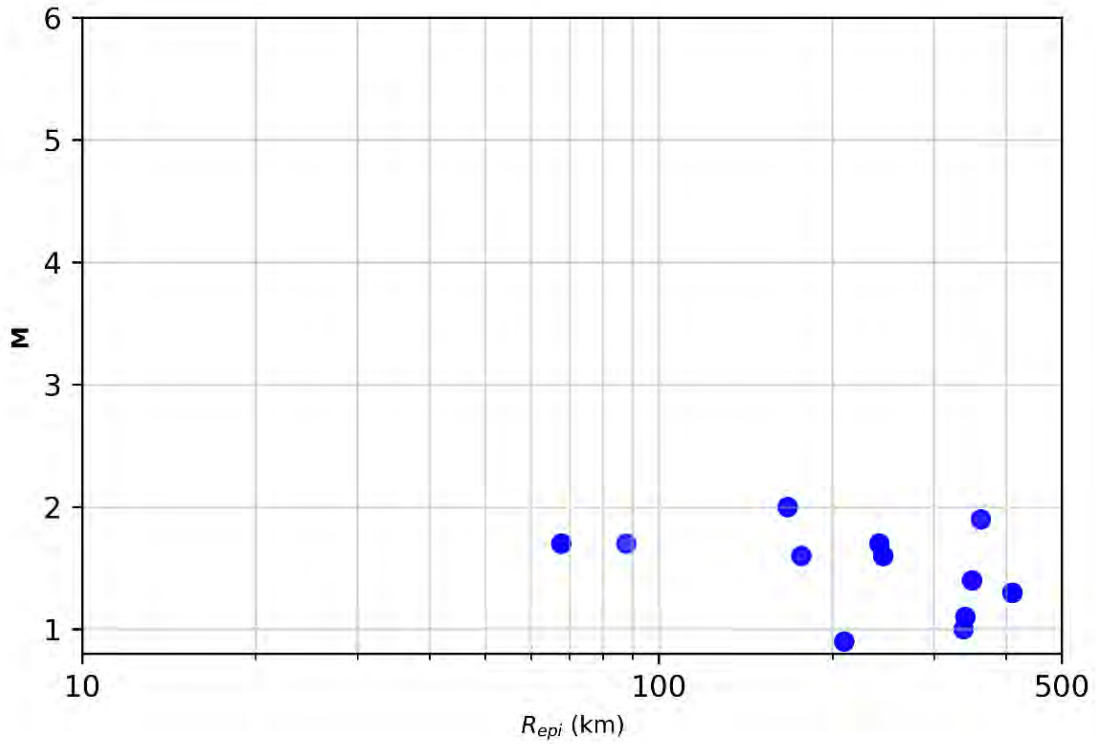

Figure 7-32. Magnitude–distance plot of the earthquakes recorded by the Duynefontyn station from 8 April 2023 through 27 June 2023.

The SNR for the recordings with an R_{epi} greater than 80 km is generally below 1 and is thus too low to provide useable information on κ. This leaves a single earthquake recorded on 5 May 2023, which was M 1.7 and 68 km from the station. The location of this earthquake is shown in Figure 7-29.

7.4.6 Temporary array ground-motion database

A Temporary Array was deployed by University of Cape Town researchers near the Dueynfontyn site from 24 July 2021 to 27 October 2021 (Quiros and Sloane, 2023). The original purpose of this array was to monitor microseismicity in the area. The GMM TI Team became aware of this array during Workshop 2 and requested that CGS hire the researchers as specialty contractors to provide estimates of κ for use in evaluating κ_0 at the Duynefontyn site.

The Temporary Array included 19 seismic stations from the University of Cape Town instrument pool and utilised 3-component geophones which recorded continuously at a rate of 200 samples per second. The locations of the seismic stations are shown in Figure 7-33. These stations recorded one earthquake, on 4 August 2021, during their deployment. The earthquake was located at latitude -33.675, longitude 18.308, and a depth of 7 km. No magnitude was estimated by Quiros and Sloane (2023) for the event, beyond identifying it as “small”. Given the low seismicity in the region, and the lack of an event identified by the regional catalogue, the magnitude of the recorded earthquake was likely below 2. The specialty contractors provided the GMM TI Team with estimates of κ from the recordings. Additional information about these κ values is given in Section 9.4.3.

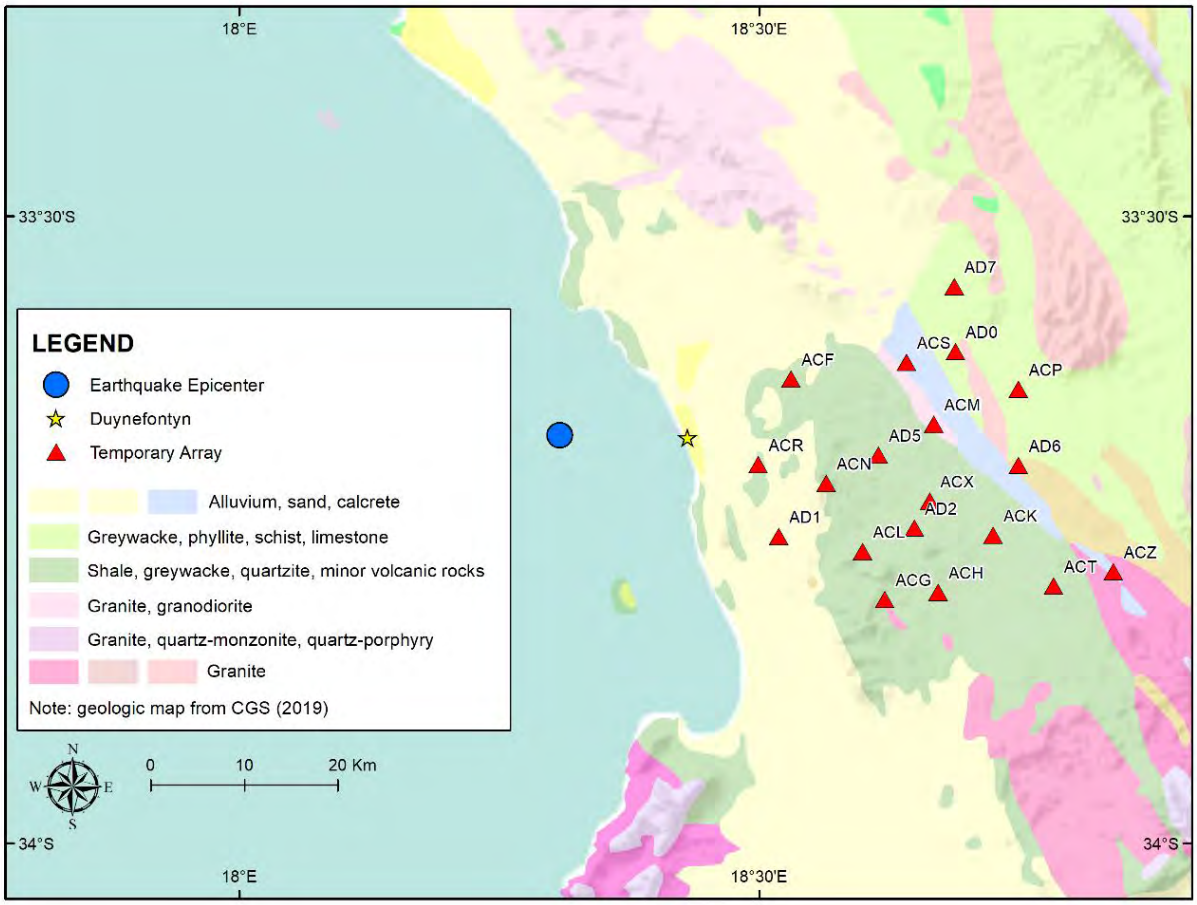

Figure 7-33. Temporary Array stations and earthquake epicentre location (from Quiros and Sloan, 2023).

7.5 REFERENCES

Beyreuther, M.; Barsch, R.; Krischer L.; Megies T.; Behr Y. and Wassermann J. (2010). ObsPy: A Python Toolbox for Seismology. Seismological Research Letters 81(3). 530-533.

Crotwell, H. P.; Owens, T.J. and Ritsema, J. (1999). The TauP Toolkit: Flexible Seismic Travel-Time and Ray-Path Utilities, Seismological Research Letters 70. 154-160.

Goldstein, P.; Dodge D.; Firpo M. and Minner, L. (2003). SAC2000: Signal Processing and Analysis Tools for Seismologists and Engineers. Invited Contribution to: Lee, W.H.K.; Kanamori, H.; Jennings, P.C. and Kisslinger, C. (Eds.). The IASPEI International Handbook of Earthquake and Engineering Seismology. Academic Press, London, England. 1613-1614.

Goldstein, P. and Snoke, A. (2005). SAC Availability for the IRIS Community. Incorporated Research Institutions for Seismology Newsletter UCRL-JRNL-211140. Lawrence Livermore National Laboratory.

Jele, V., Tabane, L. and Mantsha, R. (2024). Report on the installation of a vertical array at Duynefontyn, Western Cape, South Africa. CGS Report 2023-0198 (Rev.0).

Kennett, B.L.N. and Engdahl, E. R. (1991). Travel Times for Global Earthquake Location and Phase Association. Geophysical Journal International 105. 429-465.

Manzunzu, B. and Sebothoma, S. (2022). Determination of Shear-Wave Velocity Profile at South African Seismic National Seismograph Network Stations using Multi-Channel Analysis of Surface Waves. CGS Report 2022-0001 (Rev. 0). Council for Geoscience, Pretoria, South Africa.

Quiros, D. and Sloan, A. (2023). Estimation of Kappa Values in the Coastal Plain Between Cape Town and Saldanha Bay. Department of Geological Sciences, University of Cape Town, South Africa. RFQ SAS060.

Watson-Lamprey J.; Midzi, V.; Rathje, E.; Stafford, P. and Ulmer, K. (2023). Ground Motion Modelling White Paper for the Duynefontyn SSHAC EL-2 PSHA 2.0.

CHAPTER 8: SEISMIC SOURCE MODEL

8. SEISMIC SOURCE MODEL

8.1 OVERVIEW OF THE SEISMIC SOURCE MODEL AND CRITERIA FOR DEFINING SEISMIC SOURCE ZONES

The seismic source model (SSM) is a conceptual and mathematical representation of the physical characteristics of earthquake sources that are deemed capable of producing hazard-significant ground motions at the Duynefontyn site and the KNPS. They are identified and assessed by the SSM TI Team from all the information evaluated during the project, including records of past earthquakes, geologic evidence of active tectonic deformation, and an understanding of the current seismotectonic setting. This information was used by the SSM TI Team to model the size, location, and rate of future earthquake activity that can impact the site. The SSM TI Team also accounts for the uncertainties and variabilities associated with this information, which is a critical factor in all PSHA studies.

There are two types of sources in the SSM. Seismic source zones are regions of the Earth's crust with diffuse seismicity. Fault sources are planar fractures or fracture zones in the Earth's crust that localise seismicity. Seismic source zones are used to model the temporal and spatial distribution of seismicity in a volume of the Earth's crust where there is insufficient geologic or geophysical evidence to allow the SSM TI Team to assign past recorded earthquakes to a mapped fault. These earthquakes could have been produced by a fault that did not rupture the ground surface, and thus did not leave geological evidence for the earthquake. Alternatively, the fault could have produced surface rupture, but this surface rupture remains obscure and unidentified in the landscape. Seismic source zones are thus constructed in the SSM to account for future earthquakes that may occur on such unidentified fault sources. The modelling details ascribed to each seismic source zone are based on the geological, geophysical, and seismological characteristics of the source zone and the surrounding region of interest. In contrast, fault sources are identified and characterised from geological, geophysical, and seismological evidence of past fault slip or concentrated seismicity that clearly aligns on the fault plane. In the SSM, they are modelled to represent the occurrence of repeated future earthquakes that remain localised along the fault.

In PSHA studies, source zone boundaries are defined based on the criteria shown in Figure 8-1. The boundaries of seismic source zones have been drawn by the SSM TI Team to define a volume of crust which has relatively consistent seismotectonic characteristics when compared to adjoining seismic source zones. The specific criteria that the SSM TI Team relied on were the type of crust (e.g., Mesozoic extended crust vs. non-Mesozoic extended crust), structural grain, style-of-faulting, topography, and crustal stress state. Where the GMM requires that future earthquakes must be modelled as fault ruptures rather than point sources, future seismicity within each seismic source zone was treated by the SSM TI Team as virtual fault ruptures. The virtual fault ruptures are modelled to capture the relevant seismicity parameters that are consistent with the seismotectonic setting of the source zone. These parameters include maximum magnitude, thickness of the seismogenic crust, style-of-faulting, and fault geometry.

In practical terms, the SSM TI Team drew their preliminary assessment of the source zone boundaries while viewing the geological, geophysical, and seismological information overlain on a geologic map in ArcGIS, which is a commonly used Geographic Information System (GIS) software. The SSM TI Team arrived at the source zone boundaries through an informed

discussion of the underlying data, models, and methods, and collective agreement of the outcome (Figure 8-2)

As these seismic source zone boundaries were finalised, the SSM TI Team summarised each source zone's characteristics in Table 8-1. Section 8.3 documents the rationale and justification for each source zone boundary in detail. No alternative boundaries were deemed necessary by the SSM TI Team. The fault rupture characteristics within a source zone, such as style-of-faulting and rupture orientations, are modelled as aleatory variabilities defined by their relative frequency of occurrence. Details of how the randomisation is developed is described in Section 8.2.6. Finally, seismic source boundaries for those zones that include virtual faults were designated as strict or leaky, as described in Section 8.2.1. Strict boundaries restrict a virtual fault rupture to remain within the source zone boundary, while leaky boundaries allow a virtual rupture that originates within one source zone to extend across the boundary and into the neighbouring source zone.

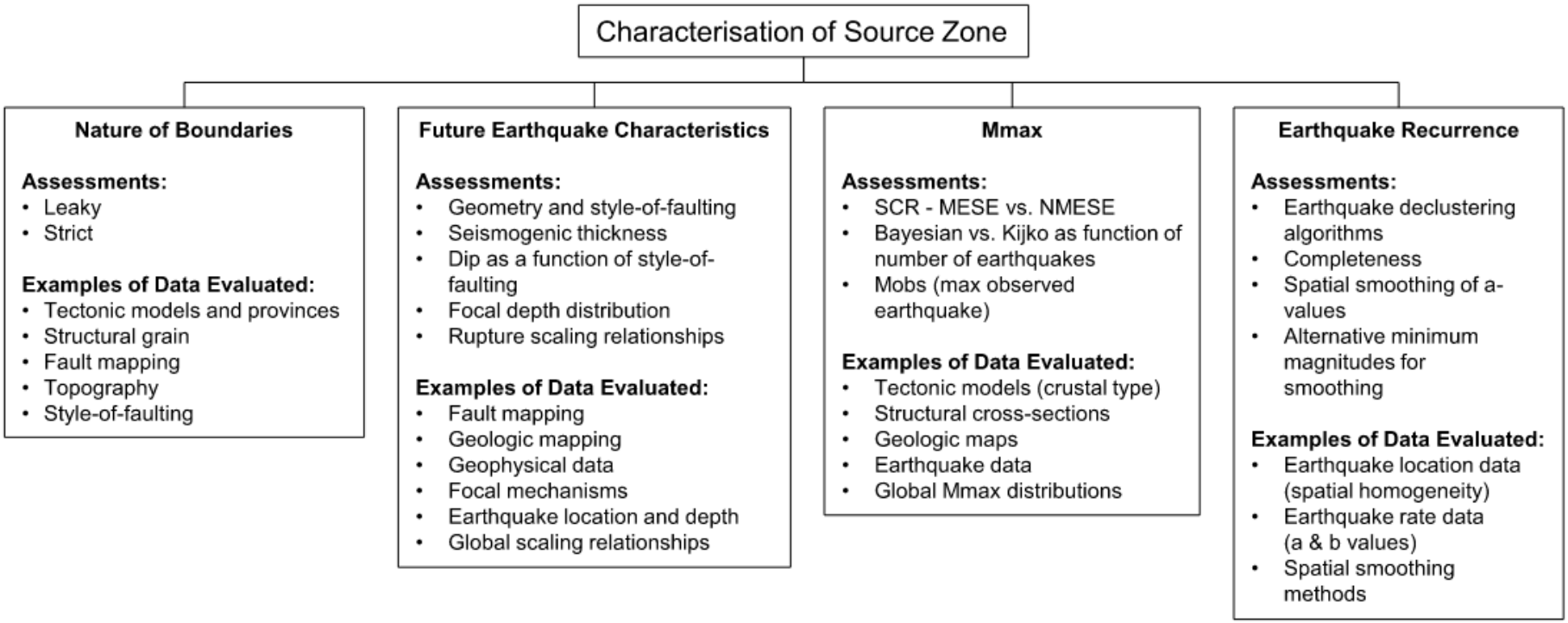

Figure 8-1. Chart summarising the evaluation and integration the SSM TI Team followed for each seismic source zone. Each of the four groups shown in the chart has a subset of specific assessments that the SSM TI Team must include (with weights to represent epistemic uncertainty) or percentages (to represent aleatory distributions) in the SSM logic tree.

Table 8-1. Summary of seismic source zone hazard inputs.

Characteristic	SDZ	ORZ	AGZ	OBZ	COZ
Seismogenic Thickness (km)	15 km [0.2] 17 km [0.6] 22 km [0.2]	15 km [0.2] 17 km [0.6] 22 km [0.2]	15 km [0.2] 17 km [0.6] 22 km [0.2]	15 km [0.2] 17 km [0.6] 22 km [0.2]	15 km [0.2] 17 km [0.6] 22 km [0.2]
Style of Faulting	Normal (20%) Strike-slip (80%)	Normal (50%) Strike-slip (50%)	Normal (90%) Strike-slip (10%)	Normal (100%)	Normal (50%) Strike-slip (50%)
Strike Aleatory Distributions	All ruptures 130º +/- 25º	Point source	Point source	Point source	Point source
Dip Aleatory Distributions	Normal faults dip to south (100%) Dip values 45º (20%) 65º (60%) 85º (20%) Strike-slip faults (dip south (50%) or north (50%)) Dip Values 75º (40%) 90º (60%)	Normal [3] Dip values 45º (20%) 65º (60%) 85º (20%) Strike-slip Dip Values 75º (40%) 90º (60%)	Normal [3] Dip values 45º (20%) 65º (60%) 85º (20%) Strike-slip Dip Values 75º (40%) 90º (60%)	Normal [3] Dip values 45º (20%) 65º (60%) 85º (20%)	Normal [3] Dip values 45º (20%) 65º (60%) 85º (20%) Strike-slip Dip Values 75º (40%) 90º (60%)
Mmax Bayesian Prior	NMESE [1.0]	NMESE [1.0]	MESE [1.0]	MESE [1.0]	NMESE [1.0]
Max Observed	E[**M**] 6.2 1969-09-29	E[**M**] 5.2 1950-09-30	E[**M**] 4.9 1969-09-11 Or E[**M**] 4.5 1969-10-10	E[**M**] 3.3 2003-04-15	E[**M**] 6.1 1912-02-20

[1] Epistemic weights are given in [brackets].
[2] Normal distribution sampled at 5 degree increments
[3] GMPEs require dip values for point sources

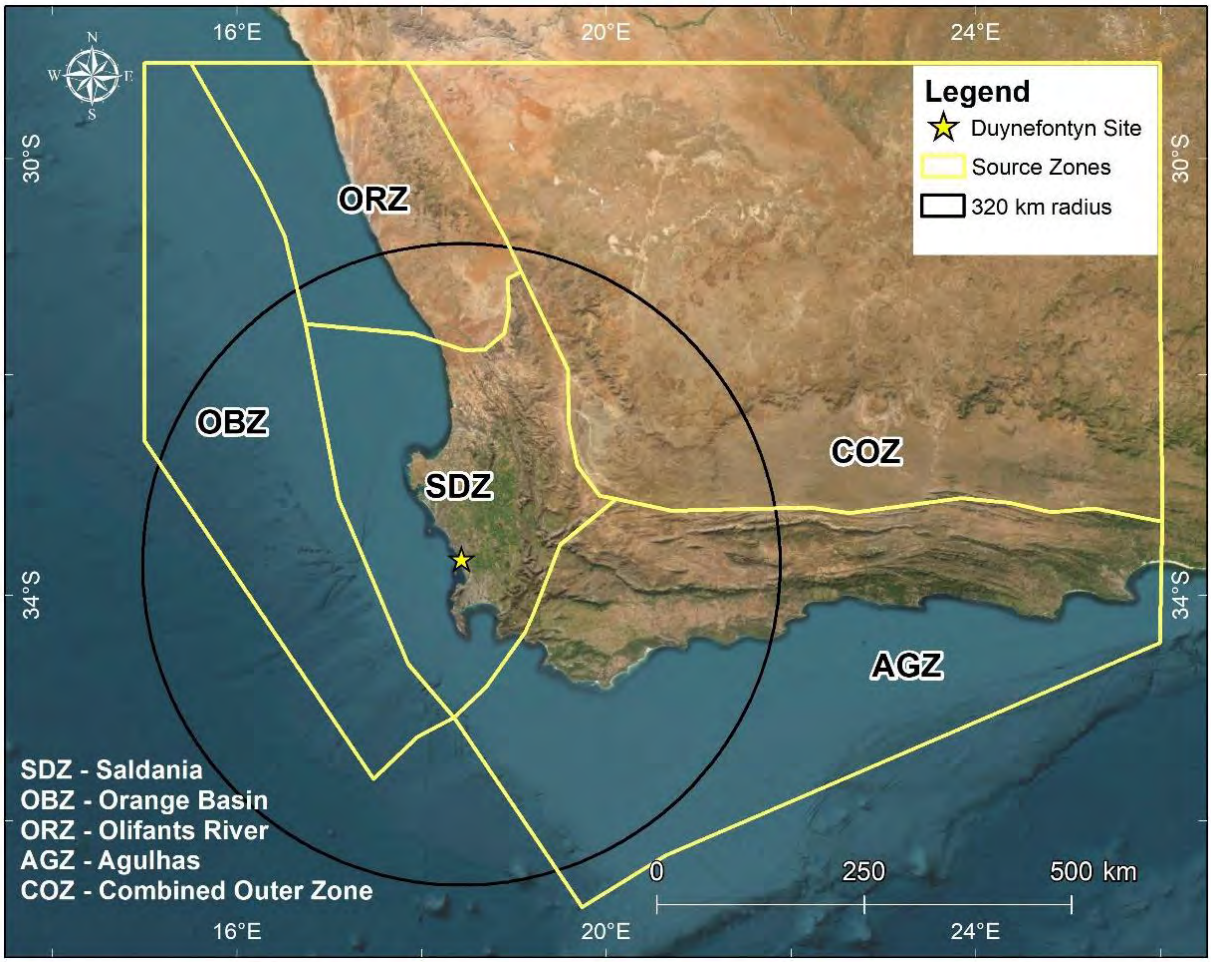

Figure 8-2. Seismic source zones defined in the SSM for the Duynefontyn PSHA.

8.2 CHARACTERISTICS OF FUTURE EARTHQUAKES IN SOURCE ZONES

Once the seismic source zones were established, the SSM TI Team assessed the characteristics of future earthquakes within each zone. Alternative interpretations of future earthquake characteristics are accounted for in the SSM by alternative branches in the logic tree. These alternative branches capture the epistemic uncertainty in the future characteristics of earthquakes in the source zones. Aleatory variability in the future characteristics of earthquakes, which is only included in the development of virtual ruptures as described in Section 8.2.6, is accounted for in the SSM by continuous probability distributions of strike and dip, and are represented by relative frequency distributions (e.g., strike = 135° ± 25°). In PSHA studies, these distributions are most commonly uniform (equally likely within the specified range) or normal (centred on a mean value), depending on the underlying geologic information. Because logic trees, by convention, are intended to represent only epistemic uncertainties and the branches are assessed as mutually exclusive alternatives, aleatory variabilities are not incorporated in the SSM logic-tree. Instead, they are captured through integration over the parameter distributions within the PSHA code. For clarity in this report, aleatory assessments are indicated as such, and the relative frequency of an aleatory variability is given as a percentage within parentheses (35%). Epistemic alternatives are assigned as relative weights by the SSM TI Team and are designated within square brackets [0.35]. Generally, the relative weights are graded in units of [0.05] or larger. Table 8-2 lists nomenclature used by the SSM TI Team in assigning weights to the logic tree branches, which was adopted from Table 3-1of Rodriguez-Marek et al. (2021).

Table 8-2. Nomenclature for subjective weights in the logic tree.

Weights	Verbal Description
1.0/0.0	Certain/Impossible
0.95/0.05	Virtually Certain/Virtually Impossible
0.90/0.10	Highly Likely/Highly Unlikely
0.80/0.20	Very Strong Preference/Cannot Preclude
0.70/0.30	Strong Preference
0.60/0.40	Weak Preference
0.50/0.50	Equally Likely/No Preference

Future earthquake characteristics include seismogenic thickness (Section 8.2.2), spatial stationarity (Section 8.2.3), spatial distribution of earthquakes (Section 8.2.4), rupture characteristics (Sections 8.2.5 and 8.2.6), focal depth distribution (Section 8.2.7), hypocentral depth ratio distribution (Section 8.2.8), maximum magnitude (Section 8.2.9), and recurrence (Section 8.2.10). Selected characteristics that feed into the zone rupture modelling are based on assessment of geologic and tectonic setting (i.e., style-of-faulting, rupture strike and dip) and these are described in Section 8.3 for each source zone.

Figure 8-3 illustrates how the different depth parameters are used in the characterisation of future earthquake ruptures. The extent of the brittle crust in which ruptures can originate is represented by the seismogenic thickness. As discussed in Section 8.2.2, this parameter is typically estimated as the depth above which 90% of the observed earthquakes occur (D90) and its uncertainty is represented by the depths corresponding to the 85% and 95% of seismicity. In the hazard calculations, contributions from earthquakes with magnitudes from the minimum magnitude (m_0) to Mmax (Section 8.2.9) are integrated. For each magnitude, appropriate empirical models linking magnitude to rupture area and the downdip geometry are used to obtain rupture parameters such as rupture length and rupture width (Section 8.2.6). To calculate the distance from the site to the source, the rupture needs to be placed in the volume of brittle crust: this requires a model for the location of the hypocentre within the seismogenic thickness. Details of this model (focal depth distribution) are given in Section 8.2.7. Finally, to determine the depth of the top of rupture (Z_{TOR}), a model representing the relative location of the hypocentre along the width of the rupture plane is needed. The hypocentral depth ratio model presented in Section 8.2.8 is used for this purpose.

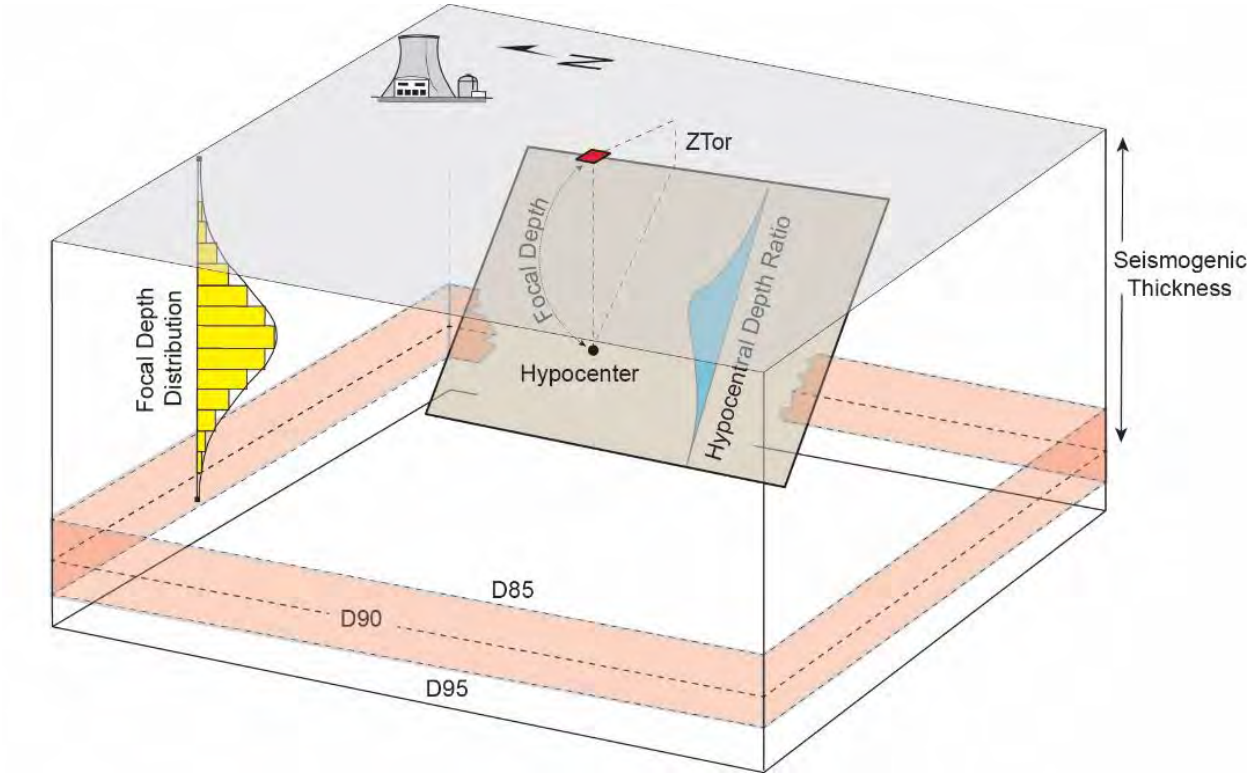

Figure 8-3. Illustration of the depth parameters required to model future earthquake ruptures and their relations. The red square is the epicentral location at the ground surface.

8.2.1 Nature of boundaries with respect to the propagation of future ruptures

In the hazard calculation procedure, finite fault ruptures nucleate on virtual faults within each source zone. The length and area of rupture for each earthquake are related to the magnitude of the earthquake being modelled. Ruptures that nucleate near a source zone boundary can either extend across the boundary (a “leaky” boundary) or be terminated at the boundary (a “strict” boundary) depending on the assessed nature of the boundary. The boundaries for each source zone were defined by the SSM TI Team based on properties related to tectonics, geology, topography, and seismicity. The SSM TI Team’s assessment of “leaky” or “strict”

depended on whether the geology at the source zone boundary precludes propagation of ruptures across it or if the larger magnitude earthquakes in the adjacent source zones are already assigned to known active fault sources. This assessment was made based on the structural fabric of one source zone contrasting or agreeing greatly with that of a neighbouring zone, for example. In addition to structural and geologic arguments to indicate whether a boundary is considered leaky or strict, implications of how ruptures are modelled must also be considered. For example, the truncation of a rupture at a strict boundary can lead to a rupture that is inconsistent with the magnitude-area scaling relationship and, in terms of maintaining seismic moment, would imply very high stress drop.

8.2.2 Seismogenic thickness

Background: Seismogenic thickness is the width of the crust or lithosphere in which most earthquakes originate. In seismic hazard analyses it defines the seismogenic zone, within which future earthquakes will occur. Earthquakes occurring within continental crust are generally confined to the brittle crust and the seismogenic zone is thus indicative of brittle-crust behaviour (Maggi et al., 2000). Spatial variations of seismogenic thickness are gradual and the processes that locally control the seismogenic thickness are poorly understood, although heat flow and the thermal conditions of the crust play an important role in controlling seismogenic thickness.

Physical considerations given by various researchers suggest that the base of the seismogenic zone is a boundary near the deepest levels of the observed earthquake focal depths. For example, Scholz (1988) identifies the 300°C isotherm as corresponding to the onset of dislocation creep in quartz, which he interpreted to control the seismic/aseismic transition zone. Tanaka (2004) and Tanaka and Ito (2002) compared high-quality thermal measurements and seismicity depth data to examine temperature as a fundamental parameter for determining seismogenic thickness. Tanaka and Ishikawa (2002) showed that the crustal seismogenic thickness mostly correlates with surface heat flow and that high geothermal gradient can be associated with shallow seismogenic thickness (Figure 8-4). Tanaka and Ishikawa (2002) compared high-quality gridded heat flow data or geothermal gradient data in Japan for temperatures ranging between 250°C and 500°C with D90, the depth above which 90% of earthquakes occur, and concluded that D90 correlates well with geothermal gradient. The evaluated temperatures for D90 fall within the typical range for defining the seismogenic zone (e.g., Fagereng and Toy, 2011). According to Nazareth and Hauksson (2004), seismogenic thickness is determined using the depth distribution of the seismic moment release. For these reasons, D90 has been used to determine the thickness of the seismogenic crust in many of the recent SSHAC Level 3 PSHA studies, including Hanford (PNNL, 2014) and the Idaho National Laboratory (INL, 2022).

Decision: The SSM TI Team adopted the D90 results (and seismogenic thickness distribution) from the analogous stable continental region setting in the Central and Eastern United States (CEUS) (EPRI/DOE/USNRC, 2012) to define the thickness of the seismogenic crust (Figure 8-5).

Technical Bases: The SSM TI Team evaluated the distribution of earthquake hypocentres within the southern Africa region to determine D90 (as well as D85 and D95, commonly used to capture the uncertainty in D90). The SSM TI Team found that uncertainty of the focal depths within southern Africa varied greatly for both tectonic and mining events. The SSM TI Team

also evaluated heat flow data for the Western Cape to determine whether there was a correlation among earthquake focal depths and the geothermal gradient. However, because of the limited number of reliable focal depth values and geothermal measurements, a clear correlation between geothermal gradient and seismogenic thickness could not be determined.

In the Duynefontyn region there are relatively few earthquakes with well-determined hypocentres, due both to the low levels of seismicity and the rather widely spaced instruments in the national seismic network. Because of the sparsity of data, large uncertainties in hypocentre depths, and limited heat flow measurements, the SSM TI Team adopted the values and their respective weights used in CEUS PSHA (EPRI/DOE/USNRC, 2012). The technical bases for this decision are that: (1) The earthquake focal depth data in the CEUS are abundant and relatively well constrained, and these data were fully evaluated by the CEUS SSHAC Level 3 study (EPRI/DOE/USNRC, 2012); (2) The SSM TI Team considered the CEUS as a reliable analogue for the Western Cape because both areas are stable continental regions, which are defined as regions composed of continental crust that has not experienced any major tectonism, magmatism, basement metamorphism or anorogenic intrusion since the early Cretaceous, and no rifting or major extension since the Paleogene (EPRI, 1994). Based on the categorisation by Wheeler (2016), the TI Team made a conclusion supported by the relative thickness of the crust above the Moho from both CEUS and Western Cape.

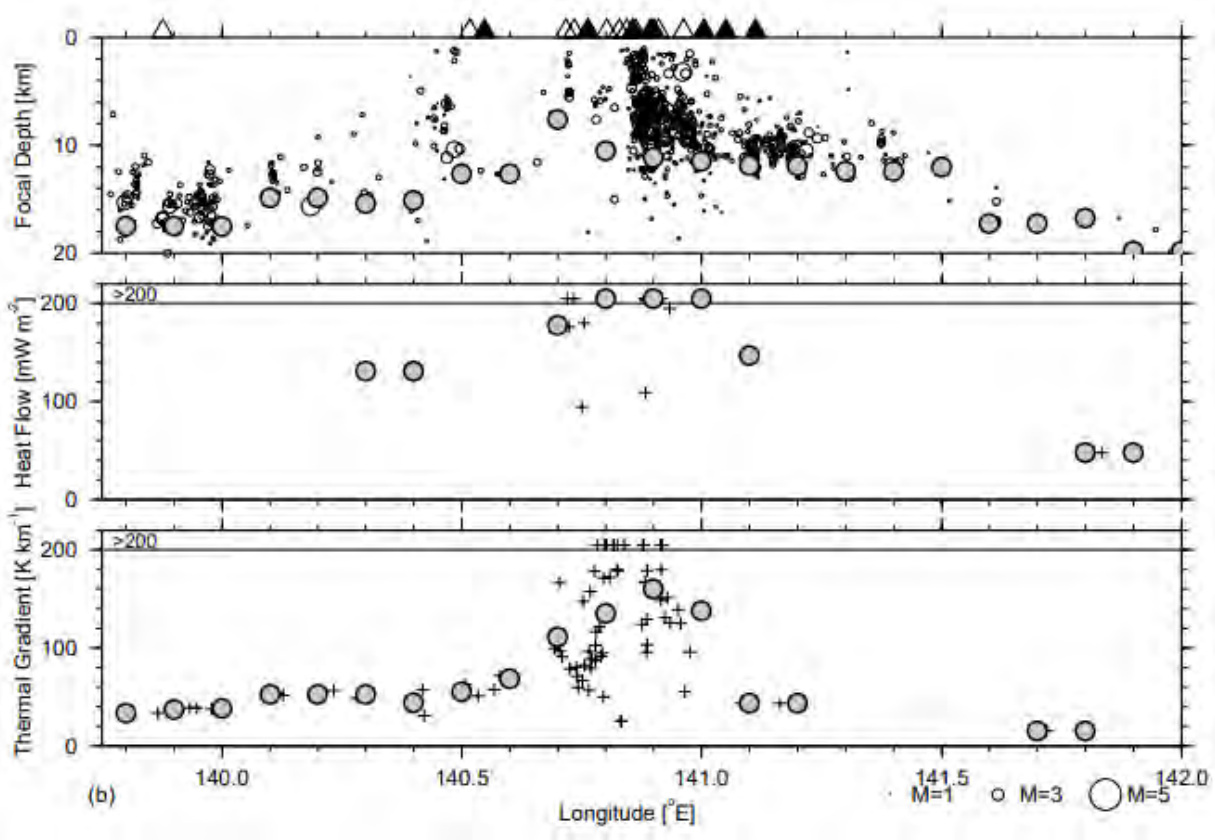

Figure 8-4. Correlation between geothermal gradient, heat flow, and focal depth in Japan (copied from Figure 2 of Tanaka and Ishikawa, 2002).

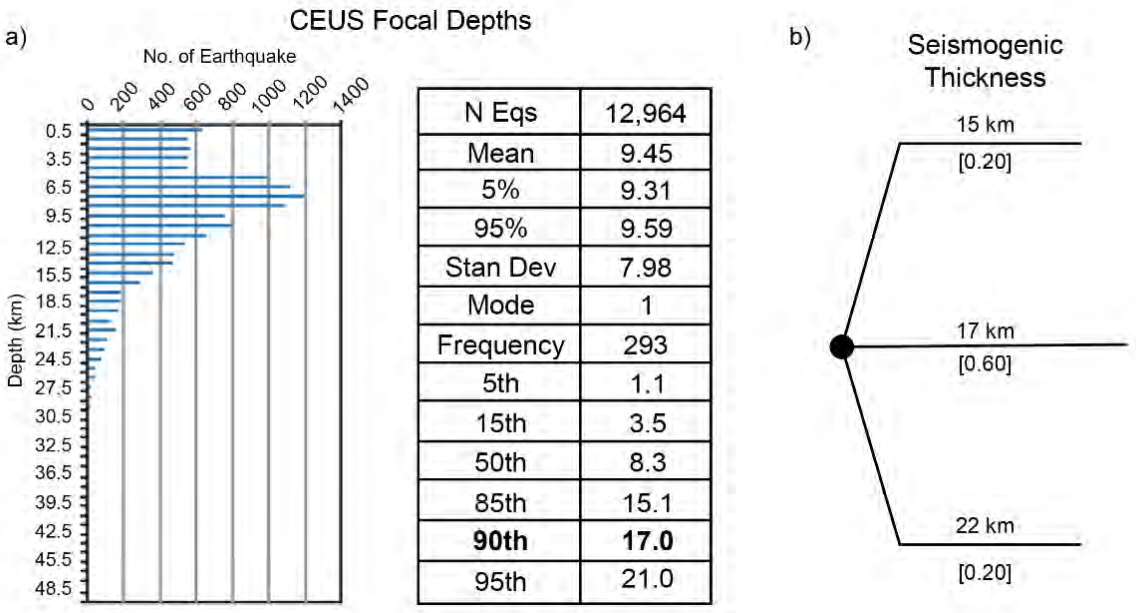

N Eqs	12,964
Mean	9.45
5%	9.31
95%	9.59
Stan Dev	7.98
Mode	1
Frequency	293
5th	1.1
15th	3.5
50th	8.3
85th	15.1
90th	**17.0**
95th	21.0

Figure 8-5. (a) Histogram of seismogenic depth for CEUS earthquakes and table with statistical parameters obtained from the data, showing D85, D90, and D95 values from EPRI/DOE/NRC (2012). (b) Logic tree for seismogenic thickness in the SSM, with depth values and their respective weights adopted directly from EPRI/DOE/NRC (2012).

Evaluation: The SSM TI Team's assessment of seismogenic crustal thickness began with an assessment of the focal depth distributions of well-recorded earthquakes. The SSM TI Team analysed D90 using all the available earthquake data (including mining events and aftershocks) in southern Africa, resulting in D85, D90 and D95 values of 7.0 km, 17.3 km and 24.0 km, respectively, as shown in Figure 8-6a. The SSM TI Team observed that these values are strongly influenced by mining events and aftershocks of the 2017 Moiyabana, Botswana earthquake. The 2017 Moiyabana, Botswana earthquake occurred in the Limpopo Mobile Belt with a focal mechanism consistent with southwestern extension of the East African Rift System (Fadel et al., 2020; Mulabisana et al., 2021; Chisenga et al., 2020). The SSM TI Team decided to remove identified mining events and aftershocks of the Moiyabana earthquake and re-analyse D85, D90 and D95. This resulted in values of 8.7 km, 10.6 km and 15.0 km, respectively, as shown in Figure 8-6b.

As part of the DDC2, some of the events in the Western Cape were re-analysed to better constrain their focal depths. The SSM TI Team determined the seismogenic depth of the Western Cape using the re-analysed focal depths, resulting in D85, D90 and D95 of 6.7 km, 7.0 km and 8.0 km, respectively (Figure 8-7). The SSM TI team determined that a strict alternative with a shallow seismogenic thickness could not be supported because of the 1969 earthquake and many of its aftershocks, which were well recorded, and quite deep. The SSM TI Team also determined that an alternative interpretation with a relatively shallow seismogenic thickness was well represented in the SSM because we adopted a focal depth distribution from the CEUS that has a relatively shallow distribution (see Figure 8-5a). In that focal depth distribution, the majority of focal depths are between 6 and 10 km.

The depth of the 1969 Ceres earthquake was 17.6 km. The 1969 Ceres event depth is consistent with D90 of 17 km assessed from southern African data (Figure 8-6) as well as

CEUS data (Figure 8-5). Smit et al. (2015) analysed 172 microearthquakes ($-1.5<M_L<0.5$) recorded in the Ceres-Tullbagh area during three months in 2012. These earthquakes delineate a zone of microseismicity extending to 15 km. The Smit et al. (2015) analysis supports the minimum seismogenic thickness of 15 km from CEUS data (Figure 8-5).

Dhansay et al. (2017) evaluated the subsurface geothermal gradient in South Africa using temperature data from hot springs and temperature point measurements from wells. The depth of the temperature measurements at the springs was set at 1 m and the depth of temperature measurements from the wells ranged from 0 to 6.083 km. Their evaluation indicated that the Western Cape is has a high geothermal gradient. Following Tanaka and Ishikawa (2002), the Western Cape should be an area with a shallow seismogenic depth. The SSM TI Team correlated the re-analysed focal depths with geothermal gradient from Dhansay et al. (2017) to evaluate whether the heat flow data could support (or refute) a shallow D90 in the Western Cape (Figure 8-8). Unfortunately, the project catalogue does not contain enough events to provide a definitive correlation either way.

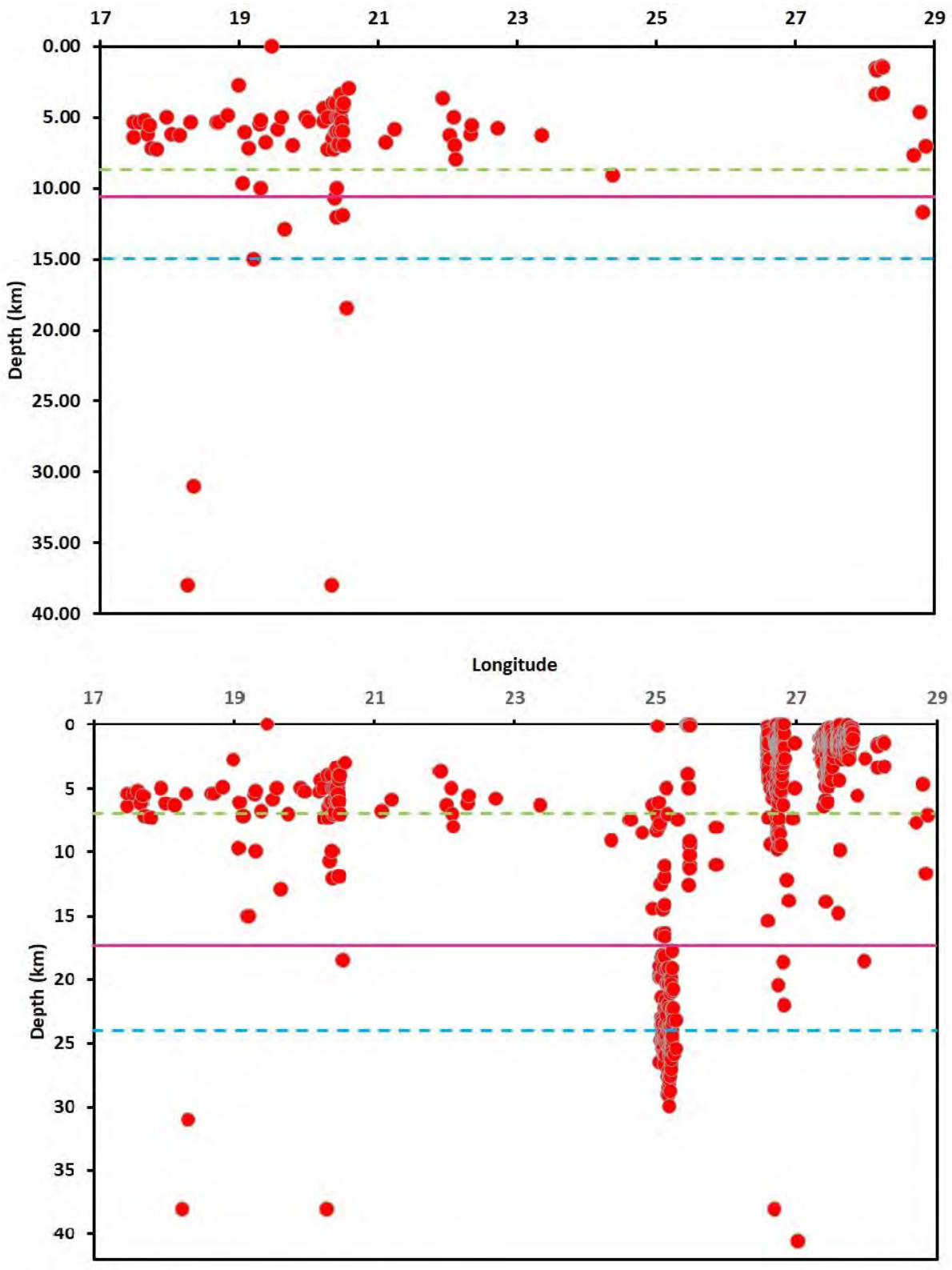

Figure 8-6. (a) D85 (blue dashed line), D90 (solid line) and D95 (green dashed line) assessed from southern African earthquake focal depths. (b) D85, D90 and D95 for southern Africa, excluding mining events and aftershocks of the 2017 Moiyabana, Botswana earthquake.

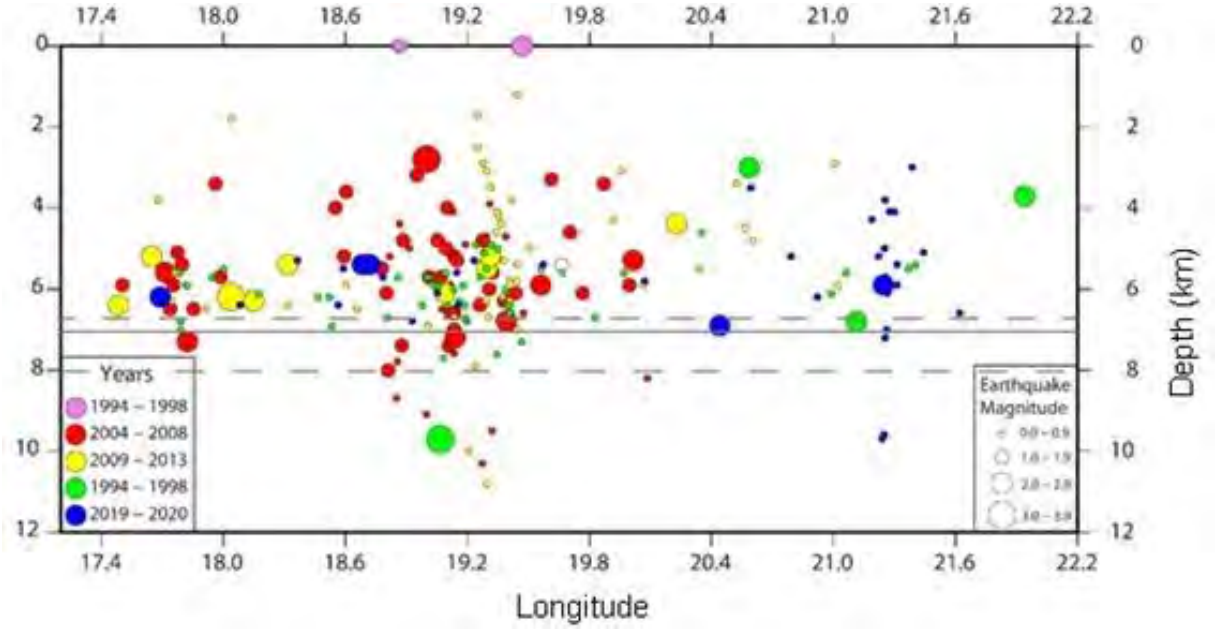

Figure 8-7. D85 (shallow dashed line), D90 (solid line) and D95 (deeper dashed line) assessed from DDC2 re-analysed earthquake focal depths.

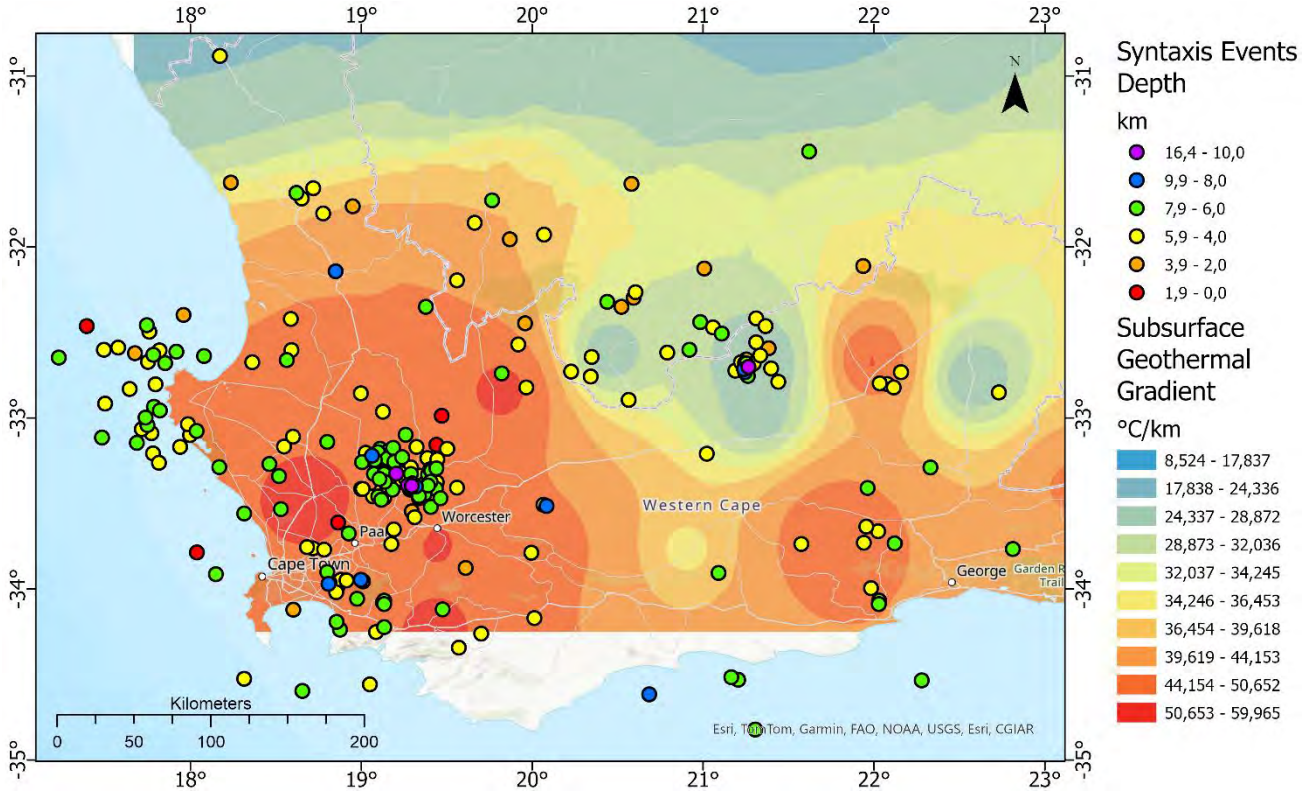

Figure 8-8. DDC2 re-analysed earthquake focal depths overlaying subsurface geothermal gradient per kilometre calculated from heat flow and heat productivity data using principles of thermodynamics by Dhansay et al. (2017).

The SSM TI Team notes that the range of reported geothermal gradients in Dhansay et al. (2017) include many values that are too high to support an assumption of a linear geothermal

gradient. For example, a linear extrapolation of 50°C/km to crustal depths (which is indicated in several locations in Figure 8-8) would suggest crustal temperatures at or above 500°C at a 10km or less. For reference, the USGS calculates that the temperature of the top of the Moho beneath the CEUS ranges between approximately 500°C and 600°C at depths between 30-50 km. (Boyd 2020). The Moho in the Western Cape is between 32 and 44 km deep (Baranov, et al, 2023), thus the SSM TI Team concluded that the high geothermal temperatures recorded in Dhansay et al. (2017) more likely reflect local high heat sources in the upper crust and extrapolating these crustal temperatures based on an assumption of a linear geothermal gradient is not realistic.

8.2.3 Spatial stationarity

Background: The assumption of spatial stationarity in seismic hazard analyses posits that the location of past earthquakes provides a reliable basis for predicting where future earthquakes are likely to occur, at least over the lifetime of the proposed facility (e.g., the next 50 years). This assumption implies that earthquake locations in the background zone are not random (at least within the next 50 years) and that there is a preference for future earthquakes to reoccur in areas where past earthquakes were concentrated. The assumption of stationarity also underlies the concept of earthquake clusters, so long as the clusters are likely to continue long enough in the future to predict areas of higher seismicity within the timeframe of the seismic hazard application. Thus, if stationarity can be established, it provides a technical basis to develop probability density maps that control the spatial distribution of future events in the seismic source model. The assumption of stationarity has been tested and accepted in many of the recent SSHAC Level 3 studies, including Hanford (PNNL, 2014) and the Idaho National Laboratory (INL, 2022). The assumption of stationarity was not applied in the Thyspunt SSHAC Level 3 PSHA (Bommer et al., 2013).

Decision: The SSM TI Team could neither verify nor refute the assumption of stationarity for the source zones in the SSM. Therefore, the SSM TI Team developed two alternative branches in the logic tree (Figure 8-9), one that develops spatial density maps of past earthquakes for predicting the location of future events assuming stationarity, and one that instead applies uniform smoothing assuming that stationarity does not apply. The SSM TI Team applied equal weight to each branch because both alternatives were deemed to be equally likely given the uncertainties in the SSM TI Team analysis.

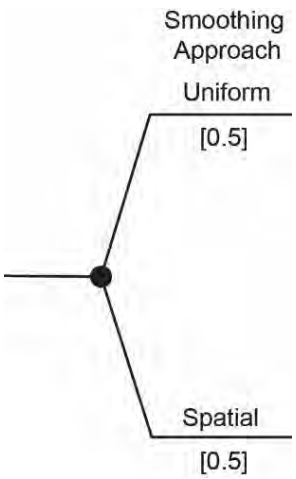

Figure 8-9. Logic tree showing the alterative branches for smoothing.

Technical basis: The SSM TI Team evaluated the location of earthquakes in the project catalogue and the details of recorded earthquake clusters in South Africa to test the stationarity assumption. These evaluations were based on the analysis methods first proposed by Kafka and Walcott (1998) and developed in subsequent analyses (e.g., Levin and Kafka, 1998; Kafka and Levin, 2000; Kafka, 2002; 2007). First, the SSM TI Team tested the hypothesis on the location of the Ceres 1969 event, using events in the catalogue prior the 1969 event as a 'Smaller earthquake catalogue'. The SSM TI Team also tested the hypothesis using only instrumental data, dividing the catalogue into events recorded using older analogue stations and those recorded using newer digital stations. The results of these analyses were inconclusive. While some of the locations of older events seemed to foretell the location of more recent events, there was no obvious correlation between older and younger events in other locations. The SSM TI Team notes that the analysis is hampered by the small sample size of earthquakes in the project earthquake catalogue, especially compared to the rich dataset of earthquakes available in the CEUS study (EPRI/DOE/USNRC, 2012). In addition, the SSM TI Team's analysis of earthquake clusters in Section 6.5 shows that event clusters in South Africa are generally short-lived, on the order of a few years to a decade. Given these observations, the SSM TI Team could not establish or disprove the assumption of stationarity requiring both alternatives and associated epistemic uncertainty, to be captured in the SSM logic tree.

Evaluation: To assess stationarity, the SSM TI Team evaluated the earthquake record in the project catalogue and analysed the data following the methods of Kafka and Walcott (1998), Kafka and Levin (2000), and Kafka (2002, 2007). Kafka and Levin (2000) tested the hypothesis that smaller earthquakes indicate where larger earthquakes are likely to occur. Kafka (2002) conducted a similar study in the CEUS, dividing the catalogue into a 'smaller earthquake' catalogue ranging from 1924 to 1987 with magnitude $M \geq 3.0$; and a 'larger earthquake' catalogue ranging from 1988 to 2001 with $M \geq 4.5$. They concluded that 91% of future earthquakes from the 'larger earthquake' catalogue are located in the areas predicted by the 'smaller earthquake' catalogue (Figure 8-10).

The SSM TI Team evaluated recorded earthquakes in South Africa following the analysis method of Kafka and Levin (2000) by dividing the catalogue into different time periods and two different magnitude ranges. These were then used in a test similar to the Kafka (2002) analysis by considering two different radii around the earthquake locations to test for possible correlations (25 km and 50 km). The first evaluation was based on the 1969 Ceres earthquake (Figure 8-11). The SSM TI Team tested the hypothesis of the location of the 1969 earthquake by dividing the catalogue into a 'smaller earthquake' catalogue ranging from 1690 to 1968 with events magnitudes $2.6 \leq E[\mathbf{M}] \leq 6.2$ and a 'larger earthquake' catalogue ranging from 1969 to 2021 with events magnitudes $4.0 \leq E[\mathbf{M}] \leq 6.1$.

The SSM TI Team also evaluated the instrumental portion of the Western Cape data by dividing the catalogue into events recorded using analogue stations and those recorded using digital stations (Figure 8-12). Thus, using the 'smaller earthquake' catalogue ranging from 1971 to 1991 with events magnitudes $1.5 \leq E[\mathbf{M}] \leq 5.8$ and the 'larger earthquake' catalogue ranging from 1992 to 2021 with events magnitude $3.5 \leq E[\mathbf{M}] \leq 5.9$ with radius criteria of 25 km and 50 km to test stationarity.

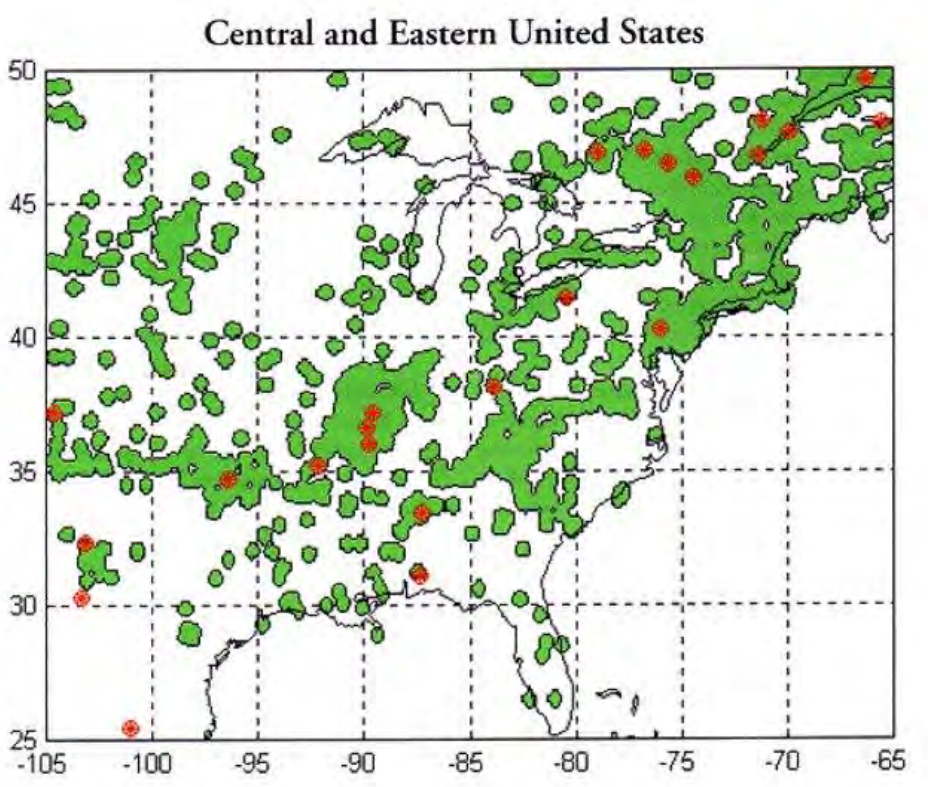

Figure 8-10. Kafka (2002) test on the stationarity hypothesis in CEUS. Green shading is the 'smaller magnitude' catalogue ranging from 1924 to 1987 with magnitude M ≥ 3.0; and red shading is the 'larger earthquake' catalogue ranging from 1988 to 2001 with M ≥ 4.5.

The results from both analyses are equivocal. For the case shown in 8-11a, the area created by drawing a 25 km radius around the 1690-1969 earthquakes appears to capture about half the earthquakes that occurred in the Ceres cluster. For the case shown in 8-11b, the area created by drawing a 50 km radius appears to capture nearly 75% of the Ceres cluster, although these larger radii circles also cover almost half the study area. The SSM TI Teams make a similar observation for the two options shown in Figure 8-12, in which earlier smaller earthquakes that occurred prior to 1992 were used to predict the location of slightly larger earthquakes that occurred between 1992 till 2021. Based solely on these observations the SSM TI Team deemed the results to be inconclusive. The SSM TI Team felt that two factors contributed to this uncertainty. First, unlike the Kafka and Levin (2000) analysis, recorded seismicity in the Western Cape is sparse and the data set of earthquakes in the project catalogue is limited compared to the data for the CEUS. Second, the short-lived nature of earthquake clusters in South Africa, as described in Section 6.5, means that even if subsequent earthquakes occur near earlier events, these last only a few years. For the assumption of stationarity to be applicable to seismic hazard analyses, these spatial correlations need to occur over tens of years or more, consistent with the engineering lifespan of the facility.

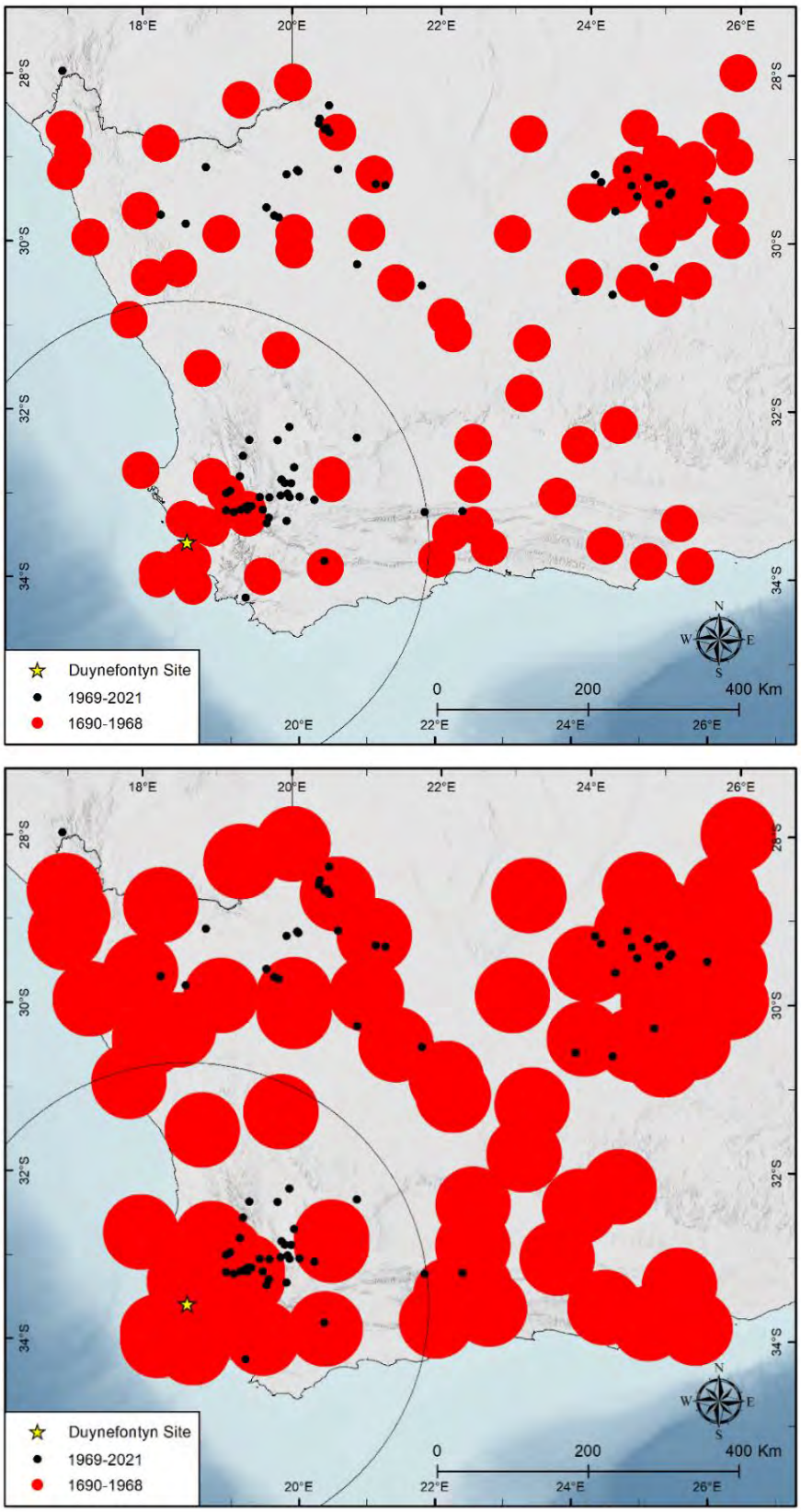

Figure 8-11. Stationarity hypothesis test on the Western Cape catalogue. Red shading is the 'smaller magnitude' catalogue ranging from 1690 to 1968 with events magnitudes 2.6 ≤ M ≤ 6.2 and 25 km (upper) or 50 km (lower) capture radius. Black circles are the 'larger earthquake' catalogue ranging from 1969 to 2021 with events magnitudes 4.0 ≤ M ≤ 6.1.

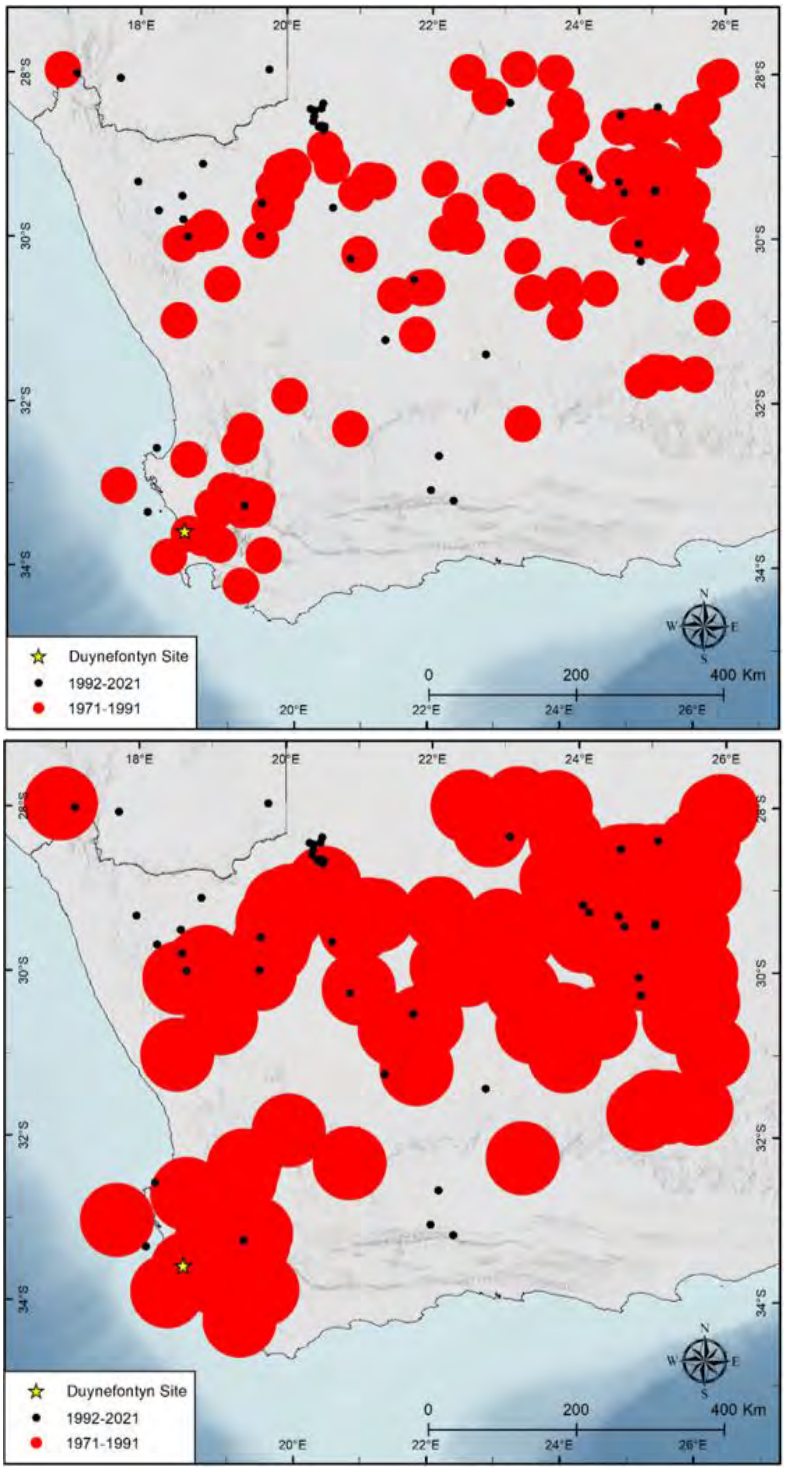

Figure 8-12. Stationarity hypothesis test on the Western Cape catalogue. Red shading is the 'smaller magnitude' catalogue ranging from 1971 to 1991 with events magnitudes 1.5 ≤ M ≤ 5.8 and 25 km (upper) or 50 km (lower) capture radius. The black circles are the 'larger earthquake' catalogue ranging from 1992 to 2021 with events magnitude 3.5 ≤ M ≤ 5.9.

8.2.4 Spatial distribution of earthquakes

Background: The spatial distribution of earthquakes is an important characteristic to capture in the SSM, as it defines where future events are more likely to occur. A uniform spatial distribution means that future earthquakes are equally likely to occur anywhere in a zone or

area. The uniform spatial distribution is often used where sparse data or low regional rates of seismicity are not sufficient to evaluate spatial stationarity. It represents the maximum entropy distribution because it maximises the uncertainty in location of future earthquakes within a zone. If spatial stationarity is assumed, that is the location of current and past seismicity is assumed to be a good indicator of the location of future seismicity, then spatial smoothing algorithms may be implemented to model the signature of seismicity rate concentrations. The following are available methods for spatial smoothing:

- Fixed kernel (Frankel, 1995).
- Adaptive kernel (Stock and Smith, 2002; Werner et al., 2011).
- Penalised maximum likelihood (EPRI/DOE/USNRC, 2012).

Each of the spatial smoothing methods uses an input earthquake catalogue with a minimum magnitude threshold. Although alternative smoothing operators can be implemented, a Gaussian operator that determines the shape of the distribution is typical in seismic hazard studies.

The kernel bandwidth defines the amount of smoothing that occurs. A smaller bandwidth keeps the density concentrated closer to the earthquake epicentre, implying higher confidence that future earthquakes are likely to be located where past earthquakes have occurred. Conversely, a larger bandwidth distributes density more widely and implies lower confidence in future events concentrating in the areas that have experienced past earthquakes.

The fixed kernel method uses a singular kernel bandwidth applied to all earthquakes, while the adaptive method allows the bandwidth to adjust based on the relative density of events, so that it will be smaller in areas with a high density of earthquakes, and larger in areas of more sparse seismicity. These two kernel bandwidth methods can be implemented using a "zone-less" approach, where smoothing is performed disregarding the source zone boundaries shown in Figure 8-2.

The penalised maximum likelihood method allows variation of both activity rate per unit area and *b*-value within modelled source zones, as described in EPRI/DOE/USNRC (2012). A limitation of the penalised likelihood method is its implementation with consideration of areal source zones, where zone-specific recurrence parameters are developed as part of the analysis. This method also results in harsh edge effects at seismic source zone boundaries because the density smoothing is not allowed to cross those boundaries to other zones.

Decision: The SSM TI Team decided on the following, as depicted in Figure 8-13:

- Include uniform density and smoothed spatial density methods, each with an equal weight.
- For spatial smoothing:
  - Use fixed kernel and adaptive kernel smoothing methods with equal weight because the SSM TI Team considered both alternatives to be equally likely.
  - For the fixed kernel method, use a kernel bandwidth of 100 km.

The description of the SSM TI Teams technical bases for the completeness methods branch and location of the 11 September 1969 earthquake branch are discussed in Section 6.9 and Section 4.3.9, respectively.

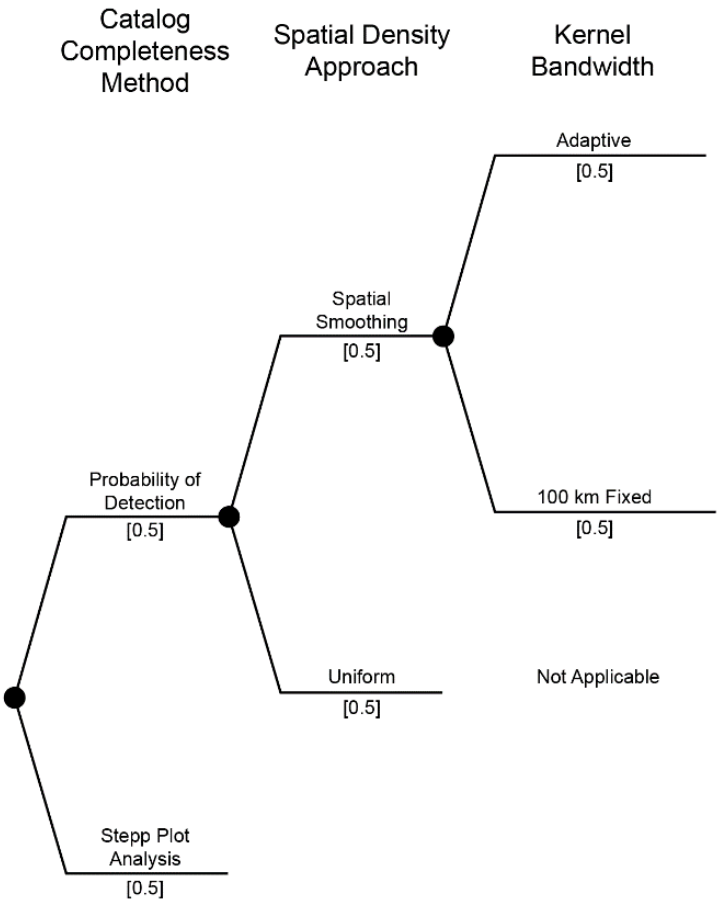

Figure 8-13. Logic tree for spatial density and catalogue completeness methods.

Technical Basis: The SSM TI Team included both uniform and smoothing spatial density models after evaluation of stationarity within the project region, as described in Section 8.2.3. The two spatial smoothing methods were selected to represent similar levels of confidence in the ability to model future earthquake locations from the current spatial concentration of seismicity across the project region and given significant uncertainty in the locations of the larger magnitude events. Specifically, the uniform density model represents the maximum entropy distribution (maximum uncertainty), whereas the spatial smoothing represents some confidence that the current distribution of seismicity is indicative of future earthquakes location. Considering the uncertainties discussed in Section 8.2.3, the SSM TI Team concluded that the application of uniform and smoothed seismicity should be equally weighted.

Many techniques are available to spatially smooth the distribution of earthquakes in a region. To select the appropriate techniques, the SSM TI Team closely examined the characteristics and pattern of seismicity in the project region (Figure 8-14). Although the project site is located centrally within the host zone, there is clustering of seismicity to the southwest and northeast of the site. In particular, a set of events located roughly 100 km northeast of the project site are also within 50 km of the host zone boundaries. The SSM TI Team's position is that the seismicity occurrence in this area should not be cut off and separated from neighbouring areas, as would occur with a method that spatially smooths zone-by-zone such as the penalised maximum likelihood method. Therefore, the SSM TI Team elected not to implement the penalised maximum likelihood spatial smoothing method.

The SSM TI Team concluded that the application of an adaptive smoothing technique or a fixed kernel with bandwidth of 100 km implies varying levels of confidence in the accuracy of earthquake locations in the catalogue, particularly for the pre-instrumental and early instrumental records. A 100-km bandwidth fixed kernel implies less confidence in the accuracy of earthquake locations in the catalogue compared to the adaptive smoothing technique. The SSM TI Team evaluated these two models as equally possible and thus assigned them equal weights.

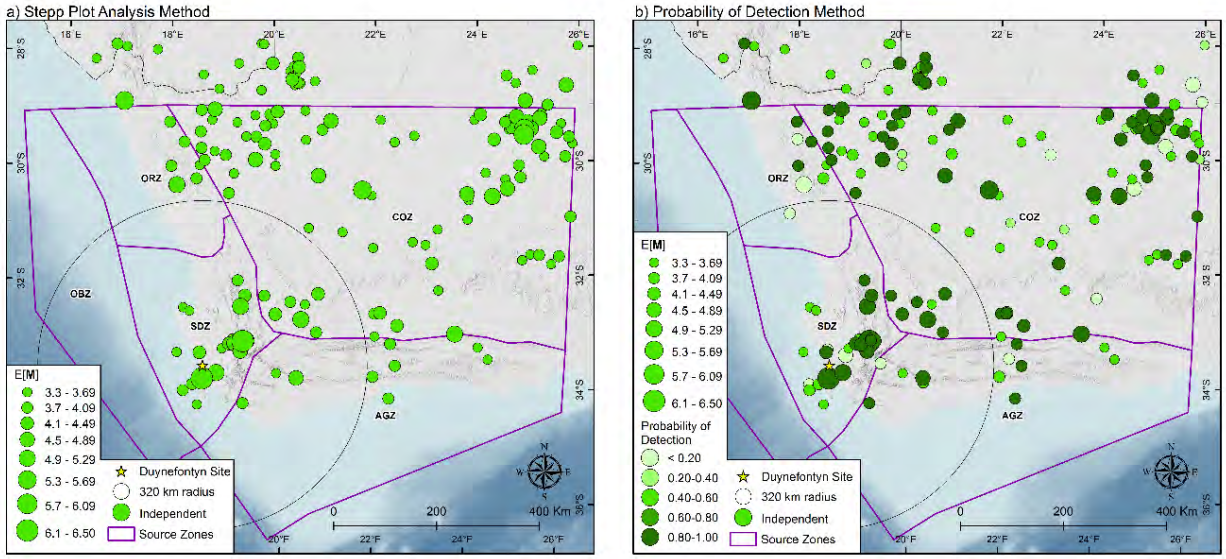

Figure 8-14. Map showing the location and magnitudes of the earthquakes in the final project catalogue used for smoothing analysis. Map (a) for the Stepp plot analysis completeness method catalogue and (b) for the probability of detection completeness method catalogue.

Evaluation: The fixed kernel and adaptive kernel smoothing methods were assessed for applicability to the project catalogue and tested to evaluate the most appropriate input parameters for each method. Consistent with other analyses of the earthquake catalogue (Sections 6.8, 8.2.10), the SSM TI Team chose a magnitude of E[**M**] 3.3 as the minimum to include for event counts.

Fixed kernel smoothing

The fixed kernel smoothing method used a Gaussian smoothing operator and constant kernel bandwidth of 100 km (Figure 8-15). Using a kernel bandwidth of 100 km assumes that there is a large amount of uncertainty in each earthquake location, such that the density is spread over a larger area. As discussed in Section 4.3, uncertainty in the location of historical earthquakes in the project catalogue can be as high as 230 km. Kernel sizes range from 26 to 80 km for adaptive kernel smoothing, as described in the following paragraphs. The fixed kernel size of 100 km, being larger than the range of adaptive smoothing kernel sizes, provides differentiation between the two types of spatial smoothing and is necessary to capture the range of uncertainty in historical earthquake locations. Contours in Figure 8-15 show that the fixed kernel size of 100 km is distinct from the uniform distribution alternative.

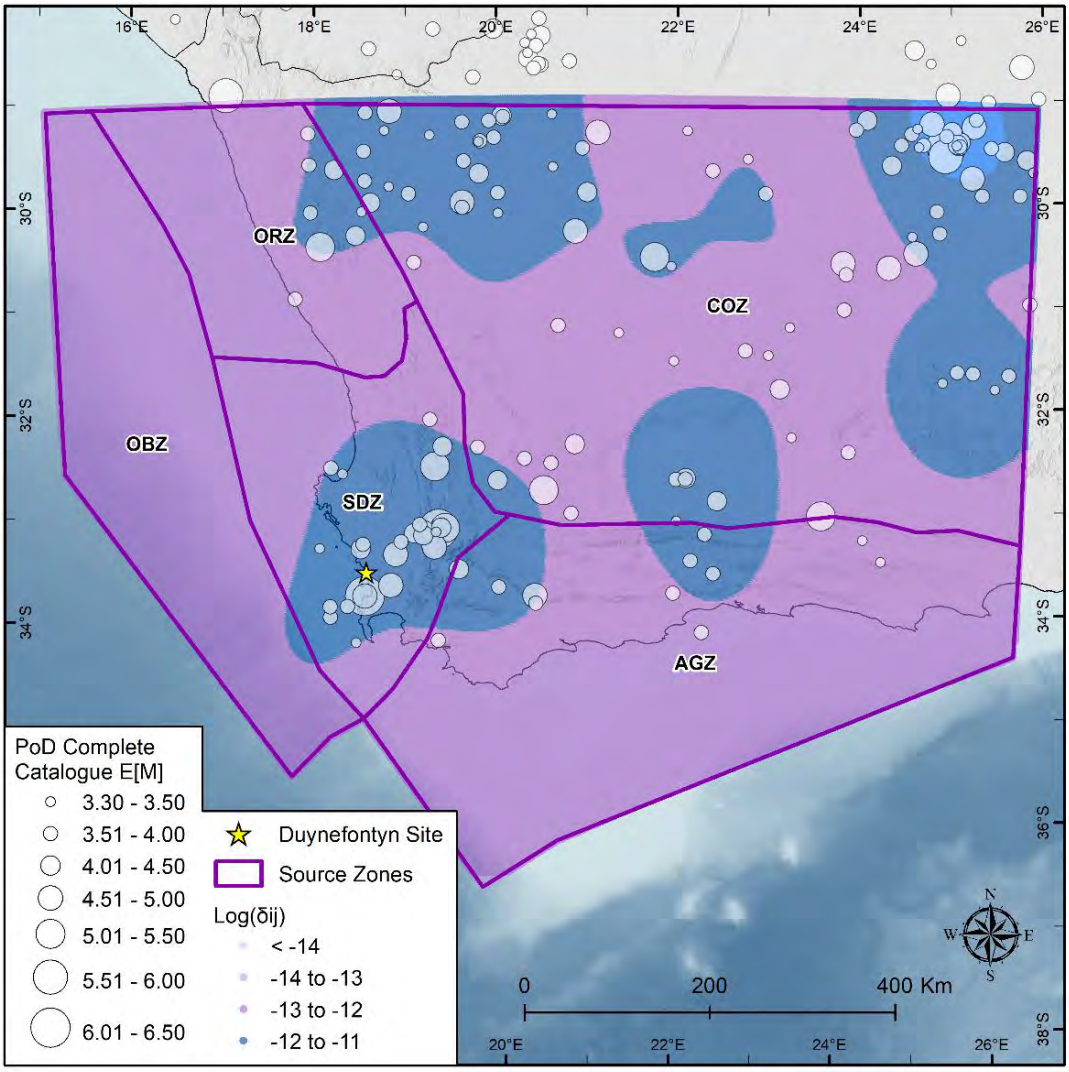

Figure 8-15. Spatial smoothing using fixed kernel bandwidth of 100 km, for PoD – probability of detection completeness catalogue, δ_{ij} is the density of earthquakes assigned to each 0.02° x 0.02° cell.

Adaptive kernel smoothing

The adaptive kernel smoothing method used in this project is that of Stock and Smith (2002). The method is a two-step process: in the first step an initial kernel bandwidth (*h*) size is determined using a maximum likelihood estimator of all earthquakes with E[**M**]≥3.3. Tests are initially conducted for possible values of *h* ranging from 0 to 100 km with 20 km increments to find the value that maximises the log-likelihood according to the procedure in Silverman (1986). Tests are then repeated narrowing the range of *h* values and reducing the increment to refine the assessment of the initial *h*. The evaluation resulted in initial bandwidth sizes of 44 km for all earthquakes. In the second step, the initial bandwidth is adjusted using the complete, declustered earthquake catalogue, decreasing the kernel size in areas of higher data density, and increasing the size in areas of sparse seismicity. Results were obtained using alternative catalogue completeness estimates. The resulting kernel sizes range between approximately 26 km for earthquakes located in regions with denser seismicity and approximately 80 km for earthquakes in areas of sparse seismicity (Figure 8-16).

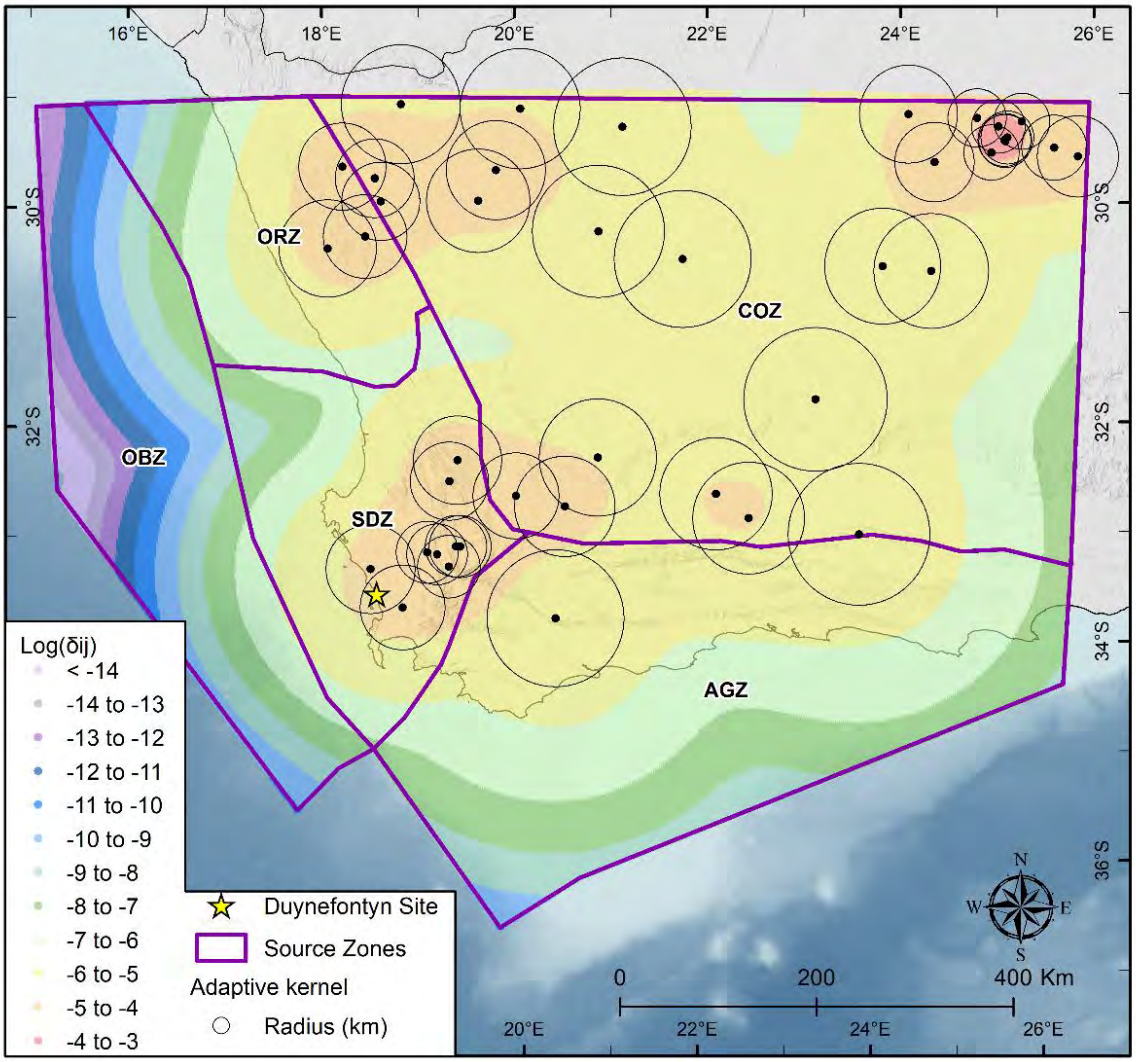

Figure 8-16. Spatial smoothing using the adaptive kernel method. δ_{ij} is the density of earthquakes assigned to each 0.02° x 0.02° cell.

8.2.5 Point sources and virtual ruptures

Background: Modern GMPEs typically use source-to-site distance metrics based on extended ruptures. The SSM TI Team must then characterise future earthquake ruptures generated in distributed seismicity zones in terms of faulting style, strike, dip, and size (magnitude-dependent). The relative frequency of faulting styles is needed to accurately represent point sources or virtual ruptures in the GMM; faulting styles are captured as an aleatory variability. For example, in the SSM, the host zone is characterised by strike-slip faults (80%) and normal faults (20%) that capture the statistical distribution of faulting styles in that zone. The distribution of faulting styles within each source zone is determined by the SSM TI Team from focal mechanisms of past earthquakes, geologic maps, cross-sections of the existing structural fabric, and 3DStress™ analyses that identifies the most likely fault orientations and styles-of-faulting given the current tectonic regime. Descriptions of the information available is provided in Chapters 4 and 5.

As demonstrated by Bommer and Montaldo Falero (2020) the computational effort of simulating these ruptures for each earthquake scenario in the hazard calculations may be

unnecessary beyond a certain distance from the site, because the loss of accuracy introduced by modelling the individual earthquake scenarios as point sources rather than as extended ruptures is usually sufficiently small to allow the distance metric in the GMPEs to be treated as epicentral or hypocentral distance.

Decision: The SSM TI Team modelled future earthquake ruptures in the host zone (SDZ) as extended virtual ruptures, while ruptures in the other source zones are modelled as point sources.

Technical Bases: Bommer and Montaldo Falero (2020) demonstrate that beyond a certain distance from the site and depending on the relative activity rates in the host zone versus distant source zones, the point source approximation should be acceptable in a site-specific hazard study. They indicate that sensitivity analyses should be conducted to verify this assumption. Provided that the assumption is confirmed by sensitivity analyses, there are at least three advantages to the use of the point source approximation in site-specific PSHA. First, the SSM TI Team does not need to characterise future rupture characteristics for distant sources. Second, the hazard computations are less intense. Third, the possibility of large earthquake ruptures extending beyond the borders of a distant source zone towards the site is avoided. Such ruptures, albeit rare, could artificially increase the hazard at the site unless the model specifically prohibits those scenarios (e.g., by imposing non-leaky boundaries or by imposing rupture orientations).

Using the recommendations in Bommer and Montaldo Falero (2020), a sensitivity analysis was conducted to verify the effect of using point sources instead of virtual ruptures in the AGZ zone. This zone is the nearest zone to the site bordering the host zone and would include rupture orientations favourable to extending ruptures toward the site. Therefore, if the sensitivity results indicate that the effect of point source approximation on hazard is negligible, the same conclusion can be extended to the remaining source zones that are farther away.

Evaluation: The results are shown in Figure 8-17 for the AGZ zone at T=0.01 and 1s (100 and 1 Hz). The point source approximation results in a difference in hazard space of 1% or less. The SSM TI Team evaluated the effect of the point source approximation as negligible and decided to model extended ruptures only in the SDZ (host) zone.

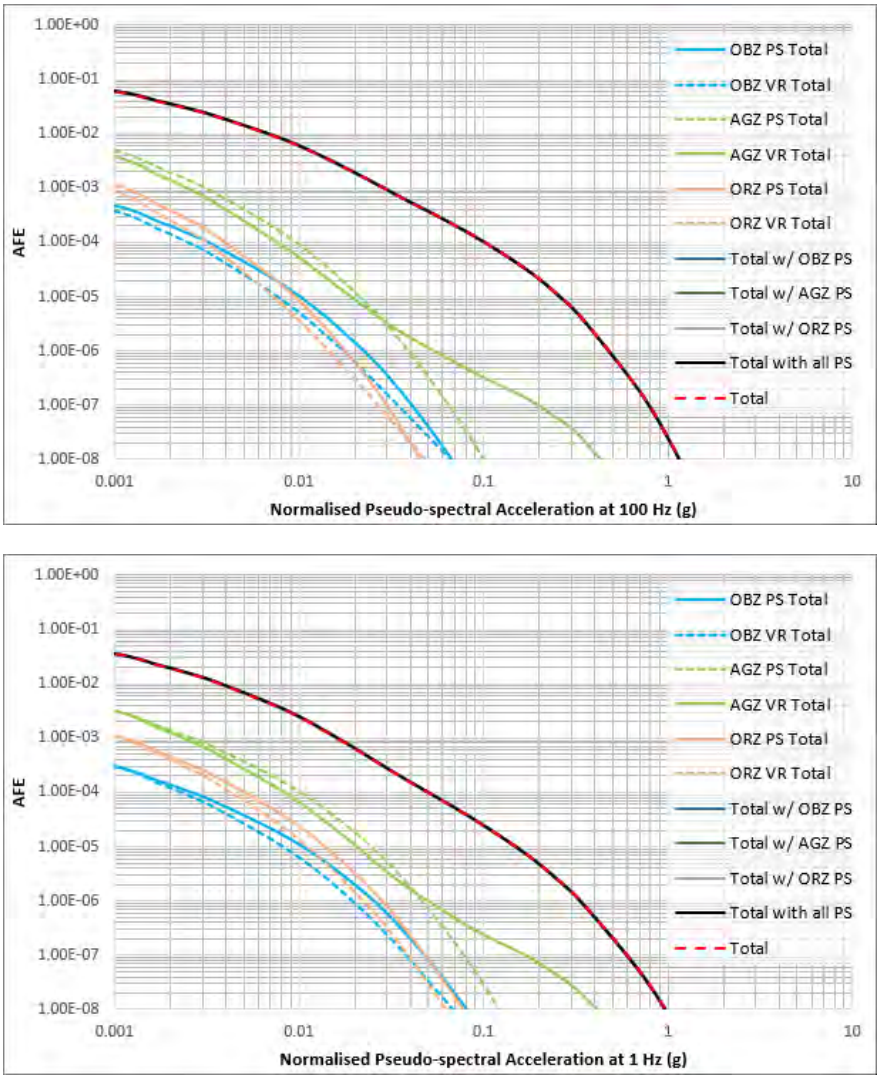

Figure 8-17. Point source approximation sensitivity test results at 100 and 1 Hz, showing minor differences in source contribution between point source (PS) and virtual rupture (VR) estimations. Note that the shape of the AGZ VR curves at long return periods is due to unrealistic rupture lengths produced by the preliminary rupture generator, and that this artifact has been corrected in subsequent versions of the generator.

8.2.6 Modelling extended virtual ruptures in SDZ

Background: The parameterisation of extended virtual ruptures requires multiple inputs: the geometry of the rupture planes, their size (rupture area and aspect ratio), and models for the location of the rupture at depth (seismogenic thickness, focal depth distribution, hypocentral depth ratio). The geometric characteristics of faults (strike, dip, and rake) are defined in Section 8.4.1, while seismogenic thickness is defined and discussed in Section 8.2.2. Focal depth distributions, and models for the location of the hypocentre within the rupture (hypocentral depth ratio distributions) are presented in Sections 8.2.7 and 8.2.8, respectively. The following discussion introduces empirical models for estimating rupture area based on magnitude and models for rupture aspect ratio.

Decision: The SSM TI Team modelled the size of future virtual ruptures in two ways, one by including a model for rupture area (RA) and aspect ratio (AR), and one by including Stafford (2014) models for rupture area and rupture width (Figure 8-18).

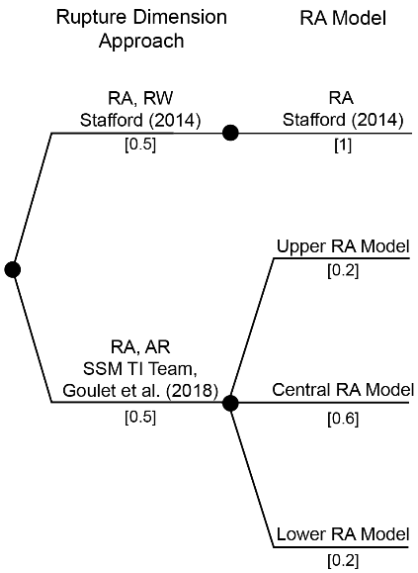

Figure 8-18. Logic tree implementation of the rupture dimension approach for virtual ruptures.

Technical Basis: The SSM TI Team included these two approaches to account for epistemic uncertainty. One rupture dimension approach (Figure 8-18) includes alternative models for rupture area (RA) and uses a rupture aspect ratio, modelled using the Goulet et al. (2018) style-of-faulting dependent model, to compute the rupture width, until the seismogenic thickness is reached. When this rupture dimension approach is selected, there is epistemic uncertainty in the rupture area model, which is represented by a weighted average of applicable magnitude-rupture area relationships and the incorporation of epistemic uncertainty. The magnitude-rupture area relationships used to obtain the weighted average RA model are those of Leonard (2014), Hanks and Bakun (2002, 2008), Wells and Coppersmith (1994), and Thingbaijam et al. (2017). The technical basis for the weights assigned to these models is provided below:

- Leonard (2014) and Hanks and Bakun (2002, 2008) each receive a weight of 0.1 because the models are inverted from the published equations, which did not use orthogonal regression, which introduces a bias.
- Wells and Coppersmith (1994) is weighted 0.3 because this model provides separate equations for estimating magnitude from rupture dimension and rupture dimension from magnitude.
- The highest weight (0.5) is given to the Thingbaijam et al. (2017) because it is the only scaling relationship based on seismic source inversion of well-recorded earthquakes. Thus, estimates of seismic moment and rupture area from Thingbaijam et al. (2017) were considered by the SSM TI Team to be well resolved compared to those derived from other published magnitude-scaling relationships.

The uncertainty in RA model is obtained by enveloping the four magnitude-rupture area relations. The weighted average RA model and its uncertainty in the second node of Figure 8-18 receive weights consistent with a 3-point approximation for continuous random variables (Keefer and Bodily, 1983).

The second rupture dimension approach (top branch in Figure 8-18) implements the equation for rupture area from Stafford (2014), which incorporates seismogenic thickness and dip, and

computes rupture width from the linear model in Stafford (2014) until the seismogenic thickness is reached.

The technical basis for the first node of the logic tree in Figure 8-18 is that the SSM TI Team concluded that both rupture dimension approaches were equally likely to be physically possible given the current debate in the seismological research community and therefore given the same weight. For example, in the third Uniform California Earthquake Rupture Forecast (UCERF) model (Field et al., 2014), fault segments are allowed to rupture simultaneously on overlapping fault segments leading to very long rupture lengths (> 500 km) with highly elongated rupture aspect ratios (25:1). However, based on numerical simulations of strike-slip faulting and an energy balance criterion near rupture tips, Weng and Yang (2017) showed that strike-slip faults fall into two categories, those with bounded rupture dimensions (less than or equal to approximately 8:1) and those with highly elongated aspect ratios (between 20:1 and 30:1). According to their simulations, there is a critical seismogenic width that controls this difference. For seismogenic widths smaller than the critical width, there are no “breakaway” ruptures (i.e., unbounded ruptures), and the rupture may become self-arresting. On the other hand, if the seismogenic width is larger than the critical width, the rupture can “breakaway”, leading to high aspect ratios. In all cases highly elongated rupture dimensions are only a concern for earthquakes with **M**>7. As shown in the evaluation below, both rupture dimension approaches yield similar results for all strike-slip earthquakes with **M**≤7.0.

Evaluation: The PSHA software models extended virtual ruptures as rectangular features with size dependent on magnitude. Many empirical relationships that relate rupture area (RA) to magnitude are available in the literature and take the general form:

8-1

$$\ln(RA) = c_0 + c_1 \boldsymbol{M}$$

Where c_0 and c_1 are coefficients of the relationship. The aspect ratio (AR) of ruptures, that is rupture length divided by rupture width, is defined by a model in the form:

8-2

$$AR = max(1, asp_1 + asp_2 \boldsymbol{M})$$

Where asp_1 and asp_2 are coefficients of a linear model.

In PSHA codes, the rupture width (RW) is usually computed from RA and AR as follows:

8-3

$$RW = \min\left(\sqrt{\frac{RA}{AR}}, RW_{max}\right)$$

where RW_{max} is the maximum rupture width obtained dividing the seismogenic thickness by sin(dip). The rupture length is then calculated as:

8-4

$$RL = \frac{RA}{RW}$$

Table 8-3 lists the published empirical scaling relationships that were evaluated by the SSM TI Team and their main characteristics. As evidenced in the table, some of the publications do not offer new relationships (i.e., Shaw, 2013; Stirling et al., 2013; Hanks and Bakun, 2014), while others present scaling relationships that are not applicable due to the very different tectonic setting (i.e., Yen and Ma, 2011) or because they are limited to a single style-of-faulting (i.e., Hanks and Bakun, 2002, 2008; Ellsworth, 2003).

Table 8-3. Empirical magnitude scaling relationships evaluated by the SSM TI Team.

Scaling Relationship	Tectonic Setting	Mag.	Fault Style[1]	Parameters in Relation to M_W	Comments
Wells and Coppersmith (1994)	Excludes subduction and oceanic slab events	**M**5.5+	SS, R, N, All	SRL, RLD, RW, RA, Dmax, Davg	SCR regressions for RA differ at 95% significance level. Used Ordinary Least Squares regression.
Hanks and Bakun (2002, 2008)	Continental strike-slip	**M**5-8.25	SS	RA	Bilinear source-scaling based for area > 537 km^2. In 2008 seven strike-slip earthquakes were added but the relationship did not change.
Ellsworth (2003)	Large magnitude SS faults	**M**5.55-8.1	SS	RA	Different equation for Area > 500 km^2. Compilation of several previous studies
Wesnousky (2008)	Active continental	**M**6.25-8	All	L	Linear scaling for large surface rupturing earthquakes with lengths greater than 15 km.
Leonard (2010)	All	For SCR, **M**5.5+	DS, SS, SCR	RA, RLD, SRL	Same data as Wells and Coppersmith (1994). Imposes a model rather than uses the empirical data directly.
Yen and Ma (2011)	Compressional - Taiwan collision zone	**M**4.6 - 8.9	DS, SS, All	Davg, RLD, RW, RA	Moment: two trends of scaling if seismic moment is less than/greater than 10^{20} Nm
Shaw (2013)	Transpressional Active Tectonics – California	~**M**5 - 8	All	RA, SL	Constant stress-drop and tri-linear scaling. Does not present new equations but compares previous studies.

Scaling Relationship	Tectonic Setting	Mag.	Fault Style[1]	Parameters in Relation to M_W	Comments
Leonard (2014)	Includes stable continental crust (SCR) DS and SS faults	Data are Mw 3.9 - 7.6	SCR, DS, SS	Davg, RL, W, RA, SRL	Updates earlier work (Leonard, 2010, 2012). Interplate relationships not included.
Hanks and Bakun (2014)	Continental strike-slip	**M**5-8.25	SS	RA	Constant stress-drop scale for **M** <6.5; RLD relationship elsewhere. No new relationships provided
Somerville (2014)	Stable continental regions	Mw 4.5-7.7	All	RA	Same as Somerville (2011). Constant stress-drop, concludes that Leonard (2010) is recommended for use with NGA East.
Thingbaijam et al. (2017)	Continental settings and subduction	Mw 5.4-9.2	SS, R, N, Subd	RA, RLD, RW	SCR events are not used in the data set but are still applicable. Used Orthogonal Regression.
Stafford (2014)	NGA-West 2 data set + Hanks and Bakun (2002 and 2008)	Mw 5-8	All	RA, RW	Develops equations consistent with PSHA assumption for maximum width.

Key: SS = strike-slip, R = reverse, N = normal, DS = dip slip (combined normal and reverse), All = all fault styles, SCR = stable continental region, SL = surface length, Subd = subduction, SRL = surface rupture length, RLD = rupture length at depth, RW = downdip width, RA = rupture area, RL = rupture length, Dmax = maximum displacement, Davg = average displacement. Mw = moment magnitude as defined by Hanks and Kanamori (1979). **M** = magnitude, Mw or equivalent. L= subsurface horizontal rupture length (km).

[1] Seismotectonic setting for which the relationships are provided.

Wells and Coppersmith (1994) has been widely used in seismic hazard analyses. The paper presents sets of empirical equations obtained by least squares regression of a dataset of 244 earthquakes. Empirical relations are provided for rupture area as a function of magnitude for various styles-of-faulting. The rupture area model by Hanks and Bakun (2002, 2008) is a bilinear model indicating that for smaller magnitudes the length and width of the rupture increases with magnitude and at a certain magnitude the length continues to increase but width becomes fixed. The model by Leonard (2010) uses essentially the same data as Wells and Coppersmith (1994) and was later updated in Leonard (2014). The main feature of this model is that it imposes consistency with the definition of seismic moment. Thingbaijam et al. (2017) use well-recorded earthquakes and high-confidence fault models in their relationships. The scaling relationships are derived using orthogonal regression, rather than least squares,

so that either the magnitude or the rupture dimension can be considered the dependent variable. Stafford (2014) develops relationships for rupture width and rupture area for shallow crustal earthquakes of all mechanisms that are fully consistent with assumptions commonly made within PSHA, particularly to avoid an artificial increase of the likelihood at the maximum width. The effect of seismogenic thickness and dip is included in the relationships. The advantage of the Stafford (2014) relationships is that the size of the rupture is capped so that very elongated rupture dimensions are not produced for very large magnitude earthquakes.

The scaling relationships for rupture area as a function of magnitude published by Wells and Coppersmith (1994), Hanks and Bakun (2002, 2008), Leonard (2014), and Thingbaijam et al. (2017) are shown in Figure 8-19 for strike-slip and in Figure 8-20 for normal faulting. Note that the relationships of Leonard (2014) and Hanks and Bakun (2002, 2008) provide magnitude as a function of rupture area and were inverted to obtain the results needed to model virtual ruptures. This inversion will introduce errors unless the original equations were developed using orthogonal regression.

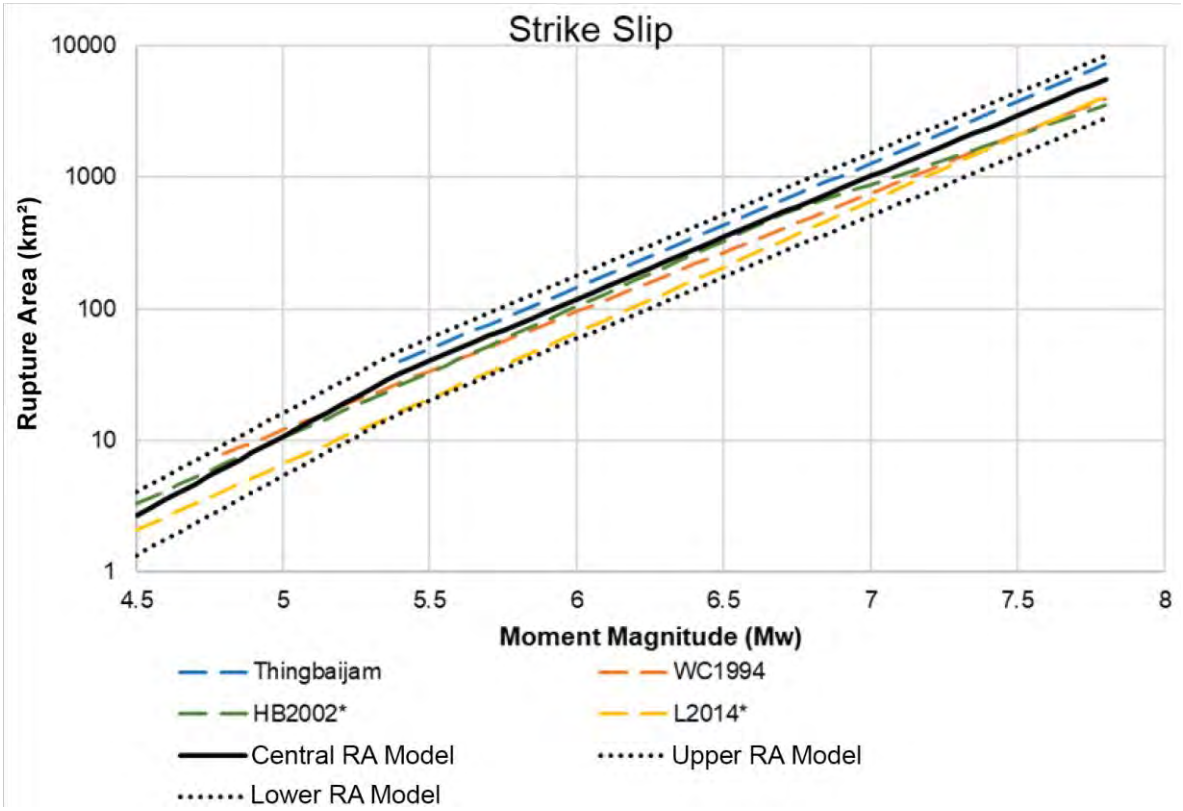

Figure 8-19. Empirical scaling relationships for rupture area as a function of magnitude for strike-slip faulting. Asterisks mark equations that were inverted to predict Rupture Area as a function of magnitude.

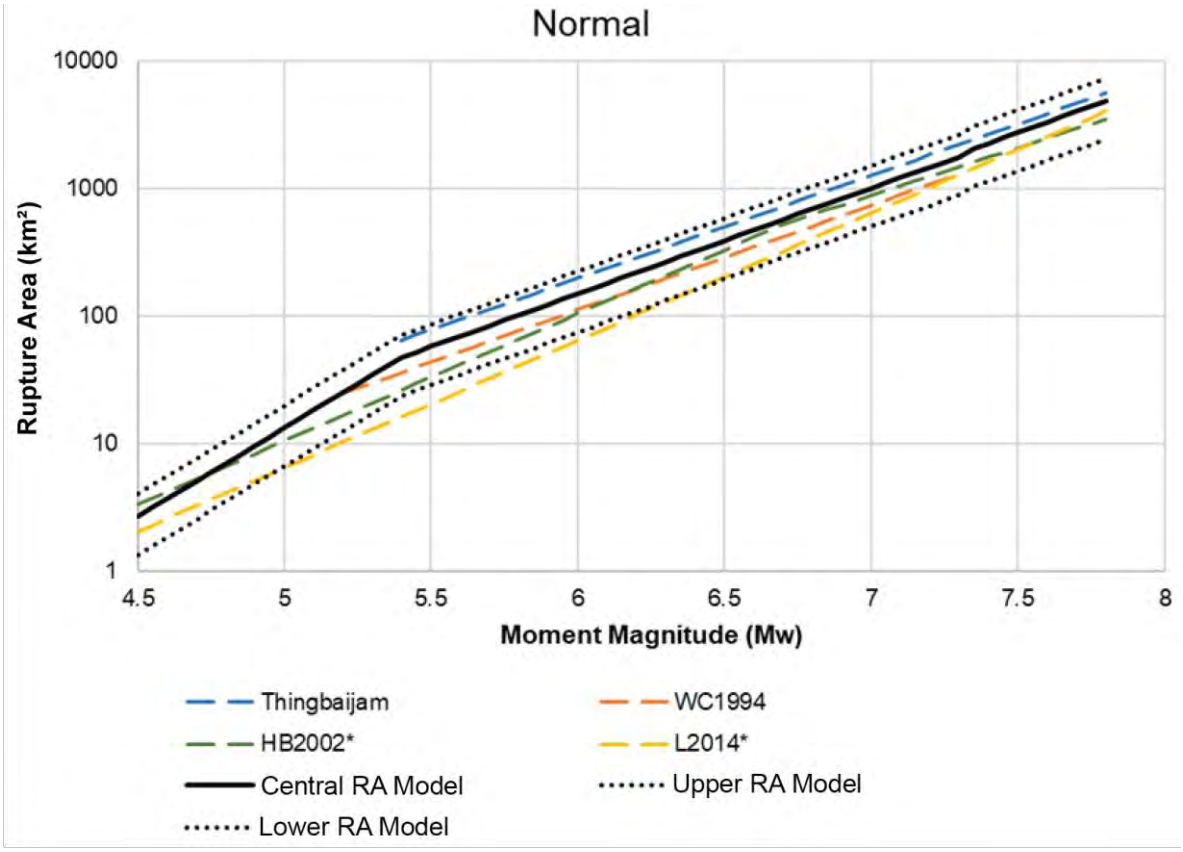

Figure 8-20. Empirical scaling relationships for rupture area as a function of magnitude for normal faulting. Asterisks mark equations that were inverted to predict Rupture Area as a function of magnitude.

The relationships of Wells and Coppersmith (1994), Hanks and Bakun (2002, 2008), Leonard (2014), and Thingbaijam et al. (2017) are represented using a three-point approximation based on Keefer and Bodily (1983) with weights as discussed earlier in this section. The three-point approximation results in a central, upper and lower model as indicated in Figure 8-18, through 8-20. The three-point approximation is used in the hazard calculation together with the style-of-faulting dependent aspect ratio model published in Goulet et al. (2018). From these two models, the rupture width and length can be computed with Equation 8-3 and 8-4.

The alternative approach to obtain rupture dimensions is to use the Stafford (2014) equations for RA and RW. RW is computed using:

8-5

$$ln(RW) = \beta_0 + \beta_1 M_w$$

where coefficients β_0 and β_1 are style-of-faulting dependent and are provided in Table 2 of Stafford (2014).

The RA scaling relationship is given by:

8-6

$$ln(RA) = \begin{cases} \gamma_0 + ln(10)M_w \; for \; M_w \leq M_{w,crit} \\ \gamma_0 + ln(10)M_w - \frac{ln(10)}{4}\left(M_w - M_{w,crit}\right) for \; M_w > M_{w,crit} \end{cases}$$

where coefficient γ_0 is dependent on style-of-faulting and is provided in Table 3 of Stafford (2014) and $M_{w,crit}$ is given by:

8-7

$$M_{w,crit} = \frac{ln(RW_{max}) - \beta_0}{\beta_1}$$

In Equation 8-7, Rw_{max} is the maximum rupture width obtained dividing the seismogenic thickness by sin(dip).

Figure 8-21 and Figure 8-22 show the rupture length obtained using Stafford (2014) equations for strike-slip and normal faulting, respectively. On each figure, curves of rupture length as a function of magnitude are shown for three seismogenic thicknesses (15 km, 17 km, and 22 km – presented in different colours) and three dips, which are 75°, 82°, 90° for strike-slip (Figure 8-21), and 45°, 65°, 85° for normal faulting (Figure 8-22).The figures show a limited effect of dip and seismogenic thickness for strike-slip faulting, and a more significant impact on normal faulting for magnitudes greater than 6.5.

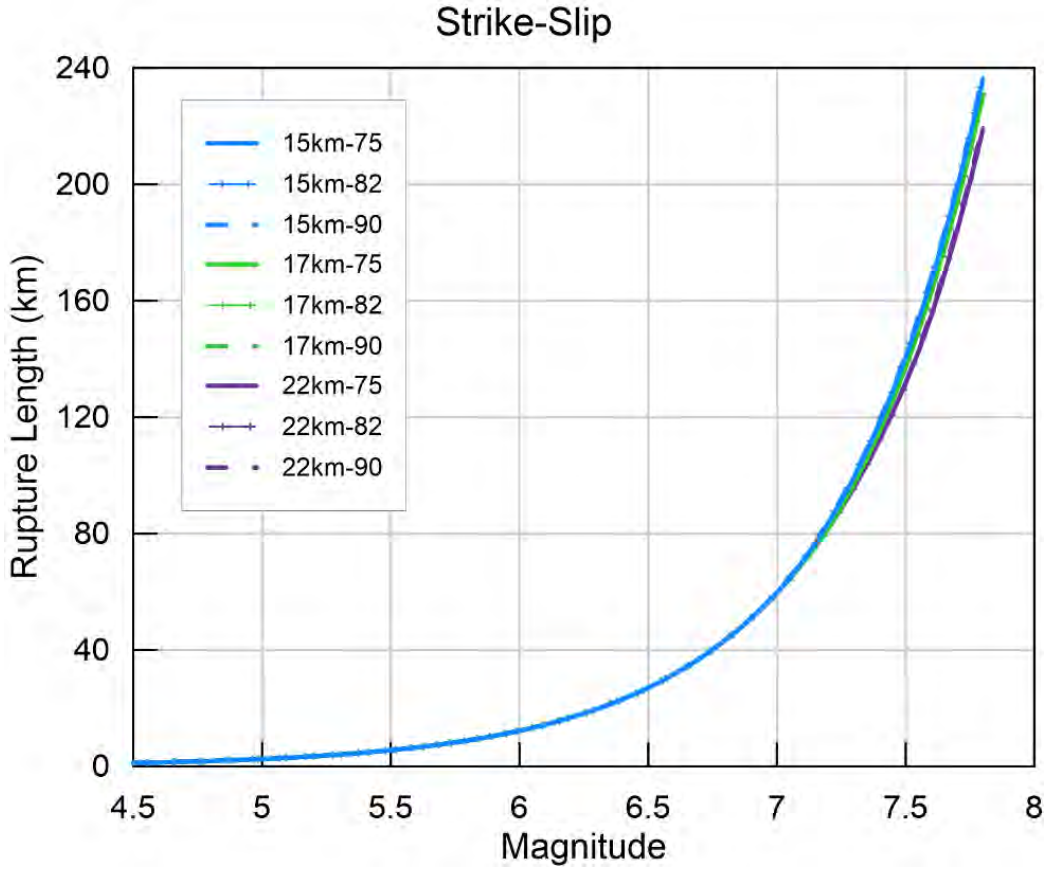

Figure 8-21. Rupture length as a function of magnitude for strike-slip faulting using the models for rupture area and rupture width by Stafford (2014) for alternative values of seismogenic thickness (15 km, 17 km, 22 km) and alternative values of fault dip (75°, 82°, 90°).

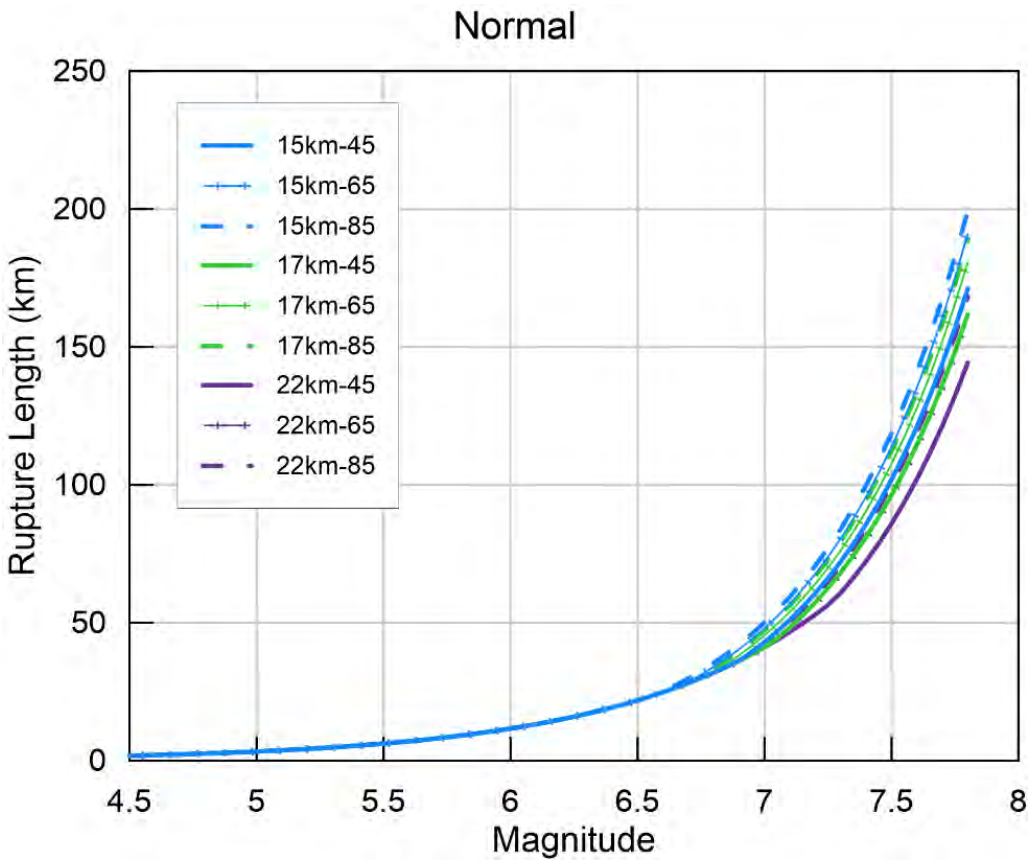

Figure 8-22. Rupture length as a function of magnitude for normal faulting using the models for rupture area and rupture width by Stafford (2014) for alternative values of seismogenic thickness (15 km, 17 km, 22 km) and alternative values of fault dip (45°, 65°, 85°).

Figure 8-23 and Figure 8-24 illustrate the effect of using different approaches to compute RL: the three black curves are obtained using the weighted average RA model and its uncertainty presented in Figure 8-19 and Figure 8-20, combined with the Goulet et al. (2018) AR model. The red curve shows RL obtained from the Stafford (2014) RA and RW models.

The figures show that RL calculated from Stafford (2014) RA and RW is generally within the range of RL obtained from the weighted average RA and its uncertainty (see Figure 8-19 and Figure 8-20). As the rupture width reaches the maximum seismogenic thickness, that is $RW=RW_{max}$, the slope of the Stafford (2014) RA relation changes, producing smaller areas compared to the weighted average RA relation from Figure 8-19, and consequently shorter RL. For a **M** 7.5 vertical strike-slip earthquake (Figure 8-23), the difference in RL predicted by the two alternative models ranges between 2% and 39% for seismogenic thickness of 22 and 15 km, respectively. For the same earthquake on a normal fault dipping 60 degrees (Figure 8-24), the Stafford (2014) model predicts RL that are between 16% (for 22 km seismogenic thickness) and 43% (for 15 km seismogenic thickness) smaller than the corresponding RL obtained with the average RA model.

For comparison, the recent **M** 7.8 Kahramanmaraş earthquake in Turkey produced a surface rupture length of just over 320 km with a rupture width of approximately 20 km (Mai et al., 2023). Assuming a vertical strike-slip fault and $RW=RW_{max}$= 22 km, the right-hand panel on Figure 8-23 shows that the weighted average RA model and its uncertainty yield RL between 130 and 380 km, while the Stafford (2014) model returns RL = 220 km.

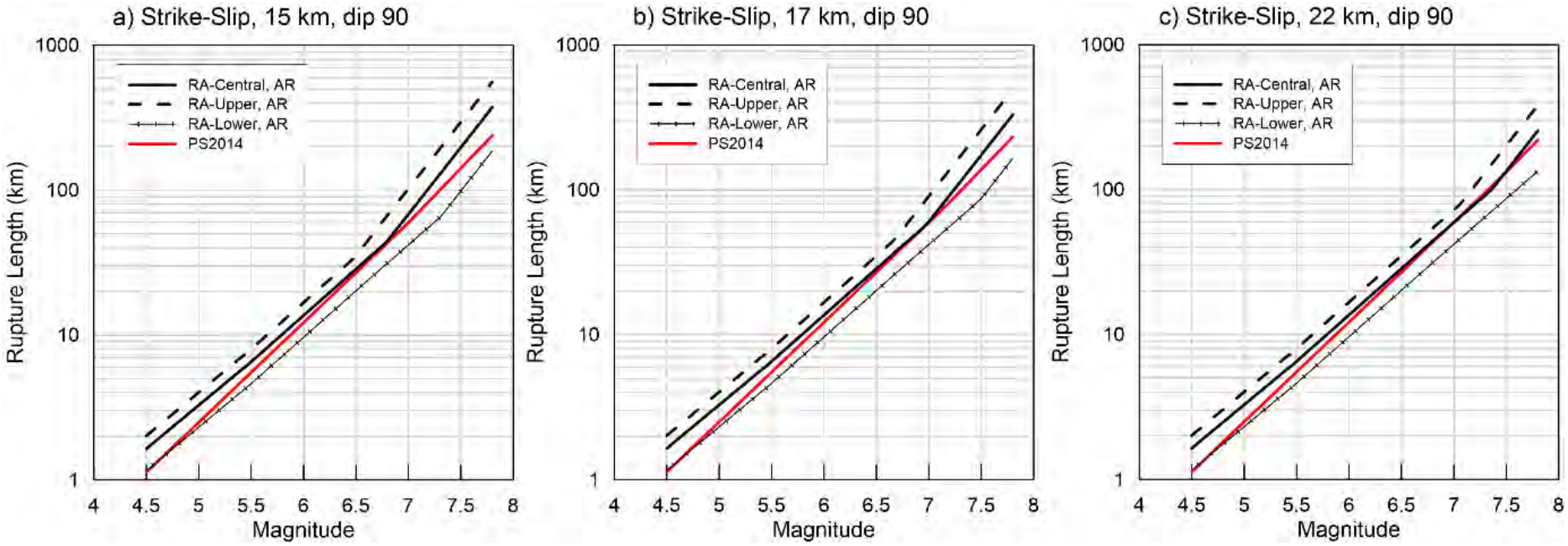

Figure 8-23. Rupture length as a function of magnitude for a vertical strike-slip fault using alternative approaches to derive rupture dimension.

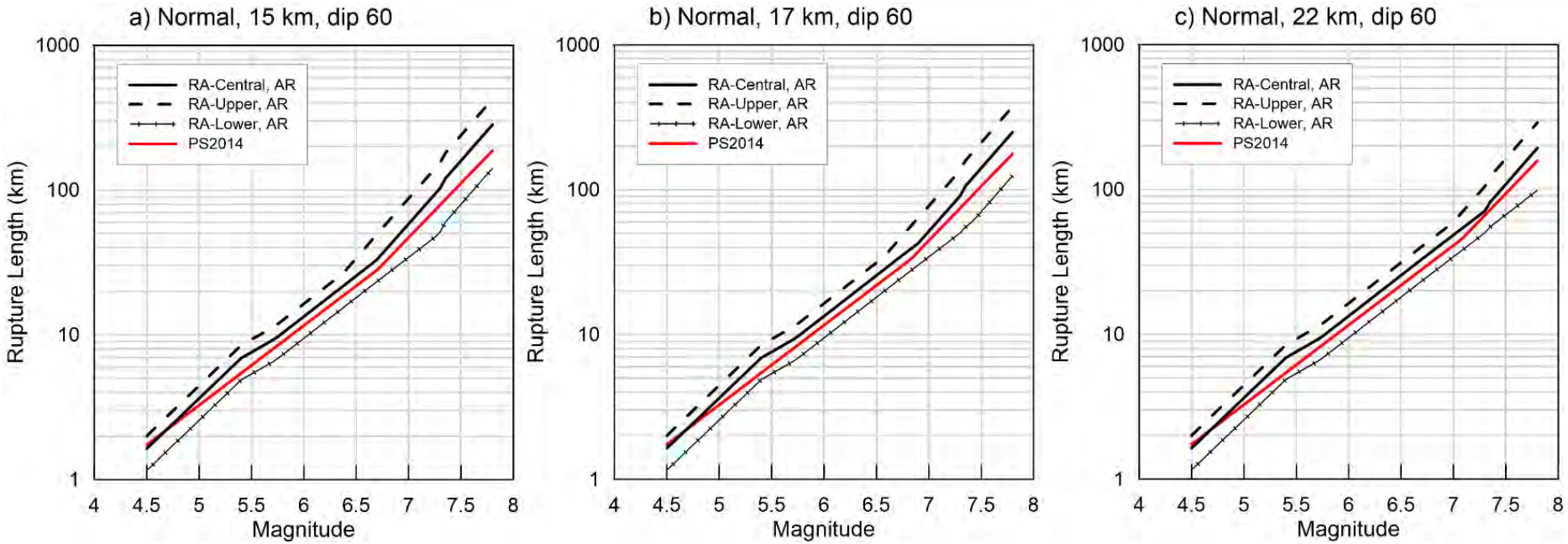

Figure 8-24. Rupture length as a function of magnitude for a 60°-dipping normal fault using alternative approaches to derive rupture dimension.

8.2.7 Focal depth distribution

The focal depth distribution (FDD) models the relative likelihood of hypocentres within the seismogenic thickness. The distribution adopted for the SSM was derived by Goulet et al. (2018) using the CEUS SSC (EPRI/DOE/USNRC, 2012) catalogue. The data from the CEUS study was trimmed by Goulet et al. (2018) to use only well-recorded earthquakes and excluding reservoir induced seismicity. Two models were developed by Goulet et al. (2018), one for the deeper focal depths occurring in parts of the Central Eastern US, and the other for the rest of the region. The SSM TI Team evaluated that the focal depths available for the project catalogue do not warrant the use of the deep model. The “rest of CEUS region” model from Goulet et al. (2018), which excludes zones of deeper seismicity, was therefore adopted for use in this study. Table 13-7 of Goulet et al. (2018), reproduced below as Table 8-4, contains the smoothed FDD, which extends to a depth of 31.5 km. For application in the Duynefontyn hazard analysis the distribution was truncated by the SSM TI Team at each seismogenic thickness (15 km, 17 km, and 22 km) and renormalised. The full table of parameters is provided in the HID (Appendix D).

Table 8-4. Smoothed focal depth distributions for CEUS earthquakes "Rest of CEUS Region" from Table 13-7 of Goulet et al. (2018).

Focal Depth (km)	Smoothed Cumulative Distribution
0	0
0.5	0
1.5	0.0123
2.5	0.0362
3.5	0.0748
4.5	0.1245
5.5	0.1865
6.5	0.2681
7.5	0.3595
8.5	0.4601
9.5	0.5442
10.5	0.6092
11.5	0.665
12.5	0.7129
13.5	0.7552
14.5	0.792
15.5	0.8252
16.5	0.8454
17.5	0.8643
18.5	0.8821
19.5	0.8986
20.5	0.9138
21.5	0.9278
22.5	0.9406
23.5	0.9522
24.5	0.9625
25.5	0.9715
26.5	0.9794
27.5	0.986
28.5	0.9913
29.5	0.9955
30.5	0.9984
31.5	1

8.2.8 Hypocentral depth ratio distribution

The hypocentral depth ratio (HDR) is defined as the depth of the hypocentre below the top of the rupture plane divided by the total depth extent of the rupture. Table 13-8 of Goulet et al. (2018), reproduced below as Table 8-5, presents smoothed HDR distributions obtained for different style-of-faulting using the NGA-West2 database. This model is a refinement of the model presented in Appendix B of Chiou and Youngs (2008). The SSM TI Team adopted the Goulet et al. (2018) model.

Table 8-5: Smoothed HDR distributions developed from NGA-West2 database (Table 13-8 of Goulet et al., 2018).

HDR	Cumulative distribution function for:		
	Normal	Strike-Slip	Reverse
0	0	0	0
0.1	0	0.025	0.03
0.2	0	0.05	0.08
0.3	0	0.09	0.14
0.4	0	0.15	0.25
0.5	0	0.24	0.36
0.6	0.05	0.35	0.47
0.7	0.10	0.53	0.58
0.8	0.25	0.72	0.69
0.9	0.5	0.86	0.83
1	1	1	1

8.2.9 Maximum magnitude (Mmax) approach

Background: The maximum magnitude (Mmax) is the largest earthquake that a seismic source is allowed to generate in the SSM. For seismic source zones, Mmax is the upper bound to recurrence curves. A distribution of Mmax values is typically determined for each source zone to account for uncertainty in the value of Mmax.

Methods for determining Mmax distribution include adding an uncertainty to the maximum observed event, the Kijko method (Kijko, 2004), and Bayesian process (Johnston et al., 1994; EPRI/DOE/USNRC, 2012). All three methods use zone-specific information from the project earthquake catalogue but result in different types of distributions.

The simplest method to develop Mmax is to consider the magnitude of the maximum observed event within each source zone, then add an increment to that value. A typical use of this approach is to add 0.5 magnitude units to the maximum observed event (Wheeler, 2009), then impose intervals of 0.25 magnitude units to produce a three-point distribution.

The Kijko method (Kijko, 2004) is an assessment of Mmax based on the observed distribution of events within a given source zone. Kijko (2004) considers alternative forms of the magnitude-frequency distribution. In the Kijko-Sellevol (K-S) method, earthquake magnitudes follow a truncated exponential model, while in the Kijko-Sellevol-Bayes (K-S-B) estimator the uncertainty on *b*-value is incorporated. A third method presented in Kijko (2004) does not assume any specific form of the distribution and is to be used when a characteristic behaviour is observed. Repeated events indicative of characteristic behaviour are not observed within SSM source zones, and are modelled only for the Groenhof Fault Source, therefore this approach is not considered further. Using any of the Kijko methods, the largest probability magnitude values in the distribution are only slightly larger than the magnitude of the maximum observed event. The assumptions inherent with the shape of the Kijko method distribution are that the earthquake catalogue is complete at the maximum observed and larger magnitudes, and that the maximum observed event is a true representative of the largest event anticipated within a source zone.

The Kijko method was originally developed using data for southern California in the U.S., a robust dataset for an active plate boundary region. The reliance of this method on source-specific occurrences of events indicates that a much better fit to the data is realised with larger event counts.

The Bayesian procedure (Johnston et al., 1994; EPRI/DOE/USNRC, 2012) draws analogies to tectonically comparable regions to estimate the Mmax for the source of interest (Wheeler, 2009). Distributions for different types of stable continental region (SCR) crust were developed by analysing data for these regions globally. In the Bayesian method, an appropriate normal prior distribution is selected for application to a seismic source zone based on the type of crust. Two prior distributions are defined within this approach that include Mesozoic extended crust (MESE), and non-Mesozoic extended crust (non-MESE). The prior distribution is then convolved with a likelihood function generated from the earthquake catalogue within the given seismic source zone (Figure 8-25). The result is a Mmax distribution based on the normal prior distribution and also accounting for the observed events within the seismic source zone.

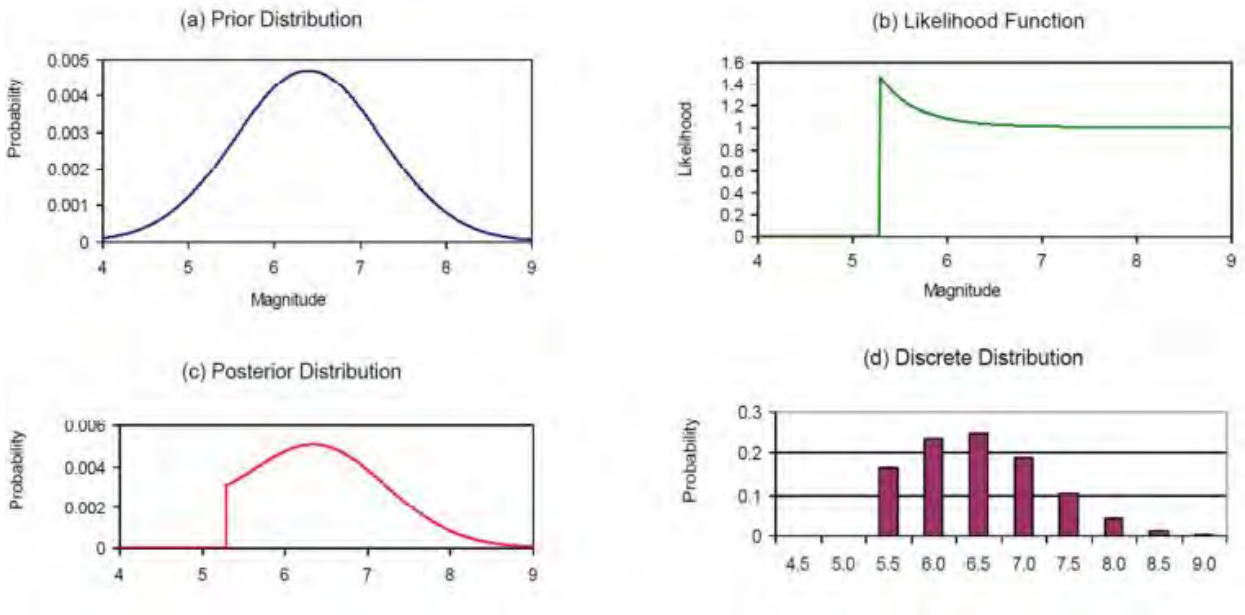

Figure 8-25. Illustration of Bayesian Mmax approach from EPRI/DOE/USNRC (2012).

Decision: The SSM TI Team implemented the Bayesian procedure (Johnston et al., 1994; EPRI/DOE/USNRC, 2012) to calculate distributions of Mmax for each seismic source zone. The SSM TI Team imposed an upper bound limit of **M** 7.8 for the Bayesian prior distributions. For OBZ a lower bound limit of **M** 5.2 was used.

Technical Bases: The SSM TI Team concluded that the strict use of maximum observed event and Kijko methods are not appropriate for the SSM given the few events in the catalogue within individual zones. As is common for studies away from active plate margins, the earthquake record is dependent on the project catalogue and not palaeoseismic data, therefore too short a record to capture large-magnitude and infrequent past earthquakes. The paucity of events in the earthquake catalogue is evidenced by low event counts and generally small magnitudes of the maximum observed event within each seismic source zone.

The SSM TI Team closely evaluated properties of the project region in relation to the tectonic criteria that define stable continental regions (SCRs) (Johnston et al., 1994; EPRI/DOE/USNRC, 2012) to confirm that crust in the project region is consistent with SCR. The upper limit of **M** 7.8 was selected because it reflects the upper bound of earthquakes within stable continental crust. The lower bound for OBZ was selected to be larger than the minimum magnitude in the hazard calculation (**M** 5.0).

Evaluation: The SSM TI Team evaluated the complete and declustered earthquake catalogue captured by each seismic source zone. No palaeoseismic data for the project region are available, which could provide markers for infrequent but large magnitude earthquakes. Without longer term indicators of large magnitude events, Johnston et al. (1994) attempted to address the issues presented by short earthquake catalogue records by developing a database of worldwide SCR events and drawing comparisons between types of SCR crust worldwide. The CEUS SSC (EPRI/DOE/USNRC, 2012) study updated the SCR event database and conducted additional analyses to update the prior distributions used in the Bayesian Mmax approach.

After careful examination of the seismic source zones and types of SCR crust analysed by Johnston et al. (1994) and EPRI/DOE/USNRC (2012), the SSM TI Team concluded that the AGZ and OBZ crust volume is consistent with the Mesozoic and younger extended crust (MESE), while all other zones are consistent with non-Mesozoic and younger extended crust (NMESE) (Table 8-6). The importance in drawing the analogy to an SCR crustal type is the peak location and distribution width that is used for the SCR prior. The maximum observed event reported for each seismic source zone is shown in Table 8-6. Seismic source zone Mmax inputs., showing small event magnitudes for the OBZ, AGZ, and ORZ. These small maximum observed events highlight why strictly data dependent Mmax methods are not appropriate for the project region. Mmax distributions using these small magnitudes would assign most of the weight on magnitudes only slightly larger than the maximum observed events.

Table 8-6. Seismic source zone Mmax inputs.

Characteristic	SDZ	ORZ	AGZ	OBZ	COZ
Mmax Bayesian Prior	NMESE [1.0]	NMESE [1.0]	MESE [1.0]	MESE [1.0]	NMESE [1.0]
Max Observed	E[**M**] 6.1 1809-12-04 On Groenhof Fault source: E[**M**] 6.2 1969-09-29	E[**M**] 5.2 1950-09-30	E[**M**] 4.9 1969-09-11	E[**M**] 3.26 2003-04-15	E[**M**] 6.1 1912-02-20
[1] Epistemic weights are numbers given in [brackets].					

The Bayesian Mmax approach requires zone-specific input parameters to develop the likelihood function to be convolved with the prior distribution. Required catalogue inputs include a minimum count magnitude (m_0), count (N) of the number of events with magnitude of m_0 and larger, and maximum observed magnitude. The SSM TI Team chose to use m_0 of 5.0 for counts of events within each zone, remaining consistent with the minimum magnitude used for the calculation of hazard. Zone-specific *b*-values are also an input for the likelihood function.

As shown in Table 8-6, the maximum observed event in the AGZ is E[**M**] 4.9 and in the OBZ is E[**M**] 3.3. With no observed events of E[**M**] 5.0 or larger for these two zones, the SSM TI Team selected a lower bound of E[**M**] 5.2, which was applied as a truncation of the prior distribution.

The Bayesian prior distributions developed by Johnston et al. (1994) and EPRI/DOE/USNRC (2012) extend to an upper bound of **M** 8.2. The SSM TI Team assembled and assessed information available for worldwide SCR events for types of crust most analogous to the project region and concluded that an upper bound of **M** 7.8 is appropriate for the project site. The upper bound was applied as a truncation to the prior distribution. The **M** 7.8 upper bound was chosen because the SSM TI Team concluded that it captured the upper bound of earthquakes that have occurred in stable continental crust. The largest magnitude earthquakes, with **M**>9.0, are associated with subduction zones. Larger magnitude

earthquakes outside subduction zones, such as the 2008 **M** 7.9 Sichuan earthquake or the 1931 **M** 8.0 Fuyun earthquake in Tibet, are in regions with overthickened crust and undergoing active convergent tectonics. The largest recorded earthquake in all of Africa was the 1910 **M** 7.3 earthquake in Tanzania.

The **M** 7.8 upper bound Mmax correlates to rupture lengths up to roughly 500 km for normal faulting and 550 km for strike-slip faulting, using the rupture area relationships described in Section 8.2.6. Following the Stafford et al. (2014) rupture length relationships plotted in Figure 8-21 and Figure 8-22, the **M** 7.8 upper bound Mmax produces rupture lengths of 150 to 250 km for normal faulting and 220 to 240 km for strike-slip faulting.

The CEUS SSC (EPRI/DOE/USNRC, 2012) developed a test to analyse the Bayesian and Kijko Mmax methods and assign a weight to each method based on applicability of the model to the input data. Kijko (2004) presents a relationship for the cumulative probability function of Mmax. EPRI/DOE/USNRC (2012) show that as the value of m^u, representing possible values of Mmax, increases, the probability reaches a limit that is less than 1 if the number of recorded earthquakes with magnitude greater than a specified threshold is less than 100. According to Kijko (2004), this limiting value can be used as an indicator that the method provides reasonable results. EPRI/DOE/USNRC (2012) used the limiting value of $P_{unbounded}(m^u > 8¼ | m^u \geq 5½)$ to assess the weight to assign to the Kijko Mmax approach; the point where the truncated probability mass equals the remaining probability mass [i.e., $P_{unbounded}(m^u > 8¼ | m^u \geq 5½) = 0.5$] represents the limit of applicability of the Kijko Mmax approach, because as much information is discarded by truncation as is retained. If $P_{unbounded}(m^u > 8¼ | m^u \geq 5½)$ is essentially zero, then the Kijko approach is at its strongest because the number of observed earthquakes is large, and it is assigned equal weight with the Bayesian approach. EPRI/DOE/USNRC (2012) provide a formula to interpolate between these two extreme cases. The test was performed for the project zone-specific earthquake catalogues consistently limiting $P_{unbounded}$ to 7.8 as was done in the application of the Bayesian method. The test yields values of $P_{unbounded}$ between 0.7 and 1, therefore the weight assigned to the Kijko approach is always zero because there are never enough earthquakes in the project catalogue to apply the method.

To implement the Bayesian method, the normal prior distribution for MESE or NMESE crustal type as specified for each source zone is truncated at an upper bound of **M** 7.8 and re-normalised. Source zone specific recurrence and catalogue inputs are used to develop a likelihood function (EPRI/DOE/USNRC, 2012). The truncated prior distribution is then convolved with the likelihood function, producing Mmax distributions specific to each source zone and zone-specific inputs. Table 8-7 shows, as an example, the resultant Mmax distribution for the SDZ using a *b*-value of 0.81. The *b*-value of 0.81, as described in Section 8.2.10, was developed using the *b*-positive method.

Table 8-7. Mmax distribution for SDZ with *b*-value of 0.81.

Magnitude	Weight
6.2	7.30e-02
6.3	7.76e-02
6.4	8.11e-02
6.5	8.33e-02
6.6	8.39e-02
6.7	8.28e-02
6.8	7.99e-02
6.9	7.54e-02
7	6.94e-02
7.1	6.24e-02
7.2	5.47e-02
7.3	4.68e-02
7.4	3.90e-02
7.5	3.17e-02
7.6	2.51e-02
7.7	1.94e-02
7.8	1.46e-02

8.2.10 Recurrence

Background: The rate of future earthquakes modelled within each seismic source zone in the SSM is represented by magnitude-frequency distribution curves. Suites of curves are developed for each source zone using parameters of *b*-value (slope) and activity rate (y-intercept or y-value at a specific magnitude) defined by the SSM TI Team.

The doubly truncated exponential distribution (Gutenberg and Richter, 1954; Cornell and Van Marke, 1969) was used to model magnitude-frequency estimates for each zone. Each magnitude-frequency curve is parameterised using correlated sets of *a*-value, *b*-value, and Mmax distribution.

To develop data-driven recurrence parameters, we implemented the log-likelihood method by Weichert (1980), which has been widely utilised in seismic hazard studies for critical facilities. The method calculates recurrence parameters by maximum likelihood estimation from the cumulative occurrence of events for magnitude bins above a minimum value. The approach

is purely data-driven, resulting in a better fit to the magnitude bins that include a greater number of events.

van der Elst (2021) introduced a new *b*-value estimator called *b*-positive. This method does not require an accurate estimate of a completeness cutoff magnitude and allows calculation of *b*-value using datasets with some level of incompleteness as well as datasets with variable levels of completeness through time. It is based on the positive-only subset of the differences in magnitude between successive earthquakes. The distribution of magnitude differences is identical to the distribution of earthquake magnitudes, i.e., the *b*-value is the same, however van der Elst (2021) concluded that positive magnitude differences are not significantly affected by detection issues typical of small magnitude events. Thus *b*-positive is considered insensitive to transient changes in catalogue completeness and can therefore be used to estimate *b*-value during periods of varying incompleteness level. If the dataset is strongly incomplete in time, van der Elst (2021) suggests removing the most incomplete portion of the catalogue.

Preliminary assessments of the *b*-value using zone-specific earthquake catalogues indicate low *b*-values, where there are sufficient events to develop such values. The generally small number of earthquakes in each zone (i.e., few magnitude bins to work with) increases uncertainty associated with already low *b*-values.

The following are approaches considered by the SSM TI Team for development of zone-specific *a*- and *b*-values to address the paucity of zone-specific data:

- Use analogue *b*-values specific to faulting mechanism (Gulia and Wiemer, 2010).
- Use published analogue *b*-values such as global SCR *b*-values or project-specific values for regions with similar crust type.
- Calculate data-driven *b*-values using the earthquake catalogue within all zones combined.
- Calculate zone-specific data-driven *b*-values.
- Calculate data-driven *b*-values using the full regional extent of the project earthquake catalogue and implement in a zoneless model.
- Use of a *b*-prior, similar to Bommer et al. (2013), which applies an extension by Veneziano and Van Dyck (1985) to the Weichert (1980) maximum likelihood fit method.
- Assess alternative minimum magnitudes used for data-driven *b*-value calculations.

Decision: The SSM TI Team made the following decisions for the activity and *b*-values approach:

- Use the project region catalogue outlined by the source zones (regional catalogue) from E[**M**] 3.3 as the basis to develop regional *b*-values.
- Use the following two methods to calculate regional *b*-values:
  - *b*-positive (van der Elst, 2021), and
  - log-likelihood (Weichert, 1980).
- Set regional *b*-values as *b*-priors to develop *a*- and *b*-values for each zone, using the source zone earthquake catalogue from E[**M**] 3.3.
- For zone OBZ, where there are no events in the project earthquake catalogue of E[**M**] ≥3.3, use the ORZ *a*- and *b*- values.

- Remove Ceres event (29 September 1969, E[**M**] 6.2 event) from zone SDZ for evaluations of zone-specific *a*- and *b*-values.

Technical Bases: Limitations of the project earthquake catalogue due to the scarcity of events were considered in the selection of an appropriate recurrence methodology for the seismic source zones. The SSM TI Team evaluated the applicability and impact of different *b*-value calculation methods and concluded that the data-driven regional catalogue *b*-values capture the spread of potential analogue b-values.

The SSM TI Team closely assessed the impact of the minimum threshold magnitude value. Magnitude bins less than E[**M**] 3.3 appear to be less complete (see Section 6.8.2.1), while a threshold value above E[**M**] 3.3 resulted in almost no change to the calculated mean *b*-values while increasing uncertainty around the mean value.

Evaluation:

Analysis of *b*-value calculation methods

The SSM TI Team and specialty contractors tested the maximum curvature (Wiemer and Wyss, 2000) of the project catalogue in an attempt to objectively determine the minimum threshold for magnitudes included in *b*-value calculations. The maximum curvature method was not successful, as the catalogue was found to be insufficiently complete for the application.

Results of the project catalogue completeness evaluations (Section 6.8) indicate incompleteness below E[**M**] 3.3. The incompleteness is apparent on plots of cumulative occurrence for the final project earthquake catalogue, for both the project region and individual zones, where there is a marked drop in cumulative occurrence for smaller magnitudes. Preliminary assessments of the minimum magnitude were performed and found little difference to the mean *b*-value for E[**M**] 3.3 or 3.7. As stated above, selecting a larger minimum magnitude resulted in greater uncertainty to the resulting mean *b*-value. The SSM TI Team chose E[**M**] 3.3 as the minimum magnitude for recurrence parameter calculations.

b-positive method

To implement the *b*-positive method, a minimum number of 100 events is required to achieve a robust estimation of *b*-value (van per Elst, personal communication to specialty contractor). While the methodology does not require completeness time intervals, to minimize the impact of catalogue incompleteness, the analysis was completed on the earthquake catalogue starting in 1966 consistent with the Stepp (1972) completeness method cutoff for E[**M**] 3.3 and with improvements in seismic networks. Within this timeframe there are 159 earthquakes which were used in the *b*-positive analysis, exceeding the minimum number required.

A regional *b*-value was developed using the *b*-positive estimator (van der Elst, 2021), and was calculated as follows:

- selected earthquakes with E[**M**]≥3.3 since 1966.
- built a vector containing only positive differences between two successive events.
- *b*-value estimated by formula A3 in van der Elst (2021).
- uncertainty established by a bootstrap technique resampled for N times, where N is the sample size.

Log-likelihood method

The log-likelihood *b*-value method following Weichert (1980) was implemented for the complete and independent project earthquake catalogue using the events within all seismic source zones of E[**M**] 3.3 and larger. Regional *b*-values were calculated for the catalogue using both completeness applications (see Section 6.8.3). Assessment of the Stepp (1972) plot completeness method is included in Section 6.8.2.3 and of the probability of detection completeness method in Section 6.8.2.4. The results of the regional catalogue log-likelihood *b*-value are plotted in Figure 8-26, calculated for probability of detection completeness (Figure 8-26a) and Stepp (1972) plot completeness (Figure 8-26b).

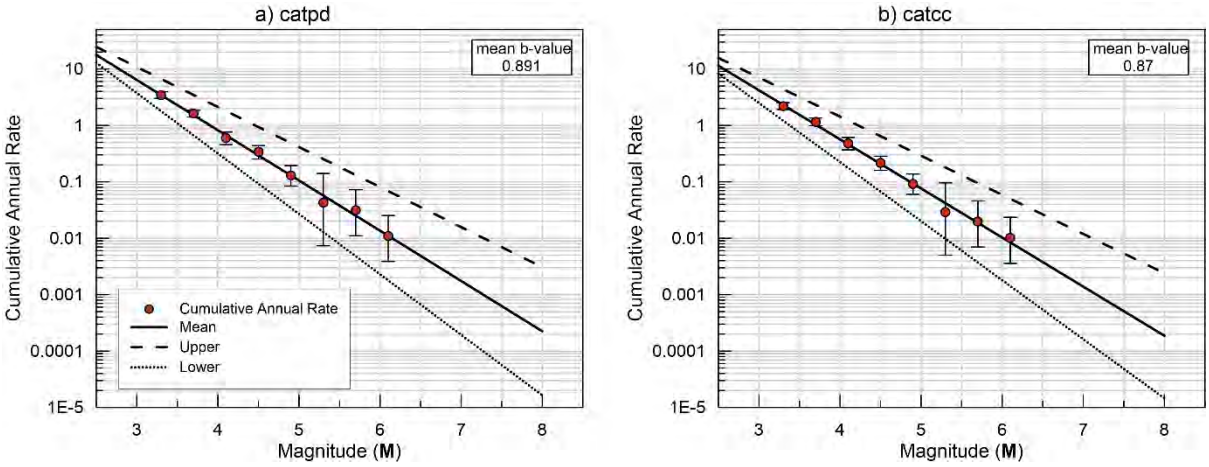

Figure 8-26. Regional catalogue log-likelihood recurrence. Applied (a) probability of detection completeness (pd) and (b) Stepp (1972) plot completeness (cc). cat – catalogue.

The *b*-positive and log-likelihood methods were developed on different assumptions and therefore represent the uncertainty in *b*-value estimates derived from alternative approaches. Table 8-8 provides the calculated regional catalogue *b*-values for comparison, including *b*-value sigma.

Table 8-8. Regional catalogue *b*-values.

Recurrence Method	Completeness Method	Mean	95th	5th	Sigma *b*
***b*-positive**	**Not Applicable**	0.830	0.961	0.750	+0.096 -0.058
Log-likelihood	**Stepp Completeness**	0.870	1.027	0.713	0.109
	PoD (probability of detection)	0.891	1.055	0.727	0.112

The SSM TI Team compiled *b*-values from studies and regions similar to the project region (Table 8-9). After close review of the available *b*-values and comparison to preliminary calculations of regional *b*-values, the available values and regional *b*-values are found to be in close agreement. Data-driven *b*-values are preferred over analogue-type values when

possible and the available *b*-values are generally captured within the range of data-driven regional *b*-values. The SSM TI Team attempted to develop *b*-values using zone-specific earthquake catalogues but found there were generally too few events of E[**M**]≥3.3 to confidently calculate *b*-value, or that the resulting *b*-values were significantly lower than expected when compared to the available values. Following the close review and consideration of available, regional data-driven, and source-specific data-driven *b*-values, the SSM TI Team elected to use only the data-driven regional *b*-values in the SSM.

Table 8-9. Available *b*-values.

Source	*b*-values	Notes
CEUS SSC (EPRI/DOE/USNRC, 2012)	0.98 to 1.02	North American Craton and Appalachian Terranes
TNSP (Bommer et al., 2013)	0.92	Weighted average for SYN and ECC
Spain SSHAC Study	1.26 ± 0.07	Iberian Massif
Gulia and Wiemer (2010)	1.07 to 1.11 0.91 to 0.95	Normal focal mechanism Strike-slip focal mechanism

Zone OBZ

The zone OBZ does not capture any project earthquake catalogue events of E[**M**]≥3.3 (Figure 8-14). However, it is unlikely that no events have occurred within the zone boundaries during the entirety of the catalogue period. Because the OBZ is located more than 100 km offshore and all seismic stations are located only east of the zone, the zone is likely to suffer from incompleteness at all magnitudes.

Neighbouring zones to the OBZ are zone ORZ to the east and SDZ to the south. The SSM TI Team considered the amount and pattern of seismicity within zone ORZ, as well as what is understood of the type and orientation of the structural fabric in zone OBZ for comparison. This information was used to select zone ORZ as a similar analogue to zone OBZ for event recurrence. The SSM TI Team chose to adopt ORZ earthquake recurrence parameters, both *b*-values and activity levels, for zone OBZ.

Application of regional *b*-value to seismic source zones

As stated previously, there are generally too few events within each seismic source zone to confidently develop zone-specific data driven *b*-values. Therefore, the SSM TI Team considered many methods for application of the data-driven regional catalogue *b*-value to the zones. There are two primary components: regional catalogue *b*-values, and the values of cumulative annual frequency of earthquakes by magnitude bin developed from the project earthquake catalogue within each zone.

Methods to apply regional *b*-values to zone-specific event occurrence include the following:

- Anchor to activity rate at a specific magnitude: The approach is simple to implement, however it uses the *b*-value directly and can therefore result in a poor fit to zone data because a single cumulative annual frequency point is used to anchor the rate curve.
- Shifted *b*-value: Rather than anchoring the *b*-value to a frequency data point, this method uses the *b*-value and shifts the rate curve to the centre of the zone data distribution.
- *b*-prior fit: EPRI-SOG (1988) extended the Weichert (1980) log-likelihood formulation to include a prior distribution for the *b*-value, specifically to stabilize the assessment in regions with limited data. The approach uses an input *b*-value as a prior, on which a weight can be specified. The weight is typically defined as the inverse of the variance of *b*-prior, and the likelihood formulation includes a penalty term that reduces the likelihood as the assessed *b*-value deviates from the prior.

The approaches above were followed for the project database and the *b*-prior fit approach was selected as it most accurately fit the data. The *b*-prior fit approach (i.e., the extended log-likelihood formulation in EPRI-SOG, 1988) was then used to obtain zone-specific earthquake recurrence parameters (*a*- and *b*-values) by imposing the regional *b*-values in Table 8-10 as priors for each zone. A very high weight was used in the fit, so that the *b*-value is effectively not allowed to vary much from the prior. As a consequence of this choice, the fit returns very small *b*-value sigma and the correlation between *a*- and *b*- is not informative. The SSM TI Team developed *a*-values, and corresponding sigmas, for each set of *b*-priors and each source zone.

Earthquake recurrence parameters (*b*-value and activity rate at E[**M**] 3.3) were coupled to capture the centre, body, and range of recurrence for each zone. Values for activity and *b*-values are provided in Table 8-10 for three magnitude-frequency distribution curves: mean, upper, and lower. The mean curve represents mean *b*-value and mean activity rate, with the upper curve plotting above the mean line and lower curve plotting below the mean line on the magnitude-frequency distribution plots (Figure 8-27). A plot exemplifying the spread of recurrence curves for zone SDZ is shown on Figure 8-27. The activity rate values provided in Table 8-10 indicate the plotted y-value at E[**M**] 5.0 correlating with the magnitude-frequency distribution lines on Figure 8-27. The seismic source zone logic tree is provided in Figure 8-28.

Table 8-10. SDZ rate parameters for recurrence.

Recurrence Method	Completeness Method	Mean		Upper		Lower	
		b-value	Activity at E[M] 5.0	*b*-value	Activity at E[M] 5.0	*b*-value	Activity at E[M] 5.0
***b*-positive**	**Stepp Completeness**	0.81	1.48E-02	0.72	2.87E-02	0.97	5.32E-03
	PoD	0.81	2.38E-02	0.72	4.52E-02	0.97	8.88E-03
Log-likelihood	**Stepp Completeness**	0.85	1.30E-02	0.67	3.51E-02	1.03	4.31E-03
	PoD	0.87	1.98E-02	0.68	5.31E-02	1.05	6.68E-03

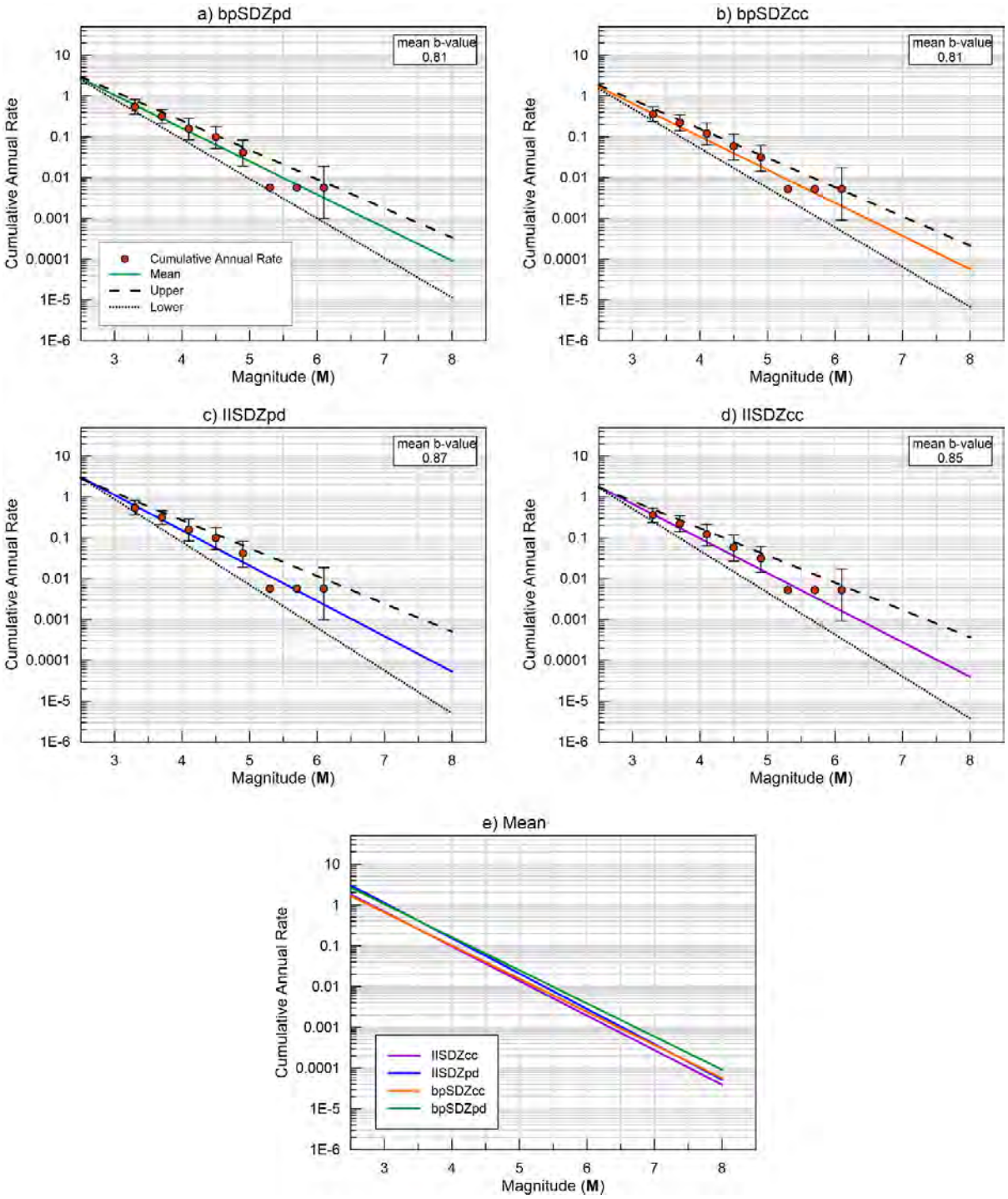

Figure 8-27. Example recurrence curves for SDZ. Spread of curves captures the centre, body, and range of recurrence parameters. Plots show rate curves for (a) *b*-positive *b*-value with probability of detection completeness catalogue; (b) *b*-positive b-value with Stepp plot analysis completeness catalogue; (c) log-likelihood *b*-values with probability of detection completeness catalogue; (d) log-likelihood *b*-values with Stepp plot analysis completeness catalogue; (e) all four mean *b*-values for comparison. bp – *b*-positive *b*-value; ll – log likelihood; pd – probability of detection; cc – completeness cutoff (i.e., Stepp plot analysis).

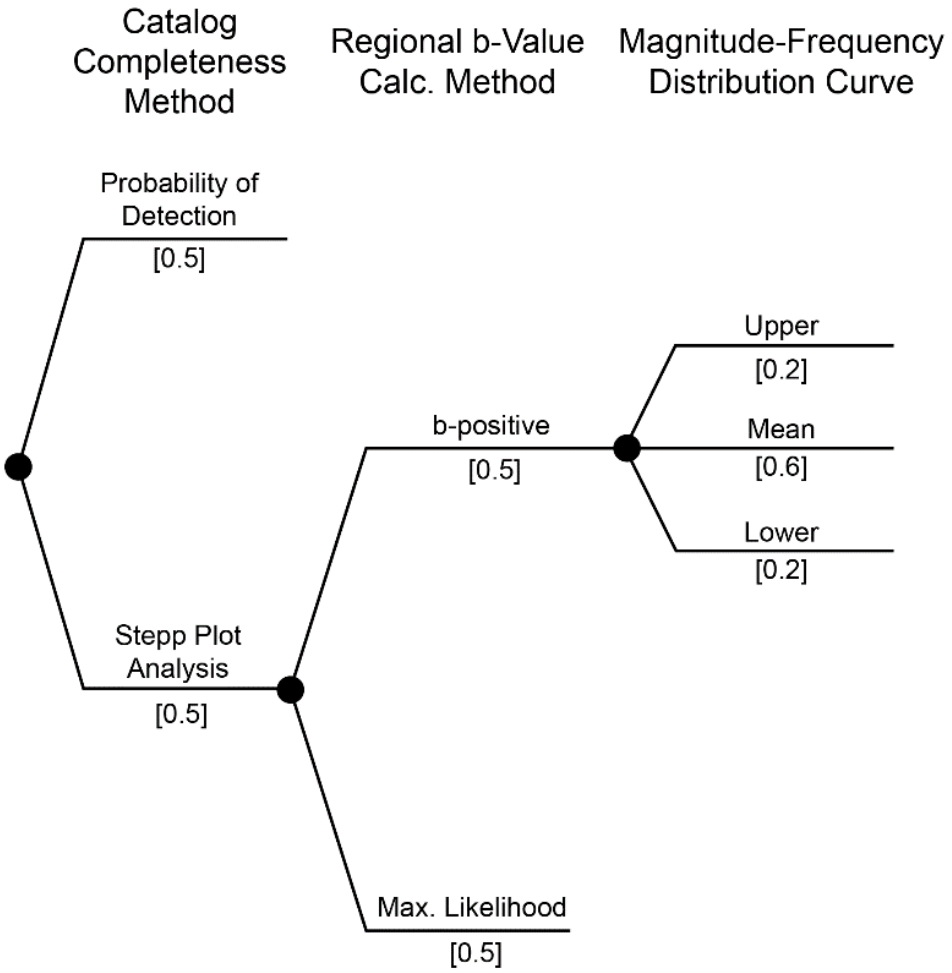

b-positive = From van der Elst (2021)
Max. Likelihood = Maximum likelihood following Weichert (1980)

Figure 8-28. Zone recurrence logic tree.

8.3 SOURCE ZONES IN THE SSM

The SSM TI Team characterised five seismic source zones for use in the Duynefontyn SSM, which are shown in Figure 8-2 and summarised in Table 8-1. Source zones were defined using the criteria discussed in Sections 8.1 and 8.2 and depicted in Figures 8-29 through 8-35. The areas beyond the boundaries of the OBZ and AGZ were not characterized by the SSM TI Team because of the large distances from the site, lack of seismicity and insufficient information regarding crustal properties offshore. Sensitivity analysis carried out during the Baseline PSHA study (Stamatakos et al. 2022) also showed that earthquakes more than 200 km from the site do not contribute to hazard. Therefore, the SSM TI Team did not include the area beyond the boundaries of the OBZ and AGZ in the source model.

8.3.1 Saldania Zone (SDZ)

The SDZ is the host zone for the Duynefontyn PSHA (Figure 8-29). It lies in the southwestern portion of the Western Cape. The SDZ consists of stable continental crust and non-Mesozoic extended crust. Its western boundary with the OBZ is primary defined by the transition from NMESE to MESE crust as highlighted by geophysical (aeromagnetic/gravity) data that define the western edge of the Orange Basin (Figure 8-29 and Figure 8-30), which marks the limit of Mesozoic extension (Broad et al., 2012; PASA, 2021). There is also a noticeable change in the structural style-of-faulting from predominantly strike-slip in the SDZ to normal faulting in the OBZ and ORZ. Similarly, the southern boundary with the AGZ is demarcated by a change in the region's structural characteristics. The boundary separates the north-northwest-striking western branch of the Cape Fold Belt from the east-west-trending southern branch (De Villiers, 1944; Söhnge, 1984; De Beer, 1990, 1998, 2002). The southern, more intensely deformed branch is dominated by east-west trending normal faults while the western branch is dominated by northwest-southeast trending strike-slip faults. The eastern boundary is marked by a significant geological change from the structural complexity of the Cape Fold Belt to the predominately undeformed Karoo Supergroup Basin, as well as the underlying Namaqua Metamorphic Province (Figure 8-31). Prominent NW and N-S oriented faults within the SDZ terminate at the boundary with the COZ.

Future earthquakes occurring within the SDZ zone are modelled as virtual ruptures. The style of faulting for future earthquakes are modelled with a relative frequency of normal (20%) and strike slip (80%). While the faults are considered to be predominantly strike-slip in nature, modelling a normal component along with strike-slip accounts for a normal-oblique component of slip. The orientations of ruptures are modelled to occur between a strike of 105° and 155° (also written 285° to 335°). The dip aleatory distributions for the zone's normal fault dips (dip to the south only) are 45º (20%), 65º (60%) and 85º (20%). Strike-slip faults have equal weight on dip towards the south (50%) and north (50%), with dip values of 75º (40%) and 90º (60%). The SSM TI Team designated all the SDZ boundaries as "leaky," consistent with long ruptures associated with an Mmax of **M** 7.8. The technical basis for this is that it is the only zone that will include virtual ruptures and the SSM TI Team determined that allowing the virtual ruptures to cross the zone boundaries would not impose artificial constraints on rupture propagation because the changes in structural grain and style-of-faulting at the boundaries are not abrupt but relatively gradual over several kilometres. In addition, sensitivity studies conducted at Workshop 3 showed that point sources could be applied in all adjacent source zones such that unrealistic long ruptures from those zones would not cross into the SDZ.

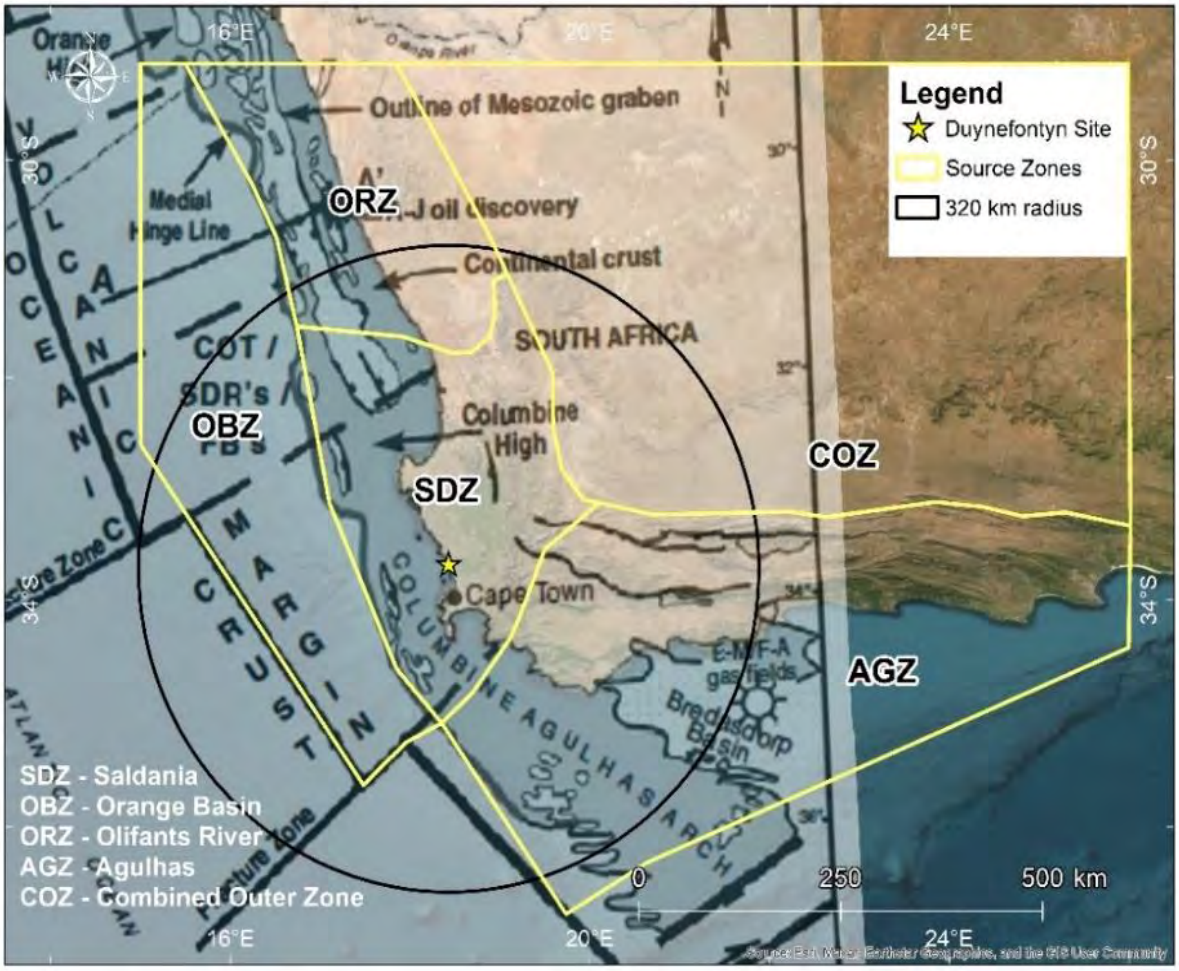

Figure 8-29. Structural features of the Orange Basin from Broad et al. (2012).

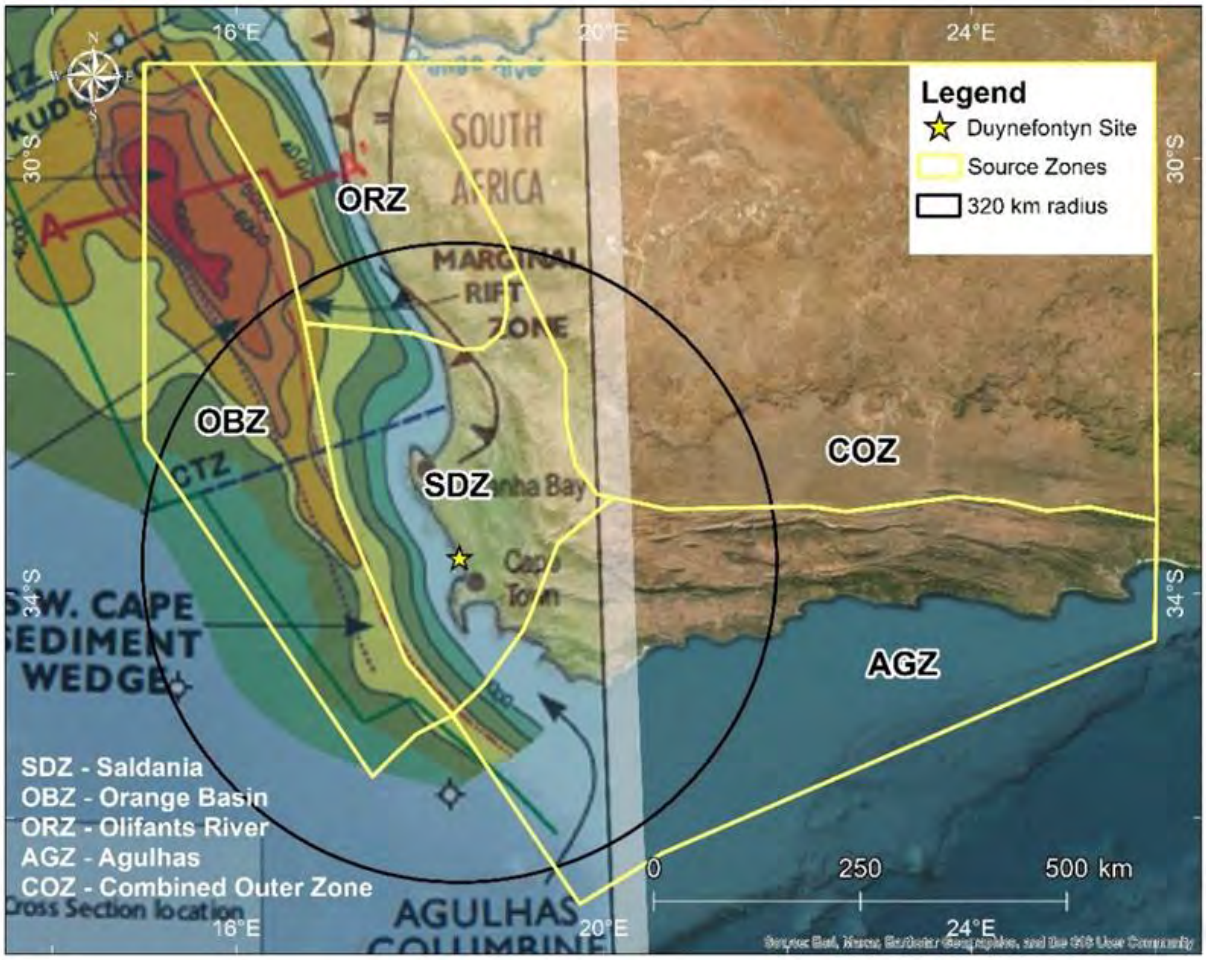

Figure 8-30. Seaward extent of the deposits comprising the Orange Basin (PASA, 2021) overlain on seismic source zones. The thrust faults are Pan African thrust zones, and the normal fault marks the position of the Great Escarpment, which is an erosional feature from the Mesozoic.

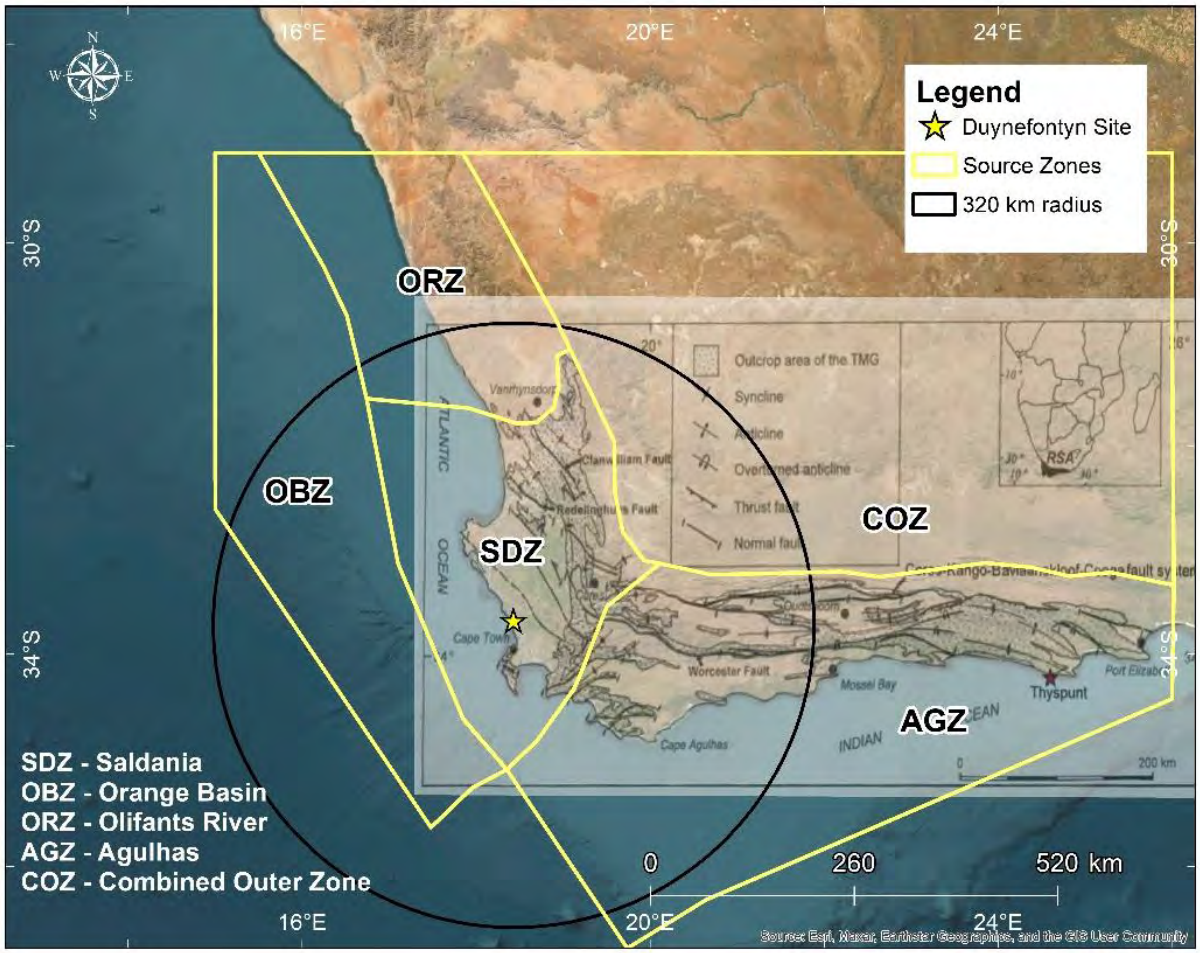

Figure 8-31. Structural style of the coastal regions of the Western Cape, from De Beer (2002), overlain on seismic source zones.

8.3.2 Orange Basin Zone (OBZ)

The OBZ is the only entirely offshore zone. It lies on the western margin of South Africa and is regarded as MESE crust (Figure 8-32). The western boundary of the OBZ is defined by the edge of the gravity anomaly shown in Paton et al. (2017) where there is a contact with oceanic crust, defined seismically by seaward-dipping reflectors. This gravity contrast is aligned with the tectonic interpretation of the seafloor by Broad et al. (2012). The area west of this boundary occurs outside of the defined model area and is composed of oceanic crust.

The style-of-faulting within the zone is 100% normal, with no strike aleatory distributions since earthquake scenarios within the zone are modelled as point sources. The aleatory distributions for the zone's normal fault dips are 45º (20%), 65º (60%) and 85º (20%).

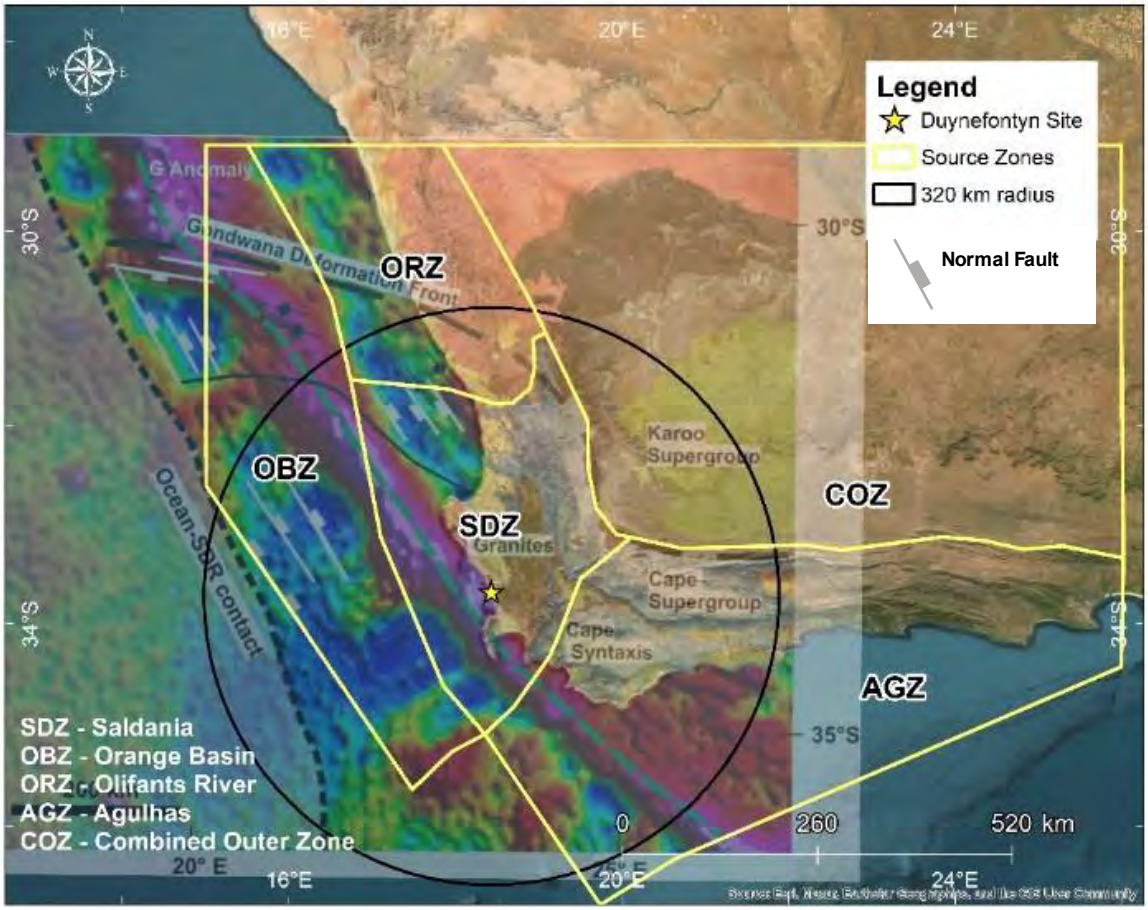

Figure 8-32. Gravity data from Paton et al. (2017) showing the transition zone from continental to oceanic crust and the edge of the continental margin, overlain on seismic source zones.

8.3.3 Olifants River Zone (ORZ)

The ORZ encompasses the area northwest of the site, which extends from the northern edge of the Cape Fold Belt into the Namaqua Metamorphic Province and is regarded as NMESE crust. This transition is observed within the geology and the structural fabric change across the zone boundary. The eastern boundary with the COZ is marked by a significant geological change from the much older Mesoproterozoic Namaqua-Natal Metamorphic Province to the younger Late Carboniferous and Early Jurassic Karoo Supergroup. Similar to the SDZ, the prominent NW-SE and N-S oriented faults terminate at the eastern boundary with the COZ. The northern boundary of the ORZ marks the limit of the seismic source model and the Western ORZ boundary is as for the SDZ.

The characteristic style-of-faulting within the zone is normal (50%) and strike-slip (50%) with no strike aleatory distributions as earthquake scenarios within the zone are modelled as point sources. The dip aleatory distributions for the zone are 45º (20%), 65º (60%) and 85º (20%) for normal faults; strike-slip faults are assigned dip values of 75º (40%) and 90º (60%).

8.3.4 Agulhas Zone (AGZ)

Geologically the AGZ encompasses the Cape Fold Belt onshore and extends offshore to the edge of the continental margin. It is bounded to the north by the COZ and to the northwest by the SDZ. The zone is mainly differentiated from its neighbouring zones by the intensity of most recent tectonic events and its structural fabric. The northern boundary of the AGZ is about 25 km north of the Ceres-Kango-Baviaanskloof-Coega fault system (CKBC). The CKBC marks the northern extent of Mesozoic extended crust and geologically, the boundary between the Cape Fold Belt and the Karoo Supergroup foreland basin (Figure 8-32 andFigure 8-33). Based on evidence in Broad et al. (2006) and Stankiewicz et al. (2007), the zone boundary is considered to represent the northernmost margin of crustal extension, consistent with the transition from thick- to thin-skinned deformation in Dr Paton's tectonic model (see Section 4.2.7). The southern boundary of the AGZ marks the edge of continental crust as well as as the model area and truncates before reaching the Agulhas-Falkland Fracture Zone to the south outside the study area (Figure 8-34). The northwestern boundary of the AGZ is the southeastern boundary of the SDZ. The crust within the zone is MESE.

The characteristic style-of-faulting within the zone is normal (90%) and strike-slip (10%) with no strike aleatory distributions since earthquake scenarios within the zone are modelled as point sources. The dip aleatory distributions for the zone are 45º (20%), 65º (60%) and 85º (20%) for normal faults; strike-slip faults dip 75º (40%) and 90º (60%).

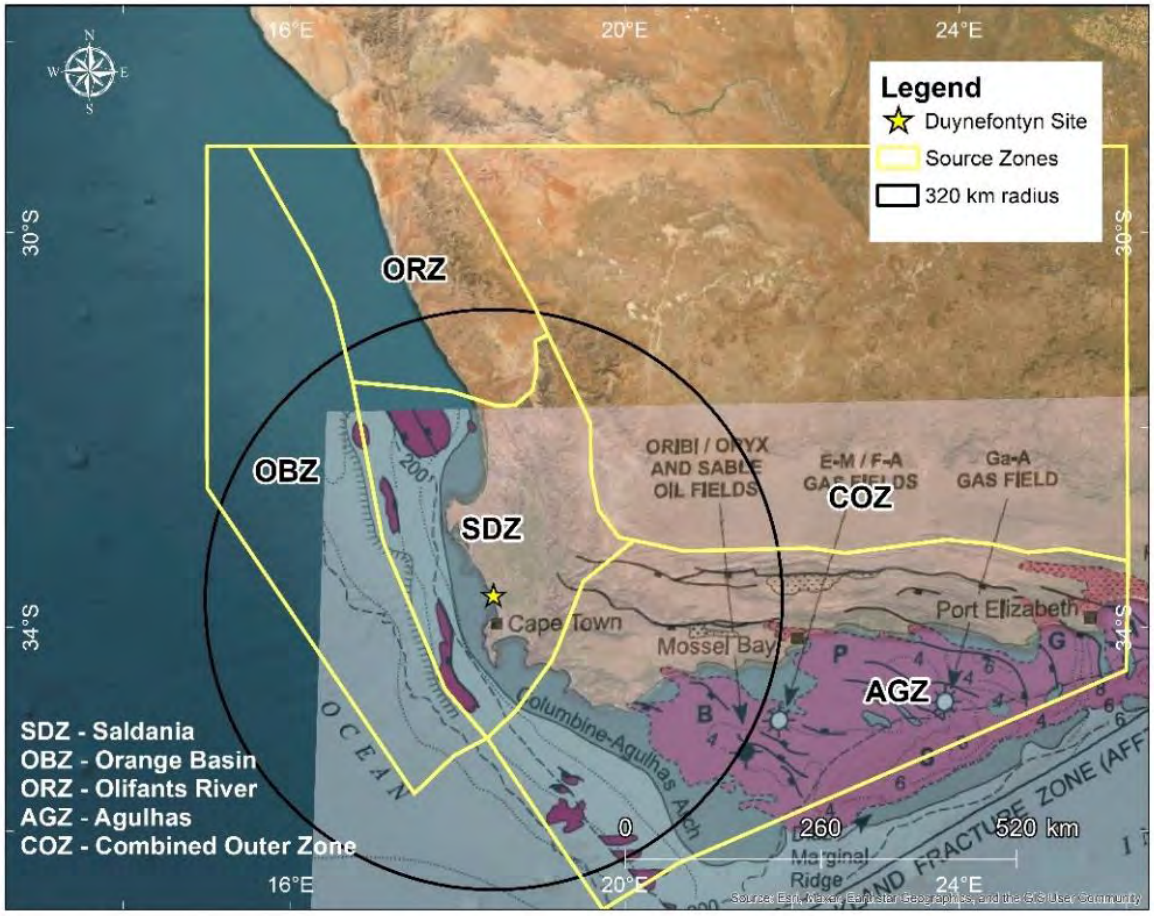

Figure 8-33. Offshore basins of the southern Cape in relation to the Agulhas-Falkland Fracture Zone, overlain on seismic source zones. From Broad et al. (2006).

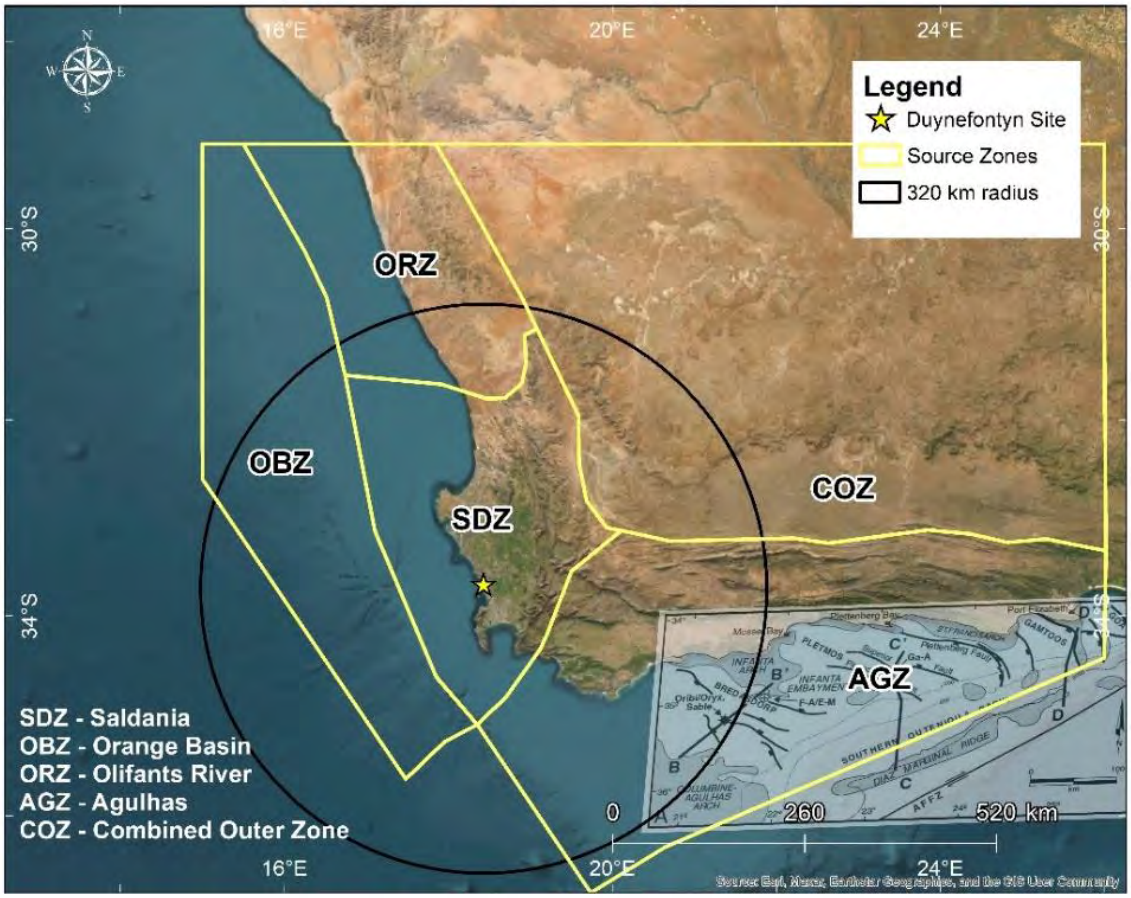

Figure 8-34. Offshore structures of the southern Cape in relation to the Agulhas-Falkland Fracture Zone, overlain on seismic source zones. From Broad et al. (2006).

8.3.5 Combined Outer Zone (COZ)

The remainder of the study area is contained within the COZ. It combines the three zones defined in the baseline study (Stamatakos et al., 2022), which include the Karoo, Namaqualand and Kaapvaal Craton zones. The COZ is composed of stable continental crust and non-Mesozoic extended crust. The SSM TI Team grouped these zones together because they were comparable given the criteria listed in Figure 8-1 and earthquakes generated in these zones are relatively distal with respect to the Duynefontyn site. The closest direct approach to the site is 180 km.

The characteristic style-of-faulting within the zone is normal (50%) and strike-slip (50%) with no strike aleatory distributions because earthquake scenarios within the zone are modelled as point sources. The aleatory distributions for fault dips in the zone are 45º (20%), 65º (60%) and 85º (20%) for normal faults, and 75º (40%) and 90º (60%) strike-slip faults.

8.4 FAULT SOURCE ASSESSMENTS

In PSHA studies, fault sources are defined as localisers of moderate- to large-magnitude earthquakes that have the potential to contribute to the seismic hazard at the site. They are typically defined and modelled as planar features in the upper crust of the Earth that can be depicted in map view as line traces, or as a series of line segments, and in the subsurface as a vertical or dipping plane (Figure 8-35).

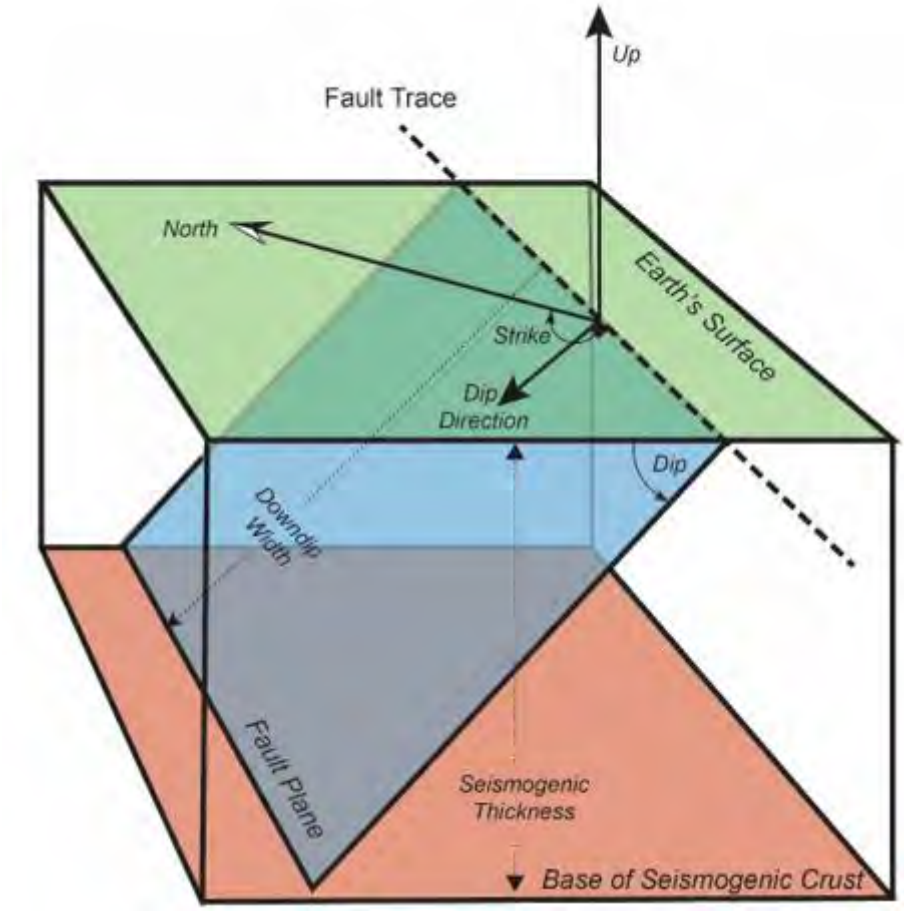

Figure 8-35. Block diagram showing the geometric parameters used to characterise fault sources in the seismic source model. Note that the most common convention for measuring strike and dip is using the right-hand rule.

Future seismicity generated by a fault source in the PSHA depend on a set of fault-specific attributes for each fault source. These attributes include:

- Fault geometry
- Style-of-faulting
- Seismogenic probability
- Characteristic magnitude and maximum magnitude
- Slip rate or recurrence rate
- Magnitude frequency distribution of future earthquake activity

8.4.1 Fault geometry

The geometric attributes needed to characterise a fault source in the PSHA are shown in Figure 8-35. These are defined by fault strike (azimuth clockwise relative to north), dip direction (90° from strike in the down-dip direction), dip (angle of the fault plane relative to horizontal), and down-dip width (measured on the fault plane from the top of the fault to its base at the boundary with the seismogenic crust). The location and geometric characteristics of fault sources are derived from a variety of data sources, including published studies, geologic maps, digital fault databases, offshore hydroacoustic images, and geophysical studies (e.g., gravity and magnetic anomaly surveys, seismic and electromagnetic imaging, or hypocentre locations). These data are used by the SSM TI Team to determine fault location (map coordinates), fault orientation (segment lengths and dip), and fault area. Estimates of fault dip are also based on structural relationships determined from geologic maps, exposures of the fault in the field and consideration of the tectonic setting of the region. Alternative interpretations in the location of a fault or its length, strike, and dip are accounted for in the SSM by alternative branches in the logic tree. These alternative branches capture the epistemic uncertainty in the geometric characteristics of fault sources.

8.4.2 Style of faulting

Consistent with the needs of the GMM, each fault source must be categorised according to one of the three end-member styles-of-faulting shown in Figure 8-36 and as described by Aki and Richards (1980). Dip-slip movement on normal and reverse faults occurs when the hanging wall moves predominantly down or up relative to the footwall due to extensional or contractional strain. Strike-slip movement occurs when the fault blocks move laterally relative to each other due to horizontal shearing forces. This horizontal shear can be dextral (right-lateral) or sinistral (left-lateral).

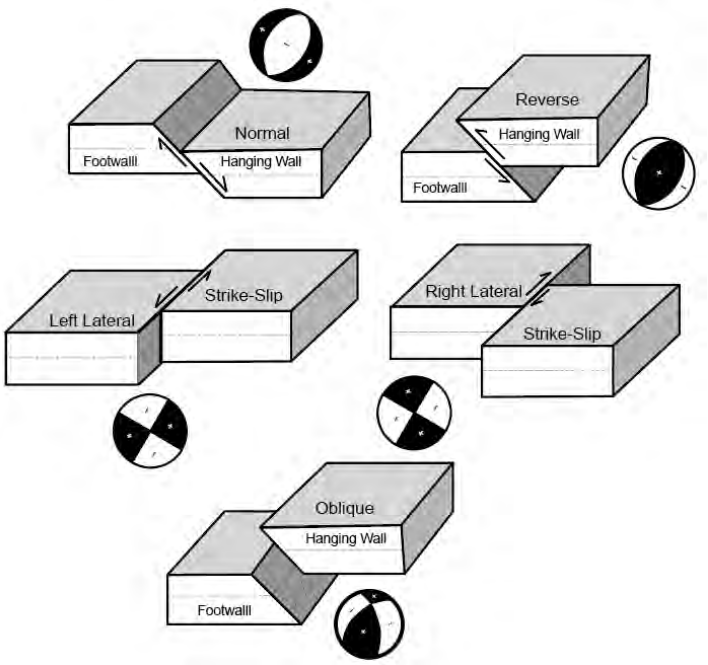

Figure 8-36. Block diagrams showing the various styles of faulting and the associated focal mechanism, or "beachball" symbol that indicates the type of slip and fault orientation that occurs during an earthquake on these types of fault sources.

The SSM TI Team's assessment of fault style is derived from published reports and papers, kinematic indicators of movements along fault planes such as piercing point offsets, slickensides, focal mechanisms or lithologic and stratigraphic displacements. In the SSM, each individual fault source is defined by a single style-of-faulting. Uncertainty regarding the style-of-faulting for an individual fault is treated as epistemic uncertainty with alternative logic tree branches.

8.4.3 Seismogenic probability

The seismogenic probability (p[S]) is the first node in the SSM logic tree. It establishes whether a fault is seismically active, and thus whether the fault has the potential to generate future earthquakes that could contribute to the seismic hazard at the site. Faults that the SSM TI Team definitively conclude to be seismically active are assigned a p[S] = 1.0. For uncertain fault activity, the SSM TI Team assigns a p[S] between 0.95 and 0.05. The value of p[S] reflects the confidence the SSM TI Team has in the likelihood that the fault or tectonic feature can generate future earthquakes that could contribute to the seismic hazard at the site. A fault source that is assigned a p[S] equal to zero is considered by the SSM TI Team to be inactive within the current tectonic regime. The assigned p[S] follows the general guidelines for all logic tree weights summarised in Table 8-2.

For cases with p[S] between 0.95 and 0.05, the fault is modelled as a localiser of future earthquakes, while the surrounding seismic source is modelled to contribute all possible future earthquakes based on a magnitude-frequency distribution derived from the project earthquake catalogue. Note that for all fault sources with a p[S] that is less than 1.0, there is a converse finite probability (1–p[S]) that the fault or tectonic feature is not seismogenic. Thus, p[S] and 1-p[S] capture the epistemic uncertainty in fault activity for each fault source (alternative interpretation of fault activity). The branch with p[S] captures the case where the fault is active and future earthquakes occur both on the fault and within the surrounding source zone. The branch with 1-p[S] captures the case in which fault is not seismically active and all future seismicity only occurs within the seismic source zone in which the fault lies.

The criteria used by the SSM TI Team to assess the p[S] of a fault includes geological evidence of activity within the contemporary tectonic regime, dynamic linkage to a nearby active fault, and the potential contribution of fault rupture to the seismic hazard at the site. The SSM TI Team considers a fault to be active, with a p[S] =1.0, if the fault is capable of generating moderate-to-large (**M**≥5) earthquakes and has demonstrative evidence of recent seismicity, displacement, or deformation of geomorphic surfaces and deposits that are Quaternary (<2.6 Ma) in age. The SSM TI Team considers a fault might be active, with a p[S] between 0.95 and 0.05, if the fault is capable of generating moderate-to-large (**M**≥5) earthquakes but lacks clear evidence for Quaternary deformation. The types of geological evidence that support the SSM TI Team's assessment of p[S] for fault sources whose activity is uncertain includes fault slip within the Pliocene (5.3 – 2.6 Ma) or perhaps even within the late Miocene (11.6 – 5.3 Ma)[1], aligned moderate- to large-magnitude hypocentres along the fault plane, or geomorphic features commonly associated with active faulting deformation. These features may include pressure ridges, pull-apart grabens, linear scarps, or triangular range-front facets. A fault, even if plotted on published geological maps, may be assigned a

[1] EPRI (1994) identifies active faults with evidence for fault slip in the Cenozoic, 66.0 Ma to the Present.

p[S] = 0.0 by the SSM TI Team if there is clear geological evidence that the fault is a relic of an earlier period of geological deformation and has remained inactive within the current neotectonic period (contemporary strain and stress regime). In the case where mapped faults are not characterised as a fault source in the SSM, the orientation and geometry of virtual ruptures within the source zone represent potential earthquake scenarios on those faults.

8.4.4 Magnitude

All faults that are included in the SSM with a p[S] ≥ 0.05 include an assessment of their potential to generate future earthquakes in terms of the largest earthquake the fault is capable of generating (e.g., Mmax) and the distribution of earthquakes with magnitudes less than Mmax that can occur on the fault.

Based on palaeoseismic data, Schwartz et al. (1981) showed that active faults or fault segments within large fault systems tend to generate similar size earthquakes within a relatively narrow range of magnitude near Mmax. Schwartz and Coppersmith (1984) referred to these repeated large-magnitude earthquakes as the fault's "characteristic earthquake," which in the current PSHA lexicon is abbreviated as Mchar. For active faults that cut Quaternary deposits in which a geologic record of faulting is preserved, Mchar is determined from the average displacement per event. The palaeoseismic analyses of the Wasatch Fault in Utah and the San Andreas Fault in California described in Schwartz and Coppersmith (1984) illustrate how the palaeoseismic record was used to quantify the displacement per event for those faults and how this translated to Mchar. Unfortunately, active faults with reliable records of prehistoric earthquakes are relatively rare in nature. Without this palaeoseismic record, Mchar is more commonly derived from scaling relationships that estimate magnitude from either fault length or fault rupture area.

As described in Section 8.2.6 and summarised in Table 8-3, the SSM TI Team evaluated eleven published fault scaling relationships. For fault sources, the SSM TI Team opted to use the magnitude scaling relationship from Thingbaijam et al. (2017) to derive Mchar from fault rupture area after comparison to other available empirical scaling relationships, including those by Wells and Coppersmith (1994), Leonard (2010 and 2014), and Yen and Ma (2011). The technical basis for this decision was that the Thingbaijam et al. (2017) model is the only scaling relationship based on seismic source inversion of well-recorded earthquakes. Thus, estimates of seismic moment and rupture area from Thingbaijam et al. (2017) were considered by the SSM TI Team to be well resolved compared to those derived from other published magnitude-scaling relationships.

To derive Mchar for fault sources, the SSM TI Team used the equation from Thingbaijam et al. (2017) that scales magnitude with rupture area given in Equation 8-8. This equation is then rearranged to solve for **M** (Equation 8-9). Fault rupture area is derived from fault length, fault dip, and thickness of the seismogenic crust. Epistemic uncertainty in Mchar is accounted for by alternative interpretations in fault length, fault dip, and the thickness of the seismogenic crust. All the logic tree combinations of length, width, and thickness (along with their associated weights) are used to calculate a distribution of rupture area. This distribution of rupture areas is then scaled to **M** using Equation 8-9 to derive the distribution of Mchar for the fault source.

8-8

$$\log_{10} RA = a + b\boldsymbol{M}$$

8-9

$$\boldsymbol{M} = (\log_{10} RA - a)/\, b$$

where **M** is moment magnitude, RA is the rupture area (km^2), and *a* and *b* are the slope and intercept of the Thingbaijam et al. (2017) relationship[2].

To capture the variability in Mchar, the SSM TI Team adopted a 0.5 (± 0.25) magnitude wide uniform (boxcar) aleatory distribution centred about the mean Mchar, following Youngs and Coppersmith (1985). This distribution is aleatory because all magnitudes within the boxcar can occur with the same relative frequency. Thus, Mmax for fault sources is defined as Mchar + 0.25 magnitude units.

8.4.5 Slip rate or recurrence rate

An important characteristic of all fault sources is the rate at which they produce earthquakes. Depending on the available geologic data and seismological data, this rate can be determined from the average rate of fault slip or from the rate at which earthquakes of a specified magnitude reoccur. In this context, slip is defined as the relative movement of geological features present on either side of a fault plane and is a displacement vector. Offset geomorphic features (e.g., stream channels, glacial moraines, fluvial or coastal terraces, truncated alluvial fans) or lithological markers (e.g., bedding, igneous dykes, cinder cones, sedimentary wedges) are common geologic features that can be used to determine the magnitude and orientation of offset. A slip rate is then calculated as the length of the slip vector divided by the period of geologic time over which this slip occurred.

The recurrence interval is defined as the average period between occurrences of earthquakes of a specified magnitude and is usually expressed as the average number of events greater than or equal to a certain magnitude per unit of time. The palaeoseismic studies needed to determine recurrence are usually restricted to geologic regimes that have experienced relatively continuous sediment accumulation over the recent geologic past, such as rivers, lakes, or alluvial fans. Recurrence is then established from well-dated exposures of offset soil or rock horizons that record individual palaeo-earthquakes, often from palaeoseismic trenches dug across an active fault trace.

The data used to assess slip rates or recurrence are inherently fault specific and depend on available geologic or geophysical data that can be used to assess fault slip or palaeoseismic information that constrains the ages of palaeo-earthquakes. The SSM TI Team's assessment of the relative weights assigned to the slip-rate or recurrence approach is a function of the fault-specific data available to assess each quantity. In ideal circumstances and with abundant palaeoseismic data yielding small uncertainties, both the presence of individual earthquakes and the timing of the recurrence interval approach would be given a higher weight relative to the slip-rate approach. This is because a slip rate provides the average behaviour of a fault

[2] The slope and intercept values are directly from Thingbaijam et al. (2017) and are different *a* and *b* to those used for the source zone MFDs in Section 8.2.10.

over a given period, while the recurrence approach provides more direct evidence of the actual timing of fault activity producing the paleao-earthquakes during the most recent period of fault activity. In low seismicity settings like the Western Cape, the data cited above that is needed to characterise slip rates or recurrence are often marginal or completely absent. In the absence of reliable fault slip data, the SSM TI Team may need to rely on indirect evidence of fault slip that may include slip estimates based on geodetic strain rates from Global Positioning Satellite (GPS) surveys or comparisons to analogous faults in similar seismotectonic environments. However, because these types of assessments are based on assumptions of fault behaviour over time, they must include large uncertainties.

8.4.6 Magnitude frequency distribution

Magnitude-Frequency Distributions (MFDs) define the relative occurrence of various earthquake magnitudes generated by a fault source. As described in Section 8.2.10, the magnitude frequency distribution for a seismic source is represented by an MFD curve. The shape and slope of the MFD curve expresses the relative frequency of increasing larger magnitude earthquakes (up to Mmax) as a function of magnitude.

The appropriate MFD for a fault source has been the subject of research for many years. Gutenberg and Richter (1954) observed that the appropriate MFD describing regional recurrence, such as for a source zone, is an exponential distribution (truncated at the Mmax). Based on rich historical seismicity and geological datasets, Schwartz and Coppersmith (1984) showed that recurrence relationships on both the Wasatch and San Andreas faults in the western United States did not follow a Gutenberg-Richter (GR) model. For moderate-to-large magnitude earthquakes, the exponential distribution underestimated observations from palaeoseismic trench studies. In response to these observations, Youngs and Coppersmith (1985) developed the characteristic earthquake distribution model, which they concluded appears to capture the fundamental behaviour of earthquake recurrence on the Wasatch and San Andreas faults and appears to apply to many other faults as well (e.g., Hecker et al., 2013).

As part of the evaluation process, the SSM TI Team considered alternative MFDs for use in defining the recurrence for fault sources (Table 8-11) as shown in Figure 8-37. In the simplified maximum magnitude model of Wesnousky et al. (1983), also referred to as the Maximum Moment Model, all of the moment rate is on a single magnitude such that minimum magnitude for MFDs (Mmin in Table 8-11 and Figure 8-37) = Mchar = Mmax. Smaller magnitudes occurring on the fault are assumed to be dependent events, mostly aftershocks. In the maximum moment model (Wesnousky et al., 1983; Wesnousky et al., 1984; Wesnousky, 1986), all strain is released in the large characteristic earthquakes, with no exponential lower-magnitude tail in the magnitude frequency distribution. The Wooddell, Abrahamson, Acevedo-Cabrera, and Youngs (WAACY) model (Wooddell and Abrahamson, 2013; Wooddell et al., 2014) is a modified version of the Youngs and Coppersmith (1985) characteristic model, modified such that rare large magnitude earthquakes above Mchar that may be associated with multi-segment ruptures of strike-slip systems can occur.

Table 8-11. Magnitude-frequency distributions evaluated by the SSM TI Team.

MFD Model	Description
Truncated Exponential	From Gutenberg and Richter (1954), the magnitude PDF is a doubly truncated exponential distribution defined by Mmin, Mmax, and the *b*-value. Useful for source zone recurrence but shown to overpredict fault source recurrence at moderate-to-large magnitude earthquakes.
Characteristic Earthquake	From Youngs and Coppersmith (1985), the magnitude PDF has two components: a characteristic portion and a lower- magnitude exponential portion. The characteristic portion is a uniform distribution, centred on Mchar. A 0.5 (± 0.25) magnitude wide uniform (boxcar) aleatory distribution centred about the mean Mchar captures the aleatory variability in Mchar. The lower-magnitude portion is a doubly truncated exponential distribution from Mmin to Mchar with a uniform *b*-value. The input parameters are Mmin, *b*-value, Mchar, ±0.25Mchar, and the percent of the total moment rate in the low-magnitude tail.
Maximum Magnitude (also known as the Maximum Moment Model)	Originally from Wesnousky et al. (1983) in which Mmin = Mchar = Mmax. Modified in Wesnousky et al. (1984) and Wesnousky (1986) to be just the characteristic earthquake without the lower-magnitude portion.
WACCY	From Wooddell and Abrahamson (2013) and Wooddell at al. (2014), the magnitude PDF has three components: a characteristic portion, a lower-magnitude exponential portion, and a high-magnitude exponential “tail.” The characteristic portion is a Gaussian distribution with mean of Mchar, standard deviation σ_M, and range from M_1 to M_2, where M_1 = Mchar – DM_1, with DM_1 being the offset between the low-magnitude tail and Mchar, and M_2 = Mchar + σ_M N_{sig}, with N_{sig} representing a multiple of standard deviations above the mean. The low magnitude portion fits an exponential distribution from Mmin to M_1 with a slope of -*b*. The high magnitude tail fits a doubly truncated exponential distribution from M_2 to Mmax and a *b*-value of b_{tail}. Parameters are Mmin, *b*, Mchar, σ_M, DM_1, N_{sig}, b_{tail}, Mmax, and percent of the total moment rate in the low-magnitude portion.

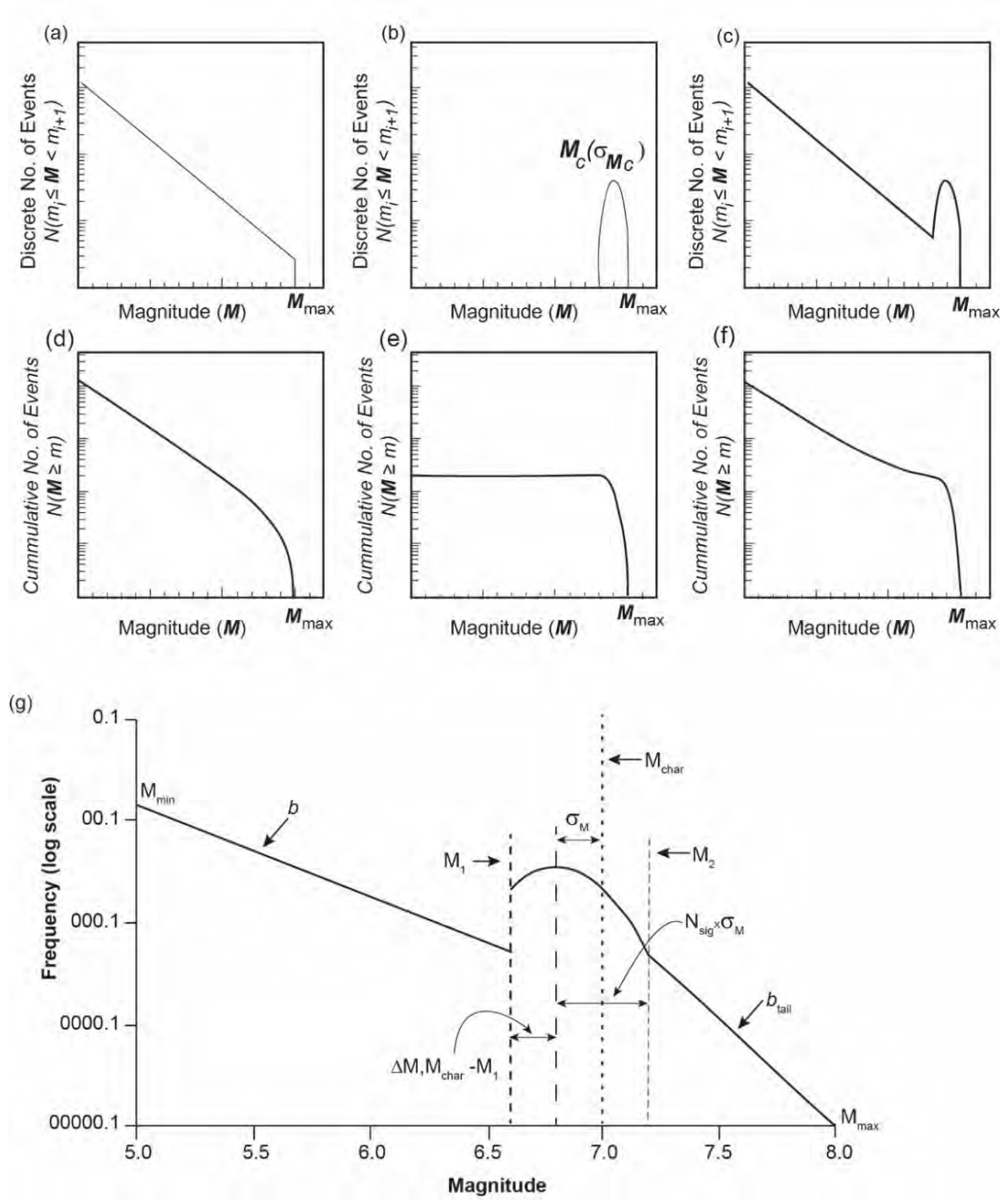

Figure 8-37. Earthquakes recurrence relationships, shown in non-cumulative (a–c) and cumulative (d–f) plots redrafted from Figure 2.3 of Bommer and Stafford (2009). (a and d) G–R model, (b and e) maximum magnitude model and (c and f) characteristic earthquake model. The WAACY model is shown in (g) and is redrafted from Figure 10-1 of PG&E (2015). See Table 8-12 for explanations of the terms shown in the figure.

8.5 FAULT SOURCES IN THE SSM

The evaluation of fault sources by the SSM TI Team began with the identification of known faults derived from a variety of data sources, including published studies, geologic maps, digital fault databases, offshore hydroacoustic images, and geophysical studies (e.g., gravity and magnetic anomalies, seismic and electromagnetic surveys, or hypocentre imaging). These data are used to derived fault length, fault area, and fault dip. The estimates of the fault dip and fault area are also based on geologic relationships, exposures of the fault, and consideration of the tectonics of the region. Geometric characteristics of these faults were then refined by the SSM TI Team based on focussed field and remote sensing investigations, including those in the Duynefontyn Data Collection (DDC) reports related to faulting and fault mapping (Cawthra et al., 2019; Claassen et al., 2024; Coppersmith et al., 2024; Cawthra and Van Zyl, 2023).

All mapped faults within 320 km of the Duynefontyn site that have the potential to generate moderate- to large-magnitude earthquakes, and thus to potentially generate hazard-significant ground motions at the site, were assessed by the SSM TI Team as potential fault sources (Table 8-12 and Figure 8-38). Table 8-12 also summarises the strike, dip, faulting style, and closest approach of these faults to the Duynefontyn site. This includes the five fault sources assessed by the SSM TI Team in the Baseline PSHA report (Stamatakos et al., 2022). In addition, the SSM TI Team also considered the proposed Milnerton lineament (also identified as the Milnerton-Cape Hangklip fault zone or the Melkbos Ridge Fault) as a possible fault source because of uncertainties surrounding its characterisation as an active fault and published technical and scientific reports that have included the Milnerton lineament, or a segment of the lineament, as contributing to or even controlling the seismic hazard at the Koeberg site (e.g., Hartnady, 2003; Dames and Moore, 1981; De Beer, 2007).

As part of the evaluation of data, models, and methods for the Duynefontyn SSHAC EL-2 study, the SSM TI Team also identified the Groenhof Fault as a potential additional fault source (labelled as GHF on Figure 8-38). The SSM TI Team assessed the Groenhof Fault based on field studies described in Coppersmith et al. (2024) and published information that the Groenhof Fault or similar basement structures may be the source of the 1969 E[**M**] 6.2 Ceres earthquake, as discussed in detail at Workshop 2 and in Smit et al. (2015).

Table 8-12. Fault sources considered in the SSM.

Fault Name	Label	Estimated Length	Style	Strike-Dip	Closest Approach to the site (measured in GIS from site to fault trace)
Table Bay Fault	TBF	22 km	Strike-Slip	NNW-SSE Vertical (± 20°)	8 km
Colenso Fault	COL	100 km	Strike-Slip	NW-SE Vertical (± 20°)	22 km
Kalbaskraal-Klipheuwel Fault	KKF	43 km	Strike-Slip	NW-SE Vertical (± 20°)	22 km
Piketberg-Wellington Fault	PWF	90 km	Strike-Slip	NW-SE Vertical (± 20°)	61 km
Worcester Fault	WOR	330 km	Normal	NW-SE to WNW-SSE to E-W down-to-the-south (75-90°)	73 km
Groenhof Fault	GHF	37 km	Strike-Slip	NW-SE Vertical (± 20°)	99 km
Proposed Milnerton Fault	MIL	115 km	Strike-Slip	NNW-SSE Vertical (± 20°)	8 km

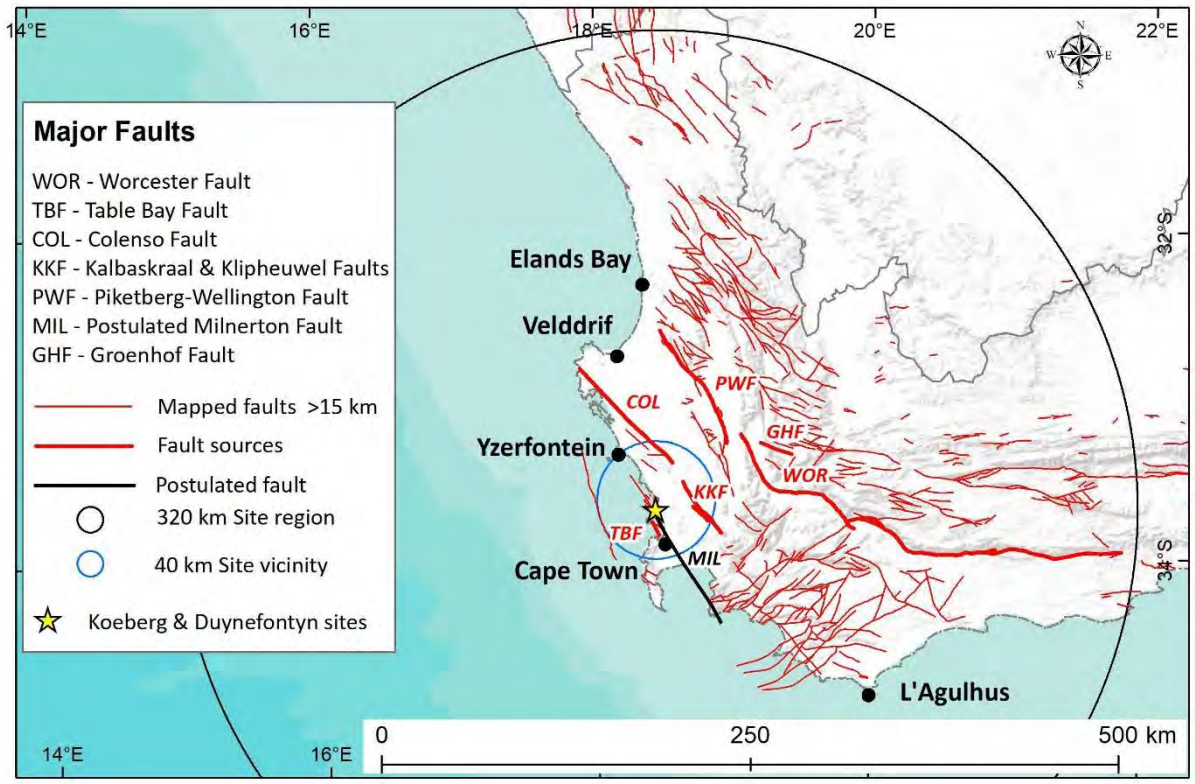

Figure 8-38. Regional mapped faults in the study area around the Duynefontyn site. The large black circle indicates the regional 320 km radius from the site (star). Major potential fault sources considered by the SSM TI Team are indicated with bold red lines. The proposed Milnerton Fault (MIL) is indicated by a bold black line.

Detailed assessments of the fault sources evaluated by the SSM TI Team listed in Table 8-12 are provided in the following subsections of this report. These include the SSM TI Team's evaluation of p[S] and supporting technical bases. The SSM TI Team assessed the style-of-faulting and geometry (strike and dip) for each fault source based on orientations of major mapped faults, stress and strain indicators, and earthquake focal mechanisms. For the Western Cape, the SSM TI Team compiled and evaluated existing focal mechanisms and kinematic indicators from relevant fault studies (Green and Bloch, 1971; Smit et al., 2015; Luden, 2015; Manzunzu et al., 2017; Manzunzu et al., 2019; Midzi et al., 2020; Moabi and Dhansay, 2021).

Much of the information used by the SSM TI Team to assess these fault sources is provided in the Duynefontyn Data Collection (DDC) reports related to faulting and fault mapping, specifically DDC3 (Cawthra et al., 2019), DDC5 (Claassen et al., 2024), DDC6 (Coppersmith et al., 2024), and DDC7 (Cawthra and Van Zyl, 2023). In all cases, the assessments began by first assigning a p[S], which is a judgment made by the SSM TI Team considering the available data, models, and methods and the criteria described in Section 8.4. This assessment of p[S] is the first node in the SSM fault source logic tree (Figure 8-39). The SSM TI Team also relied on the 3DStress™ analysis for the Western Cape region (Smart et al., 2023) using earthquake and borehole-breakout data to estimate the regional stress state based on fault orientations and displacement magnitudes. Based on this stress state, the analysis in Smart et al. (2023) identified which of the existing faults are most likely to rupture based on the slip tendency analysis of Morris et al. (1996).

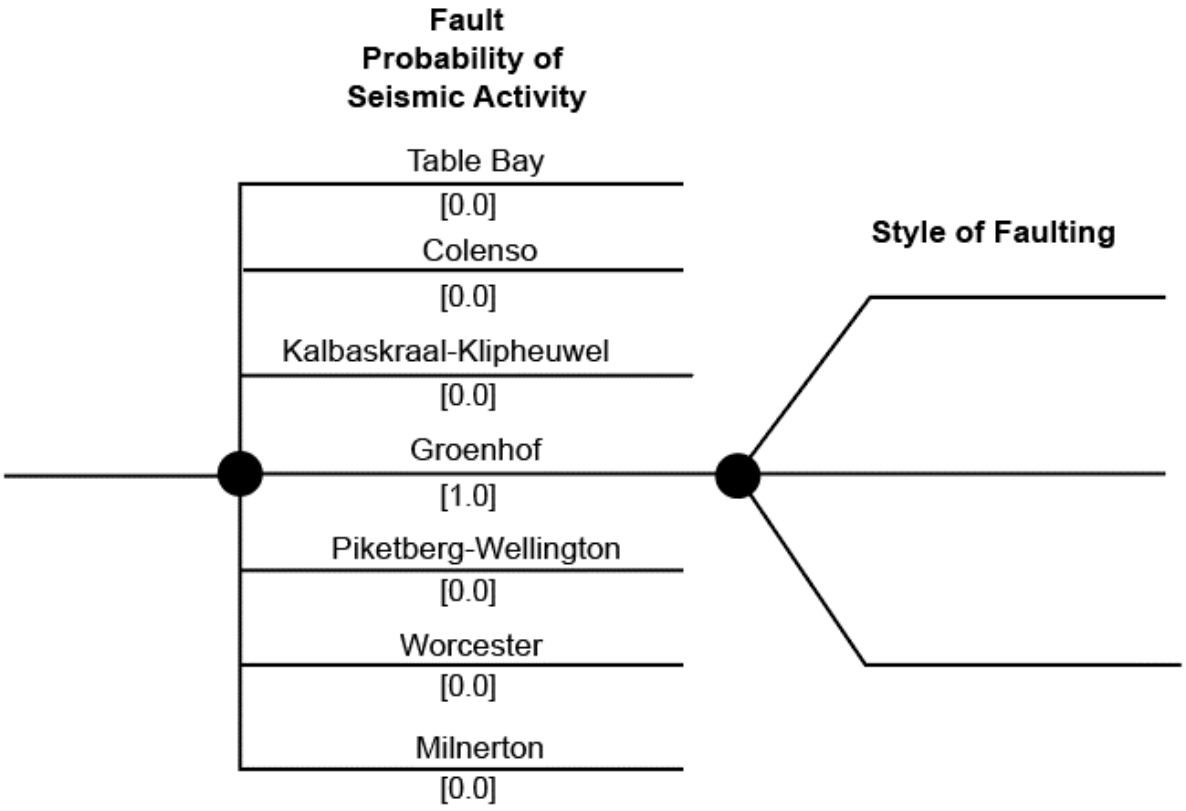

Figure 8-39. Logic tree for fault sources. The p[S] assigned by the SSM TI Team are given in square brackets below each fault name.

8.5.1 Table Bay Fault

Origin: The Table Bay fault zone was recognised as a possible offshore fault in De Beer's 2007 report (map number 00173) and formalised in peer-reviewed literature by MacHutchon et al. (2020). The delineation of this fault was based on apparent bedding truncation against a large northwest trending and linear bathymetric low that is coincident with a weakly linear magnetic anomaly (Figure 8-40). Based on a similar trend to the regional Colenso and Piketberg-Wellington faults, the authors of this paper infer that the Table Bay Fault is a major strike-slip zone. However, they described their interpretation of the Table Bay fault zone as "tentative" and a "supposition." No data was presented in MacHutchon et al. (2020) to constrain the possible age of faulting nor was any evidence revealed in their analysis to determine sense of slip or to quantify fault offset.

Decision: The SSM TI Team assigned a p[S] = 0.0 to the Table Bay Fault.

Technical Basis: The SSM TI Team carefully examined and systematically evaluated geological features revealed by the detailed multibeam bathymetry imagery in Table Bay along the trend of the mapped fault trace (Figures 8-41 through Figure 8-45). The analysis was aided by an update of Table Bay bathymetric data collected and processed in 2022 as described in Cawthra and Van Zyl (2023). The SSM TI Team's evaluation focussed on fault crossings of key geological features to identify possible strike-slip offsets. These included locations where the map traces of the Table Bay Fault crossed palaeo-drainages in seafloor bedrock and where the map traces of the fault crossed vertical or steeply dipping Cretaceous-age dolerite dykes. Although the SSM TI Team could not rule out the presence of a bedrock fault that is

aligned with bedding along the limb of a large fold and coincident with a long linear erosional scarp, no fault offsets of the palaeo-drainages or dolerite dykes were observed. While the timing of their incision is impossible to determine at this stage, these palaeo-drainage networks would likely have last been active in the most recent glacial-interglacial cycle spanning the last 125 ka. Based on the lack of observed fault offsets, the SSM TI Team concluded that, if a fault is present in the bedrock, it has not been active since the dolerite dykes were intruded into bedrock in the early Cretaceous and perhaps not since contractional deformation of the margin ended in the Palaeozoic. Therefore, the SSM TI Team ruled out neotectonic activity in Table Bay and assigned a p[S] = 0.0 for this fault.

Evaluation: Figure 8-41 shows the updated 1:50,000 scale bathymetric map for Table Bay (Cawthra and Van Zyl, 2023). The map incorporates the multibeam data collected in prior data collection campaigns, including the multibeam bathymetry data used in MacHutchon et al. (2020). The new map was completed with multibeam bathymetry collected by CGS staff in 2022, covering the onshore-offshore cadastral 1:50,000 scale sheet area 3318CD.

The map shows a distinct lack of sediment in Table Bay, although there are accumulations of unconsolidated material farther out to sea. Because of the absence of sediment, the bathymetry reveals intricate details about the bedrock fabric. In the south half of the map, granitoids are exposed and show a subdued and bulbous fabric typical of weathered granitic terranes. In the northern half of the map, Malmesbury Group sedimentary and meta-sedimentary rocks are exposed on the seafloor. The Malmesbury Group strata comprise late Neoproterozoic to earliest Cambrian turbiditic sequences of sandstones, greywackes, shales, and siltstones and their low-grade metamorphic equivalents (Von Veh, 1982). The bathymetry shows that these strata are characterised by a strong northwest-southeast structural grain dissected by small faults and fractures, palaeo-drainages, and several cross-cutting dolerite dykes. This fabric of the Malmesbury Group reflects differential erosion of steeply dipping strata of more competent sandstone greywacke and sandstone layers interbedded with less competent shale beds. Figure 8-42 shows outcrops of Malmesbury strata onshore at four locations in the southwestern Cape that depict the differential erosion and steep bedding dips that characterise the offshore Malmesbury fabric.

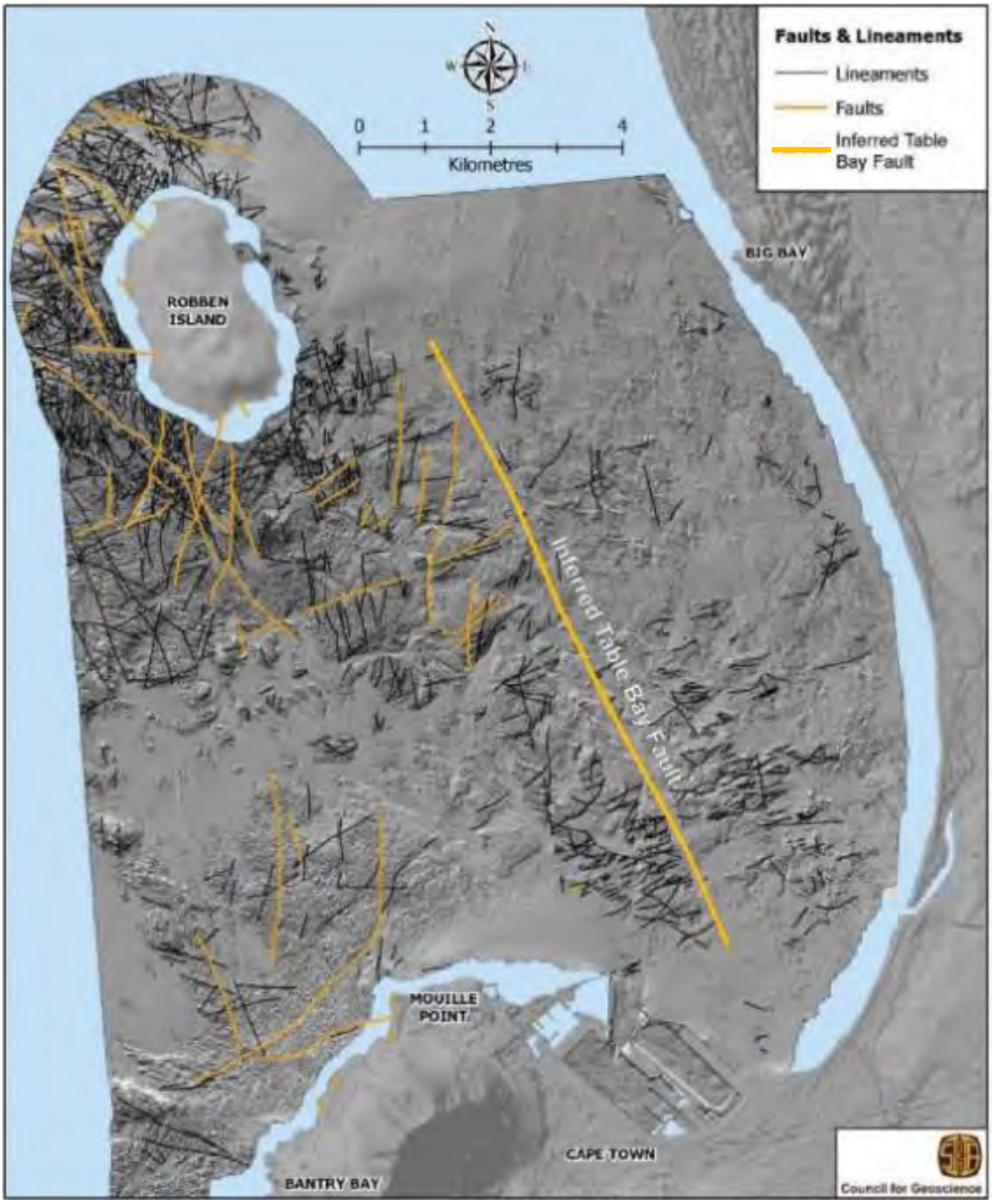

Figure 8-40. Modified reprint of figure 20 of MacHutchon et al. (2020) showing their interpreted structural lineaments, including the Table Bay Fault. In this image, the inferred Table Bay Fault lineament was enhanced and annotated for clarity.

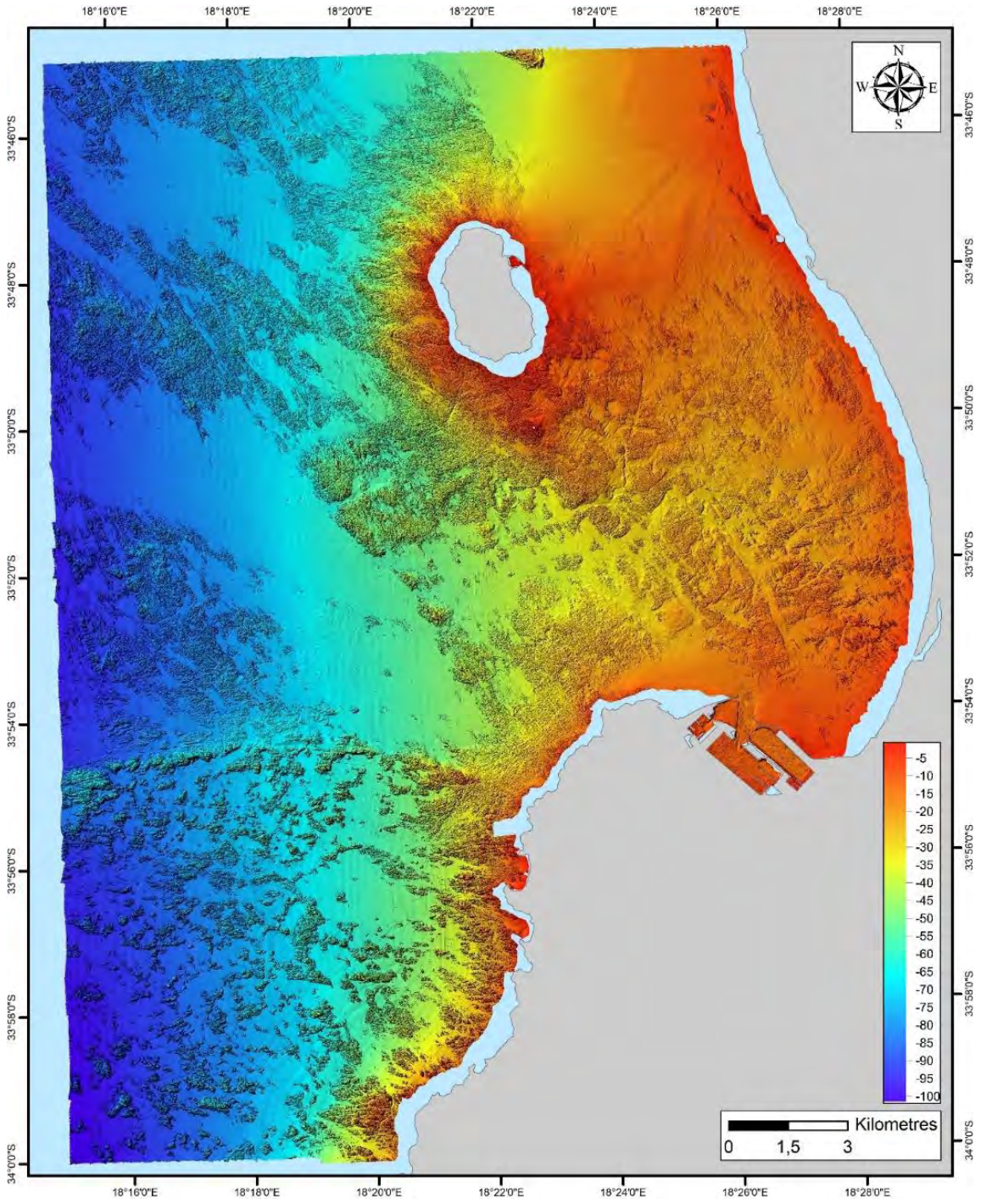

Figure 8-41. Multibeam echosounder data in the 1:50,000 scale map block of Table Bay. Rainbow colour shading shows depth in m. Reprinted from Figure 32 of Cawthra and Van Zyl (2024).

Figure 8-42. (a-d) Photographs of Malmesbury strata in outcrop at four locations around the Western Cape illustrating the differential erosion of Malmesbury lithologies in steeply dipping and vertical beds, although in some instances the Malmesbury strata are composed of finely laminated tectonic fabric that obscures the original sedimentary bedding. This differential erosion and tilting produce the pervasive fabric and structural grain observed in the bathymetric data. (e-f) Photographs of False bay Dyke Swarm dolerite.

The SSM TI Team examined geologic features in the Table Bay bathymetric map area to evaluate potential fault displacements along the trace of the inferred Table Bay Fault and to establish the sequence of geological events that explains the relative timing of observed cross-cutting relationships. Figure 8-43 shows the location of the various features evaluated by the TI Team in inset boxes numbered B1 and B2. The detailed images of these features with annotation are shown in Figure 8-44 and Figure 8-45.

In Figure 8-43, the SSM TI Team annotated a few bedding traces to highlight a first-order syncline of Malmesbury strata. The hinge line of the syncline can be traced for more than 10 km from Robben Island south-southeast towards Cape Town Harbour. This fold hinge was mapped on the beach at Robben Island by Rowe et al. (2010) as part of a syncline-anticline pair near Jan van Riebeeck's Quarry. The syncline is slightly asymmetric, with steeper dips on the west-dipping limb compared to the east-dipping limb. The erosional scarp identified as the Table Bay Fault in MacHutchon et al. (2020) is coincident with bedding on the steeper limb near the hinge line of the anticline pair. Given this geometry, one possible interpretation is that the linear erosional scarp formed due to preferential erosion along bedding planes of the steeply dipping strata and thus, it may not be related to an active fault.

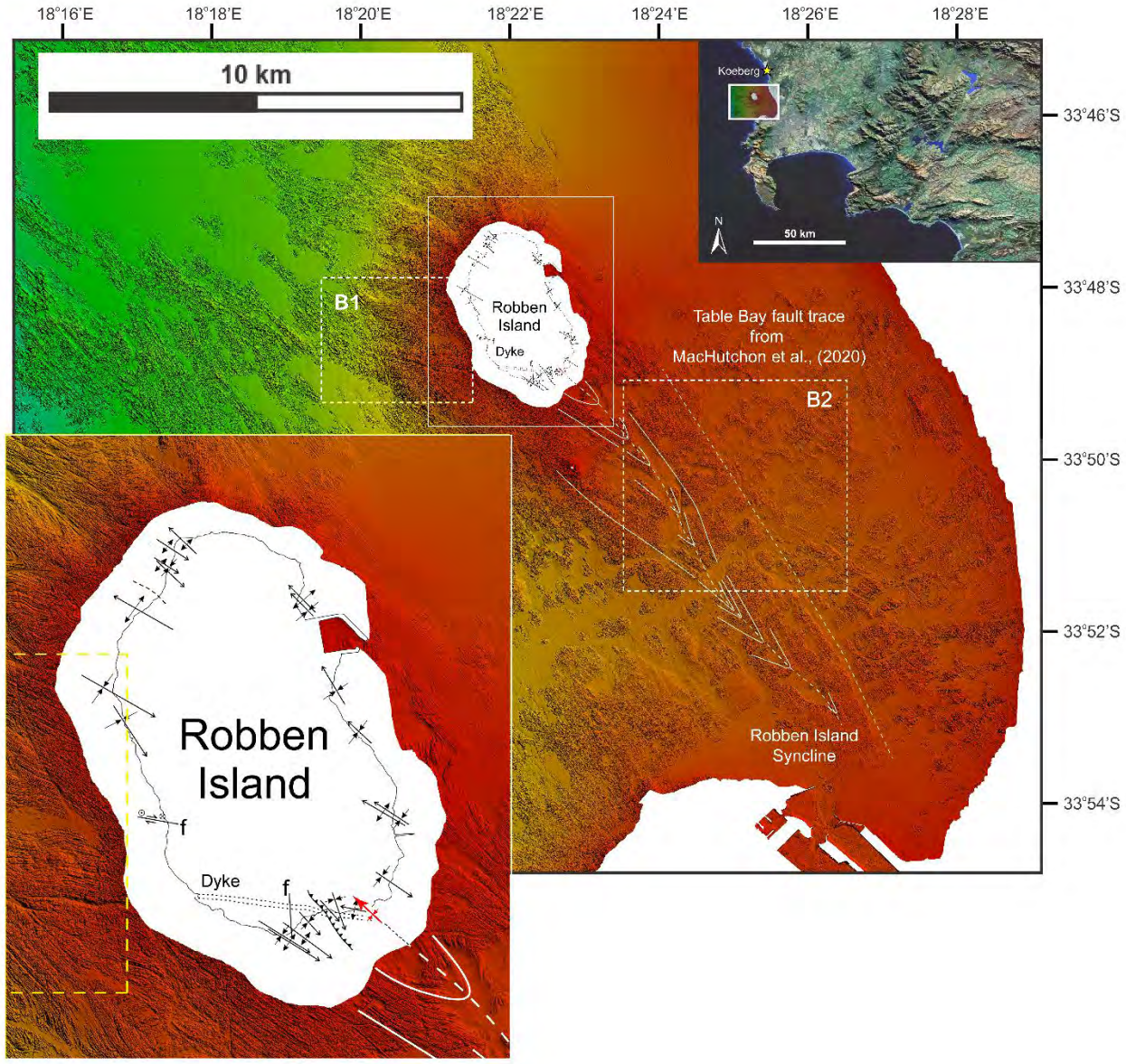

Figure 8-43. Table Bay 1:50,000 scale Bathymetric Maps showing the locations of inset boxes B1 and B2, and the line tracings illustrating the first-order syncline that extends from Robben Island south-southeast toward Cape Town Harbour. The inset shows an enlarged image of Robben Island with structural data from Rowe at al. (2010). The red-coloured syncline symbol shows the mapped fold axis of the offshore Robben Island syncline.

Box B1

In inset B1 (Figure 8-44), the SSM TI Team examined several cross-cutting relationships. First, there are several bedrock faults that disrupt the steeply dipping and folded Malmesbury strata. Second, there is a large roughly east-west trending dolerite dyke that crosscuts bedding and several of the bedrock faults. The dyke is part of the False Bay Dyke Swarm that was intruded into the crust of the Western Cape in the early Cretaceous 132.6 ± 6 Ma (Day, 1986; Reid et al., 1991; Blackeberg et al., 2011). The False Bay Dyke Swarm represents igneous activity associated with the opening of the South Atlantic during the early Cretaceous. The dykes are steeply-dipping to subvertical, with local variations between 75° to 89°dip (Blackeberg, 2011). A single False Bay dolerite dyke was also mapped across the southern edge of Robben Island

by Rowe et al. (2010). In the seafloor image, the dyke tips appear to be *en echelon*, which is a typical configuration for magma flow and dyke propagation under shear stress (Currie and Ferguson, 1970; Pollard,1987). Based on these observations, the SSM TI Team deduce the following: (1) Folding either predates or was coincident with faulting because the bedrock faults crosscut and truncate bedding. (2) The bedrock faults and folds have been inactive since the dykes intruded the Malmesbury strata in the early Cretaceous because the dyke is not displaced or offset by the bedrock faults or folds (at least within the meter-scale resolution of the image). This sequence of geological events is consistent with the seismotectonic framework in which the Malmesbury Group was folded and faulted soon after deposition in the Early Palaeozoic by compressional forces related to the assembly of Gondwana (Kisters, 2016). Dyke intrusions occurred later, when the southwestern Cape was under extensional forces related to the break-up of Gondwana. Neither of these stress conditions currently influence the neotectonics of the western Cape and thus the SSM TI Team conclude that these bedrock faults are not active sources of future seismicity.

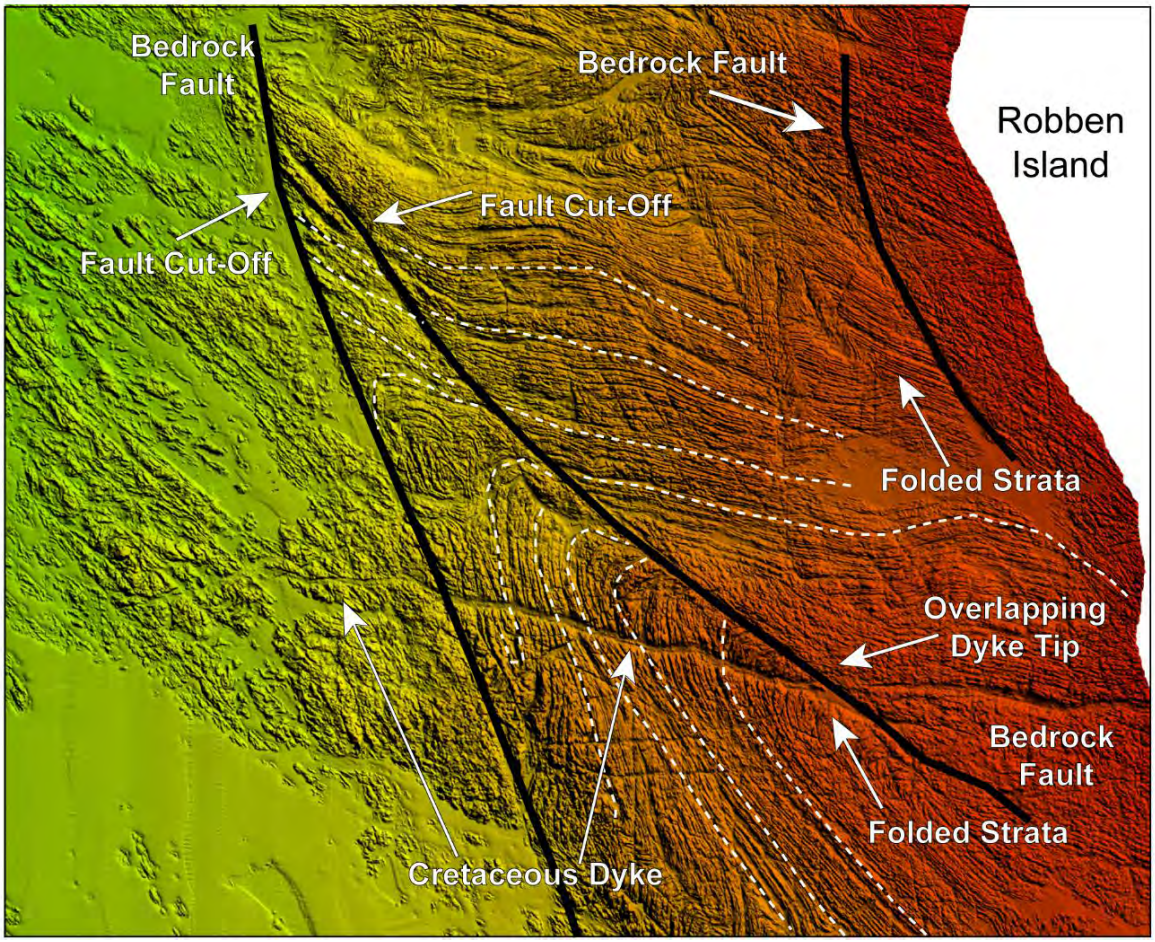

Figure 8-44. Box B1 from Figure 8-43, showing folded and faulted Malmesbury strata intruded by a Cretaceous dyke along the western shore of Robben Island.

Box B2

In Inset box B2 (Figure 8-45), the SSM TI Team evaluated a trace of the Table Bay Fault as it crosses several palaeo-drainages (incised channels) and as it crosses several dolerite dykes. The palaeo-drainages probably formed during the last time there was active incision of the bedrock, most likely from about 125 – 20 ka (Cawthra et al., 2020). The fall in sea level from

the Last Interglacial (~125 ka) to the Last Glacial Maximum (~20 ka) may have scoured out terrestrial sediments preserved in the channels. When sea level rose from the LGM position of 130 m below the present elevation, transgressive marine sediments likely filled in the channels. The SSM TI Team could not observe any fault offsets across these channels. The SSM TI Team also examined palaeo-drainages across all of Table Bay covered by the 1:50,000 scale bathymetry data and did not find any evidence that any of the palaeo-channels were offset. The SSM TI Team also could not find any visible offset of the dolerite dykes. The resolution of the bathymetry data is on the order of 5 m, therefore smaller offsets of the dolerite dyke by faults would not be visible. Therefore, the SSM TI Team concluded that if the Table Bay fault exists, it has not been active since at least the Early Cretaceous when the dolerite dykes were intruded into the Malmesbury bedrock.

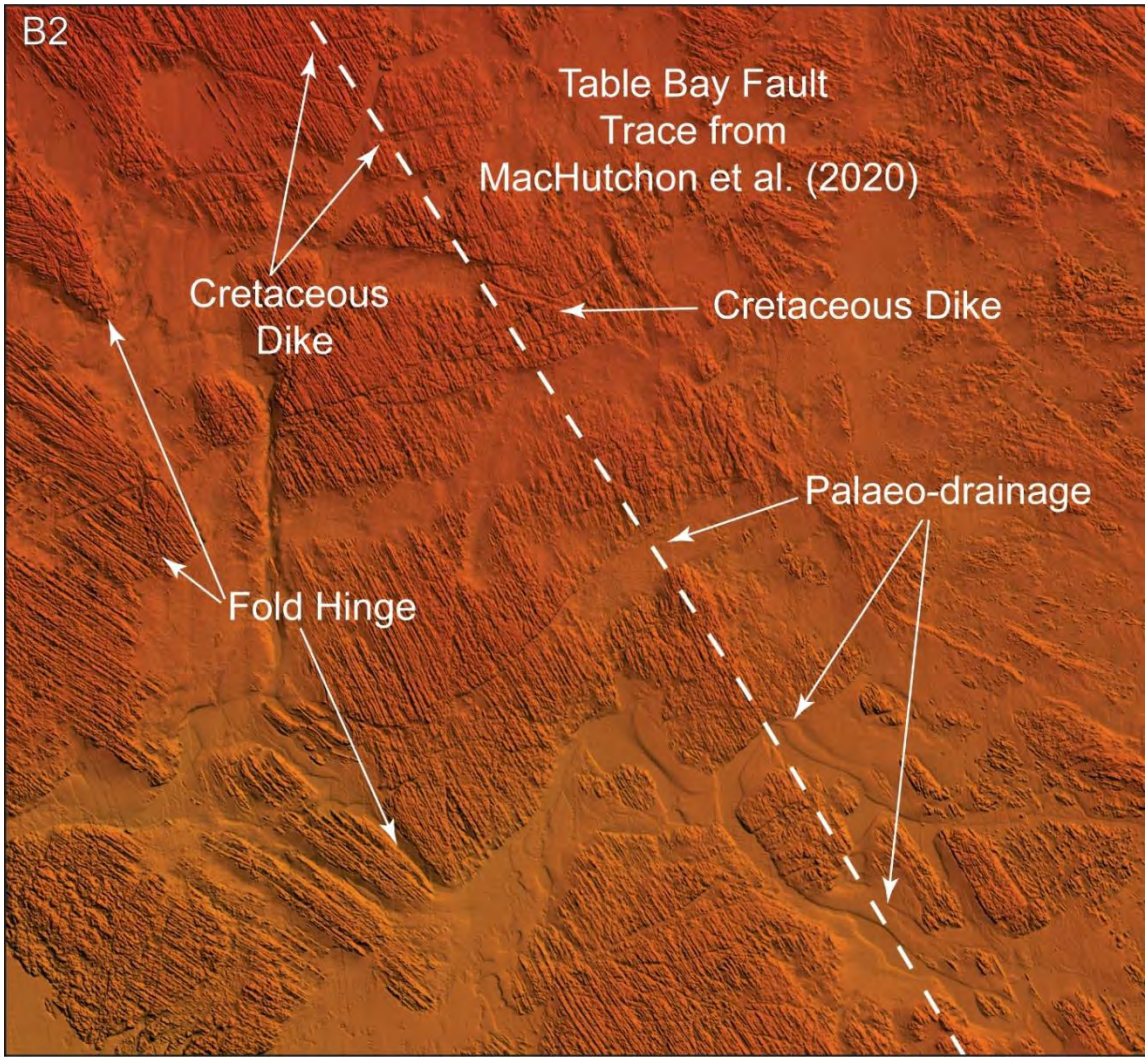

Figure 8-45. Box B2 from Figure 8-43, showing folded Malmesbury strata intruded by a Cretaceous dyke southeast of Robben Island. The image also maps the trace of the Table Bay Fault as it crosses several palaeo-drainages and Cretaceous dykes.

Summary: Based on a careful and systematic evaluation of the 1:50,000 scale bathymetric map for Table Bay (Cawthra and Van Zyl, 2023), the SSM TI Team found no evidence for fault offsets associated with the Table Bay Fault trace, nor evidence for fault slip of any of the post early Cretaceous strata imaged in the bathymetric map. Therefore, the SSM TI Team concluded that if the Table Bay Fault exists, it has not been active since at least the early

Cretaceous when the dolerite dykes were intruded into the Malmesbury bedrock. Therefore, the SSM TI Team assigned a p[S] =0 to the Table Bay Fault.

8.5.2 Colenso Fault

Origin: The Colenso Fault is a ~100 km, NW-SE striking, ~7-8 km wide anastomosing fault zone extending from Paternoster in the north to Malmesbury in the south (Figure 8-46a) that exhibits subvertical dipping and a predominantly strike-slip fault style (e.g., Kisters et al., 2002; de Beer et al., 2008; Hamel, 2015; Coppersmith et al., 2024). Although largely obscured and covered by soil, weathered bedrock and active farm land, the fault's location and extent is demarcated by various published geological maps (e.g., Visser and Schoch,1972; Theron, 1990; Roberts and Siegfried, 2009; Siegfried, 2014) that show offsets marked by juxtaposed lithostratigraphies, exposures of mylonite, silicified breccia, cataclasites and sheared granites (e.g., Kisters et al., 2002; Hamel, 2015; Kisters and Belcher, 2018) (Figure 8-46b-e). Collectively the Colenso and Kalbaskraal-Klipheuwel faults may form part of the larger, regional ~160-km-long Vredenburg-Stellenbosch (De Beer, 2007) or Saldanha-Darling-Franschhoek Fault Zone (Dames and Moore, 1976). In the seismotectonic model presented by Tankard (2022) at Workshop 2, these faults are considered synthethic Reidel shears associated with Pan-African motion along the Vredenburg Shear Zone at depth. The Colenso Fault marks the contact between the Tygerberg and Swartland terranes of the Pan-African Saldania orogenic belt along the southern and south-western edges of South Africa (Gresse et al., 2006). It abuts deformed rocks of the Cape Granite Suite against Malmesbury Group rocks, implying appreciable, but unknown vertical displacements, which could be on the order of ~1000 metres (De Beer et al., 2008). Kinematics of the area reveal that the fault initiated at about 547±6 Ma as a sinistral strike-slip fault but reversed its direction and became a dextral strike-slip fault some ~540 Ma. The reversal is attributed to the uplift of the Saldania Belt rocks as the Adamastor Ocean closed. The dextral strike-slip movement continued until the emplacement of the Cape Columbine granite at ~520 Ma (Kisters et al., 2002).

De Beer (2007) noted that the NW-SE orientation of a pre-existing ductile or brittle-ductile Vredenburg-Stellenbosch Fault Zone would be suited for reactivation in the Mesozoic and that shorter NE-striking fractures with narrow damage zones that were formed towards the end of the Pan-African deformation (Von Veh, 1982) may have been reactivated as transform faults during the Mesozoic. No evidence of movement post-dating the Mesozoic has yet been found.).

Decision: The SSM TI Team assigned a p[S] = 0.0 to the Colenso Fault.

Technical Basis: As summarised in Chapter 5, the Colenso Fault (includes the fault trace and zone) is a major tectonic feature in the proposed regional seismotectonic models of the Western Cape (e.g., Hartnady et al., 1974; Kisters and Belcher, 2018; Paton, 2022; Tankard, 2022). In addition, stress analyses undertaken reveal that under the present-day stress state, the Colenso Fault aligns with the region's preferred orientation for fault re-activation (Smart et al., 2023). Consequently, the SSM TI Team carefully considered all available geoscientific data that could be used to determine the fault zone's seismogenic probability. The SSM TI Team thoroughly evaluated the findings from a series of Duynefontyn PSHA supporting studies and activities which included marine terrace investigations (Claassen et al., 2024), onshore fault mapping (Coppersmith et al., 2024) and a micro-seismic study (Mulabisana, 2023).

Figure 8-46. (a) Location of the Colenso Fault. (b) and (c) Exposure of silicified breccia seen NNE of Darling. Photo (b) taken by Dr T. Dhansay at location S 33°20'4.86; E 18°25'0.81". (d) Mylonised shear zone exposed in bedrock at Cape Columbine (S 32°49'39.2; E 17°50'48.13" (e) Coastal exposure of a shear zone associated with the larger 8 km wide, anastomosing Colenso Fault Zone. These zones of weakness are often associated with the devolvement of gully inlets (S 32°48'55.33; E 17°54'0.30").

Based on an integrated evaluation of available information, the SSM TI Team did not find geological evidence for recent fault slip or deformation of geomorphic surfaces and deposits. The SSM TI Team concluded that the fault has most likely been inactive since at least the Miocene. Although some researchers (e.g., Sloan, 2022) suggest that microseismicity observed near Cape Town could be associated with the Colenso Fault Zone, the SSM TI

Team could not definitively make this association given uncertainty in location of hypocentres. The SSM TI Team also did not find evidence to be able to assign moderate to large earthquakes from the project catalogue to the Colenso Fault Zone. The field studies by Coppersmith et al. (2024) and Claassen et al. (2024) did not reveal any evidence of young deformation consistent with the criteria described in Section 8.4.3. This latter criterion is especially telling given the low denudation and erosion rates for the Western Cape, on the order of 3 to 5 m/My (Scharf et al., 2011, Bierman, 2023). Thus, any geomorphic features created by fault slip on the Colenso Fault would be preserved for a significant period of geologic time. Although the SSM TI Team recognises that this is a major crustal feature in the Western Cape, the geologic record summarised above does not support including the Colenso Fault Zone as a fault source in the SSM.

Evaluation: The SSM TI Team's evaluation included the results derived from marine terrace studies (Claassen et al., 2024); onshore fault studies (Coppersmith et al., 2024); a micro-seismicity study (Mulabisana, 2023) and additional geologic lines of evidence in the assessment of the Colenso Fault as a fault source.

Marine Terrace Studies

Claassen et al. (2024) undertook detailed identification and mapping of marine terraces to evaluate the potential for surface tectonic faulting, deformation and tectonic warping between Bekbaai and Duminypunt where the Colenso Fault Zone is projected to occur (e.g., De Beer et al., 2008). Granitic exposures on either side of the embayment show several exposures with mylonite, silicified breccia, cataclasites, and sheared and fractured granites, confirming the fault's presence. These structural zones of weaknesses weather negatively to produce perpendicular, parallel and obliquely orientated intermittent inlets/gullies and surge channels cross-cutting the coastal margin that often make palaeoshoreline identification difficult, especially for the lower platforms. Despite this, a review of previous palaeoshoreline studies (Visser and Schoch, 1973) and additional detailed fieldwork (Claassen et al., 2024) confirmed a series of three stepped marine terrace platforms in the area (Figure 8-47 and Figure 8-48):

- A presumed mid-Holocene (~6 kya) platform at elevations ranging between 3.2 – 3.6 m amsl (~ 3.5 m amsl) identified between Cape Columbine and Tieties Bay and east and west of Rooisteen.
- A 6 ± 1m amsl platform ranging from a minimum of 4.9 m amsl to a maximum of 7.2 m amsl of presumed MIS 5e age (~125 kya)
- A rock-cut 9 ~±1 m terrace ranging from 8.4 - 10.8 m amsl of presumed MIS 11 age (~400 kya).

In addition, between the Cape Columbine and Rooisteen headlands a coast-parallel wave-cut notch (Figure 8-49) occurs some 80 - 350 m inland. The notch appears to be cut into northward sloping cross-bedded, light-grey biocalcareous-siliclastic aeolianite (palaeodune material), which is capped by a calcrete layer associated with the Langebaan Formation occurring at elevations of between ~20 - 40 m amsl. Although the base of the cliff is not well defined, at isolated areas with limited cover a shoreline angle was measured at 9.0 – 11.5 m amsl, which is tentatively correlated to the sea-level highstand associated with the mid-Pleistocene MIS 11. A similar observation is made by Visser and Schoch (1973) that records a 9.75 m bank of beach gravel immediately below the lime-rich cliff north of the Cape Columbine lighthouse and Kleinwesbaai. All three marine terrace platform altimetries are correlated across the area with

no obvious recognisable indications of vertical displacement (Figure 8-48) for at least the last ~400 ky (Claassen et al., 2024), while recognising the limitations or scientific assumptions that underpin this conclusion:

Fieldwork undertaken to map and correlate palaeosea-level indicators are subject to elevation measurement accuracy and precision inaccuracy (<0.5 m, usually centimetres). Field measurements were taken with a differential GPS, however, in general, due to the presence of cliffs or other natural features impeded the optimal satellite reception of the GPS signal, the average accuracy obtained varied in the centimetre range. Subjective uncertainties in the identification and interpretation of palaeosea levels well as ranking criteria used to define their quality and reliability.

Marine terrace studies are only able to access vertical neotectonic displacement along faults. Small to medium scale horizontal displacement associated with a strike-slip fault system may not be detected. Within a regional context and considering the variation within a given palaeo sea-level elevation and age range, small vertical displacements can be difficult to identify or assign to neotectonics, rather than eustacy. The lack of geochronology for marine terraces at various elevations along the southwest Cape coastline requires the authors to assume that these undated terraces occurring at a particular elevation can be correlated to surrounding terraces occurring at a similar height and of known age in the area as it relates to existing, albeit sparse geochronology as well as inferred from global averages.

Figure 8-47. (a) Scattered pebbles and shells noted on a 6.2 m amsl platform by Cape Castle (S 32°49'57.03"; E 17°51'5.00"). (b) Broad planed wave-cut platform (WCP) observed south of Cape Castle (S 32°50'2.50"; E 17°51'2.55"). (c) A ± 4.9 marine platform at Tietiesbaai of which the shoreline angle could not be identified due to dune cover (S 32°50'7.83"; E 17°51'21.74"). BE refers to the backedge of the terrace. (d) Bevelled wave-cut platform at ± 5.861 m amsl (S 32°54'35.38"; E 17°51'32.54"). SC refers to sea cliff; SLA refers to shoreline angle. (e) Wave-cut platform with granite pebbles and cobbles located at ± 6.8 m amsl, interpreted as a possible storm deposit (S 32°54'20.46"; E 17°51'30.98").

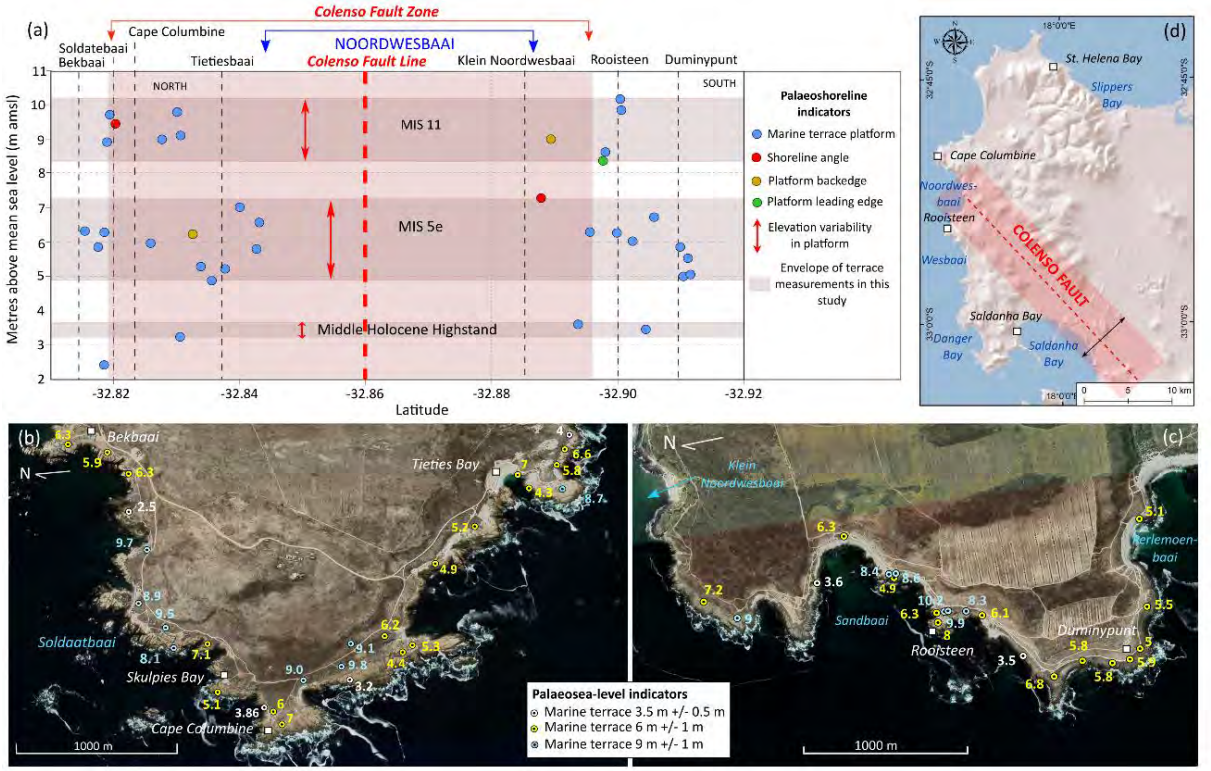

Figure 8-48. (a) Shoreline indicator correlation diagram for the area between Bekbaai and Duminypunt within the greater Velddrif / Saldanha area defined by Claassen et al. (2024). Relatively good correlation is found between the upper Holocene highstand (presumed ~3.5 m amsl), the presumed MIS 5e terraces (~6 ± 1 m amsl) and presumed MIS 11 terraces (~9 ± 1 m amsl). The Colenso Fault is projected to run through Noordwesbaai. No obvious offset of terraces is noted across the fault trace. (b) Palaeoshoreline indicators identified during fieldwork between Bekbaai and Tieties Bay and (c) between Klein Noordwesbaai and Duminypunt. (d) Index map denoting the projected occurrence of the Colenso Fault.

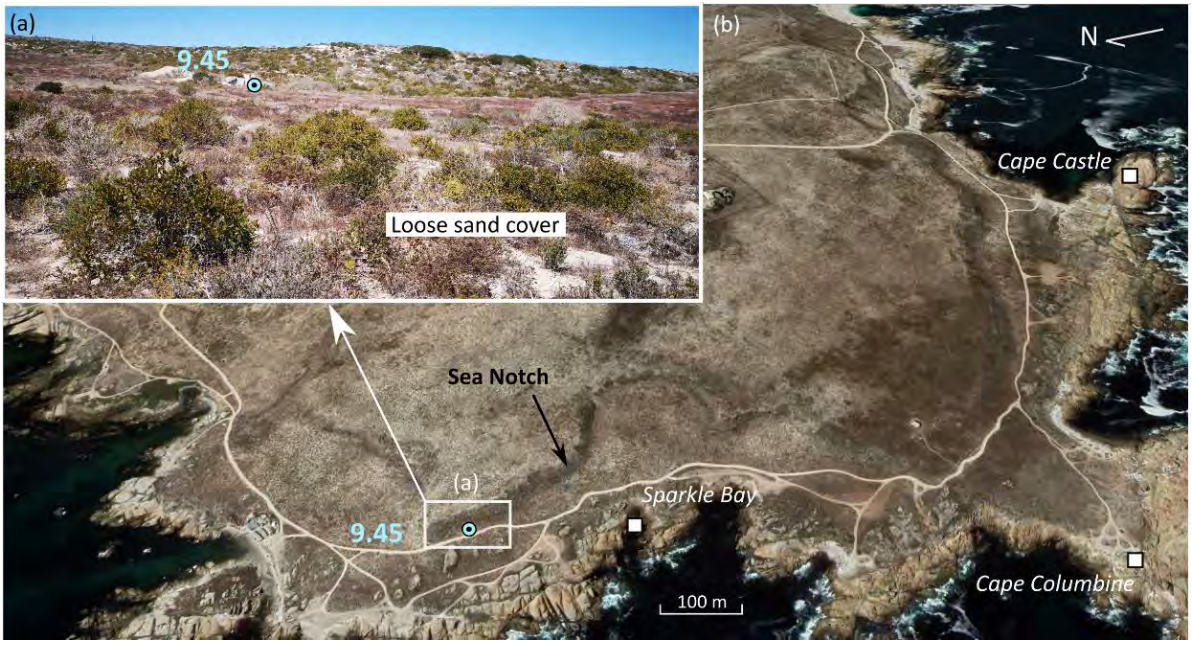

Figure 8-49. (a) and (b) Coast parallel wave-cut notch carved into palaeodune sediments. Although the base of the notch could not be measured on bedrock, a few isolated bedrock exposures close to the base of the cliff, not covered by sediment, all provide elevations of between 9-10 m amsl and so the notch may be associated with mid-Pleistocene (MIS 11). Figure (a) is located at (S 32°49'13.32"S; E 17°51'9.65").

Onshore Fault Studies

Quaternary mapping was undertaken by Coppersmith et al. (2024) to determine recency or limit the age of faulting, slip rate and fault geometry. Mapping and additional desktop interpretation of a high resolution 2 m digital elevation model in the vicinity of the Colenso Fault Zone (Figure 8-50) were aimed at assessing possible offset or surface disruption of Quaternary sediments as well as aeolianite and an associated calcrete cap overlaying the fault zone (Coppersmith et al., 2024). West of the Cape Columbine lighthouse, a 2 - 3 m wide brecciated bedrock shear zone exhibits mylonised zones indicating the shearing occurred at considerable depth and associated pressure (Figure 8-46d). The presence of mylonite and lack of clay gouge indicate that the fault zone formed deeper in the seismogenic crust and may thus be a “rootless” exhumed fault zone.

A desktop review of the DEM, southeast along strike of this bedrock shear, did not identify any surface disruption to the aeolianite. The aeolianite is also frequently overlain by a thick (>3 metres) solution-hollowed hardpan, calcrete cap. The calcrete cap lacked shearing and recemented features at surface as observed during fieldwork. The SSM TI Team assumes that if the cap was brittlely deformed and offset by faulting, it would also take considerable geologic time to erode (especially given the slow erosion rates in the region) and re-cement an offset within the calcrete cap that could not be otherwise detected in the DEM or in the field (Figure 8-51).

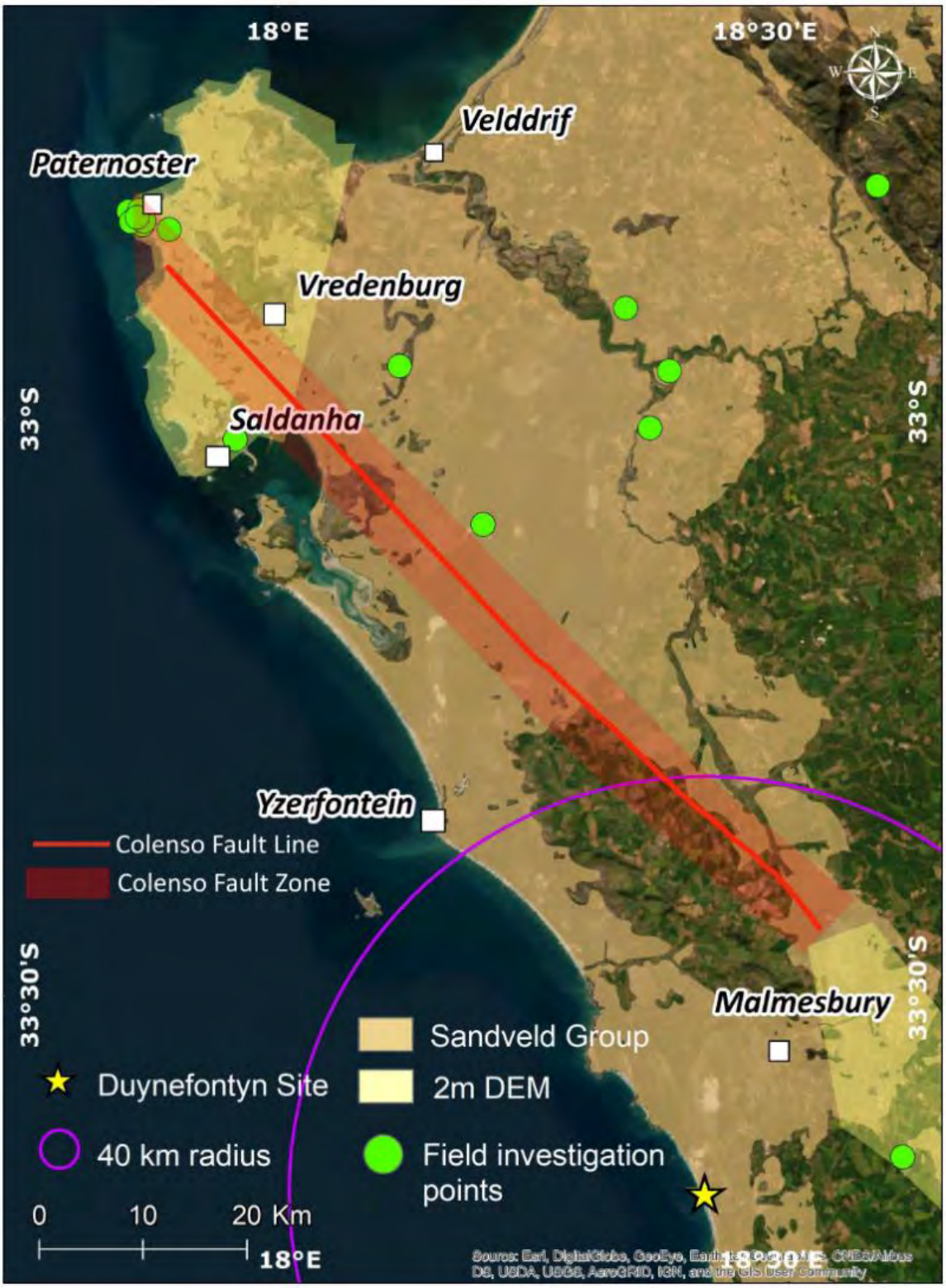

Figure 8-50. Map showing Quaternary mapping sites/ field investigation points along the Colenso Fault and the location of the 2 m DEM used for desktop analysis.

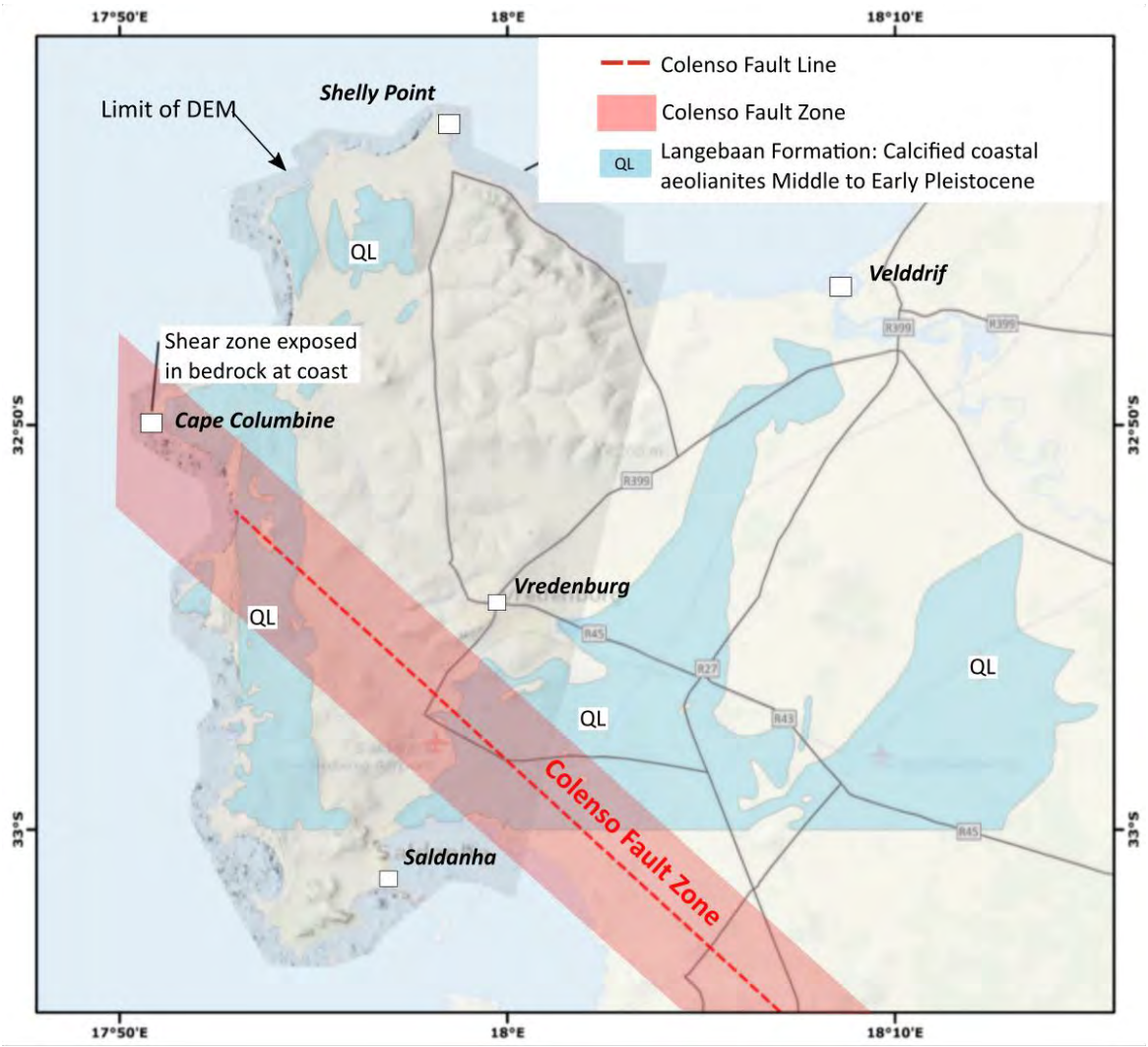

Figure 8-51. Map showing the mapped extent of the Langebaan Formation with respect to the mapped Colenso Fault.

Micro-seismicity Study

The SSM TI Team also reviewed and interpreted the findings of a microseismicity study (Mulabisana, 2023) conducted along the length of the Colenso Fault aimed at assessing its activity. Seven stations were deployed over a six month period from September 2022 - February 2023 and recorded 16 events. Only five events were recorded near the Colenso Fault and were concentrated along a weak alignment parallel to the fault but offset 5-10 km to the northeast (Figure 8-52). If these hypocentres are on the Colenso Fault, these data would imply a dip of approximately 60º to the northeast. The average error ellipse on three hypocentre locations were between 0.8 and 9.2 km. Waveform data was not clear enough for focal mechanism analysis and depth evaluation, and considering location uncertainty, the SSM TI Team decided that the seismicity could not be utilised as a reliable indicator of activity along the fault.

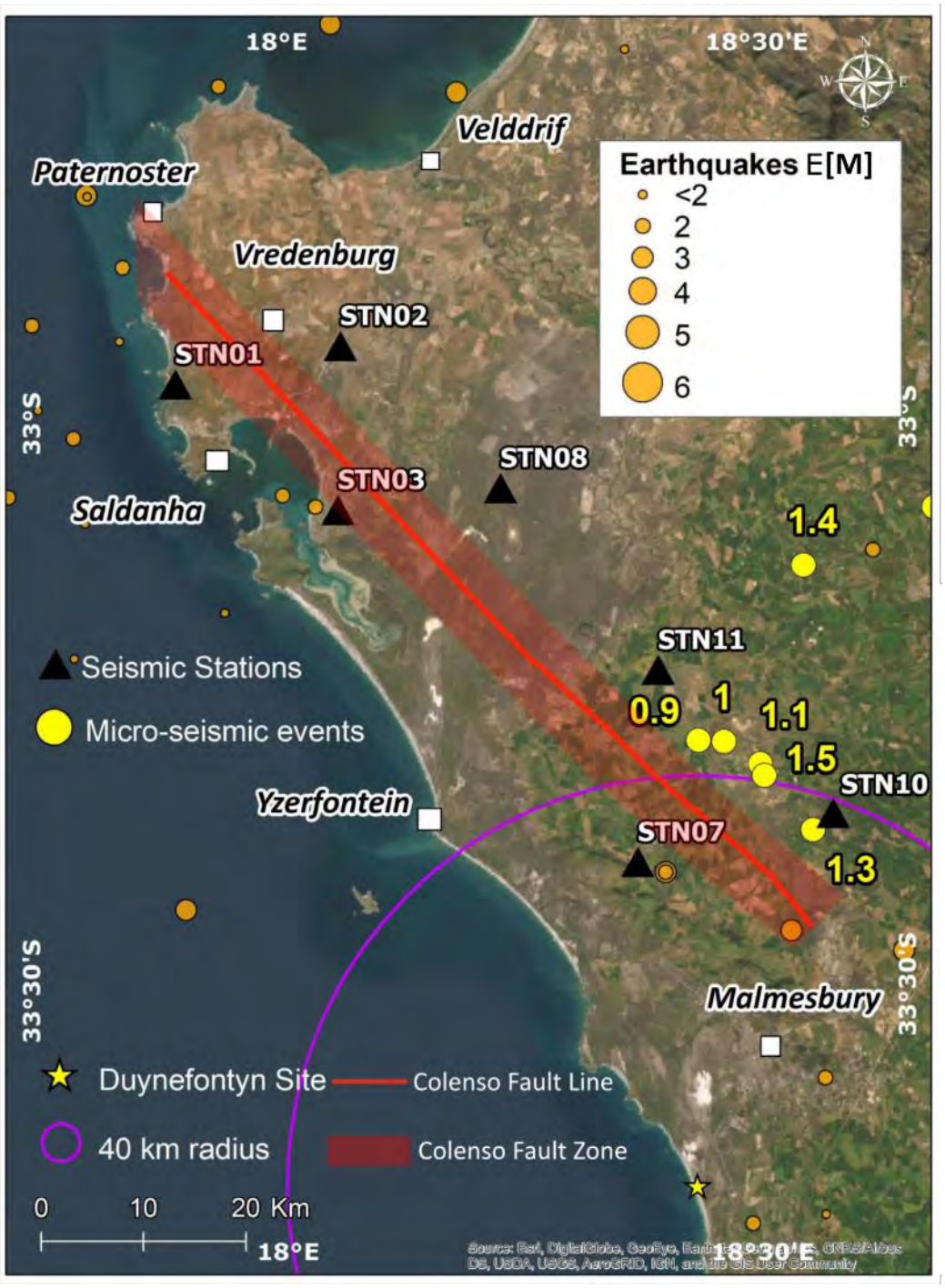

Figure 8-52. Map showing the location of micro-seismic events recorded by Mulabisana (2023) near the Colenso Fault.

Additional lines of geologic evidence

The SSM TI Team undertook a full evaluation of the contrasting views regarding Miocene and younger neotectonics along the west coast of South Africa. There are contrasting views concerning the spatial aspects, sense, magnitude and timing of deformation associated with the current tectonic regime (e.g., Roberts et al., 2011, 2013). Varying interpretations of data related to geologic, palaeontologic and geochronologic evidence are used to either infer tectonism (Krige, 1927; Tankard, 1976a, b; Coetzee, 1978a, b; Rogers, 1982; Dingle et al.,

1983; Coetzee and Rogers, 1982; Roberts and Brink, 2002) or non-tectonic eustacy (Hendey, 1981; Pether, 1994; Pickford, 1998; Pether et al., 2000; Compton et al., 2006; Roberts et al., 2011; Baby et al., 2020) as the reasons for the perceived variation in observed elevations of some Neogene marine terraces and deposits.

The SSM TI Team considered the various arguments and associated evidence for possible SE marginal Neogene tectonic downwarping along a NE-SW axis (Cape Micro Plate hypothesis) (Figure 8-53) between Saldanha Bay and Cape Town (Partridge and Maud, 1987, 2000) in response to activity possibly associated with the Colenso Fault.

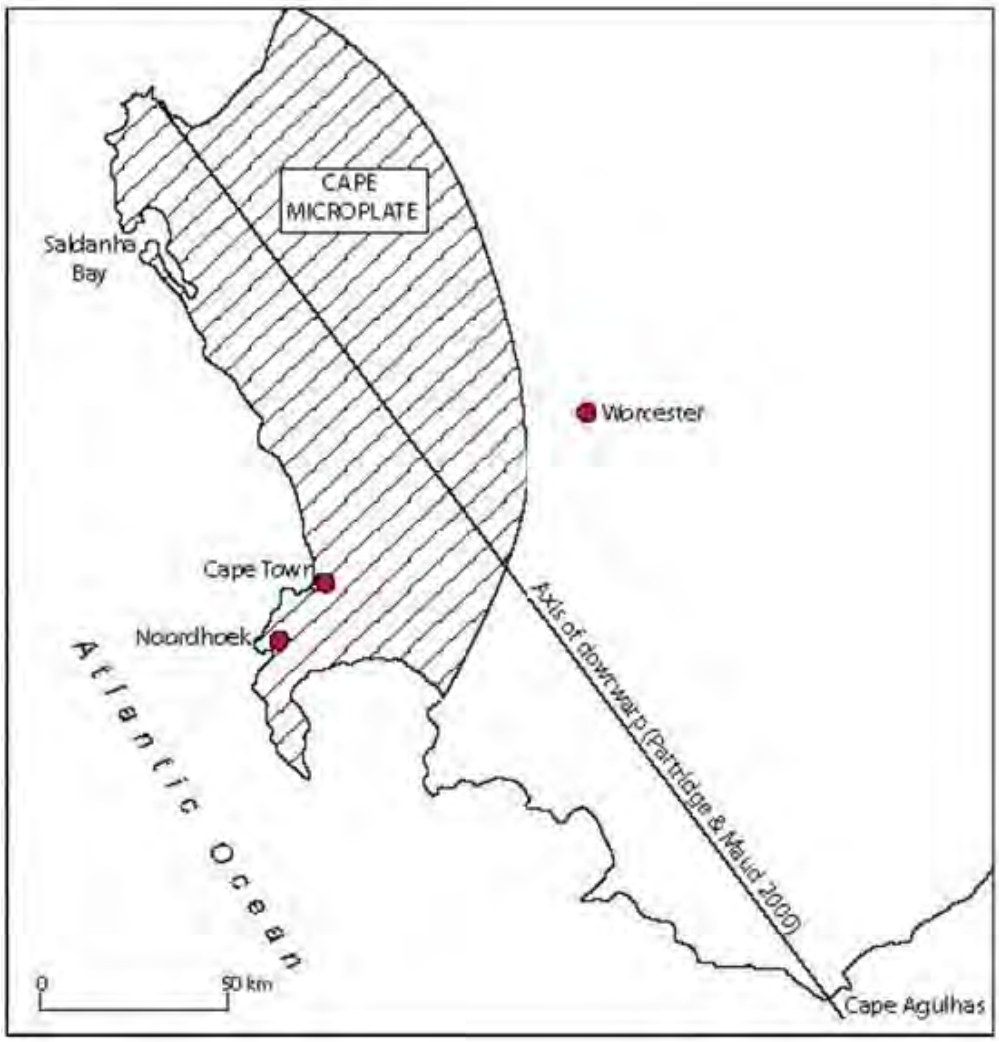

Figure 8-53. The NE-SW axis of downwarp proposed by Partridge and Maud (1987, 2000) in the Western Cape.

Within the greater Saldanha Bay region, the occurrence of numerous boreholes in the greater Velddrif and Geelbek area enabled the creation of various interpolated lithostratigraphic palaeotopographic surfaces (Figure 8-54) (Claassen et al., 2024). Assessing these palaeo-surfaces enables the analysis and evaluation of any possible palaeoshoreline indicators that may be present or any evidence of offset from nearby faults such as the Colenso Fault Zone. The interpolated bedrock palaeotopography beneath Cenozoic cover between north of St. Helena Bay and south of Yzerfontein is derived from 180 boreholes (Botha and Thompson, 1977; Rogers, 1980; Timmerman, 1985a, b; Baron, 1990; Conrad, 2013a, b) and revealed two

NE-SW trending palaeovalleys. These bedrock depressions were first identified by Rogers (1980) and later detailed and named by Roberts et al. (2011, 2013, 2017) as the Langebaanweg and Geelbek embayments (Figure 8-55a, b). The additional collation of boreholes not included by Roberts et al. (2011, 2017) have refined the demarcation of these palaeotroughs that appear linked by a NW-SE trending trough behind a granite bedrock high NE of the Langabaan Lagoon (Figure 8-54 and Figure 8-55b). The valleys are predominantly developed in comparatively less competent Malmesbury Group metasediments.

Large portions of the valleys are below current sea-level with the maximum depth of 68 m bmsl reached along the centre of the Langebaanweg depression. The valleys allowed the accretion of >100 m of cover sediment in places. Some authors (Rogers, 1980; Roberts et al., 2011) recognise the occurrence of fluvial sands, silts, clays and peat material of the Miocene Elandsfontyn Formation at the base of these valleys, implying an Early Miocene or older age for their incision (Figure 8-55a, b). Roberts et al. (2011) proposed that they were carved during the Oligocene regression by the proto-Berg River, which they postulate originally flowed in a SW direction, exiting into the ocean at the eastern Saldanha Bay shore. These sediments are conformably overlain by the Middle Miocene to Early Pliocene marine/estuarine Varswater Formation, and covered by aeolian deposits, mainly of Quaternary age. The newly collected data confirms the initial observations by Roberts et al. (2011, 2013) (Figure 8-54 and Figure 8-55b).

After careful evaluation of interpolated palaeosurfaces (Roberts et al., 2011, 2013, 2017; Claassen et al., 2024) and their altimetry in relation to the sequence of deposition and erosion of lithostratigraphic units in response to eustacy (Claassen et al., 2024), the SSM TI Team agreed that the variation in the elevation of marine and terrestrial deposits along the coast used to infer the proposed downwarping and fault activity are best attributed to sea level changes without the need for major localised neotectonism (Roberts et al., 2011, 2013; Claassen et al., 2024). This, in turn, suggests a lack of tectonic activity, including fault slip on the Colenso Fault, since at least the Miocene.

Summary: Based on careful consideration of available geological, geomorphological, and seismicity data, the SSM TI Team determined that there is no evidence for recent fault slip on the Colenso Fault. This includes the lack of deformation in marine terrace platforms and calcrete surfaces. The SSM TI Team did not find any evidence of fault slip within the Pliocene or event Miocene nor was there any evidence of geomorphic features commonly associated with active faulting deformation. Where bedrock deformation is mapped, the fault exposures are mylonitic and lack a clay gouge indicating that the observed shearing must have occurred at considerable depth and pressure. This observation suggests that these exposures are exhumed fault features from the deeper crust and that Colenso Fault has remained inactive within the current neotectonic period (contemporary strain and stress regime). Hence, the SSM TI Team assigned a p[S] = 0.0 to the Colenso Fault.

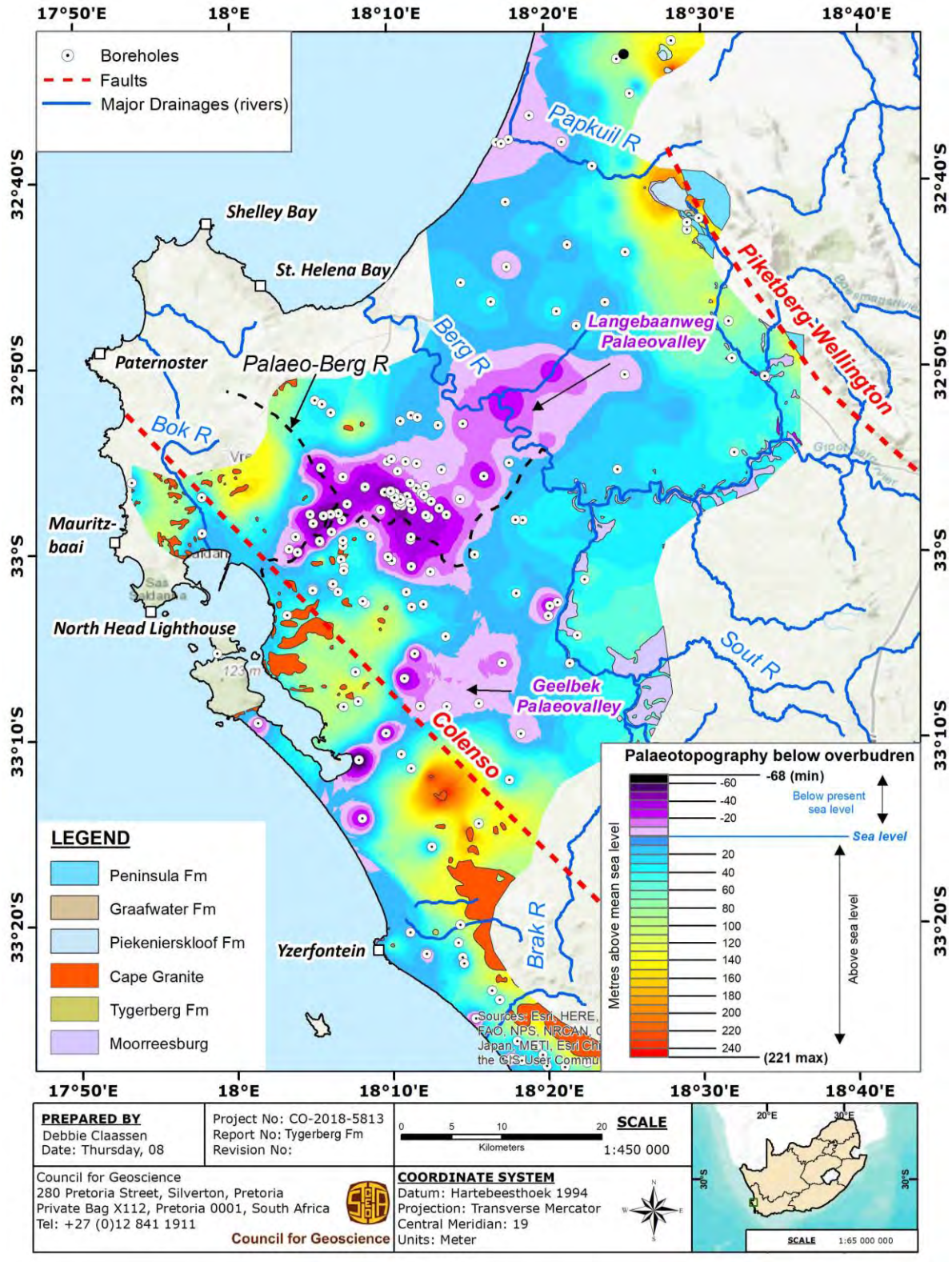

Figure 8-54. Palaeobedrock topography interpolated from borehole data for the area between St. Helena Bay and south of Yzerfontein. Note the two NE-SW trending palaeovalleys. The southernmost valley reaches depths of 68 m bmsl.

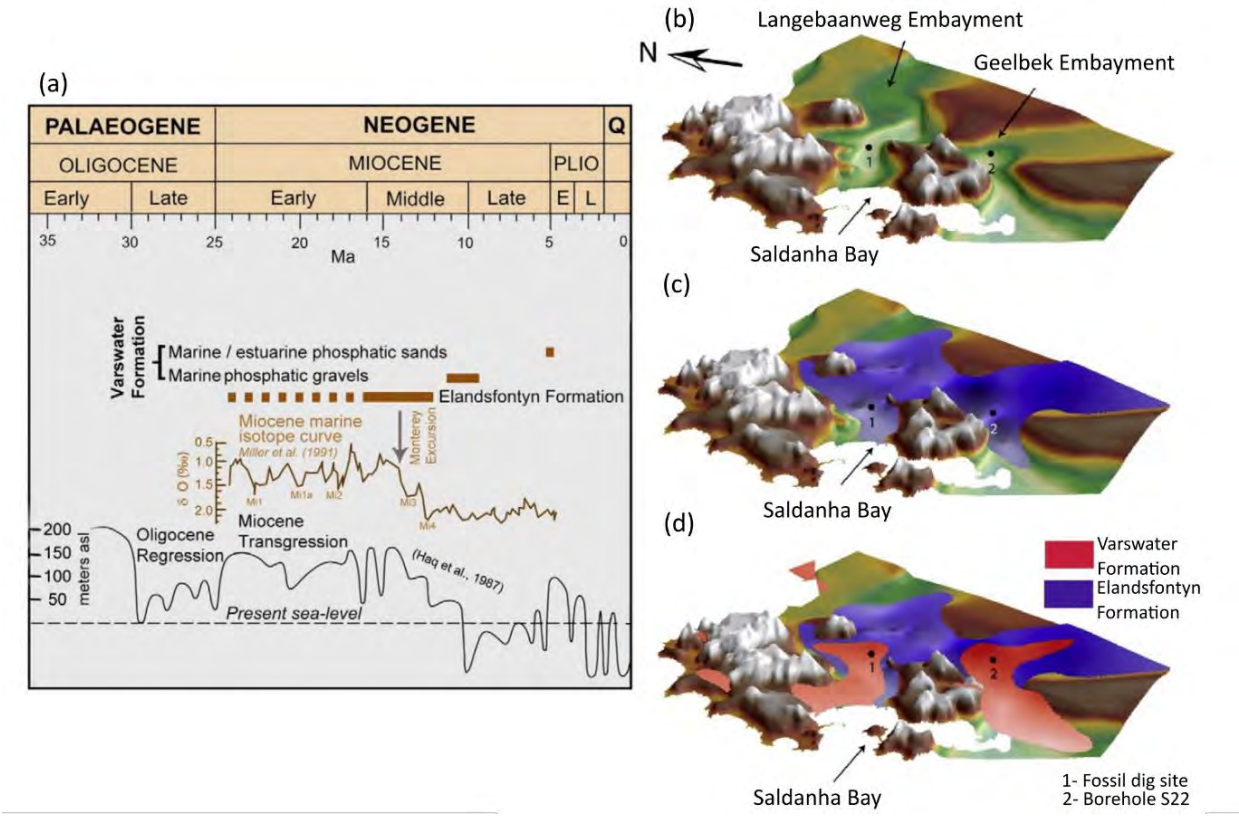

Figure 8-55. (a) Miocene marine isotope curve (Miller et al., 1991) and sea level curve (Haq et al., 1987) compared to the stratigraphy of the Elandsfontyn and Varswater formations in the Saldanha Bay area (Roberts et al., 2011, 2013).

8.5.3 Kalbaskraal and Klipheuwel faults

Origin: The NW-SE striking Kalbaskraal and Klipheuwel faults are located within the Tygerberg terrane of the Saldania Belt (Figure 8-56 and Figure 8-57). The faults form boundaries of graben-like basins filled with Early- to Mid-Cambrian rift clastics of the Klipheuwel Group. They were first mapped by Rogers and Schwarz (1907). According to Haughton (1933b), the Klipheuwel Group is an assemblage of clastic deposits that were laid down long after intrusion of the Cape Granites and after partial erosion of the older Malmesbury Group strata. Kisters and Belcher (2018) and De Beer (2007) describe the rocks of the Klipheuwel Group as coarse-clastic conglomerates and poorly sorted sandstones, arkoses, and intercalated shales that unconformably overlie shales and phyllites of the Swartland complex and Malmesbury Group and the granitic rocks of the Cape Granite Suite. They have been interpreted to represent a rift-related precursor to the Cape Supergroup (Tankard et al., 2009) or late-stage molasse-type basins more closely related to the Pan-African evolution of the Saldania Belt (e.g., Gresse et al., 2006).

The Kalbaskraal Fault is composed of several separate subparallel strands marked by zones of vein quartz breccia. The Klipheuwel Fault is a major fracture with a zone of brecciation and shearing about 1 km wide, and like the Kalbaskraal Fault, may possibly split up into several separate fault strands. The syntectonic deformation of the surrounding Cape Granite Suite in the Darling batholith, as well as the many co-planar fault mylonites mapped, support a structural zone of intense shearing that was established during Pan-African times (Cambrian), but possibly active as late as the Mesozoic as the NW-SE orientation of extensional

reactivated pre-existing ductile or brittle-ductile Vredenburg-Stellenbosch Fault Zone (De Beer et al., 2008). Field observations from Coppersmith et al. (2024) noted a lack of observed gouge along the co-planar mylonites along the northern section of the Vredenburg-Stellenbosch fault. This indicates that the mylonites represent deformation that occurred when this section of the fault was near the base of the brittle crust and has since been exhumed.

The extent and possible connectivity of the Kalbaskraal and Klipheuwel faults with surrounding faults, such as the Colenso Fault, are uncertain because of poor exposures and extensive Cenozoic cover. According to De Beer et al. (2008), the Kalbaskraal and Kipheuwel faults may have been reactivated during the Mesozoic extension of the Western Cape and may be connected and linked with the Colenso Fault. This proposed linkage to the Colenso Fault is based simply on along-strike projections of fault traces. In the Baseline Report (Stamatakos et al., 2022), the Kalbaskraal and Kipheuwel faults were considered as possibly linked to the Colenso Fault, giving rise to a maximum fault length of the Colenso Fault of 150 km. De Beer et al. (2008) suggests that the Klipheuwel Fault could be a possible extension of the Mamre Fault line, if the Mamre is extended south-eastwards, giving rise to a 65 km long fault.

Decision: The SSM TI Team assigned a p[S] = 0.0 to the Kalbaskraal and Klipheuwel faults.

Technical Basis: Based on a careful review of available geologic information from the literature and geologic mapping of Cenozoic deposits, the SSM TI Team did not find evidence for fault slip within the Pliocene (5.3 – 2.6 Ma) or even within the late Miocene (11.6 – 5.3 Ma). There are no moderate- to large-magnitude hypocentres aligned along the fault plane, nor did the SSM TI Team find any geomorphic features commonly associated with active fault deformation. In addition, the presence of mylonites and lack of fault gouge indicate that shearing took place at substantial depth and pressure within the crust and may therefore be a “rootless” exhumed fault zone. The SSM TI Team therefore concluded that the faults are relics of an earlier period of geological deformation and have remained inactive within the current neotectonic period (contemporary strain and stress regime).

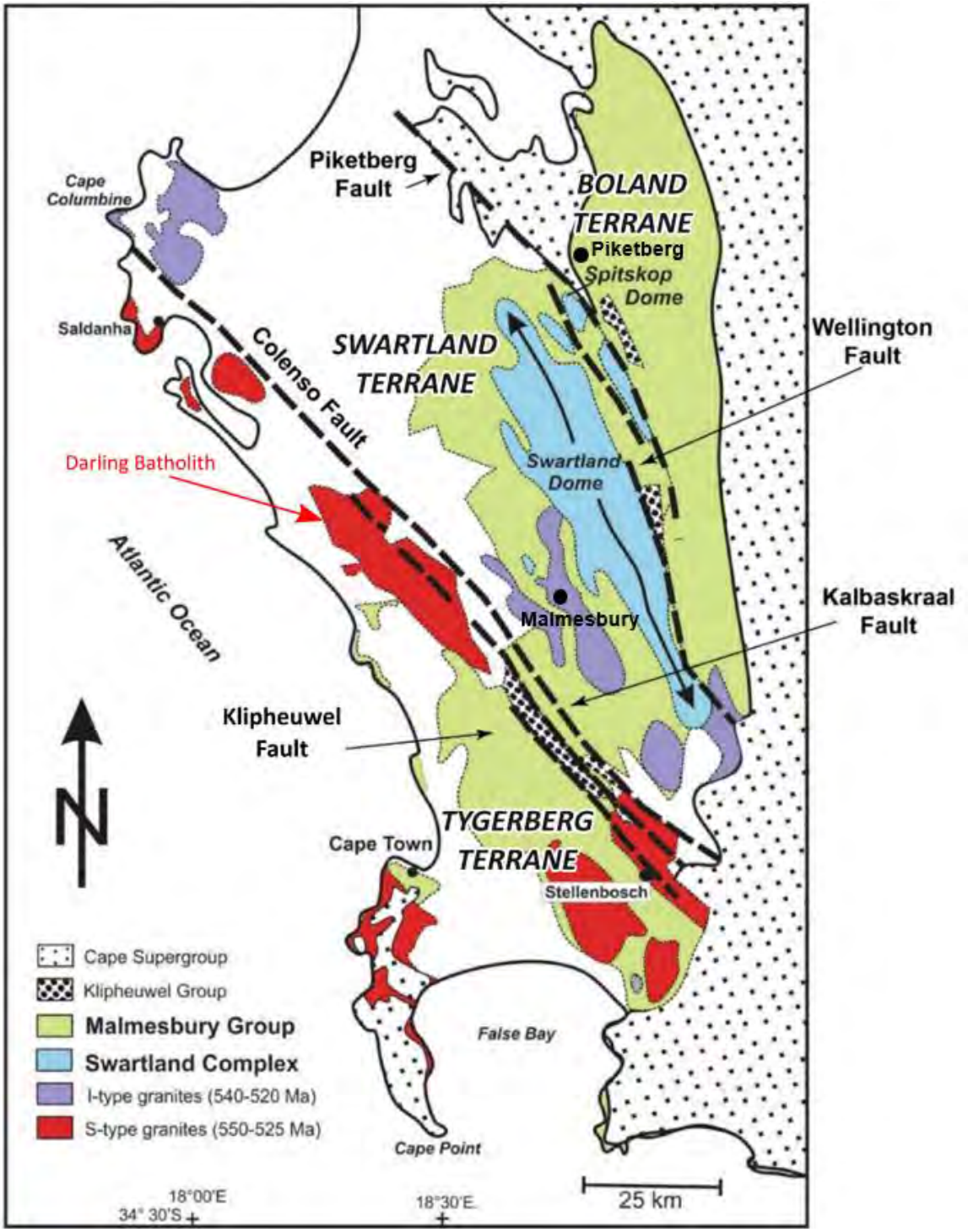

Figure 8-56. Schematic geologic map of the western Saldania Belt. Map shows subdivisions into three tectonostratigraphic domains (Tygerberg, Swartland, and Boland), separated by strike-slip faults and intruded by plutons of the Cape Granite Suite. The figure was adapted from Figure 4.13 of Kisters and Belcher (2018).

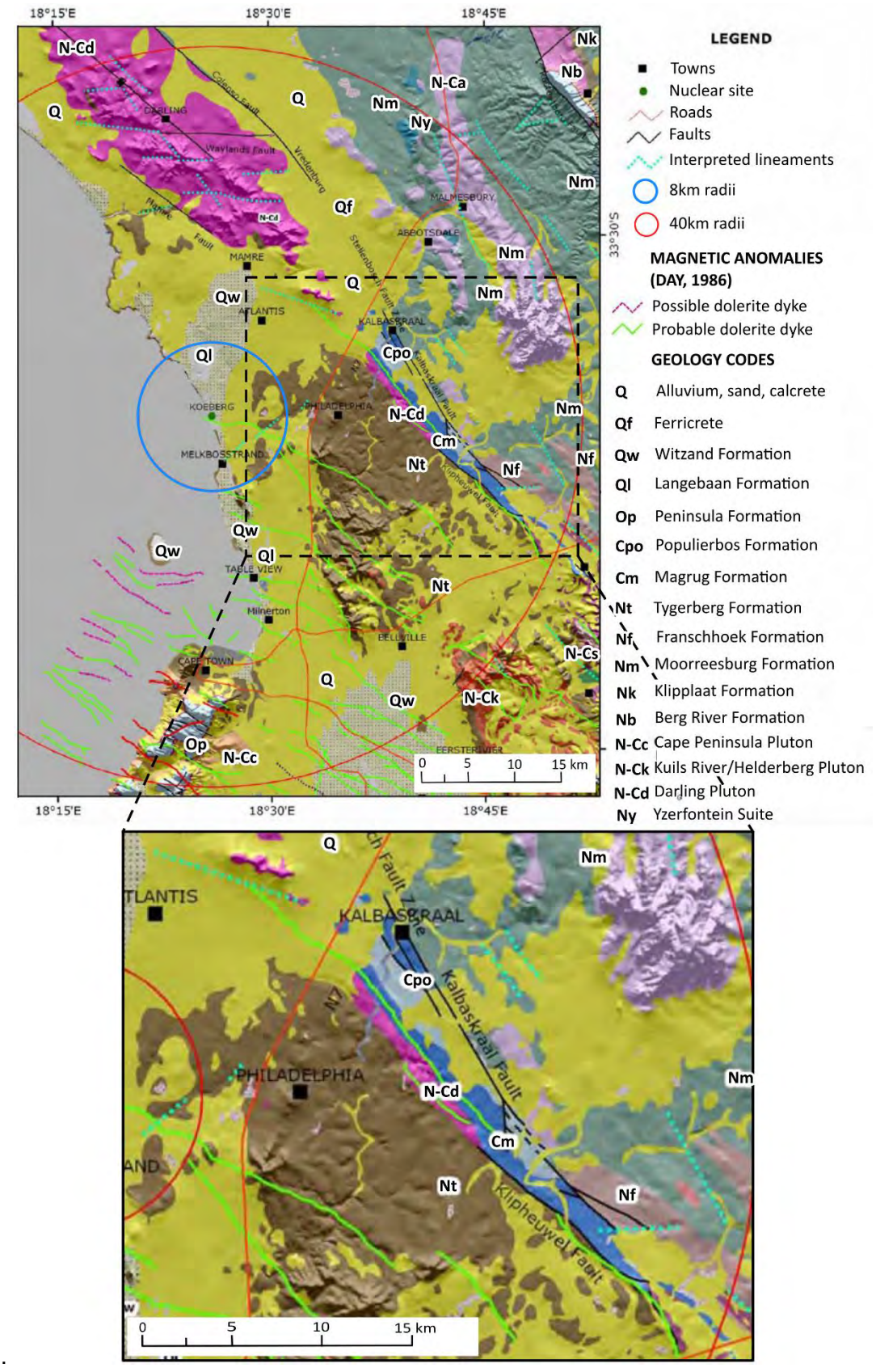

Figure 8-57. Geological map of the Site Vicinity (red circle), based on 1:250,000 scale map 3318 Cape Town used to construct Figure 3 of De Beer (2007). Excerpt shows position of the Kalbaskraal Fault.

Evaluation: The SSM TI Team reviewed the geologic literature (e.g., Kisters and Belcher, 2018; De Beer et al., 2008), fault maps (De Beer, 2007), digital elevation data and the earthquake record to identify any evidence of fault displacement or active seismicity. None was found. There is no geologic evidence for any fault slip since the Miocene. The SSM TI Team concludes that a possible connection to the Colenso fault is speculative because it is based solely on their similarity in geometry (NW-striking strike-slip faults) and the spatial proximity to one another on the geologic map (Figure 8-56 and Figure 8-57).The SSM TI Team has assigned a p[S] = 0.0 to the Colenso Fault (Section 8.5.2), so even if the Kalbaskraal and Klipheuwel faults can be linked with the Colenso Fault, they no longer contribute to the seismic hazard at the Duynefontyn site.

Coppersmith et al., 2024) examined locations where the Kalbaskraal Fault crosses the Diep River to determine whether recent fault slip could be observed and documented. Just downstream (southwest) of the town of Kalbaskraal, there are three fault splays of the Kalbaskraal Fault that cross the Diep River as shown in the digital elevation model (DEM) (Figure 8-58). The river course here follows a rectangular drainage pattern that is dominated by left-stepping bends, although right-stepping bends are also present. The left-stepping bends of the river course appear to coincide with some of the fault lineaments. However, these same fault lineaments appear to coincide with right-stepping bends in smaller drainages located just south of the Diep River. Although this pattern could arise from conjugate crossing normal faults, the observation of a contrasting sense of apparent fault slip from the observed rectangular drainage pattern is more likely. The SSM TI Team therefore concludes that the left and right-steps of the Diep River reflect erosion of bedrock within an orthogonal network of pre-existing fractures and bedrock faults, and do not indicate fault slip.

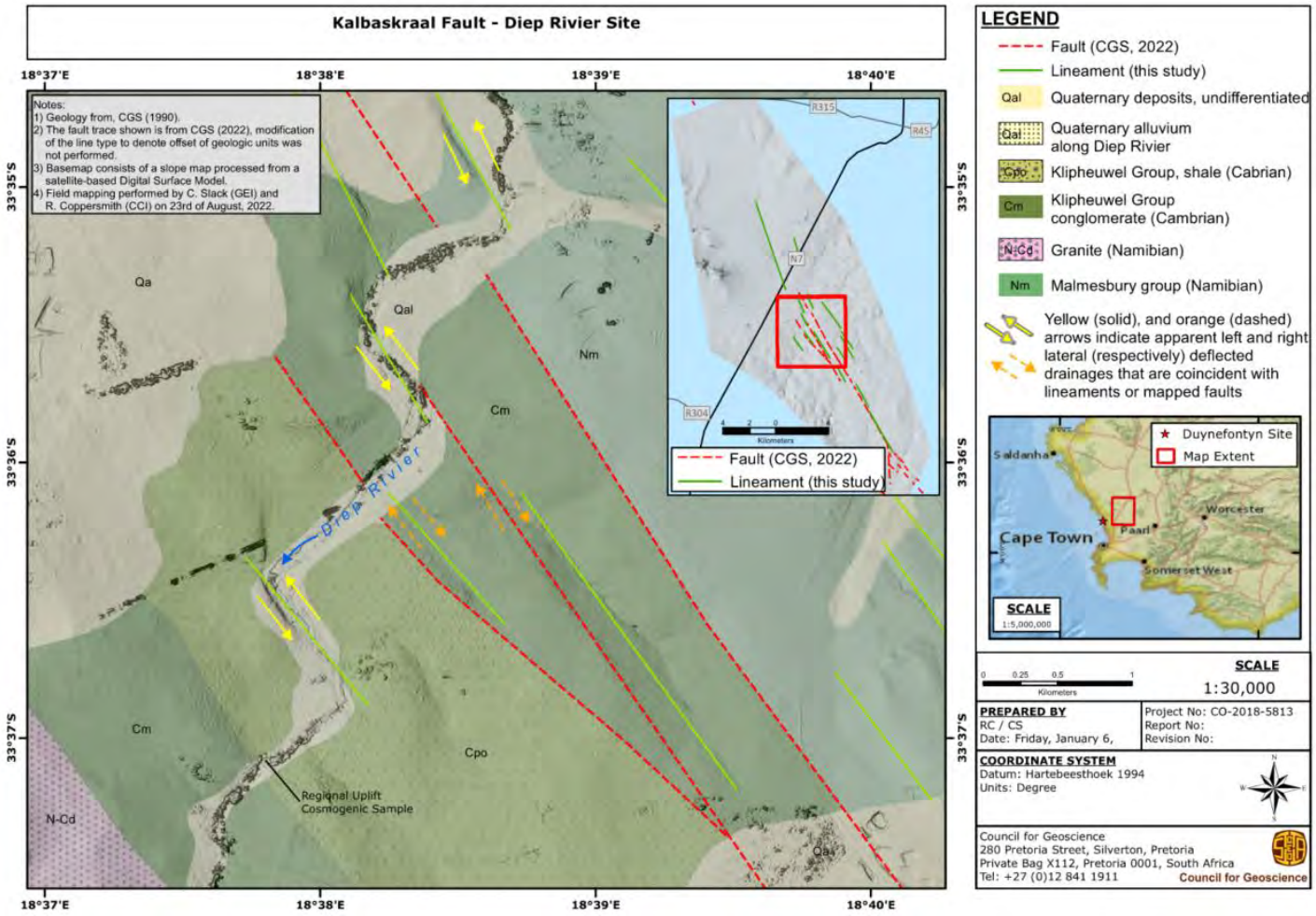

Figure 8-58. Geologic map along the Diep River. Red dashed lines show location of the Kalbaskraal Fault from De Beer et al. (2008), green lines are lineaments from this study. Arrows show apparent relative lateral movement of drainages that are coincident with the faults and / or lineaments. Note there is both apparent right- and left-lateral movement (Coppersmith et al., 2024).

8.5.4 Worcester Fault

Origin: The Worcester fault zone was originally mapped by Rogers and Schwarz (1907). The fault zone consists of a series of fault segments totalling 330 km in length. The fault segments trend northwest–southeast in the Western Cape and east–west in the Eastern Cape, with a broad bend at the syntaxis. Evidence for the fault becomes difficult to discern to the east near the coast, but the trends towards Mossel Bay (De Beer, 2005) (Figure 8-59). The east–west portion of the Worcester Fault is a Cape Fold Belt thrust fault reactivated in the Mesozoic as a steep normal fault with south side down (Gresse et al., 1992; De Beer, 2005). The throw of the Worcester Fault is reported to be a minimum of 3,811 m (Söhnge, 1934) and up to 6 km in the syntaxis of the Cape Fold Belt near Worcester (De Beer, 2005). The majority, if not all, of this normal displacement occurred during Mesozoic extension (Middle Jurassic to Middle Cretaceous time). De Beer (2005) reports that faulting of the Jurassic-Cretaceous Uitenhage Group sediments deposited in depocentres along the Worcester Fault may have occurred until the Late Cretaceous. The fault appears to have remained an important structural weakness until Late Cretaceous to early Cenozoic times, as shown by its association with plugs of olivine melilitite of early Cenozoic age (De Beer, 2005). The fault strikes NW-SE between the towns of Tulbagh and Worcester along the trace most relevant to this study, extending to within about 70 km of the Duynefontyn site (Figure 8-60). Prior to the recent field mapping by Coppersmith et al. (2024), little was known about the movement in the Cenozoic. The only evidence for postulated Cenozoic faulting was documented at an outcrop east of the town of Suurbraak by J. Viljoen in the 1980s. De Beer (2005) re-visited this site and attempted to confirm the interpretations by Viljoen with limited success, concluding that if Quaternary alluvium was offset, it had not been active for at least 1.3 Ma based on estimating the age of unfaulted alluvium.

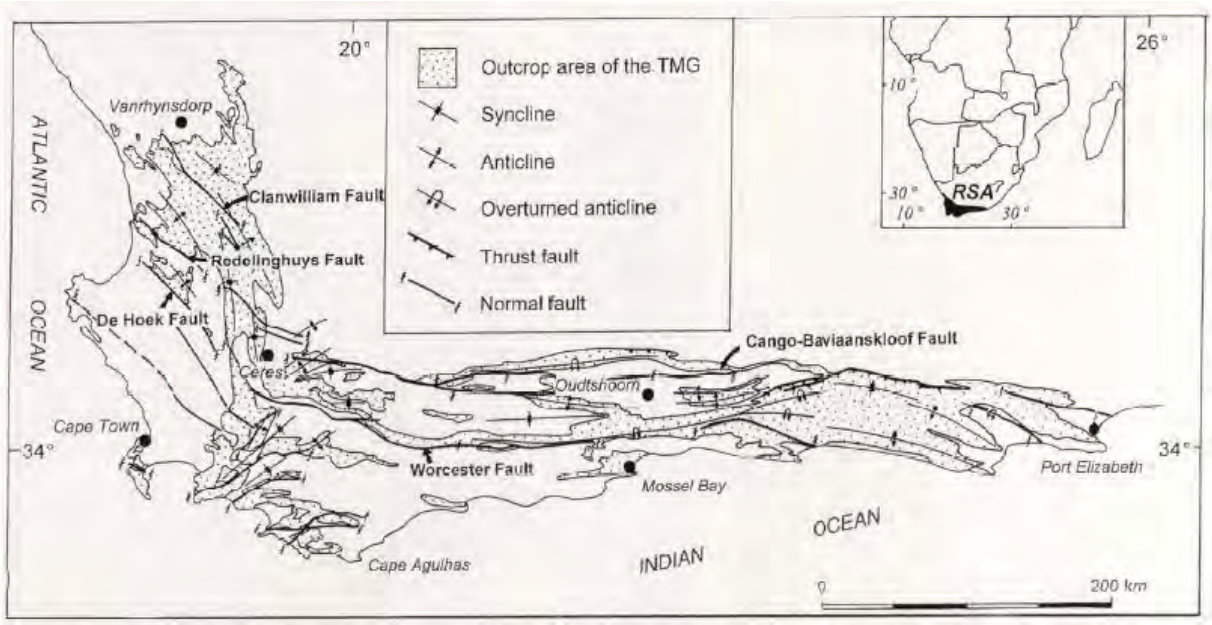

Figure 8-59. Map showing extent of Worcester Fault (De Beer, 2005).

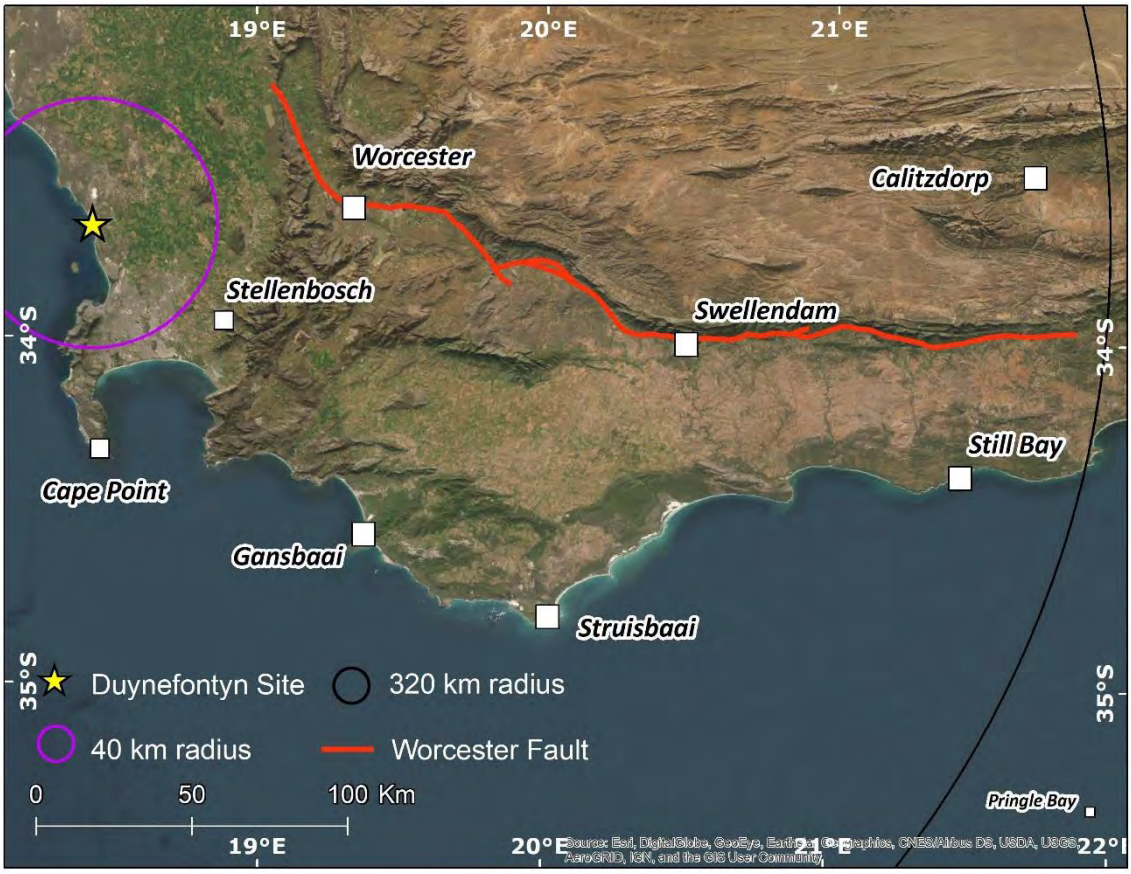

Figure 8-60. Map of Worcester Fault trace relative to the Duynefontyn site.

Decision: The SSM TI Team assigned a p[S] = 0.0 to the Worcester Fault.

Technical Basis: The SSM TI Team focussed on the review of past studies that evaluated the fault for post-Mesozoic movement. While many authors address the Worcester fault system as it relates to its significance in the Mesozoic (e.g., Gresse and Theron, 1992), the SSM TI Team determined that the most relevant publications to determine the seismogenic probability includes studies by De Beer (2005), Thyspunt PSHA (Bommer et al., 2013), and the recent field mapping efforts by Coppersmith et al. (2024). These studies evaluate key localities along the strike of the fault, typically where Cenozoic deposits are draped over the fault trace and therefore recency can be evaluated. De Beer (2005) focussed on a single outcrop where faulting is speculated to offset Quaternary alluvium with a great deal of uncertainty. The Thyspunt PSHA (Bommer et al., 2013) evaluated the results of the De Beer (2005) study and performed some desktop reconnaissance indicating a list of arguments for and against fault activity. The SSC TI Team for Thyspunt assigned a p[S] = 0.2, concluding that the fault was most likely non-seismogenic. Coppersmith et al. (2024) mapped two key locations along the fault, the first being the same road cut as evaluated by De Beer (2005), and the second the Tweefontein farm alluvial deposits near the Hex River. This study did not find evidence for faulting in the Quaternary. Based on the assessments of Coppersmith et al. (2024), the SSM TI Team concluded that this fault is non-active.

More broadly, the SSM TI Team did not find evidence for fault slip within the Pliocene (5.3 – 2.6 Ma) or perhaps even the late Miocene (11.6 – 5.3 Ma). There are no aligned moderate- to

large-magnitude hypocentres along the fault plane, or geomorphic features commonly associated with active faulting deformation.

Evaluation: The evaluation of the Worcester Fault came from three major studies that looked at the recency of faulting. The SSM TI Team summarised each study as part of the consideration in including the fault as a source in the SSM. The evaluation of each study is summarised below:

De Beer (2005)

The author presents evidence of possible neotectonic reactivation—two small faults, each with down-to-the-south displacement of 0.5 m, —first reported by J. Viljoen (personal communication to the author) in a road cut east of Swellendam (De Beer, 2005; Figure 8-61). The author notes that these faults do not displace the unconformity between units A and B. Unit A is a channel cut into mid-Early Cretaceous (pre-drift onset, 126 Ma) Kirkwood Formation. Unit B is composed of gravel and cobbles overlying a terrace cut into unit A (Figure 8-61). The ages of units A and B are unknown. Unit A may be related to the alluvial plain of the palaeo-Tradouw River and its west-flowing tributary at the foot of the Langeberg Mountains. Assuming this is the case, some 20 m of further incision of the course of the Tradouw River into Bokkeveld Group rocks has occurred since deposition of unit A. Using broad estimates of the long-term average rate of incision of the modern Tradouw River into the coastal platform in post-Miocene time (at a rate of ~80 m in 5.3 Ma), the author estimates that 20 m of incision would have taken at least 1.3 Myr, and that the most recent period of faulting could not have been younger than middle Pleistocene.

Figure 8-61. Road cut east of Zuurbraak showing evidence of interpreted neotectonic reactivation of the Worcester Fault. Photo from north (left side of outcrop) to south (right side of outcrop). Coordinates: -34.003329° 20.705839° (a) Mosaic compiled by J. Vijoen in the late 1980s. From top unit to bottom unit: Unit B – is composed of gravel and cobbles overlying a terrace cut into Unit A. Unit A – is a fluvial channel cut into C-Kk. C-Kk – mid-Early Cretaceous (126Ma) Kirkwood Formation bedrock (b) photograph of the road cut as viewed by De Beer (2005).

Only the southernmost portion of the section was open for investigation in 2005, the northern part having been overgrown due to the heavy rainfall in this region. C-Kk is Kirkwood Formation mudstone, A is a unit of gritty conglomerate deposited in a channel, and B is a gravel- and cobble-containing unit overlying unit B with a horizontal unconformity. The two subvertical solid lines depict faults that affected the Kirkwood and unit A, but not unit B (De Beer, 2005).

Thyspunt PSHA (Bommer et al., 2013)

The Thyspunt SSC TI Team evaluated the Worcester Fault as a potential fault source for the Thyspunt SSHAC Level 3 PSHA study. The fault source only came within approximately 260 km of the Thyspunt site, located in the Eastern Cape near Cape St. Francis. The fault was considered a fault source in the PSHA model with a seismogenic probability (p[S]) of 0.2. Other characteristics of the fault are shown in the logic tree from the Thyspunt PSHA study in Figure 8-62.

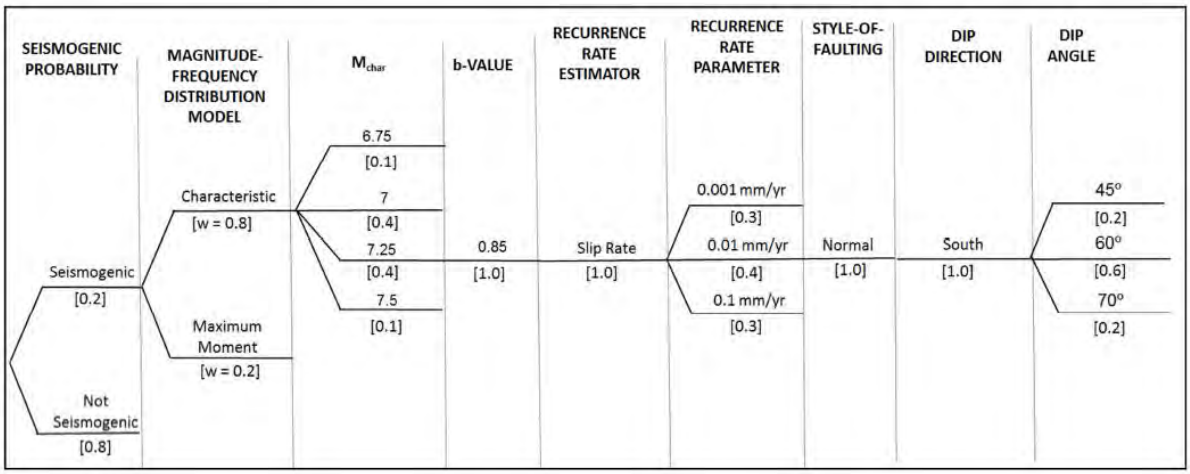

Figure 8-62. Logic tree for the Worcester Fault source from the Thyspunt PSHA (Bommer et al., 2013) which includes the source-specific epistemic uncertainties.

The Thyspunt SSC TI Team conducted limited reconnaissance mapping and office-based interpretations of aerial photographs and DEMs. While the authors concluded that there is no direct evidence to indicate that the Worcester Fault is currently seismogenic based on the study's criteria, the authors included the fault in the seismic source model with a low p[S] for the reasons summarised below:

- The Worcester Fault subparallels the Kango Fault which has experienced multiple latest Pleistocene to Holocene surface-faulting earthquakes.
- The Worcester Fault is structurally associated with the Kango Fault in that both faults share a common geologic history of Mesozoic reactivation of an older Palaeozoic compressional structure. The Worcester Fault, therefore, may be favourably oriented to be reactivated in the present tectonic regime.
- There is a possible association between the Worcester fault zone and seismicity in the Ceres area. Near Ceres, the Groenhof Fault, which is considered a possible source for the 1969 E[**M**] 6.2 Ceres earthquake, may be the structural stepover between the Worcester and De Hoek faults (Green and Bloch, 1971; De Beer, 2005).

Current Assessment

In contrast, the SSC TI Team's evaluation indicates that the Worcester Fault is not currently seismogenic for the reasons summarised below:

- Low rates of denudation and inferred rock uplift for the region encompassing the Worcester Fault are consistent with the long period of inactivity (1.3 Myr or longer) inferred for the road-cut exposure of the fault near the Tradouw River as described by De Beer (2005). Denudation rates and geomorphic evolution of the Cape Fold Belt determined through the use of *in situ*–produced cosmogenic ^{10}Be show similarity between catchment-averaged denudation rates (determined from river sediment samples) and denudation rates on interfluves (determined from bedrock samples) (Scharf et al., 2011, 2013). ^{10}Be-based denudation rates of the Cape Fold Belt fall between 1.98 ± 0.23 m/Myr and 7.95 ± 0.90 m/Myr; these rates are among the lowest in the world (Scharf et al., 2013; Bierman et al., 2014) (Figure 8-63). Sample locations in the vicinity of the Tradouw River near the Viljoen road-cut locality yielded denudation rates of 6.13 ± 0.68 m/Myr and 4.72 ± 0.54 m/Myr (comparable to the average rate of 5.4 m/Myr) measured for drainage basins farther to the east by Bierman et al. (2014). Both Scharf et al. (2013) and Bierman et al. (2014) conclude that the topography of the Cape Fold Belt is approximately steady state, neither increasing nor decreasing in relief.

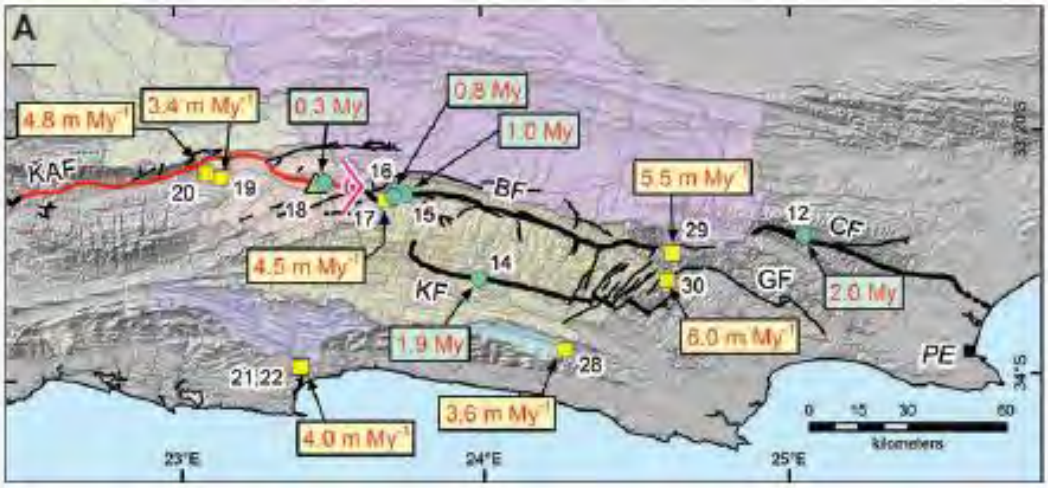

Figure 8-63. Sample location map with minimum limiting ages for pediment samples (green) and erosion rates for river samples (yellow). CF-Coega Fault, GF-Gamtoos Fault; KAF-Kango Fault (Quaternary-reactivated segment shown in red); KF-Kouga Fault; BF-Baviaanskloof Fault; PE-Port Elizabeth (Bierman et al., 2014).

- The observation that the youngest deposits (unit B), estimated to be older than middle Pleistocene (older than ~1.3 Ma), in the road cut described above, are not displaced by faulting is supported by a reconnaissance investigation of 1:10,000–scale colour aerial photographs, which failed to indicate a recent fault scarp along the expected lateral continuation of the faults (De Beer, 2005).
- Thick, consolidated alluvial scree deposits covering the Worcester Fault in another road cut at the foot of the Langeberg Mountains north of Riversdale also showed no evidence of faulting (De Beer, 2005). The age of the scree deposits is unknown.

- High geomorphic surfaces (possible pediments locally overlain by Grahamstown Formation [Tg]) in the eastern part of the mapped Worcester Fault appear unfaulted based on interpretation of aerial photographs and Google Earth images, which show no evidence (lineaments or scarps) of surface faulting (Figure 8-64). Drainages on either side of the high geomorphic surface are incised approximately 50 m to 100 m below the surface. Van Zyl (1997) groups unfaulted surfaces directly east of the end of the mapped Worcester Fault with other extensive flat erosional surfaces as part of the "terrestrial African surface." Following Maud (1996), Van Zyl interprets these surfaces as relicts of topography that existed prior to the drop in sea level in the Miocene at approximately 18 Ma. The surfaces, which are primarily developed on Bokkeveld shale, are capped by silcrete, ferricrete, or Tertiary gravel (Van Zyl, 1997). The unfaulted surfaces that project across the eastern Worcester Fault may be equivalent in age to high terrace remnants underlain by cemented pediment gravels mapped as Tg that are recognised elsewhere in the Eastern Cape and Oudtshoorn Basin areas. The Tg and underlying pediment surface at the bedrock alluvium contact are generally considered to be Miocene in age. Hagedorn (1988) reports results of two electron spin resonance tests that indicated ages of 7.3 Ma and 9.4 Ma, respectively, for two samples of the silcrete caps on pediment remnants in the Little Karoo. According to these ages, the pediments date from the upper Miocene, but they could be even older if their formation was not synchronous with the silcretisations. Along the coast near the hypothesised trend of the Worcester fault zone, regional marine terrace data sets do not indicate any deviations from the regional data to suggest Pliocene or Quaternary deformation (Figure 8-65). In particular, the regional marine terrace compilation does not indicate any significant vertical deformation across the projected trends of the Worcester Fault to the coastline (Hanson et al., 2012).

Figure 8-64. Google Earth image showing unfaulted geomorphic surface (pediment or eroded pediment) across the mapped trace of the Worcester Fault (Bommer et al., 2013). Tg-Grahamstown Formation.

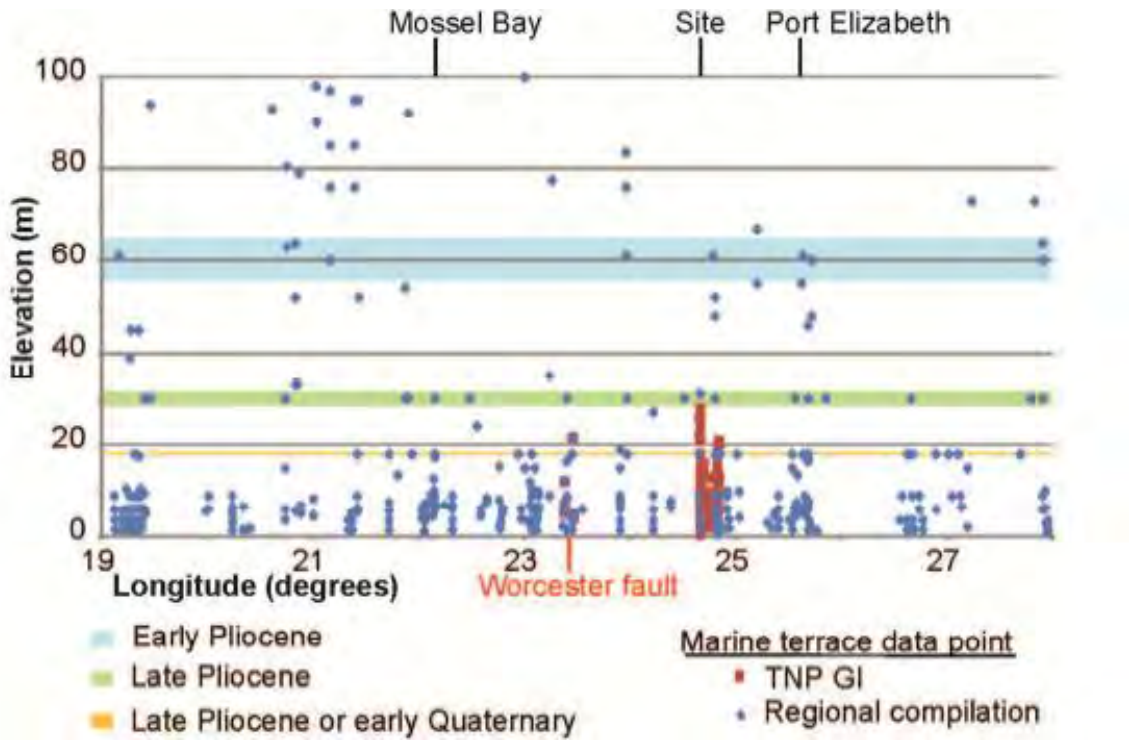

Figure 8-65. Summary diagram showing the correlations of Pliocene and Quaternary marine terraces from west of Mossel Bay to east of Port Elizabeth (Bommer et al., 2013). The "Site" referenced in the figure is Thyspunt.

Coppersmith et al. (2024)

As part of the mapping effort, two sites were evaluated for evidence of recency of movement. These sites are referred to as the Suurbraak Site, which is along R324 (location of De Beer (2005) study), and the Tweefontein Site. These sites reside along the east and west sections of the fault (Figure 8-66).

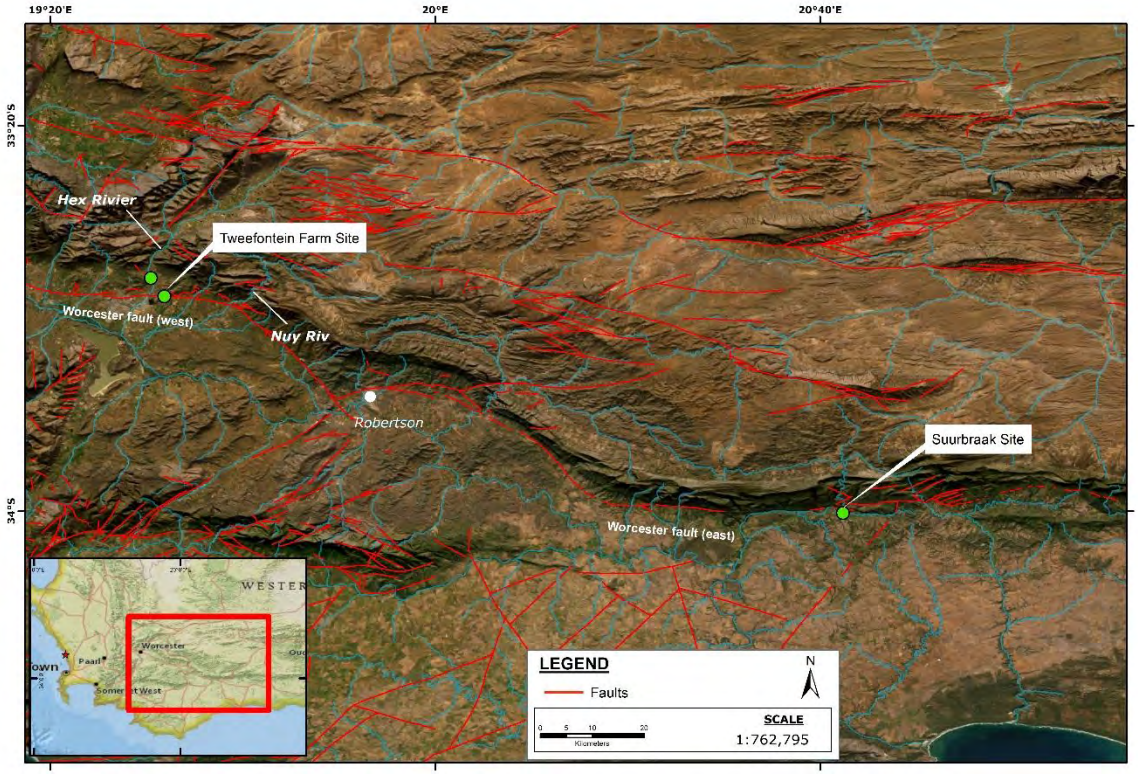

Figure 8-66. ArcGIS satellite imagery with fault trace annotated in red and showing locations of the Suurbraak Site and Tweefontein Farm site along the Worcester Fault.

The authors re-occupied the roadcut site from De Beer (2005), referred to as the Suurbraak Site in this study. Considerable effort was made to clean off the base of the outcrop to expose the top of bedrock, but a complete cleaning of the outcrop was not conducted due to time limitations. In a couple of places there were apparent offsets in the bedrock that, upon further cleaning, were verified to be steps related to jointing in the rock (Figure 8-67). The authors did observe similar hardened ribs within the alluvium as was described by De Beer (2005). However, these were present at several places along the outcrop and appeared to be due to a weathering phenomenon rather than faulting. Where the more indurated “ribs” of alluvium were observed, alluvial stratigraphy could be observed transecting the ribs and interpreted as unfaulted.

The authors mapped three alluvial unit packages below the vegetation line. From oldest to youngest these included: Unit 10, a gravel-to-boulder sized stratified unit with some sand, typically clast supported; Unit 20, a medium-to-coarse sand layer with some gravel; Unit 30, a gravel-to-boulder sized stratified unit with some sand. There were no pedogenic soil horizons observed between the stratigraphic units to suggest a sustained period of stability occurred between deposition of the units.

Unit 20 was particularly noteworthy because it persists laterally up canyon (north) above the Kirkwood formation, and well downstream (south), over the presumed fault as mapped in previous studies. The base of Unit 20 (of unknown age) was interpreted as not offset. The authors indicated that the rationale applied in the previous study by De Beer (2005) that estimated the age of the upper alluvium by approximating an average incision rate to the nearby Tradouw River seemed reasonable (~1.3 Ma). Coppersmith et al. (2024) collected six

samples for Cosmogenic burial analysis, two from Unit 10, two from Unit 20, and two from Unit 30 (Figure 8-67). The samples were analysed by Dr Paul Bierman using the two-isotope ($^{26}Al/^{10}Be$) isochron burial method. Using a variety of plausible assumptions, the data from samples at the Suurbraak Roadcut suggest an age for the fan sediment of ~1.2 My (Appendix E). These dates are consistent with the estimated age presented by De Beer (2005).

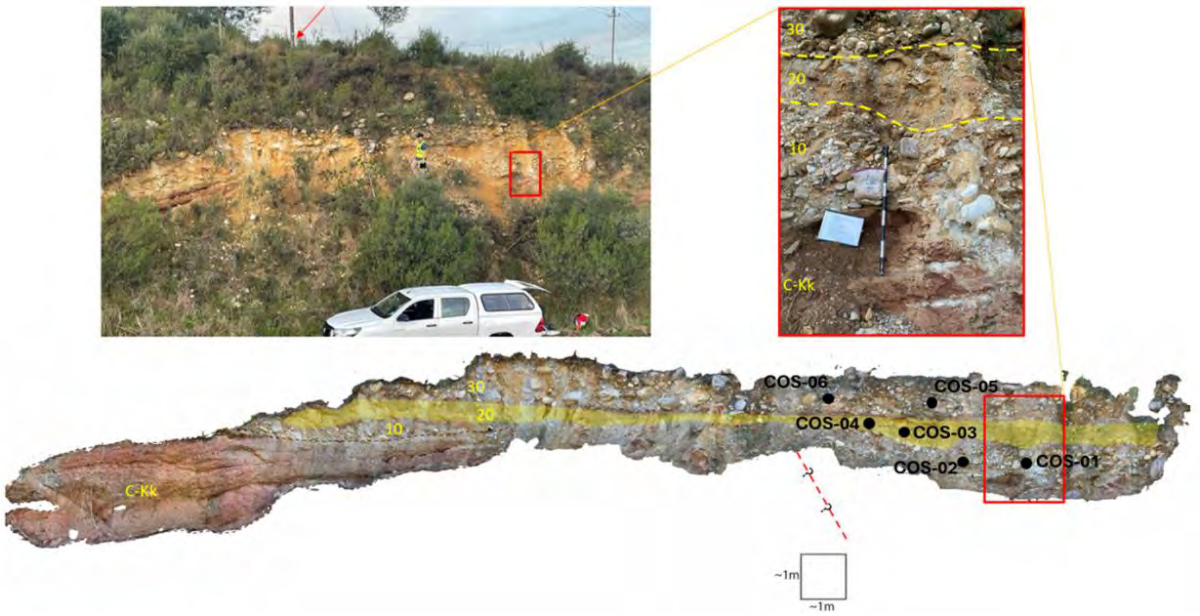

Figure 8-67. Suurbraak Site. (a) Overview photo of outcrop. Arrow points to power pole that also appears in 1980s site documentation. Rectangle shows approximate location of rectangle shown in (b) and (c). (b) Orthorectified photomosaic of outcrop. The approximate location of the queried fault is located from scaling off of the 1980s annotated photograph. Units labelled on outcrop are referred to in the text. (c) Cleaned off portion of outcrop showing geologic units observed. Note apparent step in bedrock, interpreted to be jointing, to the right of the staff (for scale).

The Tweefontein Farm Site is located on the west section of the Worcester Fault just east of the town of Worcester. The Tweefontein Farm Site includes an approximately 10-metre-thick package of alluvial sediments within the Worcester Basin. The site was visited by the SSM TI Team in August 2022. During this initial reconnaissance of the site it was noted that there were possible buried pedogenic soil horizons within the terrace. The location of the Worcester Fault near the terrace is somewhat poorly constrained but is interpreted to be near the geomorphic rangefront (De Beer et al., 2008) (Fugure8-68). The purpose of further evaluating this site was the following:

- Determine if the fault passes through the terrace.
- Determine if there is evidence of fault displacement of the terrace.
- Estimate the age of the terrace using relative and absolute age dating techniques.

There are three primary drainages that coalesce in the Worcester Basin, they include: Hex River, Nonna River, and Nuy River. Of these major rivers, the Hex River located approximately 1.5 km to the west has the greatest depositional influence at the site. In addition to the Hex River, immediately north-northeast of the Tweefontein Terrace is the Langkloof River. The headwaters of the moderately sized Langkloof River (Figure 8-68) extend approximately 6 kilometres toward the peak of Tierberg.

The basin fill from the three highest order (primary) drainages and additional contribution from lower order drainages such as the Langkloof have formed a broad alluvial valley. Typically, the active stem of the primary drainages has incised the adjacent alluvial terrace on the order of a 3- to-4 metres. Well-defined flights of terraces along the three aforementioned rivers are absent or obscured through agricultural and anthropogenic modifications. The Tweefontein terrace is one of the few exceptions to this generalisation within the Worcester Basin. It appears that the approximately 25-metre-high escarpment associated with the Tweefontein terrace is due to the proximity and orientation of the sizeable lower-order drainage (Langkloof River) to the active channel of the Hex River. The 25-metre-high scarp between Qal1 and Qal2 is interpreted as an erosional feature caused by gradual incision by the Hex River. Elsewhere within the basin, drainages are more commonly subparallel to each other, resulting in a composite landform fill. In the case of the Tweefontein terrace, the outboard end of the alluvial fan (toe) has been eroded away from the southerly flow from the Hex River, resulting in a prominent terrace riser escarpment.

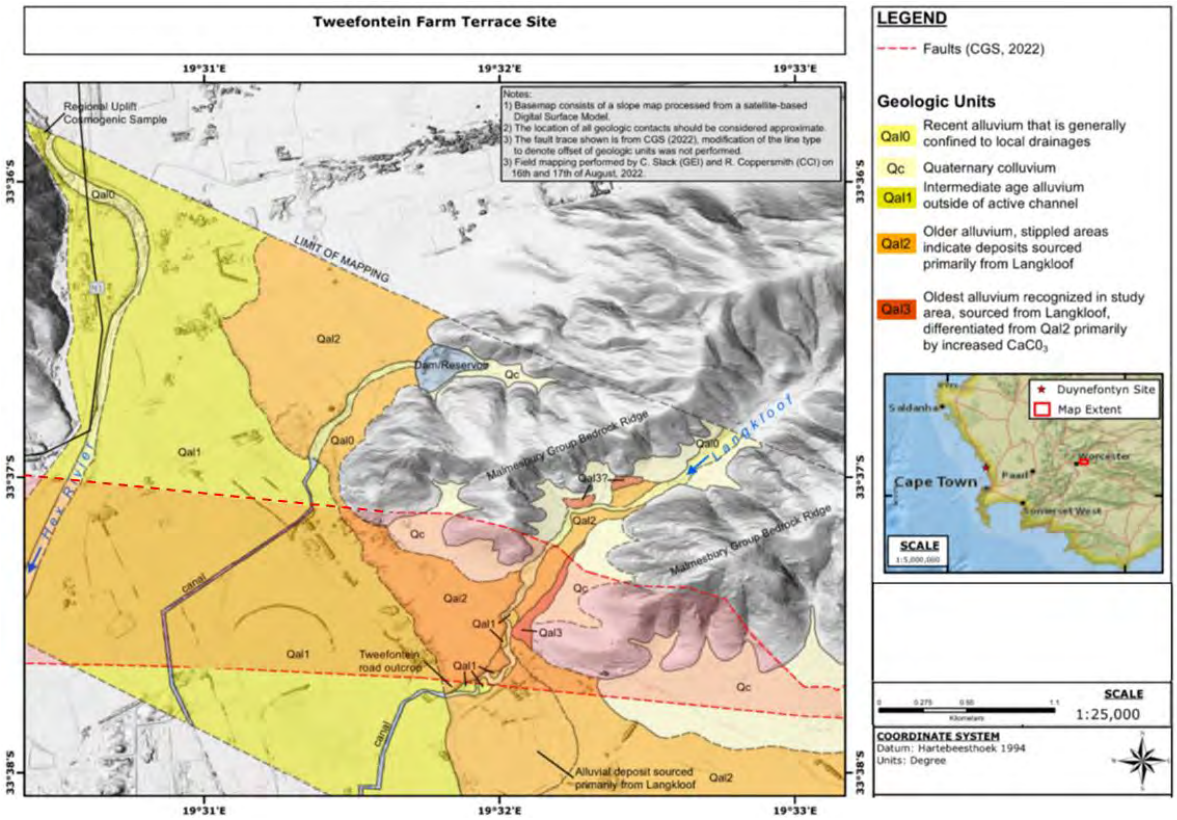

Figure 8-68. Quaternary geologic map of Tweefontein Farm Terrace (Coppersmith et al., 2024). Dashed red lines and red shading shows uncertainty in exact location of fault trace. The Qal2 terrace is positioned in the centre of the fault zone where no fault scarp is expressed in the surface or within the roadcut outcrops.

Desktop and field mapping at the Tweefontein Farm Site and surrounding vicinity could not identify evidence of Quaternary faulting. It should be noted that the DEM used for the desktop analysis did not filter out vegetation (i.e., LiDAR), and there is considerable ground disturbance that could obscure evidence of surface faulting. With that limitation acknowledged, it appears likely that the rangefront fault passes below the Unit Qal2 (Tweefontein Terrace) and is not faulted.

As part of previous work performed for the Thyspunt site (Bommer et al., 2013), several soil descriptions were conducted in soils that ranged from 5 ka to ~130 ka near the town of de Rust. The climate and lithology of the parent material of the soils at Tweefontein and de Rust differs appreciably, however, it provides a rough comparison in soil development with respect to age. With these limitations in comparisons in mind, the summed soil development at Tweefontein was in considerable excess of what was observed and described at the Kango Site. Summing of these three buried soils also does not take into consideration the additional soil development at the ground surface. Based on these observations it suggests the Tweefontein Terrace is likely older than 31ka (OIS 2) and 131ka (OIS 6). In addition to using the soil development as a relative age dating tool to estimate the age of the deposits at Tweefontein, Coppersmith et al. (2024) took several Cosmogenic samples that were collected at the driveway road cut outcrop. Cosmogenic samples were taken near the base of the terrace and near the top of the terrace to capture the age of the alluvial sequence. Results of these samples indicate that the upper unit was deposited about 0.7 Ma and the lower unit about 2.3 Ma, indicating the terrace is a early to mid-Quaternary unfaulted landform.

Summary: Based on a careful and systematic evaluation of Quaternary field mapping at the Hex River and Suurbraak roadcut site, along with assessment of remote sensing data, the SSM TI Team found no evidence for Quaternary faulting along the Worcester Fault. Therefore, the SSM TI Team concluded that the Worcester Fault has not been active within the Quaternary and possibly since at least the early Miocene.

8.5.5 Piketberg-Wellington Fault

Origin: In the terminology of terranes of the Malmesbury Group, the Swartland terrane is interpreted to be separated from the Boland terrane by the Piketberg-Wellington Fault (Figure 8-56). This fault is poorly exposed, and its actual trace and location are controversial (Rabie, 1948, 1974a, b; Slabber, 1995; Belcher, 2003; Kisters and Belcher, 2018). Rabie (1974b) postulated the presence of the fault to account for the juxtaposition of sheared and transposed rocks of the Swartland complex in the west against weakly deformed rocks of the Boland domain in the east. Around Piketberg in the northern area of the fault, several northwest-trending, anastomosing fault strands occur and are associated with quartz veining. Where faulting can be identified with certainty, rocks of the Cape Supergroup have been displaced, forming downfaulted outliers surrounded by Pan-African basement. This suggests a significant component of post-Cape Supergroup displacement along the fault, with both a normal sense of movement and downthrow to the east, as well as transpressional strike-slip sense of movement on other segments of the fault.

Along its southern extent, the trace of the Piketberg-Wellington Fault is not visible and can only be inferred (e.g., Theron, 1992). Despite this, Frimmel et al. (2013) suggest that the fault represents the major terrane boundary in the western Saldania Belt, but it should be emphasised that neither the location nor the extent or actual timing and kinematics of the fault have been established with any certainty.

In the geological literature, evidence for the Piketberg-Wellington Fault as well as its location were inferred based on:

- A change in structural style on each side of the fault (Rabie, 1948).
- Distinct lithological variations in the area (Rabie, 1974a, b).
- The occurrence of springs and extensive quartz veining (Hartnady et al., 1974).

- Localities where the Table Mountain Group inliers (Piketberg and Riebeeck Kasteel) have been down faulted during the Mesozoic (Theron, 1992).
- The location of the Bridgetown Formation, being accreted into its present position during terrane accretion (Rozendaal et al., 1999).

Due to the circumstantial evidence for the fault, the exact location has been in dispute (Hartnady et al., 1974; Rabie, 1974b; Visser et al., 1981; Slabber, 1995; Rozendaal et al., 1999) and its existence was questioned by De Villiers (1979).

Decision: The SSM TI Team assigned a p[S] = 0.0 to the Piketberg-Wellington Fault.

Technical Basis: Through a detailed desktop and field survey that included analysis of outcrops on optical (remote sensing) data and field mapping and observations, the SSM TI Team found no evidence for active faulting on the Piketberg-Wellington Fault.

Specifically, the SSM TI Team focussed on the review of past studies that evaluated the fault for post-Mesozoic movement. Recent field mapping efforts by Coppersmith et al. (2024) studied key localities along the strike of the fault, typically where Cenozoic deposits are draped over the fault trace and therefore recency could be determined. The SSM TI Team did not find evidence for fault slip within the Pliocene (5.3 – 2.6 Ma) or the late Miocene (11.6 – 5.3 Ma), aligned moderate- to large-magnitude hypocentres along the fault plane, or geomorphic features commonly associated with active faulting deformation. Based on the assessments of Coppersmith et al. (2024), the SSM TI Team concluded that this fault is not currently seismogenic. Therefore, the SSM TI Team infers that the Piketberg-Wellington Fault has likely not been active since at least the Mesozoic when the last evidence of significant faulting occurred in the southwestern Cape.

Evaluation: The SSM TI Team reviewed the structural style, lithological contrasts, and faulting within the Table Mountain Group sandstone inliers in an attempt to determine recency of movement. Further, a lack of Quarternary deposits along the significant rangefront implies very low sedimentation rates, and therefore, very low uplift rates in the region.

Structural style

Belcher (2003) showed that the boundaries between the different fabrics identified by Rabie (1974b) correlate with the boundary between the upper and lower units identified in his study and can be explained by regional whale-back folding without the use of major faulting. Parts of Rabie's (1974b) Swartland Terrane (Figure 8-56) have a similar structural style to the Boland Terrane. Because no structural difference was noted directly on either side of the Piketberg-Wellington Fault, the use of this varying structural style for defining the terrane boundaries is considered obsolete.

Lithological contrasts

Belcher (2003) investigated this area in detail and found no lithological or metamorphic contrasts on either side of the Piketberg-Wellington Fault in its present location, nor the location proposed by Rabie (1974a). Furthermore, the rocks on either side of the Piketberg-Wellington Fault, belonging to the Moorreesburg and Porterville Formations, are shown to have different provenances.

Faulting within the Table Mountain Group sandstone inliers

The displacement of the Table Mountain Group only indicates that these faults were active in the late Palaeozoic and into the earliest Mesozoic (e.g., Theron, 1992). There is no evidence to indicate if these faults are Pan-African-aged and were later reactivated during the Mesozoic, as suggested by Rozendaal et al. (1999), nor if there has been neotectonic activity. Hartnady et al. (1974) suggested that there are few places along the fault that show evidence of no post-Cape movement.

Recency of movement

The Piketberg-Wellington Fault was further investigated in task DDC6 of the Duynefontyn PSHA (onshore fault mapping; Coppersmith et al., 2024) and studied by the SSM TI Team. Prior to performing a field mapping campaign, desktop lineament mapping was performed to identify sites to target. In general, the most promising sites were located along the fault and were the focus of the mapping effort. The three sites of focus, from southeast to northwest, include the Platkloof River, Boesmans River, and Aurora (Figure 8-69).

Summarising the work of Coppersmith et al. (2024), the Piketberg Fault is the northern extension of the Piketberg-Wellington fault and is mapped as a series of subparallel, northwest trending faults within the Piketberg mountain range north of the Berg River. Published mapping by Visser and Theron (1973) delineates a rangefront trace that is typically defined by the Table Mountain Group to the northeast juxtaposed against the Malmesbury Group to the southwest.

The Platkloof River is one of the larger drainages that emanates from the Piketberg block. There were several topographic lineaments identified in the desktop mapping where the Platkloof River crosses the geomorphic rangefront. At the rangefront there is a dam, which was cut into an alluvial terrace (Figure 8-70). Exposures of the terrace along the bank of the reservoir indicate the deposit is generally a massive, well-sorted, loose, quartz-rich sand but these deposits are modified by anthropogenic activity and overgrown with vegetation. Coppersmith et al. (2024) estimated that the terrace may be ~10 ka in age based on the loose, unconsolidated nature of the deposits and relative height above local base level. Further they reported no systematic offset of the Platkloof River terrace was observed on either side of the dam based on walking the terraces directly over the mapped bedrock fault.

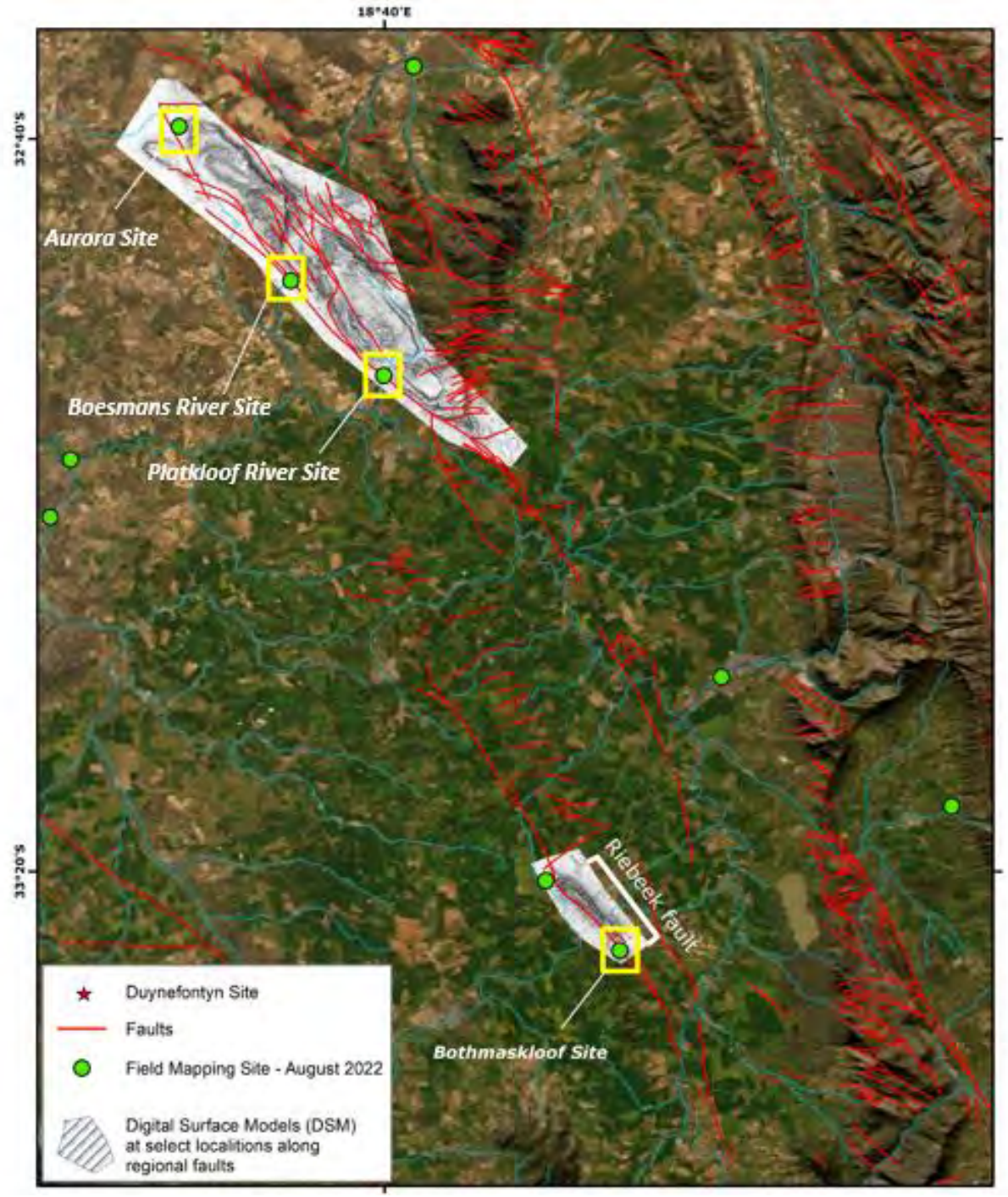

Figure 8-69. Mapping sites along the Piketberg-Wellington Fault.

Figure 8-70. View to the southwest downstream across the impounded Platkloof River. Arrows point to top of terrace surface above the high-water line of the reservoir. The location is -32.882099°, 18.666318°.

The Boesmans River is another southwesterly-flowing drainage off the Piketberg rangefront. Where the Boesmans River reaches the base of the geomorphic rangefront, the river widens appreciably from a narrowly incised bedrock channel within the Table Mountain Group to a broad flat-floored valley of the Malmesbury Group (Figure 8-71). Similar to the Platkloof River, the alluvial deposits consist of massive, well-sorted, loose, quartz-rich sand, and at the foot of the rangefront, the active channel within the broad valley floor is poorly defined. There is minor topographic relief within the alluvial deposits on the order of 2 metres. In both cases, lineaments observed in the desktop assessment appeared to be related to differential erosion, rather than surface faulting.

Figure 8-71. View to the northwest across the Boesmans River valley. Arrow is pointing to active channel and the location of regional cosmogenic uplift sample location. The planar topography northwest and outboard of the alluvial valley is bedrock. Coordinates for this location are: -32.795656°, 18.581714°.

At the northwestern end of the Piketberg block the rangefront fault splays into discrete bedrock faults. There were several topographic lineaments observed in the desktop assessment within the vicinity of the town of Aurora. Several of these were visited, but, the topographic, tonal and linear drainages observed in the desktop assessment were interpreted to be the result of differential weathering. There were no systematic offsets observed in the region. There was also a general lack of Quaternary deposits in this area.

Summary: Three field sites along the geomorphic range-front of the Piketberg fault zone that displayed promise for evaluating recency of faulting were investigated by Coppersmith et al. (2024). At all of the sites there was a scarcity of Quaternary deposits. The relative lack of alluvial sediments and terraces point toward low sedimentation rates in this area. No evidence of surface faulting was noted, which is consistent with the findings of Belcher (2003). Additionally, no evidence of offset drainages or persistent knickpoints at the range-front were observed. Based on the field and desktop analyses it is interpreted that there has not been surface faulting in at least Cenozoic times. Further, based on results of regional erosion rates, it is concluded that the range-front exists because of differential erosion in the present-day landscape rather than from active faulting.

8.5.6 Groenhof Fault

Origin: The occurrence of a series of strong earthquakes from 1969 to 1972 in the Ceres-Tulbagh area (Figure 8-72), including the E[**M**] 6.2 Ceres Earthquake, resulted in several investigations by geologists and seismologists in search of ground failure and possible surface rupture. The fault that caused the 1969 Ceres E[**M**] 6.2 earthquake was identified from aftershock sequences by Green and Bloch (1971). The epicentre of the main shock was positioned about 5 km northeast of the linear, west-northwest to east-southeast trending zone of aftershocks. A microseismicity analysis by Smit et al. (2015) further delineated the location and geometry of the fault plane in the subsurface. De Beer (2005, 2007) interpreted the earthquake to be associated with the Groenhof Fault, which they characterised as a reactivated Mesozoic fault in the structural syntaxis of the Western Cape.

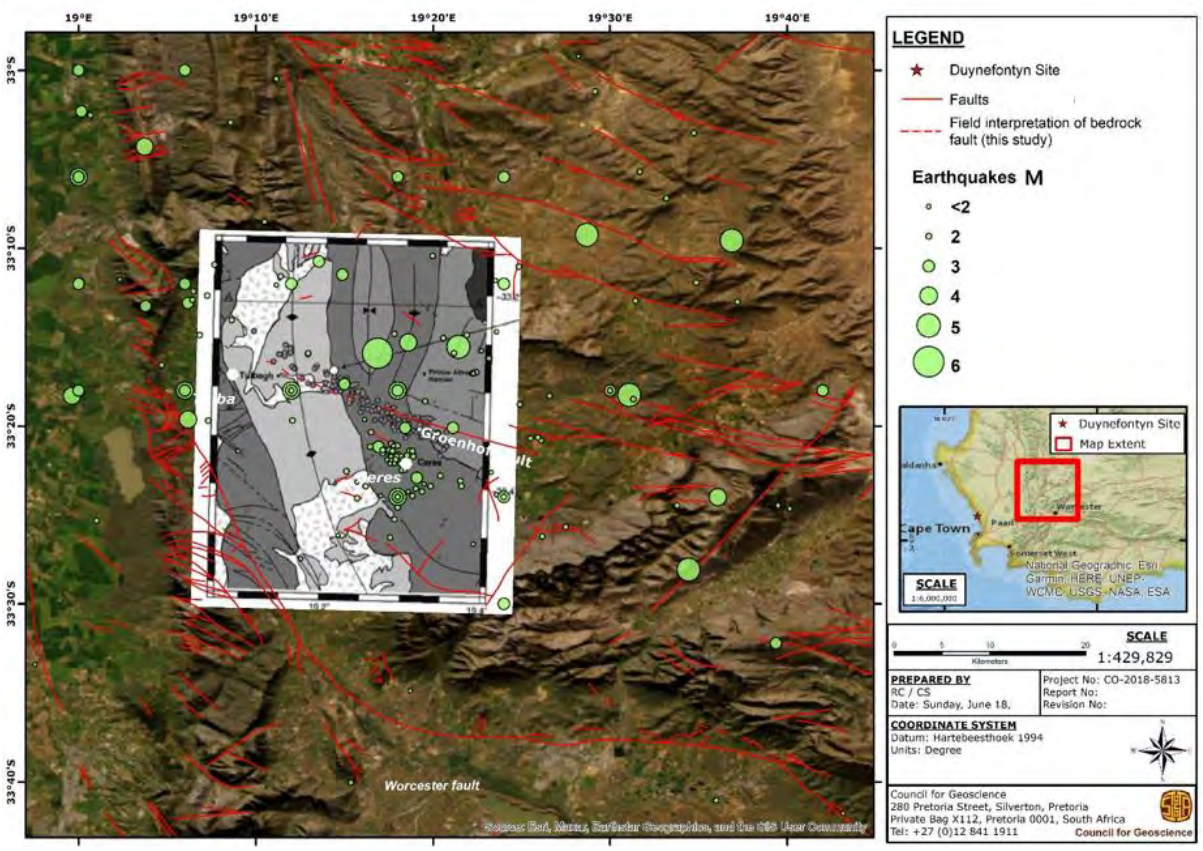

Figure 8-72. Map showing the Groenhof Fault with various seismicity datasets overlain on the ArcGIS satellite image. Green dots indicate locations of earthquakes from the project catalogue. The georeferenced figure is from Smit et al. (2015) and shows the alignment of aftershocks from the 1969 E[M] 6.2 mainshock (seen as large green dot just north of mapped fault trace). Note that the location of Ceres earthquake in the project catalogue differs slightly compared to the location in Smit et al (2015).

The fault was evaluated by the SSM TI Team as a possible fault source given the evidence that this fault is a localiser of moderate-magnitude earthquakes. In the DDC mapping activities, Coppersmith et al. (2024) mapped an unnamed fault from the previously published CGS map by Gresse (1997) and found evidence of a bedrock fault zone consistent with the orientation of focal mechanism data and microseismcity data from previous studies.

Decision: The SSM TI Team assigned a p[S] = 1.0 to the Groenhof Fault Source (GFS).

Technical Basis: The SSM TI Team carefully examined and systematically evaluated geological and seismological data to evaluate and characterise the Groenhof Fault. The fault was identified from the mainshock of the 1969 Ceres event and associated aftershocks (Green and Bloch, 1971). These datasets were evaluated by the SSM TI Team to understand the spatial association of the fault plane relative to the CGS mapped fault (Gresse, 1997) and topographic lineaments as seen in satellite imagery. An analysis of the focal mechanism for the Ceres mainshock by Kruger and Scherbaum (2014) provided insight on the geometry of the fault plane, which indicated a steeply dipping, left-lateral rupture that aligned with the microseismicity study from Smit et al. (2015) along the northwest striking plane.

These data laid the foundation for field mapping efforts by Coppersmith et al. (2024) who focussed on mapping geomorphic landforms and Quaternary surfaces to assess surface rupture and recency of faulting in the proximity of the seismicity data. The main findings from

this study revealed a distinct bedrock fault zone with little to no evidence of historical surface rupture. Based on the strong spatial correlation between the Ceres mainshock, aftershocks, microseismicity, and the location of a bedrock fault, the SSM TI Team concluded this was a fault source capable of generating moderate-to-large magnitude earthquakes. Further, geological and focal mechanism data provided sufficient information with regard to geometry and, to some degree, slip-rate to characterise the fault source in the SSM model.

While field mapping did not find direct evidence of surface rupture in response to the Ceres 1969 earthquake, the fault is spatially associated with seismicity data in the subsurface along with a bedrock fault at the surface, that included the presence of fault gouge. Therefore, the SSM TI Team concluded that the Groenhof Fault is capable of generating future moderate-to-large magnitude earthquakes and should be included as a fault source in the model.

Evaluation: The SSM TI Team evaluated seismicity datasets and findings from the geological mapping to assess the Groenhof Fault as a seismic source in the SSM (Green and Bloch, 1971; Smit et al., 2015; Keyser, 1974; Kruger and Scherbaum, 2014).

Seismicity Datasets

Green and Bloch (1971) present the results of an aftershock study carried out by the Bernard Price Institute of Geophysics (BPI) following the deployment of a temporary local seismograph network. As shown in Figure 8-73, the aftershocks delineate a near-vertical structure with an orientation close to the strike of the mapped Groenhof Fault. The authors note that the dashed line that represents the aftershock fault plane is almost parallel to the Groenhof Fault, along with some of the secondary faults on the northern end of the Worcester Fault. At Workshop 2, Sloan presented a compilation of aftershock studies (Green and Bloch, 1971) and microseismicity data (Smit et al., 2015) that aligned with the postulated extension of the Groenhof Fault appearing continuously from Ceres to Tulbagh (Figure 8-73). During the presentation, Sloan (2022) concluded that it was possible that an identifiable fault could be present, but there was no major structure expressed in this region of the Cape Supergroup. He further summarised that the microseismicity aligned well with WNW-ESE plane of left-lateral focal mechanism of Kruger and Scherbaum (2014) and that it may be associated with a fault plane.

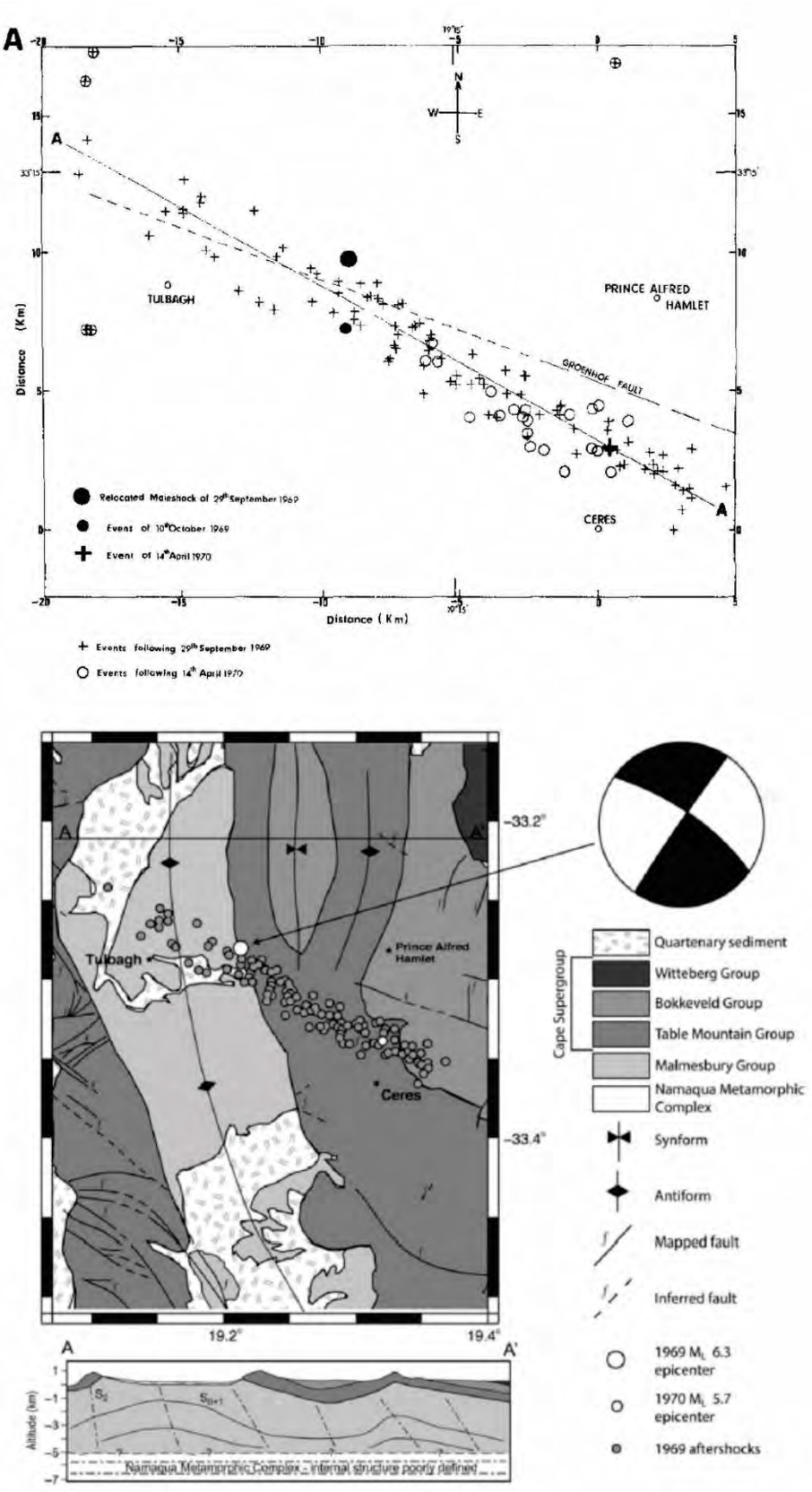

Figure 8-73 (a) Aftershock sequence from Green and Bloch (1971) showing an alignment of small magnitude earthquakes in a linear trend from the town of Ceres to Tulbagh. (b) Microseismicity map from Smit et al. (2015) study showing alignment of microseismicity. Focal mechanism of 1969 mainshock indicates a near-vertical, left-lateral fault plane solution from Kruger and Scherbaum (2014).

The SSM TI Team agrees with the interpretation in Kruger and Scherbaum (2014) that the aftershock sequence from Green and Bloch (1971) is consistent with a left-lateral solution from the mainshock focal mechanism. The microseismicity study by Smit et al. (2015) recorded microseismic events over a 3-month period in 2012, in which 172 events were recorded with magnitudes ranging from $-1.5 < M_L < 0.5$. The events delineated a 5-km wide, subvertical zone active to a depth of 15 km as seen in Figure 8-74 a-c.

Smit et al. (2015) interpreted that the microseismically active zone is guided by inherited structures in the basement geology. Geologic mapping by Coppersmith et al. (2024) considered the conclusions from these seismicity studies to guide geologic mapping efforts, as discussed below.

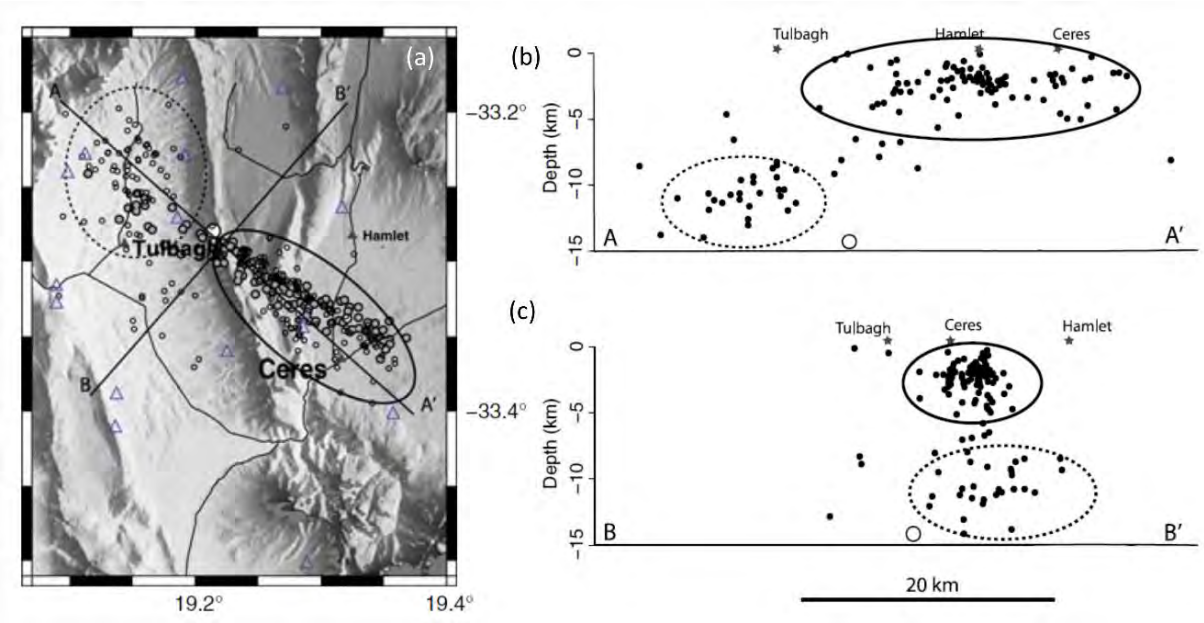

Figure 8-74. (a) Location of all microseismic events and (b and c) cross-sectional views observed by Smit et al. (2015). The grey-filled circles show the aftershocks from the 1969 M6.3 event, and the large open circle shows the 1969 mainshock (Green and Bloch, 1971). The depth of the 1969 event is estimated by Smit et al. (2015) just shallower than the maximum depth of 15 km from Kruger and Scherbaum (2014).

Geological Mapping

The SSM TI Team observed that the various epicentres of seismicity aligned with a topographic lineament that persists from the northern part of Ceres in the east to the northern end of Tulbagh in the west. The topographic lineament is defined by an alignment of linear drainages, notches, vegetation lines, and scarps. The lineament transects the southern end of a north-plunging syncline within the Cape Supergroup. At the topographic low of the axial valley is a farm adjacent to the Wakkerstroom Nature Reserve that is the main access point to the area. This area was targeted by the SSM TI Team for further geologic mapping and is documented in the onshore fault report by Coppersmith et al. (2024). Following desktop analysis of the DEM and aerial imagery, two sites were selected for more detailed mapping. These sites include the Wakkerstroom Site in the axis of the syncline, and the Tulbagh site, located in agricultural fields north-northeast of the town of Tulbagh (Figure 8-75).

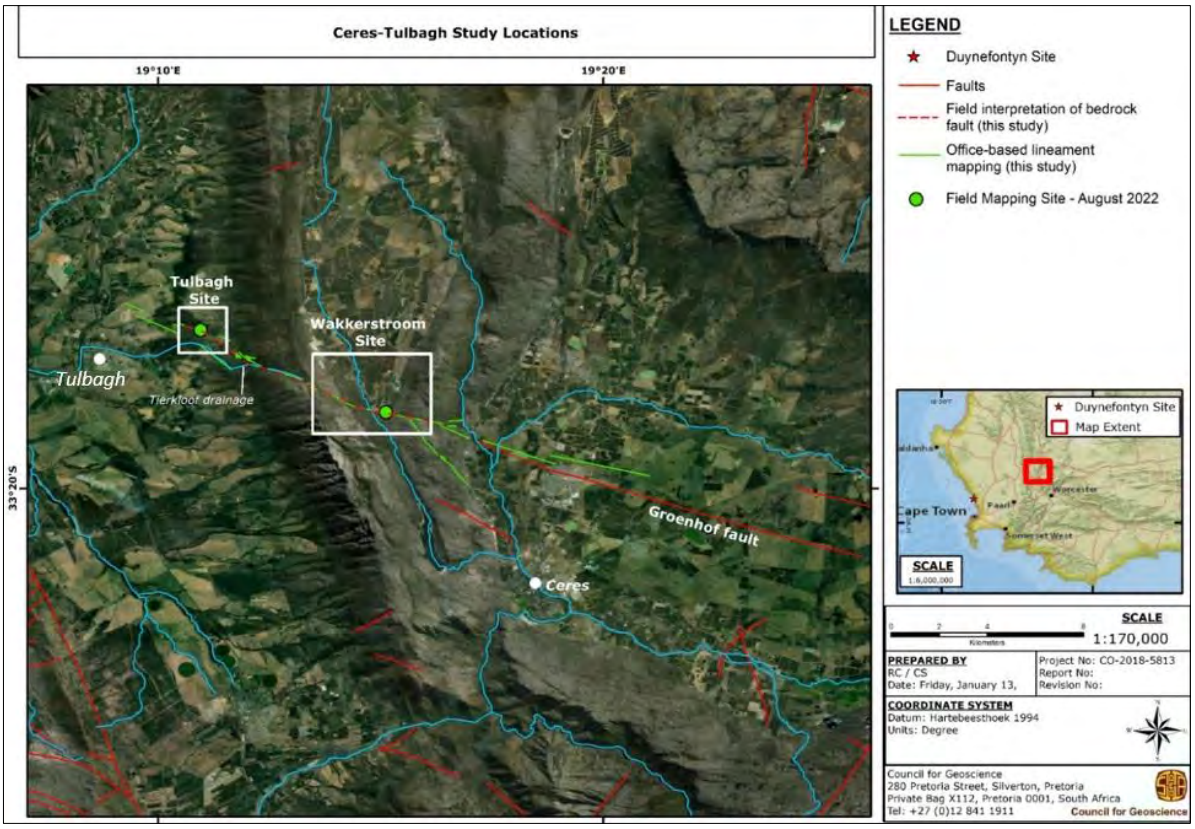

Figure 8-75. ArcGIS satellite imagery with annotations showing locations of the Wakkerstroom study area and Tulbagh study area and the postulated extension of the Groenhof Fault.

The Wakkerstroom site is located where the lineament transects the syncline and two drainages, the Koekedou River (to the west) and an unnamed drainage downstream of the Wakkerstroom Dam (Figure 8-76). These two drainages coalesce south of the lineament and are impounded by the Ceres Dam farther to the south. The drainages are separated by a planar surface. This area was targeted to (1) determine if there was an alluvial cover on the planar surface between the two drainages, and (2) determine if the scarps identified in the imagery offset the Quaternary deposits associated with the two drainages.

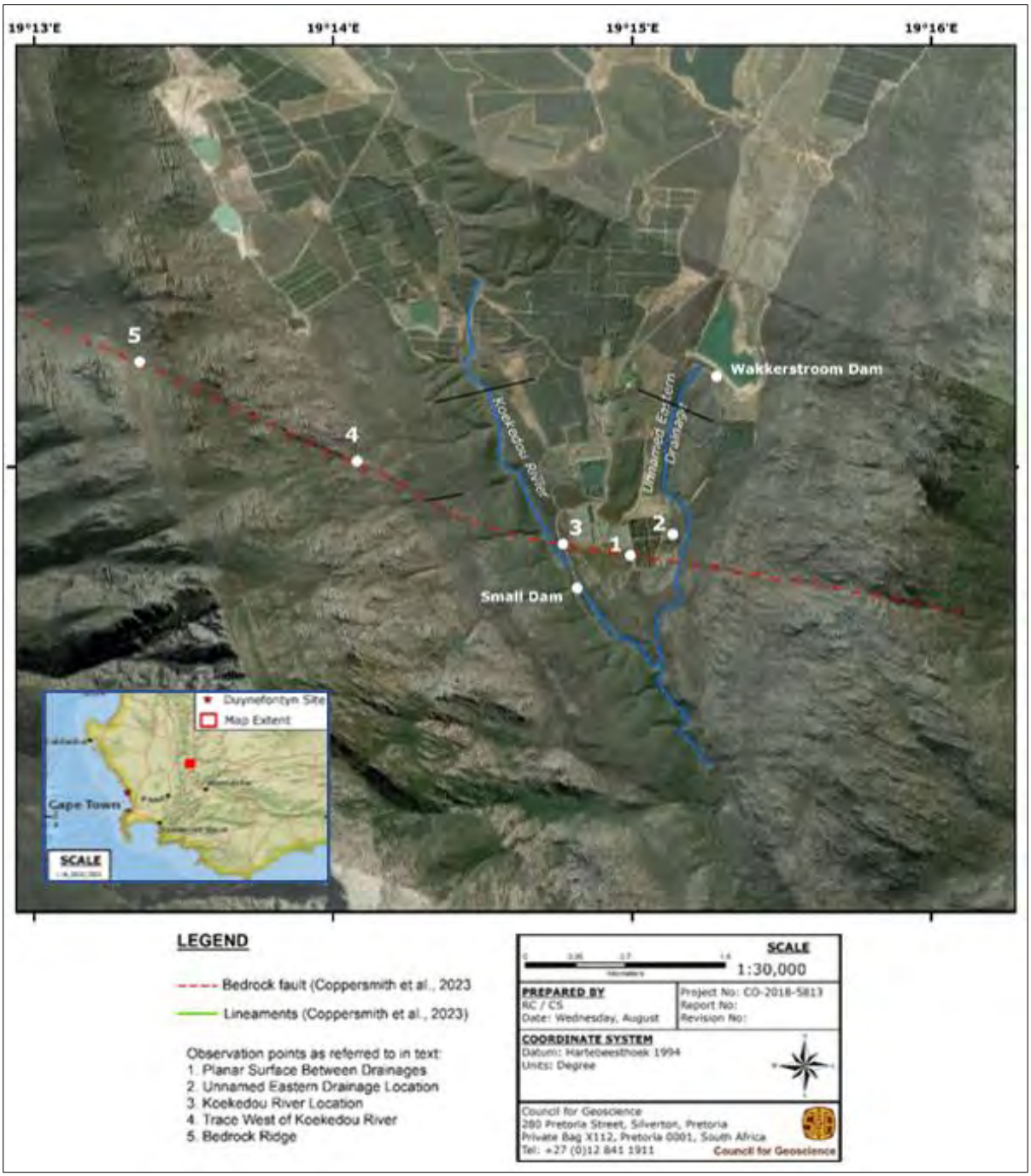

Figure 8-76. ArcGIS satellite imagery with annotations showing the location of the Wakkerstroom site. Numbers indicate localities visited during field mapping.

The observations from each of the locations on the map are summarised below. Details of each location are documented in more detail within the onshore fault mapping report by Coppersmith et al. (2024).

Location 1: The authors indicated several seeps and severely weathered, crushed quartzite bedrock that is interpreted in part to be the fault gouge (Figure 8-77). No kinematic indicators such as slickenlines could be identified within the road cut.

Figure 8-77. Photo of roadcut at west side of planar terrace (location 1 in Figure 8-76). Exposure is of severely weathered and crushed quartzite bedrock (location 33°18'15.69 19°14'45''). Note yellow field notebook for scale.

Location 2: The authors observed an approximately 1-metre-high scarp, south side down. It appeared this scarp was the result of differential erosion along the lineament and did not represent a recent surface offset due to the discontinuous nature of the scarp along strike. The surface was composed of stripped bedrock overlain by a thin (~0.5 m to 1 m) package of Holocene sand. The bedrock scarp could be interpreted as an older (pre-1969) fault scarp that has since been covered, a zone of differential erosion along the lineament from nearby fluvial processes, or surface rupture from the 1969 earthquake. The thin, mobile package re-worked sands covering the bedrock did not provide sufficient stratigraphic horizons to evaluate for recency or slip-rate.

Location 3: The authors observed no perceptible offset in the bedrock channel, or knickpoint in the stream near the trend of the fault trace to suggest there had been a significant amount of displacement in the Late Quaternary.

Location 4: The authors traversed along the trend of the fault west of the Koekedou River to an elevation of 930 m. Two notable observations were made at elevations of 850 m and 930 m along the fault trace. At an 850 m elevation, a recent road cut at the fault trend exposed a clayey gouge zone ≥ 5 m wide. Coincident with the exposed clayey material, was a spring as seen in Figure 8-78.

Figure 8-78. Left: Geologist standing on excavated clayey gouge coincident with spring activity along projection of the fault (at location 4 in Figure 8-76). Right: View looking to the west from near location 4 on Figure 8-76. Arrows point along projection of bedrock fault. White shade structures reside on the planar surface at the axis of the syncline that separates the Koekedou River from the unnamed drainage to the east.

Location **5**: During field mapping Coppersmith et al. (2024) noted the fault continuation up the ridge on the west side of the Wakkerstroom site. At the top of the ridge, along the fold limb, there are prominent steeply dipping marker beds, which were used to measure lateral offset along the fault. Utilising GIS, imagery, and the DEM, the SSM TI Team further evaluated this site to determine if offset and slip rate could be quantified across the zone. The evaluation resulted in left-lateral fault slip measurements as shown in Figure 8-79.

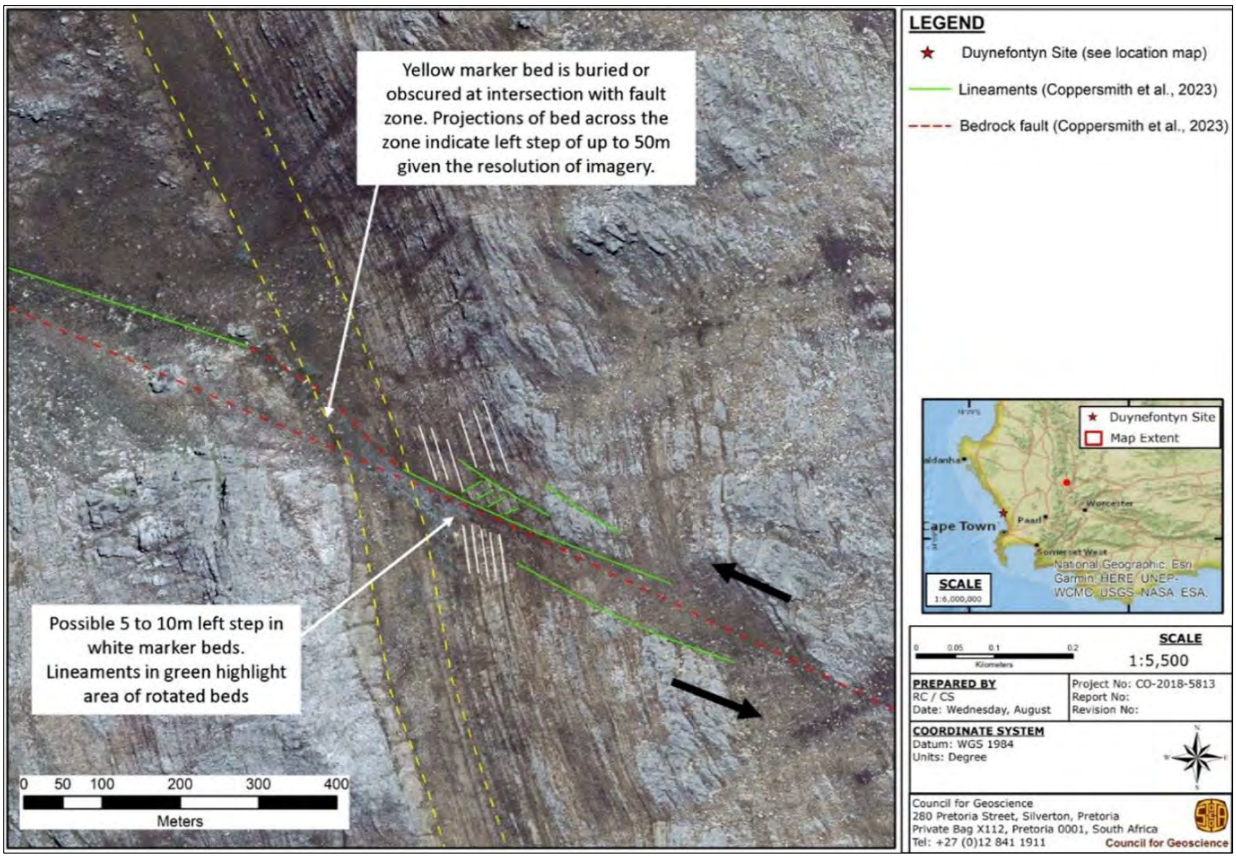

Figure 8-79. Map of fault cutting the fold limb on the western edge of the Wakkerstroom site. The red dashed line is the mapped bedrock fault, and the green lines are lineaments (Coppersmith et al., 2024). The major marker bed crossing the zone is highlighted by dashed yellow lines and the small marker beds are highlighted by white lines.

The SSM TI Team identified possible small amounts of fault slip given the uncertainty in the imagery of bedding rotations along the fold limb bedding. Upon initial mapping, it appeared that major marker beds had little to no offset. However, the resolution of the imagery is limited and therefore some lateral slip could be accommodated across the zone that is not fully visible. At a finer scale, structural complexities such as rotated bedding and small-scale splays were observed, with total displacement difficult to quantify. Projections of bedding orientation across the fault zone provided a maximum left-lateral offset across the zones. The small marker beds highlighted in white in Figure 8-80 indicated offset on the order of 5 to 10 m, while the larger marker bed highlighted in yellow indicate a maximum of 50 m of offset.

Summary: The SSM TI Team evaluated the geologic mapping by Coppersmith et al. (2024) that provided an accurate location for the Groenhof Fault. Based on analyses of the DEM and field observations, there is evidence of a northwest trending fault in the bedrock outcrops that is approximately coincident with the seismicity associated with the 1969 earthquake. The bedrock fault persists as a clayey gouge zone across the area and aligns with the regional fault, seismicity, and focal mechanism data. It is interpreted that the clayey gouge is an indicator of recent fault slip. However, because there are no kinematic indicators within the gouge, it is difficult to conclude if the gouge is a result of subsurface fault slip that created a conduit for a spring or slip at the surface. The clayey gouge is unique to this fault and may be a strong indicator of what recent fault zones look like in the Western Cape. When compared to the other faults in the Western Cape, no gouge existed even when the Cape-bedrock fault

was clearly observed. The Quaternary deposits at the Wakkerstroom and Tulbagh sites were limited and are significantly disturbed (anthropogenically) or too young to provide a meaningful strain gauge to evaluate recency of the fault trace. The fault exposed in the bedrock fold limb provided the SSM TI Team with a maximum lateral offset across the fault zone of 50 m.

Groenhof Fault Source Model: The characteristics of the Groenhof Fault Source logic tree are shown in the logic tree in Figure 8-80.

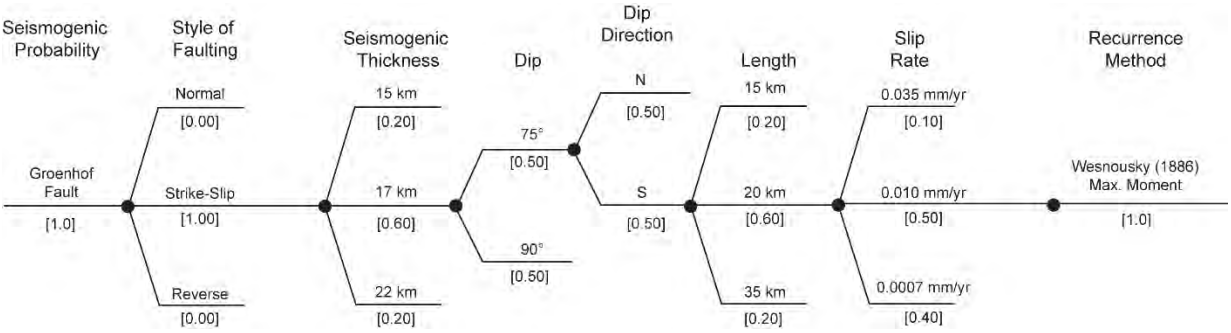

Figure 8-80. Logic tree for the Groenhof Fault source.

Style of Faulting

The Groenhof Fault is expressed in the geology as a linear, steeply dipping shear zone. Focal mechanism data by Kruger and Scherbaum (2014) show a steeply dipping, NW oriented fault plane with left-lateral motion consistent with linear aftershock sequences and micro seismicity (Green and Bloch, 1971; Smit et al., 2015) as shown in Figure 8-73b. Given these observations, the SSM TI Team characterised the Groenhof Fault as a strike-slip fault with a weight of 1.0.

Seismogenic Thickness

The depth of the 1969 earthquake is estimated to have a focal depth of around 15 km to 17 km from Kruger and Scherbaum (2014). Given the uncertainty in the focal depth and to remain consistent with the regional assessment of seismogenic thickness within the host source zone (see Section 8.2.2), the SSM TI Team developed the following seismogenic thickness distribution:

- 15 km [0.2]
- 17 km [0.6]
- 22 km [0.2]

Dip and Dip Direction

The dip and dip direction of the Groenhof Fault was entirely based on the results from the focal plane solution analysis performed as part of the Thyspunt PSHA (Bommer et al., 2013), which reviewed several existing studies, and later published within Kruger and Scherbaum (2014). These results show near-vertical fault plane solutions as seen in Figure 8-82. The analysis of the focal mechanism data was summarised in the Thyspunt PSHA (Bommer et al., 2013) and included below in Table 8-13.

Table 8-13. Summary of focal mechanism solutions for the Ceres mainshock from the Thyspunt PSHA (Bommer et al., 2013).

	Reference	Strike	Dip	Rake	Style	Method
1969-09-29 Ceres Mainshock	Fairhead and Girdler (1971)	131	82	~0	Strike-Slip	First-motion polarities of teleseismic P and PKP phases. Main fault plane selected based on strike of aftershock distribution from Green and Bloch (1971).
	Green and McGarr (1972)	317 to 321	~90	~0	Strike-Slip	First-motion P-wave polarities of 42 WWSSN long-period seismograms; main fault plane selected based on strike of aftershock distribution from Green and Bloch (1971).
	Maasha and Molnar (1972)	44 and 133	82	~0	Strike-Slip	First motion polarities and P-wave spectra for seismic moment determination.
	Shudofsky (1985)	310	82	180	Strike-Slip	Rayleigh-wave inversion and body-wave modelling.
	Wagner and Langston (1988)	124 and 217	88	~0	Strike-Slip	Waveform inversion and fitting of digitised long-period WWSSN data. Use both P and SH waves.
	Foster and Jackson (1998)	305 or 215	87	3	Strike-Slip	Waveform inversion and fitting using WWSSN body-wave data. Use both P and SH waves.
	Krüger et al. (2011)	305	78	1.2	Strike-Slip	Moment tensor inversion using scanned and digitised WWSSN data. Use both body- and surface waves.

The focal mechanism analysis results in a range of strike and dip measurements. The range of dip values from past analyses is provided in Table 8-13, with values ranging from vertical to 78 degrees, and both north and south dip directions. Based on these data, the SSM TI Team developed the following dip and dip direction distributions:

- **Dip**
  - 75° [0.5]
  - 90° [0.5]
- **Dip Direction**
  - North [0.5]
  - South [0.5]

Fault Length

To model future ruptures along the Groenhof Fault source, the SSM TI Team made an assessment of the characteristic rupture length in order to develop estimates of Mchar. The potential rupture length was measured using a combination of the previously mapped fault east of Ceres by Gresse (1997), recently mapped extension of the fault east of Ceres by Coppersmith et al. (2024), and seismicity data that suggests additional extension to the west of Tulbagh (Smit et al., 2015). Further, the northwest extension of the fault across the Tulbagh valley is consistent with the interpretation by Keyser (1974) who mapped the fault consistent with all three segments totalling 35km length. The section lengths used to define the Mchar lengths are shown in Figure 8-81.

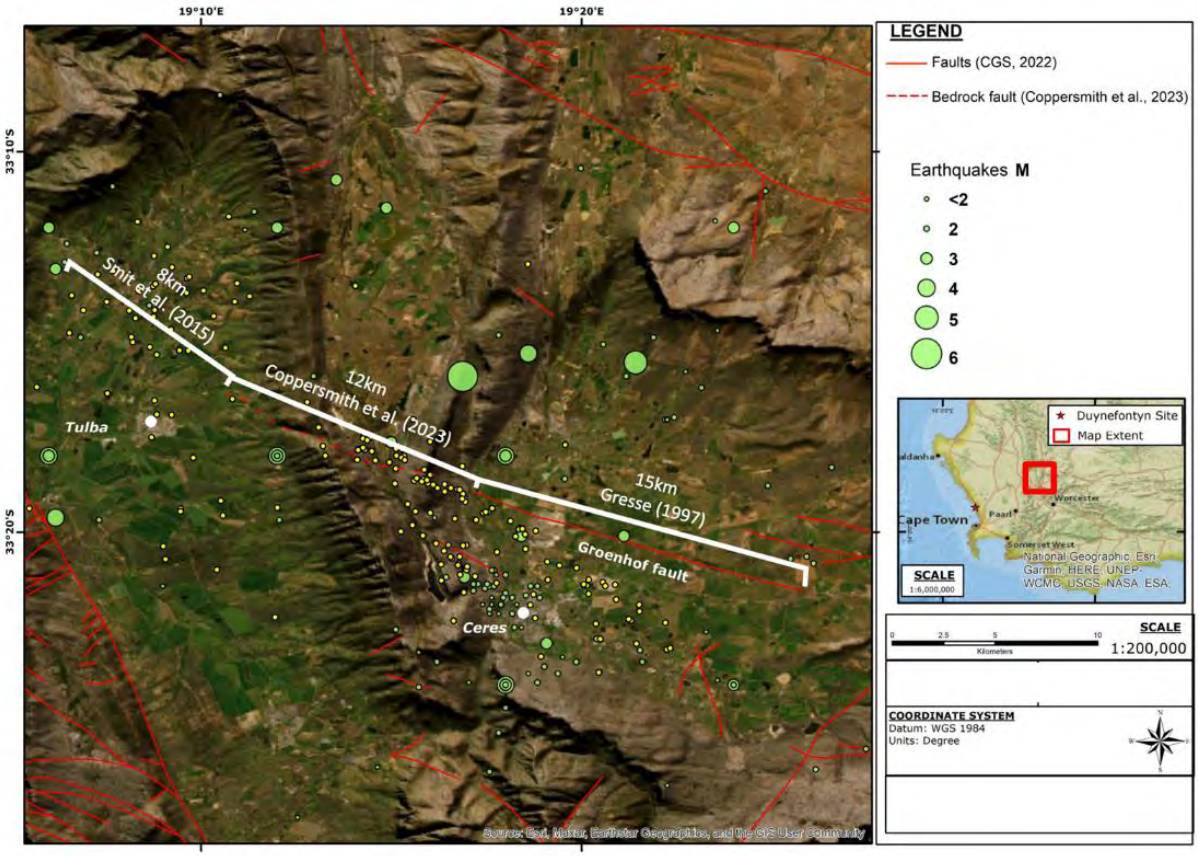

Figure 8-81. ArcGIS satellite imagery with annotations showing the Groenhof Fault trace and earthquake epicentres from the project catalogue.

Provided these lengths and to account for uncertainty, the SSM TI Team developed the following lengths to be used to estimate (Mchar) along the Groenhof Fault source:

- 15 km [0.2]
- 20 km [0.6]
- 35 km [0.2]

The technical basis for the weights was that the 15 km and 35 km represent minimum and maximum lengths of the fault. The 20 km length represented the mapped faults from Coppersmith et al. (2024) and Smith et al. (2015).

Characteristic Magnitude (Mchar)

A distribution for characteristic magnitudes (Mchar) was calculated using the relationship for strike-slip faults developed by Thingbaijam et al. (2017). Rupture areas were calculated using the rupture geometry parameters (seismogenic thickness, dip, and characteristic rupture lengths) from Table 8-14. Mmax for the Groenhof Fault is defined as 0.25 magnitude units above the largest Mchar value (**M** 6.77 + 0.25 = **M** 7.02). The resultant Mchar weights were the weighted means of the input logic-tree branches.

The SSM TI Team assessment of dip shows that the variable dips have minimal impact on rupture area. Therefore, the SSM TI Team decided to simplify the logic tree for hazard calculations to a single dip of 82.5° (average of 75° and 90°).

Table 8-14. Summary of GSF Mchar distribution.

Rupture Length (km)	Length Weight	Seismogenic Thickness (km)	Thickness Weight	Dip[1] (°)	Dip Weight	Mchar Rupture Area (km^2)	Mchar	Resultant Mchar Weight
15	0.2	15	0.2	82.5	1	226.9	6.20	0.04
15	0.2	17	0.6	82.5	1	257.2	6.26	0.12
15	0.2	22	0.2	82.5	1	332.9	6.38	0.04
20	0.6	15	0.2	82.5	1	302.6	6.33	0.12
20	0.6	17	0.6	82.5	1	342.9	6.39	0.36
20	0.6	22	0.2	82.5	1	443.8	6.51	0.12
35	0.2	15	0.2	82.5	1	529.3	6.59	0.04
35	0.2	17	0.6	82.5	1	600.1	6.65	0.12
35	0.2	22	0.2	82.5	1	776.6	6.77	0.04

[1]Note that for the hazard calculation, the average dip from 75° and 90° is used to simplify the calculations.

Slip Rate and Recurrence

As described in the evaluation of geological mapping section above, field observations did not provide strain gauges to estimate offset, short, or long-term slip rates. Therefore, the SSM TI Team characterised the slip rate distribution for the Groenhof Fault based on the potential offset fold limb measured in the bedrock at the Wakkerstroom field site. Based on GIS mapping, there are several distinct metasedimentary beds that cross orthogonal to the fault trace. Analysis of the imagery and elevation data suggest it is permissible to allow 5 to 50 m of left-lateral faulting of these bedrock stratigraphic markers. This postulated total offset could have occurred any time during or within the Cenozoic and thus provides a long-term slip rate if the permissible offset has occurred since formation of the fault. As described in Section 8.5.6, De Beer (2005, 2007) suggested that the Groenhof Fault was likely reactivated in the Late Mesozoic in the structural syntaxis of the Western Cape. By providing a broad distribution that includes long- and short-term slip rates, the SSM TI Team concluded that they accounted for epistemic uncertainty in the timing of fault initiation, the most recent event, and recurrence intervals. To simplify the distribution of age and offset scenarios, the SSM TI Team averaged the slip rates for the time periods that consider faulting since the Cenozoic, Early Quaternary, and the Middle to Late Quaternary (Table 8-15).

For a seismogenic depth of 17 km (highest weighted logic tree branch), and an average dip of 82.5 degrees, the model (considering alternative RLs) implies an average recurrence interval for E[**M**] 6.2 (corresponding to the Ceres event) of approximately 11 thousand years (11,092 years). For depth 15 km this lowers to about 9,700 years and for depth 22 km it increases to about 11,800 years. In comparison, for seismogenic depth of 17 km, average dip of 82.5 degrees, the model using slip rate of 0.01 mm/yr implies an average recurrence interval of about 38,800 years, and for the smallest slip rate (0.0007 mm/yr) implies an average recurrence interval of 555,000 years. The weighted average recurrence interval obtained for the Ceres Earthquake considering the three slip rate alternatives is 44,000 years.

Table 8-15. Slip rate estimates for the Groenhof Fault based on offset stratigraphic markers.

	Time Frame	Offset (m)	Age (years)	Slip rate (mm/yr)	Average slip rate (mm/yr)	SSM slip rate distribution (mm/yr)
Faulting since mid-Late Quaternary	Late Quaternary	5	500,000	0.0100	0.0500	
		10	500,000	0.0200		
		25	500,000	0.0500		
		30	500,000	0.0600		
		50	500,000	0.1000		**0.035 [0.1]**
	Mid-Quaternary	5	1,000,000	0.0050	0.0200	
		10	1,000,000	0.0100		
		25	1,000,000	0.0250		
		30	1,000,000	0.0300		
		50	1,000,000	0.0500		
Faulting since Quaternary	Early Quaternary	5	2,600,000	0.0019	0.0100	
		10	2,600,000	0.0038		
		25	2,600,000	0.0096		**0.01 [0.5]**
		30	2,600,000	0.0115		
		50	2,600,000	0.0192		
Faulting since Cenozoic	Neogene	5	23,000,000	0.0002	0.00100	
		10	23,000,000	0.0004		
		25	23,000,000	0.0011		
		30	23,000,000	0.0013		
		50	23,000,000	0.0022		**0.0007 [0.4]**
	Paleogene	5	66,000,000	0.0001	0.0004	
		10	66,000,000	0.0002		
		25	66,000,000	0.0004		
		30	66,000,000	0.0005		
		50	66,000,000	0.0008		

The Cenozoic time frame allows 5 to 50 m of slip over an averaged time frame of 23 to 66 Ma. This results in a long-term slip rate of 0.0007 mm/yr. The low, long-term slip rate implies infrequent earthquakes with occasional large magnitude earthquakes that are large enough to have displaced the surface incrementally over a long period of time. This observation is consistent with field observations by Coppersmith et al. (2024) who observe very old and stable landscapes in the proximity to the fault source. Given these factors, the SSM TI Team gave this slip rate a weight of 0.4.

The Early Quaternary timeframe allows 5 to 50 m of slip over the Quaternary time frame of 2.6 Ma. This results in a slip rate of 0.01 mm/yr. When compared regionally, this relatively low slip-rate is comparable to fault slip rates observed along the down-to-the-south normal Kango Fault in the Eastern Cape of South Africa. The Kango Fault is an east-west normal fault and is part of the larger Ceres-Kango-Baviaanskloof-Coega fault system extending from near the Groenhof Fault in Ceres to the east along the entire southern coast of South Africa. In the Thyspunt PSHA (Bommer et al., 2013) the Kango Fault was determined to have a short-term slip rate of 0.1 mm/yr and a long-term ("out of cluster") slip-rate of 0.01 mm/yr. Given that the Ceres region is positioned along the eastern extent of the same fault system, it is reasonable to assume that the Groenhof Fault has a comparable Quaternary history. Further, the Ceres earthquake provides evidence that the Groenhof Fault remains active and is capable of generating moderate-to-large magnitude earthquakes. Given these factors, the SSM TI Team gave this slip rate a weight of 0.5.

The Mid- to Late Quaternary slip rate allows 5 to 50 m of slip averaged over only the last 0.5 to 1 Ma. This results in an average slip rate of 0.035 mm/yr. This slip rate implies frequent large magnitude earthquakes that commonly rupture the surface throughout the Quaternary. Contrary to this, field observations suggest an old landscape with little to no active Quaternary processes that would be expected surrounding repeated surface ruptures. Further, the Late Quaternary to Holocence drainages in the valley where they intersect the Groenhof Fault lack evidence of horizontal offset that would be expected with 5 or 10s of metres of left-lateral slip. Given these lines of evidence, the SSM TI Team gave this slip rate a weight of 0.1.

Recurrence model

To model the recurrence of earthquakes along the Groenhof Fault source, the SSM TI Team used the Maximum Magnitude Model (aka Maximum Moment Model) by Wesnousky (1986). As shown in Figure 8-37 from Section 8.4.6 the Maximum Moment Model accounts for the moderate to large characteristic earthquake on a fault source and is similar to the characteristic magnitude model by Youngs and Coppersmith (1985) with the exception that there are no exponentially distributed events at small earthquake magnitudes. Given the presence of small-magnitude earthquakes in the vicinity of the Groenhof Fault source that are already modelled in the background source zone recurrence rate, the SSM TI Team chose to not use the Truncated Exponential Model (Gutenberg and Richter, 1954) or the Characteristic Model (Youngs and Coppersmith, 1985) to avoid double counting lower magnitude events.

8.5.7 Proposed Milnerton Fault

Origin: The postulated Milnerton - Cape Hangklip Fault Zone or Milnerton Fault is a NW-SE trending, ~114 km long strike-slip fault first proposed by Dames and Moore (1976) and later strongly championed by Dr Hartnady of the University of Cape Town and Umvoto Africa (Pty)

Ltd (Figure 8-82). Dames and Moore (1976, 1981) provided no data to constrain the possible age of faulting nor was any evidence provided during their investigation to determine sense of slip or amount of offset associated with the fault. They stated that the fault is based on *"circumstantial evidence"* and that, "*conclusive evidence for the fault does not exist"*. The feature was considered by Dames and Moore (1981) as a fault source in the original seismic design basis for the currently operating Koeberg Nuclear Power Plant (Section 13.1, Dames and Moore studies), but not in any subsequent PSHAs (Kijko et al., 1999; Rizzo, 2008) nor did the SSM TI Team include it as a fault source in the Baseline Report (Stamatakos et al., 2023). However, the possibility of its presence as an active tectonic fault should not be ignored and requires further investigation (Dames and Moore, 1976; De Beer, 2004, 2007; Stamatakos et al., 2022).

The Milnerton Fault Zone is inferred to be present in both the on- and offshore environments, initiating offshore, some 6-10 km NW of Koeberg/Duynefontyn, then extending across the Cape Flats and False Bay areas to its most southern on land extent across the Hangklip and Rooi-Els areas before terminating 5-10 km offshore (Dames and Moore, 1976; Hartnady, 2003) (Figure 8-82). The fault's location as interpreted by Dames and Moore (1976, 1981) appears slightly different than that of Hartnady (2003), who envisioned the proposed fault occurring slightly more towards the NE near the fault's northern extend and slightly more SW towards its southern extent than Dames and Moore (1981) (Figure 8-82b). Hartnady (2003) also elected to show the proposed feature as a fault line rather than the roughly 5-6 km fault zone indicated by Dames and Moore (1981). No justification is provided for the width of this fault zone by Dames and Moore (1981). The fault does not occur on any of the published geological maps of the area (Haughton, 1933a, b; Visser and Schoch, 1973; Theron, 1984a, b, c; Theron, 1990; De Beer et al., 2008; Siegfried, 2019). Discerning its presence or absence in the area is undoubtably hindered by the presence of extensive Neogene-Quaternary cover of the Sandveld Group and the densely populated and built-up areas of the Cape Flats that make obtaining reliable geophysical surveys results difficult (Dames and Moore, 1976; De Beer, 2007). Direct geoscientific evidence to support the existence of such a major structural discontinuity is thus lacking.

Its location and extent as defined by Dames and Moore and Hartnady (2003) was based on interpretation of five points of circumstantial geoscientific evidence all deemed to be associated the occurrence of a single fault zone within both the onshore and offshore settings (Dames and Moore, 1976, 1981, Hartnady, 2003; De Beer, 2004; Claassen et al., 2024). Circumstantial evidence points used to argue the proposed fault zone are:

1. The morphology of the Cape Flats as an expression of a sizeable shear zone.
2. Brittle deformation observed in exposures of the Malmesbury Group near Bloubergstrand.
3. An interpreted shear or fault zone east of Cape Hangklip identified on Landsat imagery.
4. Historical seismicity in the Cape Town region.
5. An NNW trending bathymetric anomaly mapped on the seafloor 8 km west of Koeberg.

For ease of reference, the location of each of these data points are provided in Figure 8-83.

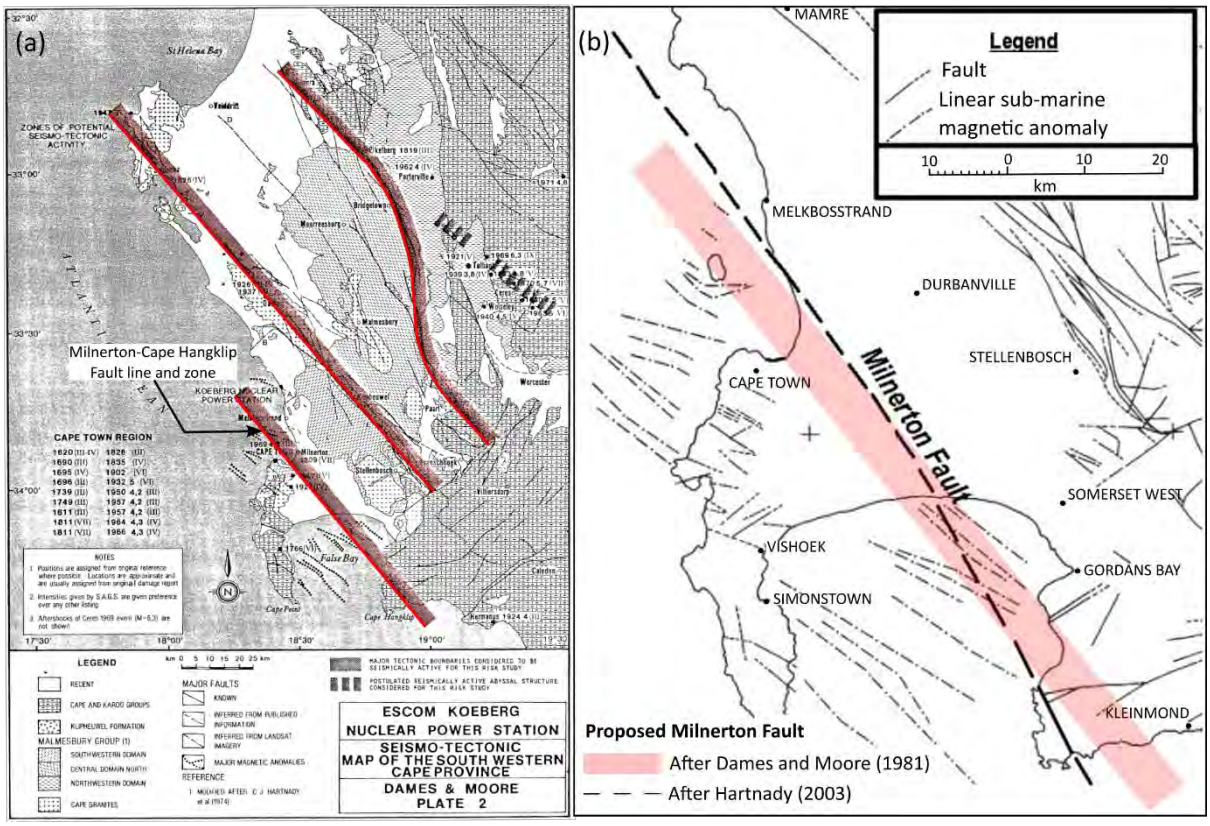

Figure 8-82. The location of the Milnerton Fault as proposed by (a) Dames and Moore (1976, 1981) and (b) Hartnady (2003), copied from Plate 2 of Dames and Moore (1981). The depiction of the faults in (a), solid lines and shaded zones, was the interpretation of the original authors and has no special significance to the SMM TI Team's evaluation.

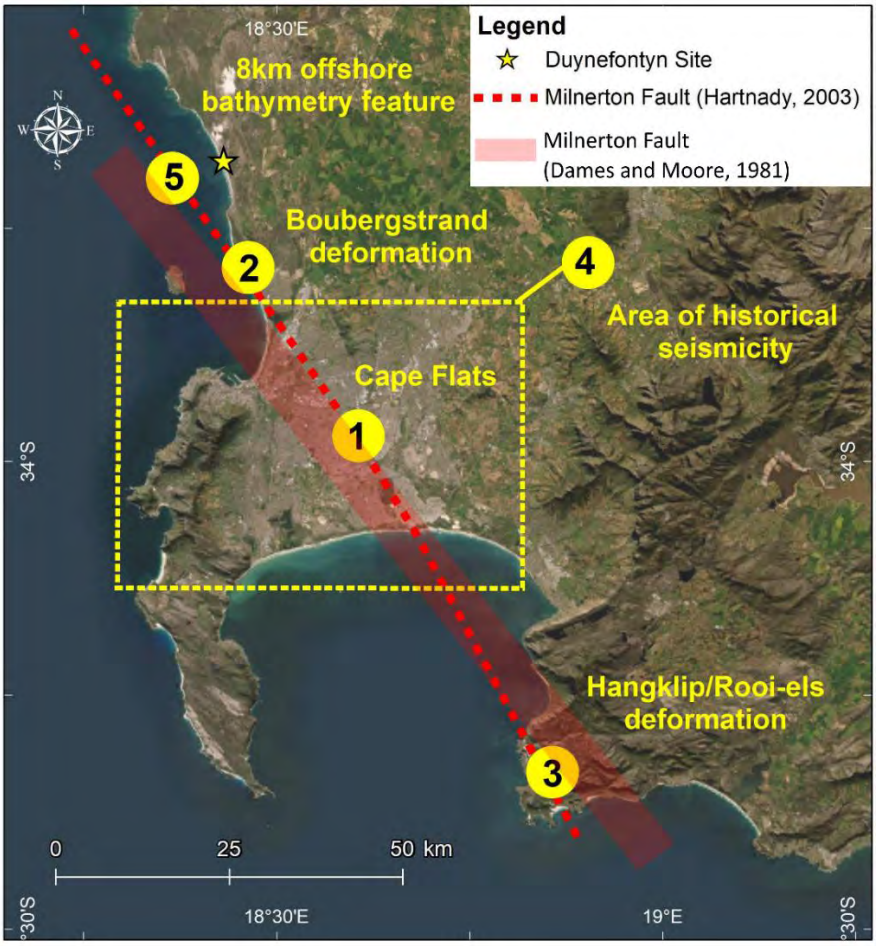

Figure 8-83. The location of circumstantial geoscientific data points of arguments originally outlined in the proposal of the Milnerton Fault Zone by Dames and Moore (1976, 1981) and fault line by Hartnady (2003).

Decision: The SSM TI Team assigned a p[S] = 0.0 to the Milnerton Fault Zone.

Technical Basis: Considering the ambiguity associated with the Milnerton Fault Zone and the fact that it has gained public notoriety as the main source of seismicity in the Cape Town area (e.g., Gosling, 2011; Becker, 2020; Theunissen, 2020) as well as published technical and scientific reports that include it as contributing to, or controlling the seismic hazard at the Koeberg site (e.g., Hartnady, 2003; De Beer, 2007; Dames and Moore, 1976, 1981), the SSM TI Team decided to re-investigate and scrutinise the validity of the original proposers' circumstantial points of evidence in accordance with current geoscientific data in the region. The SSM TI Team's evaluation consisted of a comprehensive review of existing data that included regional geomorphology, geology, on- and offshore aeromagnetics and seismicity data (Von Buchenröder, 1830; Haughton, 1933a, b; Von Vey, 1982; Day, 1986; De Beer, 2004, 2007; Cole, 2007; Cole et al., 2007a, b; Raath et al., 2007; Fugro, 2007). The SSM TI Team also undertook additional data collection activities aimed at investigating the fault's presence or absence, location, characteristics, and activity (T. Dhansay personal communication, 2021; Cole, 2022; Albini and Flint, 2023; Claassen et al., 2024; Cawthra and Van Zyl, 2023; Claassen et al., 2024; Mulabisana, 2023).

The SSM TI Team re-assessed and evaluated the validity of each of the geoscientific points of argument originally outlined in the inference of the Milnerton Fault Zone (Dames and Moore,

1976, 1981; Hartnady, 2003). The SSM TI Team could not find conclusive evidence that a fault zone of the kind proposed by Dames and Moore (1976, 1981) and Hartnady (2003) exists, nor any evidence of fault slip in the Quaternary (2.6 - present), the Pliocene (5.3 – 2.6 Ma) or even the late Miocene (11.6 – 5.3 Ma). There are no aligned moderate- to large-magnitude hypocentres along the fault plane, or geomorphic features commonly associated with active faulting deformation. Therefore, the SSM TI Team did not consider the proposed Milnerton Fault to be an active seismic source.

Evaluation: The SSM TI Team evaluated and assessed the detailed geological and geophysical evidence cited in support of the Milnerton Fault Zone at each of the five locations discussed above. For each location, the evaluation by the SSM TI Team includes the set of arguments cited in the literature in support of the Milnerton Fault Zone (*Arguments*) and the SSM TI Team's assessment of that evidence (*Assessment*). Investigations and analyses undertaken by the Duynefontyn Data Collection supporting studies, to determine possible neotectonic activity associated with such a proposed fault zone (*Activity*), is also outlined.

The Cape Flats

Argument: The Cape Flats is a relatively flat area defined by a broad, low-lying topography blanketed by Quaternary cover and flanked on either side by mountainous Table Mountain Group relief, with the Cape Peninsula Mountains to the west, and the Hottentots Holland Mountains to the east (Figure 8-84a, b). Haughton (1933b) was the first geologist to provide a possible geological explanation for the landscape morphology, suggesting that it was indicative of a sizeable shear zone. He proposed that the Cape Flats were the result of faulting within a rift-valley-type structure or series of stepped faults in what would have been a synclinal trough bounded by anticlinal structures on either side (Figure 8-84c); this interpretation was accepted by Dames and Moore (1976) as circumstantial evidence for the Milnerton Fault Zone.

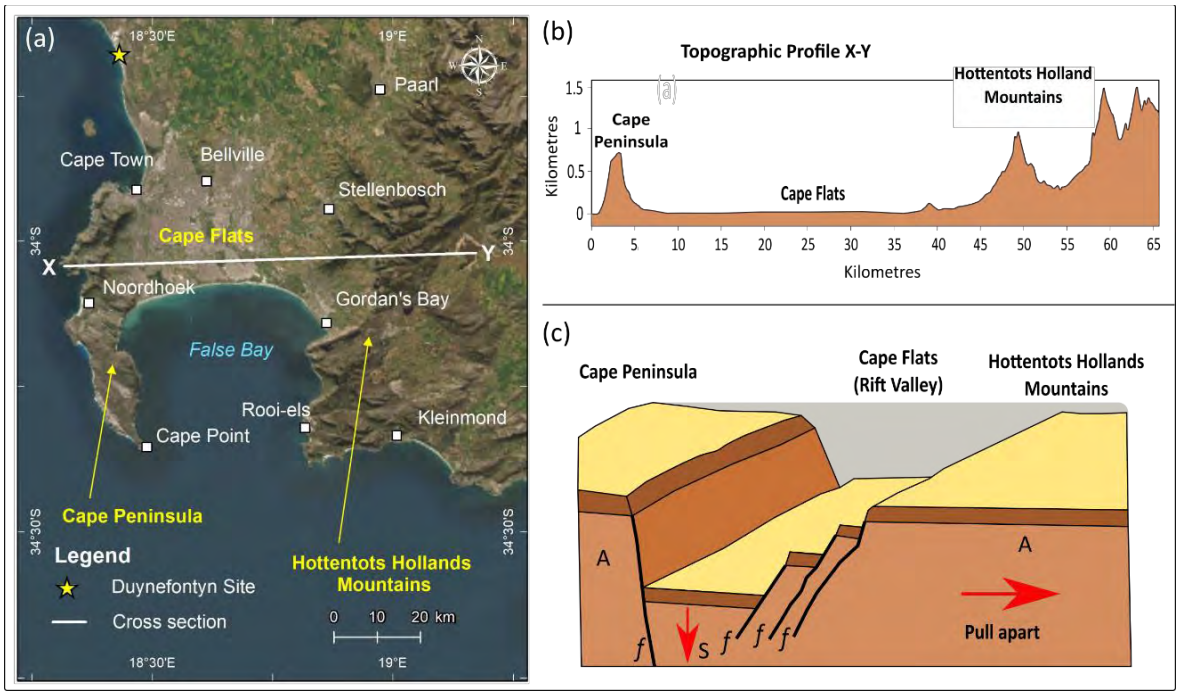

Figure 8-84. (a) Locality map of the Cape Flats showing (b) the position of the topographical profile X-Y. (c) A sketch to illustrate the structural mechanism that Haughton (1933b) proposed for the formation of the Cape Flats. A and S show upthrown and downthrown blocks in the rift valley.

Sloan (2022) also presented unpublished interpretations by Dr Hartnady at Workshop 2 that argued high yielding groundwater boreholes drilled into intensely fractured bedrock at the Cape Flats provide evidence for a buried fault zone, which he believed to be the proposed Milnerton Fault Zone.

Another line of possible evidence cited in support of the Milnerton Fault Zone are the observed onshore magnetic anomalies northeast of Cape Town. Cole et al. (2007a) mapped a NW-SE linear magnetic anomaly identified as a possible large fault zone and interpreted to be possibly part of the Milnerton Fault Zone. Raath and Cole (2007) conducted follow-up ground magnetic, multi-electrode resistivity and gravity surveys (Traverse 1, 2 and 3) (Figure 8-85) to try and confirm the presence of the Milnerton Fault Zone. All survey results were ultimately inconclusive, being unable to prove or disprove the existence of the Milnerton Fault Zone.

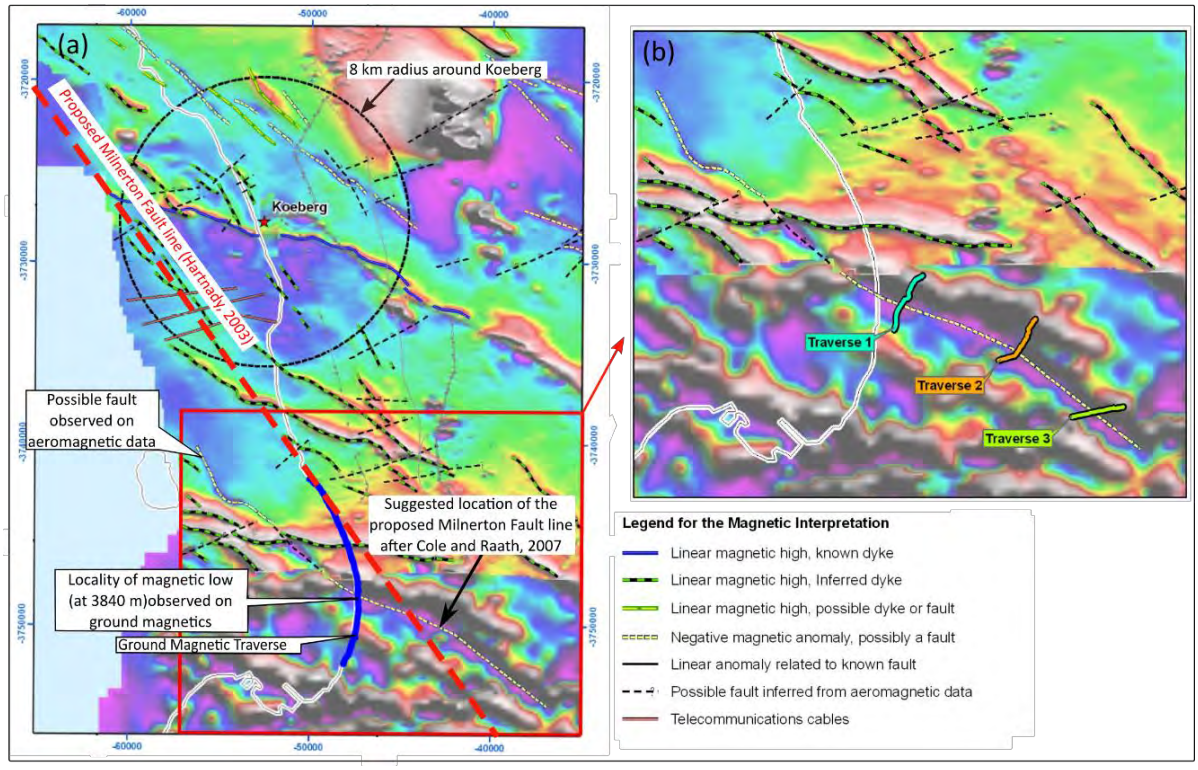

Figure 8-85. (a and b) Airborne magnetic maps showing the locality of the three gravity traverses conducted across the linear magnetic feature possibly associated with the hypothesised Milnerton seismic source (Cole and Raath, 2007).

Assessment: At the time of Haughton's (1933b) interpretation, eustacy studies were in their infancy (e.g., Krige, 1927) and although authors did map marine bedrock-cut terraces and marine-related deposits (Rogers, 1905, 1906; Haughton, 1931, 1933a, b) as it relates to sea-level change along the South African coastline at the time, the impact of sea-level fluctuations was not considered as a possible explanation for the Cape Flats' morphology.

Subsequent research has revealed that over the last 5 My repeated cycles of sea level fluctuations associated with erosion, sediment transport and deposition processes, have greatly influenced the sculpting of the landscape, contributing to the formation of the flat plains, estuaries, barrier systems, and dune fields that now characterise the surface morphology and subsurface lithostratigraphy of the Cape Flats (Compton, 2004; Hay and Seyler, 2008; Roberts et al., 2013; Lecea et al., 2016) (Figure 8-86). Major regressive periods, such as the Oligocene

(~ 25 Mya) and the last interglacial (~20 kya), when sea-levels dropped ~125 m bmsl, left the Cape Flats and the entire bottom of False Bay exposed to weathering and erosion processes resulting in the removal of material from higher areas and the formation/erosion of valleys (Figure 8-86). Borehole data (Henzen, 1973; Vandoolaeghe, 1989; Wessels and Greef, 1980; Hay, 1981) used to interpolate palaeobedrock topography beneath overburden cover, confirm that the top of bedrock occurs far below sea-level up to 13 km inland across large portions of the Cape Flats. A large ~5-km-wide, ~ 8.5-km-long, V-shaped, NW-SE trending, coast perpendicular palaeovalley is cut into strata of the Malmesbury Group reaching a maximum depth of 53.69 m bmsl along the western side of the Cape Flats (Figure 8-87).

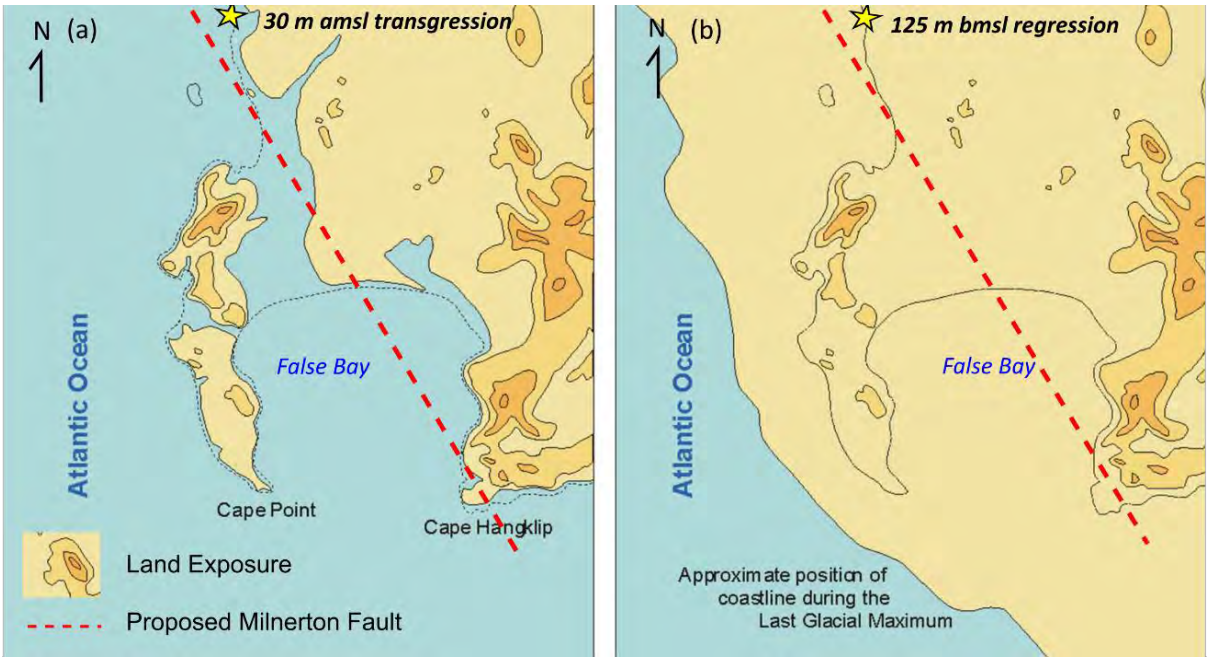

Figure 8-86. (a) The southwestern Cape shoreline shape with a 30 m higher sea level that occurred during the Pliocene, and (b) a 125 m lower sea level during the last glacial maximum 20,000 kya (after Compton, 2004). The location of the proposed Milnerton Fault as defined by Hartnady (2003) is also indicated.